IMPROVED CHARACTERISATION AND MODELLING OF MICROBUBBLES IN BIOMEDICAL APPLICATIONS

Jean-Pierre O'Brien

A thesis submitted in partial fulfillment

of the requirements for the degree of

Doctor of Philosophy

at

University College London.

Department of Mathematics

University College London

2013

I, Jean-Pierre O'Brien, confirm that the work presented in this thesis is my own. Where information has been derived from other sources, I confirm that this has been indicated in the thesis.

ABSTRACT

Interest in coated microbubbles as agents for therapeutic and quantitative imaging applications in biomedical ultrasound has increased the need for their accurate modelling. However, effects such as gas diffusion, the properties of the coating and changes in bubble behaviour under repeated ultrasound pulses are still poorly understood. The work described in this thesis attempts to develop new theoretical descriptions of microbubble behaviour to address this challenge.

In the first part of the thesis, a model of gas exchange into and out of bubbles in tissue under a varying external pressure is developed and applied to the computationally simpler problem of decompression diving. It is concluded that gas diffusion can explain bubble growth and the model validates current decompression algorithms. In the second part of the thesis, a revised equation of motion for microbubble oscillation is proposed that includes the effects of gas diffusion and a time-dependent surfactant surface concentration. This is subsequently incorporated into a nonlinear wave propagation model to account for these additional effects in the response of microbubble contrast agents to ultrasound excitation. Furthermore, the accuracy of a recently proposed computationally efficient method of modelling nonlinear propagation through a polydisperse bubble population is investigated. However, the approximation is concluded to be insufficiently accurate for parameter regimes corresponding to biomedical ultrasound.

The results from the new model for microbubble dynamics indicate significant changes in both bubble behaviour and the character of the propagated pulse, demonstrating better agreement with experimental data than predictions from existing models. The results strongly suggest that changes in bubble dynamics are dominated both by surfactant shedding on ultrasonic timescales and gas diffusion over longer timescales between pulses. Incorporating such time-dependent phenomena in ultrasound imaging algorithms should lead to better quantitative agreement with experiment and guide future improvements in the clinical implementation of microbubble contrast agents.

ACKNOWLEDGEMENTS

I am immensely grateful to my supervisors Dr Nick Ovenden and Dr Eleanor Stride for their advice, enthusiasm and encouragement throughout my PhD. This work would not have been possible without their friendly support and I feel privileged to have worked with such passionate, knowledgeable and inspirational people.

I would like to thank EPSRC for their funding throughout this PhD as well as VR Technology and the Knowledge Transfer Network (sponsored by EPSRC) for their funding during my six month internship at VR Technology. My thanks go to Dr David Leppinen for his useful discussions on bubble modelling and especially Nick Bushell, who was a constant source of ideas, inspiration and poetry during the internship.

As a mathematician who has a natural fear of laboratories, I am indebted to all those who provided me with experimental data against which to compare my theoretical models, and then took the time to explain to me so patiently what it was they had provided me with. Consequently, my thanks go to Dr Helen Mulvana, Dr David Thomas, Sheetal Sanak and particularly Jacopo Viti.

Finally I would like to thank my parents, Keith and Chantal. Without their belief and constant support, I would not have achieved so much. I owe them everything.

CONTENTS

LIST OF FIGURES

LIST OF TABLES

NOMENCLATURE

Variables

B_b	Interior of bubble b
$c_b(t)$	Concentration of gas inside bubble b
$c(\boldsymbol{x}, t)$	Gas concentration
$C(\boldsymbol{x}, t)$	Surfactant concentration
L	Reflection coefficient
m	Mass
M	Molar mass
n	Number of moles
$p(\boldsymbol{x}, t)$	Pressure
$R(t)$	Bubble radius
$\dot{R}(t)$	Bubble radial velocity
$\ddot{R}(t)$	Bubble radial acceleration
t	Time
T	Transmission coefficient
$\boldsymbol{u}$	Velocity
V	Volume
θ	Azimuthal angle
ϕ	Elevation angle
$\Gamma(t)$	Surface concentration of surfactant
ψ	Velocity potential
ν	Volume difference

Constants

a	Attenuation
B	Tissue bulk modulus
$\mathcal{C}$	Wavespeed
C_p	Specific heat
D	Diffusivity
E	Tissue modulus of tissue elasticity
G	Universal gas constant
k	Wavenumber
k_H	Henry's constant
K	Thermal conductivity
N	Number of bubbles/number of radius bins
T	Temperature
T_x	Tissue length in x-dimension
T_y	Tissue length in y-dimension
V_T	Volume of tissue affected by bubble growth
Z	Acoustic impedance
α	GT/M
β	Gas volume fraction
δ	Damping coefficient
γ	Polytropic index
κ	Adiabatic stiffness
λ	Wavelength
μ	Shear viscosity
μ_{s}	Shell surface viscosity
ρ	Density
σ	Surface tension
ω	Angular frequency
ω_{N}	Natural frequency
Ω	Extinction cross-section

Functions

$\langle \bullet \rangle$	Average
$h_n^{(1)}(x)$	n$^{\text{th}}$-order spherical Hankel function of the first kind
$j_n(r)$	n$^{\text{th}}$-order spherical Bessel function
$P_n^m(x)$	Legendre polynomial of degree n and order m
$Y_n^m(\theta, \phi)$	Spherical harmonic
$n(R)$	Scatterer density

Sub- and superscripts

$\bullet_0$	Initial/typical medium value
$\bullet_b$	Bubble
$\bullet_{\text{eff}}$	Effective medium
$\bullet_{\text{eq}}$	Equilibrium value
$\bullet^{\text{ex}}$	Exciting
$\bullet^{\text{ext}}$	Exterior
$\bullet_g$	Gas
$\bullet^i$	Type of gas: N_2, He or O_2
$\bullet^{\text{inc}}$	Incident
$\bullet^{\text{int}}$	Interior
$\bullet_l$	Liquid
$\bullet_{\text{s}}$	Surfactant
$\bullet^{\text{sca}}$	Scattered
$\bullet_v$	Vapour
$\bullet_\infty$	Value in the bulk medium at infinity

CHAPTER 1

INTRODUCTION

1.1 Background and motivation

Microbubbles within the human body arise both naturally and artificially as a result of injection. If arising naturally, from gas dissolved in the blood coming out of solution, they can have potentially harmful effects (Bert, 1878), including vessel occlusion (Hsu et al., 1992), joint damage (Edmonds and Thomas, 1972) and neurological effects (Todnem et al., 1991), if the escape of gas is not controlled in some way.

However, not all bubbles are unsafe; for instance, ultrasound is a real-time and safe non-invasive method of imaging inside the human body (Kaul, 2008). In order to enhance the contrast of the image, contrast agent microbubbles have been used extensively in the last 25–35 years. These microbubbles, of radius less than $8\,\mu$m, and stabilised by an outer coating, can easily traverse the circulatory system without the risk of occlusion.

The effectiveness of bubbles in enhancing the contrast between the blood vessels carrying them and the neighbouring tissue is due to the difference in density and compressibility between the gas inside the bubbles and the liquid surrounding them (Stride and Saffari, 2003). When excited by ultrasound (frequencies of ~ 1–$15\,$MHz are used in medical imaging) the microbubbles oscillate nonlinearly, radiating back to the receiver a proportion of the incident ultrasound energy. The harmonic content in the radiated signal can be exploited to achieve even greater contrast in the image since the surrounding tissue produces a predominantly linear response.

These particles also have applications in gene and drug delivery (Ferrara, Pollard and Borden, 2007). The close proximity of these particles to cell walls can lead to disruption of the cells' transport systems as they oscillate, providing an opportunity for uptake of a drug

encapsulated inside the bubble or a gene attached to its surface. By attaching a ligand to the bubble that is directed at a particular cell surface receptor, targeted drug or gene delivery can be achieved when applying ultrasound locally to the microbubbles.

However, the behaviour of microbubbles is by no means fully understood. In particular, the manner in which a dense population of resonant microbubbles responds and interacts with the incident and scattered ultrasound fields cannot as yet be described theoretically (Stride and Saffari, 2005). For instance, when the volume fraction of bubbles is high, sound scattered by one bubble is likely to impinge on others which in turn will re-scatter the sound to further bubbles and so on, known as "multiple scattering". Attempts have been made to simplify the equations governing multiple scattering by assuming small amplitude oscillations of the bubbles (Commander and Prosperetti, 1989), but these assumptions are not valid at the ultrasound frequencies and pressure amplitudes typically used in medicine when the bubbles are likely to be resonant and their oscillations highly nonlinear.

Furthermore, the stability of microbubbles in the human body is enhanced by the presence of surfactants adsorbed onto their surfaces. This coating reduces both the surface tension of the microbubble and the diffusion of gas into the surrounding liquid. Such surfactants will also affect the microbubble's characteristics (Stride, 2008), particularly its time-dependent behaviour. Current theories assume that the total mass of surfactant on the bubble surface remains constant during insonation. It has been postulated, however, that surfactant "shedding" can occur leading to changes in bubble dynamics between consecutive oscillations (Borden et al., 2005). On longer timescales, the diffusion of gas out of the bubble has an important effect on the equilibrium bubble size (Fyrillas and Szeri, 1994, 1995) and consequently, also upon the response of the bubble. Thus over the several minutes required for an ultrasound scan, the bubble population may be changing significantly, but currently, models fail to take such phenomena into account.

1.2 Outline of the thesis

The aim of this thesis is to address some of the outstanding problems in this field and develop novel mathematical descriptions of phenomena which are common to modelling nonlinear wave propagation through a population of bubbles as well as bubble growth in tissue. This section provides a brief overview of the subject of the thesis and content of the individual chapters. The relevant background literature is reviewed at the start of each chapter according to the specific topic under investigation.

The work described in Chapter 2 investigates the relatively slow process of gas diffusion into tissue and attempts to model bubble growth during slow pressure changes. A literature review of diffusion theory as applied to bubbles is presented in Section 2.1 followed by a review of literature highlighting the challenges of understanding decompression sickness and a history of decompression models in Section 2.2. A model is subsequently developed where the problem is reduced to a two-dimensional block of tissue surrounded by blood vessels, containing bubble nuclei that can never shrink below a certain size and the gases – which are assumed to comprise the breathing gas dissolved in the blood – are nitrogen, helium and oxygen. The diffusion of each gas into and out of the tissue is governed by a separate diffusion equation, where the convection term in the equations can be neglected since the bubble wall velocities are small. These equations are used to calculate the flux of gas across the boundary of each bubble thus enabling the radius to be calculated.

The coupled tissue-bubble model simulates bubble growth in tissue during decompression in Section 2.4. At the start of the simulation, depth and gas mixture profiles are prescribed that simulate realistic dive scenarios. The entire problem is solved numerically using a finite difference scheme and the time-evolution of the bubble radii are recorded. By repeating this for a number of different dive profiles, conclusions may be drawn about bubble growth in tissue that enables further validation of current diving practices and decompression algorithms.

An equation of motion that aims to take into account the time-dependent behaviour of a lipid-coated microbubble during repeated exposure to ultrasound pulses is developed in Chapter 3. To better understand the problem, a literature review of free and encapsulated bubble dynamics models is presented in Sections 3.1 and 3.2 respectively. Initially, a Rayleigh-Plesset type equation models the microbubble's oscillations in the sound field. To account for the fast rate of change in lipid concentration on the bubble surface during oscillation, it is assumed there is a finite maximum packing concentration above which surfactant is "shed" into the bulk (external) fluid. Close to equilibrium however, the concentration of surfactant on the bubble surface is assumed to be governed by Langmuir adsorption except at high concentrations when the surfactant is assumed to be insoluble. By coupling this equation of motion including modified surfactant boundary conditions, with a surfactant-dependent surface tension, behaviour observed in recent experiments can be successfully explained. For the slower rate of diffusion, separate convection-diffusion equations for air, perfluorocarbon and surfac-

tant in the bulk solution are coupled with the equation of motion. The governing equations are initially analysed using a multiple scales approach leading to conclusions about the typical timescales on which shedding occurs. The equations are subsequently solved numerically for a single bubble and the results compared with data from acoustical and optical experiments.

Chapter 4 introduces multiple scattering and Section 4.1 presents a literature review of some of the main theories that have been developed, corresponding to the much faster timescale of an ultrasound pulse. Particular attention is drawn to the nonlinear scattering theory in Section 4.3.1 which will be used subsequently in this thesis, and for which it is important to note the parameter regimes when the model is an accurate approximation.

The nonlinear scattering theory is investigated further in Section 4.4, particularly an attempt to reduce its computational complexity by approximating the bubbly medium as a series of sheets of homogeneous scatterers. A linearised analytical approach is taken to this approximation by examining the reflected and transmitted coefficients in the medium by assuming a population containing two different sizes and each sheet alternates from one bubble type to the other. This work is validated with the full numerical solution to the problem and conclusions are drawn about the homogeneous sheet approximation's validity.

In Chapter 5, a new nonlinear scattering model is presented where the individual lipid-coated microbubble equation of motion developed and coupled with the gas diffusion theory in Chapter 3, is incorporated into the nonlinear scattering model investigated in Chapter 4 to arrive at a model for ultrasound propagation through a population of microbubbles that accounts for the time-dependent behaviour of the microbubbles: specifically, the slow timescale of gas diffusion into and out of the bubbles and the fast timescale dynamics of surfactant shedding that occurs over the course of an ultrasound pulse. The model is solved numerically for a series of pulses travelling through a contrast agent suspension and the results are compared to experimental data by analysing the harmonic content of the propagated signal. The effect of using a different surface tension term as well as varying the concentration of bubbles in the solution and the incident frequency are investigated. To reduce computational complexity, it is assumed that there is sufficient time between pulses for the bubbles to return to an equilibrium state, thus negating the need to solve the full diffusion problem during the pulse interval.

Finally, Chapter 6 presents the conclusions of this thesis as well as suggestions for further work.

1.3 Publications and conference talks

- JP. O'Brien, E. Stride and N. Ovenden, (in press). Surfactant shedding and gas diffusion during pulsed ultrasound through a microbubble contrast agent suspension. *Journal of the Acoustical Society of America*. (Accepted for publication in April 2013)

- JP. O'Brien, N. Ovenden and E. Stride, 2011a. Accounting for the stability of microbubbles to multi-pulse excitation using a lipid-shedding model. *Journal of the Acoustical Society of America*, 130(4), EL180–EL185

- E. Stride, N. Ovenden and JP. O'Brien, 2011. Numerical methods in nonlinear acoustics in bubbly liquids. In: C. Vanhille and C. Campos-Pozuelo eds. *Computational Methods in Nonlinear Acoustics: Current Trends*. Research Signpost, pp. 47–68

- JP. O'Brien, N. Ovenden and E. Stride, 2011b. On the dissolution of microbubble contrast agents in an ultrasound field. In: *Proceedings of Meetings on Acoustics*. Vol. 12

- JP. O'Brien, 2011. Decompression model for divers. In: 53rd British Applied Mathematics Colloquium (11th–13th Apr. 2011). Birmingham, UK

- JP. O'Brien et al., 2010. Nonlinear propagation models for ultrasound propagation through a polydisperse bubble population. In: 16th European Symposium on Ultrasound Contrast Imaging (19th–21st Jan. 2010). Rotterdam, The Netherlands

- JP. O'Brien, 2010. *The unified or complete decompression model for divers*. Technical report. VR Technology, 23/25 Bridge Street, Baille Gate Industrial Estate, Sturminster Marshall, Dorset, BH21 4DB, UK

CHAPTER 2

BUBBLE DIFFUSION MODELLING

This chapter investigates the effects of gas diffusion on bubble growth in tissue. Literature reviews of bubble diffusion and decompression theories are outlined in Sections 2.1 and 2.2 respectively. In Section 2.3, a model for bubble growth within the body is developed by assuming pressure changes are sufficiently slow that convection can be ignored. This is applied to decompression diving in Section 2.4 in an attempt to validate current decompression algorithms and practices.

2.1 Overview of diffusion theory

A pure gas bubble in a liquid has a permeable boundary that allows gas to diffuse in and out. Due to surface tension, the pressure of gas inside the bubble will be higher than outside, leading to a negative diffusion gradient and the tendency for the bubble to dissolve. The rate of dissolution will depend on, for example, the size of the bubble and the concentration of gas in the liquid in the bulk solution. On the other hand, when the partial pressure of gas in the bulk is higher than in the bubble, it will grow. In certain cases, a bubble oscillating in the presence of an ultrasound field may experience a *net* positive gas gradient over one pulse cycle causing growth, a phenomenon known as "rectified diffusion".

For a concentration $c(\boldsymbol{x}, t)$ and bubble wall velocity $\boldsymbol{u}$ in a fluid with gas diffusivity D, the problem can be modelled using a convection-diffusion equation,

$$\frac{\partial c}{\partial t} - D\nabla^2 c + \boldsymbol{u} \cdot \nabla c = 0$$

and an equation of motion for the bubble, for instance the Rayleigh-Plesset equation (B.2.14). Progress was made by Epstein and Plesset (1950) for a quasi-stationary bubble by assuming the motion of the wall was slow which meant the convection term could be ignored and the two

equations decoupled. By including the effects of surface tension, it was shown that the bubble dissolves if the bulk concentration is less than the concentration of gas inside, and grows if the liquid is supersaturated with gas.

In the dynamic situation, the problem is more complicated because the convection term cannot be ignored and the equation of motion must be solved simultaneously. Furthermore, the condition at the bubble wall must be applied to a moving boundary. Since the governing equation is nonlinear, progress was made by assuming small amplitude oscillations around the equilibrium and linearising the equation of motion. Blake (1949) accounted for the moving boundary by assuming it remains fixed but the concentration of gas at the bubble wall changes as if it were moving, whereas Hsieh and Plesset (1961) expanded the boundary condition using a Taylor series about the equilibrium position of the bubble wall. Both of these papers arrived at a pressure amplitude threshold above which rectified diffusion occurred and the bubble grows. However, these results are limited to small bubble oscillations.

The first nonlinear approach including the moving boundary was made by Eller and Flynn (1965) who performed a boundary-layer analysis in Lagrangian coordinates and obtained the first two terms in the expansion. Crum and Hansen (1982) generalised the analysis of Eller and Flynn and included more accurate terms in the perturbation expansion. Numerical solutions for the convection-diffusion equation in the bulk were obtained by Kamath and Prosperetti (1990) who showed that away from saturation, Eller and Flynn's theory tended to over-predict the threshold driving pressure amplitude for rectified diffusion and under-predicted the growth rates of bubbles at conditions above the threshold.

Experimental data were obtained by Crum (1980) at frequencies of 22 kHz which reported growth rates away from the threshold that exceeded the predictions of Eller and Flynn's theory. Crum also found that surfactant material on the surface of the bubble had an effect on the growth rate that could not be explained by modifications to the surface tension in the theory. Experiments at bubble sizes less than 20 μm were carried out by Holt and Gaitan (1996) at a driving frequency of 20.6 kHz. Not only were they able to obtain a rectified diffusion threshold, they also obtained the size of bubbles that were stable in the sound field, where neither growth nor dissolution occurred.

The work in this chapter develops a diffusion model applicable to microbubbles in tissue in the absence of an ultrasound field. Consequently, rectified diffusion is negligible and the

convection term in the equation can be dropped, allowing the diffusion equation to be solved independently, similar to the earlier work by Epstein and Plesset. Henry's law is also used to derive a concentration condition on the boundary of the bubble that, along with the ideal gas law, allow the dynamics of the bubble to be modelled. In the next chapter, the problem of an oscillating bubble is considered and the full diffusion equation including the convection term analysed.

This model has applications in any situation where the velocity of the bubble wall is small. It is applied to the scenario of a SCUBA diver performing a decompression dive in an attempt to model bubble growth inside the tissue. The profiles for these dives were obtained from qualified technical divers and are considered "standard" dives. For completeness, dives to different depths using various gas mixture profiles are used with the model and the size of the bubbles recorded. A literature review of decompression theory and models follows in the next section.

2.2 Overview of decompression theory

During a dive using compressed gas, inert gas dissolves into the diver's tissues at depth. Due to the higher partial pressure of the gas in the lungs at depth, there is a diffusion gradient across the arteries and gas diffuses into the blood. This supersaturated blood is pumped around the body where the dissolved gas diffuses into the diver's tissues.

On ascent and decompression, this process occurs in reverse and inert gas is eliminated. The partial pressure of dissolved gas is higher in the tissues than the blood, so it diffuses back out and is eventually breathed out via the lungs. However, if the rate at which the inert gas diffuses out of tissue, or is "off-gassed", is not controlled, it could potentially come out of solution and form bubbles. The consequences of this, including a literature review, are discussed in the next section.

2.2.1 Microbubbles in the human body

The behaviour and effects of microbubbles *in vivo* are poorly understood and this remains a much-debated field. With regards to the causes of decompression sickness (DCS), there is evidence that microbubbles are directly involved in the symptoms and there appears to be a relationship between the size and number of bubbles and the risk of DCS. However, no one has as yet been able to pinpoint the exact location in the body where a "bend" occurred (Bove and Davis, 2003). In fact, it may be that a number of traumas in the body are required before

signs of DCS are displayed and the diver is at risk of injury. Whether DCS is caused by the cavitation effects of microbubbles or as a result of the occlusion of blood vessels is also not understood. Again, it could be that both mechanisms are involved to different degrees when a diver presents with symptoms of DCS.

Below the current understanding of the possible mechanisms that could contribute to DCS is summarised. It would be desirable to take these effects into account in any decompression model in order for the diver to ascend safely and efficiently from the water. The mechanisms that appear relevant start with microbubble nucleation and include their coalescence in the blood stream (since this could increase the likelihood of vessel occlusion) and finally their destruction or removal from the body.

2.2.2 Nucleation *in vivo*

Predicting nucleation in any environment is a difficult task. The partial pressure of the gas and the shape and surface properties of the nucleation site (if there is one) all affect the rate at which the gas will come out of solution. At some point, enough gas molecules will have gathered to break away from the nucleation site and form a bubble. Usually a change in conditions – such as temperature, pressure or surface tension – would lead to nucleation or accelerate the processes that cause it.

In the body, there is the added complication of not knowing where, when or how many bubbles are formed and therefore incorporating nucleation in a decompression model will be difficult if not impossible with current understanding of the process. Below is an outline of the theories of bubble nucleation with particular attention paid to the theories of bubbles *in vivo*.

The two types of bubble nucleation are known as homogeneous and heterogeneous. Homogeneous bubble nucleation takes place in the absence of an identifiable nucleation site such as a foreign body, and is due to the electromagnetic forces between the gas molecules no longer being sufficient to keep the gas dissolved in solution. It has been shown that for such nucleation to happen, high pressure differences of about 140 MPa are required (Fisher, 1948). These conditions are unlikely to ever be found in the human body of a decompression diver so this particular theory can be neglected for the purposes of modelling (Blatteau et al., 2006).

The second type of nucleation can occur at much lower levels of supersaturation and requires a site (for example at a tissue boundary or a particle in the blood). Where these nucleation sites occur is a much-debated topic and one that will be discussed briefly.

One possibility is that bubbles could form on the boundary of a vessel wall. The crevice model, first applied by Harvey et al. (1944), further analysed by Atchley and Prosperetti (1989) amongst others and extended by Chappell and Payne (2006) to include diffusion of gas through the crevice wall, is that they form in hydrophobic crevices along capillary walls where the surface tension of the concave surface of a bubble under pressurisation would help to explain the stability of these nucleation sites. Moreover, nucleation at these sites could be aided by viscous adhesion as discussed below. However to date, crevices have not been seen to exist in the human body let alone nucleation occurring from one (Blatteau et al., 2006).

Alternatively, bubbles could form around ions or plasma particles that are present in the blood (Dunning, 1969; Ward et al., 1983). Another theory by Sette and Wanderlingh (1962) and Walder and Evans (1974) is that bubbles nucleate around the vapour trails left by cosmic rays as they pass through bones. However, it has not been proven in the literature that these trails are nucleation sites *in vivo*.

Once formed, bubbles would be expected to either dissolve rapidly due to surface tension or rise to the surface of a standing liquid. Several stabilising mechanisms have been suggested and having reviewed these theories, Fox and Herzfeld (1954) and Yount (1979, 1982) concluded that gas nuclei could be stabilised by surface-active particles. These surfactants effectively counteract the surface tension of the bubble that would naturally cause a bubble to dissolve in a static environment. This theory was used in the development of the 'Varying Permeability Model' (VPM), described in Wienke (2008).

The effects of exercise is another much-debated aspect of decompression sickness and whether exercise hinders bubble formation or actually aids it. Experiments on rats by Wisløff, Richardson and Brubakk (2003, 2004) and on humans by Dujić et al. (2004) and Blatteau et al. (2005) support the theory that a bout of high-intensity aerobic exercise prior to the dive reduces the number of microbubbles in the blood. Wisløff, Richardson and Brubakk suggest that nitric oxide produced during exercise reduces the hydrophobicity on endothelial sites, thus inhibiting nucleation. On the other hand, NO has been shown to increase bubble numbers in sedentary rats (Wisløff, Richardson and Brubakk, 2003). It could be that it is not just the NO but the exercise itself that reduces the number of bubbles mechanically. Additionally, heat shock proteins (HSP) are thought to affect bubble growth, but exactly what role they play is unknown. For example, heat shock pre-treatment prior to diving enhanced the expression of HSP and

protected rats from air-induced lung embolisms (Huang et al., 2003) so it is conceivable that exercise-induced HSP could have the same effect.

On the other hand, it is conjectured that exercise increases the number of microbubbles in the blood through a number of different physical mechanisms resulting from the movement of the tissues. One important set of experiments was conducted by Powell, Waligora and Norfleet (1992) who observed "a reduction in whole body gas phase formation in individuals who were bed-rested as compared with themselves when fully ambulatory", in subjects decompressed from 0.1 MPa to 0.043 MPa. The results suggested a hypothesis relating "stress-assisted nucleation to the continual formation of gas micro-nuclei".

One such "stress-assisted" nucleation mechanism is Reynolds cavitation whereby flow through a constricted tube leads to an increase in velocity and a drop in pressure (as a result of Bernoulli's law). Such pressure drops could be sufficient to encourage heterogeneous bubble nucleation "in the streaming of extracellular fluid during musculoskeletal activity" (Blatteau et al., 2006).

In addition, viscous adhesion where two closely opposed surfaces separated by a thin film are suddenly pulled apart causing a large drop in pressure, could be sufficient to cause homogeneous bubble nucleation or alternatively encourage heterogeneous nucleation. Fick (1911) ascribed this phenomenon to the formation of bubbles in joints as a result of movement and it has been associated with "ageing joints, injury or structural pathology" (Blatteau et al., 2006) which could be accelerated during diving. The sudden formation of bubbles in this manner could be followed by a rapid collapse which would potentially lead to cavitation damage.

For example, experiments by McDonough and Hemmingsen (1984a,b, 1985a,b) suggested that mechanical movements were the primary cause of stress-assisted nucleation in trout, catfish, sculpin, salamanders and crab, possibly by a hydrodynamic cavitation mechanism.

Such stress-assisted nucleation could take place in limbs, joints and possibly also around the heart valve. The formation of bubbles has been witnessed for some mechanical heart patients (Biancucci et al., 1999; Girod et al., 2002) near to and after closure of the valve. Thus arterial microbubbles (microbubbles present in the arterial blood system of the body) formed at the heart could be another important factor in DCS. However, evidence suggests otherwise

(Bove and Davis, 2003). If this were a major cause of the bends, then one would expect a region of the body that is well supplied with arterial blood, such as the brain, to display trauma in divers who have died as a result of DCS. Although these microbubbles could contribute to some skin bends, they categorically do not contribute to neurological DCS in the brain (Tikuisis and Gerth, 2003).

The effects of exercise during and after a dive depend on a number of factors including temperature and the phase of pressure exposure, as described by Vann et al. (2011). For instance, exercise whilst under pressure increases inert gas uptake and risk of DCS; however, exercise whilst decompressing increases inert gas elimination and thus decreases the risk of DCS. Conversely, in a cold environment or during rest, uptake is reduced thereby decreasing DCS risk during the dive, but increasing the risk during decompression. Furthermore, if exercise occurs after a dive whilst tissues are still supersaturated, the rate of bubble formation and risk of DCS increase (Vann, 2004).

An interesting point to note is that microbubbles do not seem to form in veins (Lee et al., 1993), so they may form in tissues or capillaries and migrate into the vascular system via diffusion or convection (Blatteau et al., 2006).

Furthermore, anecdotal evidence that dehydration in divers contributes to the risk of DCS could be explained by the fact that it leads to reduced blood flow to certain areas by constricting blood vessels, or a decrease in the surface tension of the bubble, thus reducing their propensity to dissolve and encouraging bubble growth during decompression. Experiments on swine by Fahlman and Dromsky (2006) showed that the dehydrated test subjects manifested severe DCS sooner than the hydrated animals.

The rate at which bubbles nucleate is also notoriously difficult to predict. In scenarios where the supersaturation is high, bubble nucleation sites could be close together and bubbles may coalesce as they form, leading to random nucleation times. The significant factors that govern initial growth are unclear, but molecular diffusion eventually governs final growth (Jones, Evans and Galvin, 1999).

2.2.3 Coalescence

The mechanisms for coalescence in the body are even less well understood than those for nucleation. These mechanisms can be broken up into five distinct processes, as detailed in Dhainaut and Johansen (2002). Firstly, the bubbles collide, followed by a flattening of the

contact surface. Then the liquid film between the two bubble surfaces drains away until that film attains a critical thickness. At this point the film ruptures and the two bubbles join, forming an ellipsoid bubble.

How the bubbles coalesce is partly governed by the Weber number, We, a ratio of a fluid's inertia to its surface tension. If We is less than 1, bubble coalescence will always occur. On the other hand, if We is greater than 1, bubble coalescence will be determined by film-drainage (Postema et al., 2004).

It may be possible to consider the rate at which microbubbles coalesce in the body although any value would be derived in a highly idealised situation. For instance, the coalescence rate can be written as a function of the efficiency of coalescence and the collision frequency (Miura and Vinogradov, 2008). Such numbers can be derived for a vertical column of water, but subsequent calculations require supercomputers (Prince and Blanch, 1990). More critically, coalescence is reliant on turbulence within the fluid flow. In the case of blood, the low Reynolds number of the flow precludes much turbulence thus it is probably safe to say that this type of coalescence is not a major factor in the human body.

2.2.4 Microbubble elimination

As mentioned above, under static conditions, any bubble will dissolve into the fluid as a result of the positive diffusion gradient caused by the surface tension on the bubble. Moreover, the smaller the bubble, the greater the force exerted on the bubble by the surface tension and the larger the diffusion gradient. In fact, for bubbles in the micrometer size range (as would be present in the body), one would expect them to dissolve in less than a second; however Doppler scans (Brubakk et al., 1981; Mazurel et al., 1985) on humans show that in diving situations, microbubbles can survive for tens of seconds to minutes in the blood stream. The mechanisms for stabilising microbubble nuclei in the blood stream, as already alluded to, are not well understood. However, there are other mechanisms that could explain how microbubbles are eliminated from the blood.

One such mechanism relates to the pulmonary system. Microbubbles that appear in the venous blood system will eventually find their way back to the heart where the blood will be pumped to the lungs in order to be reoxygenated. The lungs thus proceed to eliminate the microbubbles during the gas exchange process (although the exact mechanism is not completely understood) thus leading to the lungs becoming known as "bubble filters" (Butler and Hills,

1979). However, the lungs may not remove all of them and the Arterial Bubble Model by Imbert et al. (2004) takes this possibility into account.

A patent foramen ovale (PFO), or "shunt", in the heart could lead to microbubbles bypassing the natural bubble elimination mechanisms of the lungs and persisting in the circulatory system leading to an increased risk in DCS. However, studies report conflicting conclusions as to the nature and severity of the PFO risk and even whether there is any risk at all.

For instance, one study by Bove (1998) showed that 37% of patients with DCS had a PFO, 61% of whom had neurological DCS. There were large shunts in 52% of DCS victims compared with 12.2% in a control group.

On the other hand, between 20% and 34% of the adult population have a PFO of some form and Cross et al. (1992) found there to be no difference in the incidence of the bends between different groups of divers.

In addition, any decompression model involving bubbles will have to include the effects of the oxygen window on the dissolution of bubbles *in vivo*. This effect arises as a result of the metabolism of oxygen by the body and the high solubility of carbon dioxide in blood (Behnke, 1951).

At steady state, the sum of the partial pressures of dissolved gas in a living animal's tissue is usually less than atmospheric pressure, in a phenomenon known as the "oxygen window". This is because metabolism lowers the partial pressure of oxygen in tissue compared with the arterial value. In addition, the binding of oxygen to haemoglobin, as well as the high solubility of carbon dioxide that results from aerobic respiration meaning its partial pressure contribution is small, leads to a relatively small partial pressure drop between tissues and arterial blood. However, under pressure, extra oxygen is dissolved in the blood since the haemoglobin is already saturated. Tissues will tend to satisfy their oxygen need from blood because it is easier to absorb from than haemoglobin. Since the carbon dioxide released will exert a much smaller partial pressure, there is a net drop in the partial pressure of the blood across the tissue. If the diver is off-gassing at this point, part of the gas that diffuses out of the tissue can be "taken up" by this oxygen window. The net result is a reduction of the gas tension in the venal blood system and a decline in the tendency for bubbles to form. In fact it could be possible to ascend without ever supersaturating the blood by allowing only enough gas out of the tissue to replace the oxygen that was metabolised. However such decompression profiles would take days and the diver is likely to run out of air well before they get out of the water.

2.2.5 Current decompression models

In this section, a review of decompression models that have been or are still used by divers in some guise is presented. The first decompression models by Boycott, Damant and Haldane (1908) remained largely unchanged for 50 years. They were based on experiments conducted on goats and neglected to model any bubble growth. Instead, the body was modelled as six "compartments" representing different tissue types. Diffusion of gas into and out of the compartments was modelled using an exponential diffusion equation and the coefficient of diffusion for each compartment, known as the tissue "half-time", differed, representing the diffusivity of the tissue. Highly vascular tissue such as the brain would have a "fast" half-time whereas tissue with poor blood supply such as bone would have a "slow" half-time.

To ensure safe decompression, the diver has to maintain tissue saturation in each compartment below a defined safe "over-pressure" limit as they off-gas. These models were updated by Workman (1957) who added more compartments with different half-times as he noticed the earlier tables were inadequate for long, deep dives. The next major step was taken by Bühlmann (1983) who published the ZH-L16 decompression tables, using 16 compartments and based on experiments conducted on a human volunteer. These extended the previous theory and adjusted the tissue half-times for different gases but did not address the fundamental issue of bubble growth in tissue.

To address this deficiency, Yount (1979, 1982), Yount and Hoffman (1986) developed the 'Varying Permeability Model' (VPM) which assumes that bubble nuclei are always present in water and tissues. The nuclei are said to be stabilised by a proteinaceous or lipid skin and can be compressed under surface tension or at depth to a minimum size, whereupon the skin of the bubble becomes impermeable and can no longer shrink. On ascent, gas can diffuse into the bubble through the permeable skin causing it to grow. To inhibit this, the partial pressure of gas in the tissue compartment must be maintained below the gas pressure inside the bubble, hence ensuring the diffusion gradient is always negative with respect to the bubble. To calculate the compartmental gas pressure, Yount used the Haldane theory with Bühlmann's ZH-L16 numbers.

Yet this approach proved to be too aggressive. Consequently, Wienke (1990) included a variable gradient term: the safe value below which the pressure inside the compartment had to be maintained depended on the depth and the total volume of gas out of solution in all the

compartments. Other variables were included in the calculation that took into account, for example, any prior dives in the previous 24 hours. This new model was called the 'Reduced Gradient Bubble Model' (RGBM).

However, both of these models assume that each bubble exists in isolation and neglect to take into account neighbouring bubble growth and any possible interaction. Furthermore, the assumptions about varying permeability and a maximum over-pressure for each compartment are heuristic methods of achieving a working model and have little scientific foundation.

2.3 A diffusion model for a bubble population in tissue

For the purposes of this thesis, the model used is a two dimensional rectangular region of tissue in which there are a fixed number of randomly distributed microbubble nuclei from which it is possible for bubbles to grow.

Importantly, pressure changes happen sufficiently slowly that the effects of convection can be ignored in the diffusion equation.

Furthermore, the boundaries of the block of tissue are supplied by blood containing dissolved gas from which the tissue is "fed" and into which gas coming out of solution dissolves. It is assumed that the blood has an infinite capacity to hold dissolved gas and the partial pressures of the gases are instantaneously at equilibrium with the breathing gas.

The effects of surface tension and tissue elasticity on the growth of bubbles and the concentration of gases inside them have all been taken into account. Since there is little difference in the diffusivity of different gases in water, it is assumed that they were the same and constant for each gas.

2.3.1 Assumptions

To reduce the complexity of the problem, a number of assumptions are made in order to construct a model from which qualitative estimations of microbubble growth in tissues can be obtained. The implications of these assumptions are discussed in Section 2.5. First of all, it is assumed that the blood is instantaneously saturated at the ambient partial pressure of the breathing gas. This assumption neglects to take into account the approximately one minute it takes for the blood to circulate around the body and for excess gas dissolved in the blood to be breathed out. It also fails to take into account dissolved gas from other tissues through which the blood will have flowed in order to get there.

Secondly, it is assumed that the effect on surface tension of any surfactants follows a cubic power law (Atchley, 1989). Additionally, diffusivity through the bubble surface is assumed to scale according to a quadratic power law. Whilst there is little information in the literature on the effects of surface coatings on diffusion, it seems sensible to make a heuristic judgement that diffusivity scales with the surface area of the bubble.

Thirdly, since the bubbles are expected to remain small compared with the size of the tissue, it is assumed that the tissue elastic modulus remains linear throughout and that the values for the bulk modulus in certain tissues can be used to obtain values for the pressure inside the bubble due to the force of the tissue pushing back on the expanding bubble.

Fourthly, it is assumed that the bubbles only interact with the gas dissolved in the blood via the tissue i.e. the gas diffuses into the tissue before diffusing into the bubble. This is a reasonable assumption as long as the bubbles are not near the edge of the tissue.

Fifthly, bubbles cannot escape from a tissue. Upon reaching the edge, they are pushed back inside the tissue i.e. their centre moves. Furthermore, if two bubbles intersect, they coalesce immediately and instantaneously, which is not in keeping with theory (Postema et al., 2004) but simplifies the problem. Experiments by Giribabu and Ghosh (2008) with bubbles and non-ionic surfactants suggest that up to quite large surfactant concentrations, bubble coalescence happens within 30 seconds or so. On the scale of slow pressure changes that can take minutes, it can be concluded that instant coalescence is a reasonable assumption. In addition the bubbles are assumed to be spherically symmetric. This is valid given small bubbles and small pressure gradients across tissues.

2.3.2 Governing equations

The diffusion of gas into and out of the tissue is governed by the usual diffusion equation where convection has been neglected since it can be assumed that the bubbles and tissue are quasi-static. The evolution of the concentration $c^i = c^i(x, y, t)$ of gas i in the tissue, where i takes superscripts N_2, He and O_2 for nitrogen, helium and oxygen respectively, is given by,

$$\frac{\partial c^i}{\partial t} = D\nabla^2 c^i \tag{2.3.1}$$

where ∇^2 is the usual two dimensional Laplacian and D is a diffusivity constant. Assuming that pressure and concentration throughout the bubble are constant, the initial condition is,

$$c^i(x, y, 0) = c^i_0 \tag{2.3.2}$$

and the boundary conditions on the edge of the tissue of dimensions ($T_x \times T_y$), given a partial pressure of gas i in the breathing gas $p^i(t)$, are,

$$c^i(0,y,t) = c^i(x,0,t) = c^i(T_x,y,t) = c^i(x,T_y,t) = k_H^i p^i(t),\ \forall x,y \in T_x,T_y \tag{2.3.3}$$

Henry's law is used here to link the pressure and concentration of gas via Henry's constant k_H,

$$c = k_H p \tag{2.3.4}$$

At constant temperature, equation (2.3.4) states that the amount of gas dissolved in a particular mixture is proportional to the pressure p exerted by that gas.

The concentration of dissolved gas in the tissue within the interior B_b of the b^{th} bubble where there are N bubbles in the tissue, is equal to the concentration of gas inside the bubble at time t, $c_b(t)$,

$$c(x,y,t) = c_b(t),\ \forall\ (x,y) \in B_b,\ b = 1,\ldots,N \tag{2.3.5}$$

There are two physical mechanisms by which the size of the bubble changes: firstly, due to ambient pressure changes and secondly, as a result of gas diffusion into and out of the bubble.

In order to account for pressure changes, the gas inside the bubble is assumed to behave like an ideal gas. Consequently the ideal gas law is used to relate the pressure p, the volume of the bubble V, the number of moles of gas n, the mass of the gas m and the temperature T,

$$\begin{aligned} pV &= nGT \\ &= \frac{mGT}{M} \\ &= m\alpha \end{aligned} \tag{2.3.6}$$

where M is the molar mass of the gas, G is the universal gas constant and $\alpha \coloneqq GT/M$.

Within the bubble, the pressure is assumed to be spatially uniform and, given an initial mass m_0, the rate of change of the total mass of gas in the bubble is given by the flux across its surface area A,

$$m(t) = m_0 + \int_0^t AD\ \frac{\partial c}{\partial r}\bigg|_{r=R(t)}\ \mathrm{d}t \tag{2.3.7}$$

In the case of a spherically symmetric bubble, the surface area equals $4\pi R^2$, so differentiating with respect to t leads to,

$$\frac{dm}{dt} = 4\pi R^2 D \left.\frac{\partial c}{\partial r}\right|_{r=R(t)} \tag{2.3.8}$$

In order to model the pressure evolution of the bubble more accurately, it is necessary to consider pressure changes due to the changes in concentration of the three main gases. Therefore, writing superscripts N_2, He and O_2 as before, equation (2.3.8) can be rewritten using (2.3.6),

$$\begin{aligned}
\frac{d}{dt}\left[\left(\frac{p_b^{N_2}}{\alpha^{N_2}} + \frac{p_b^{He}}{\alpha^{He}} + \frac{p_b^{O_2}}{\alpha^{O_2}}\right)V\right] &= 4\pi R^2 D \left.\frac{\partial\left(c^{N_2} + c^{He} + c^{O_2}\right)}{\partial r}\right|_{r=R(t)} \\
\frac{d}{dt}\left[\left(\frac{p_b^{N_2}}{\alpha^{N_2}} + \frac{p_b^{He}}{\alpha^{He}} + \frac{p_b^{O_2}}{\alpha^{O_2}}\right)\frac{R^3}{3}\right] &= R^2 D \left.\frac{\partial\left(c^{N_2} + c^{He} + c^{O_2}\right)}{\partial r}\right|_{r=R(t)}
\end{aligned} \tag{2.3.9}$$

Moreover, the pressure inside the bubble p_b situated within a volume of tissue affected by its growth V_T, can be written as the sum of the ambient pressure p_0 and the pressures due to the surface tension σ and the tissue modulus of elasticity $E \coloneqq B/V_T$, given a tissue bulk modulus B,

$$p_b = p_0 + \frac{2\sigma}{R} + \frac{4\pi}{3}R^3 E \tag{2.3.10}$$

Therefore, equation (2.3.9) is written in terms of the concentration of each gas inside the bubble c_b^i alone by using (2.3.4), and $R_b(t)$ is the radius of the b^{th} bubble containing a total gas concentration $c_b^{\text{tot}} = c_b^{N_2} + c_b^{He} + c_b^{O_2}$,

$$\frac{d}{dt}\left[\left(\left(\frac{c_b^{N_2}}{\alpha^{N_2}k_H^{N_2}} + \frac{c_b^{He}}{\alpha^{He}k_H^{He}} + \frac{c_b^{O_2}}{\alpha^{O_2}k_H^{O_2}}\right)\frac{p_0 + \frac{2\sigma}{R_b} + \frac{4\pi}{3}ER_b^3}{\frac{c_b^{N_2}}{k_H^{N_2}} + \frac{c_b^{He}}{k_H^{He}} + \frac{c_b^{O_2}}{k_H^{O_2}}}\right)\frac{R_b^3}{3}\right] = R_b^2 D \left.\frac{\partial\left(c_b^{\text{tot}}\right)}{\partial r}\right|_{r=R_b(t)} \tag{2.3.11}$$

2.3.3 Non-dimensionalisation

Introducing dimensionless variables, denoted by primes, using a characteristic timescale τ and an initial microbubble nucleus size r_0,

$$c^i = c_0 c^{i\prime} + c_0^i, \qquad t = \tau t', \qquad r = r_0 r', \qquad x = r_0 x', \qquad y = r_0 y', \qquad R = r_0 R'$$

$$\sigma = r_0 p_0 \sigma' = \frac{r_0 c_0}{k_H^{N_2}}\sigma', \quad E = \frac{p_0}{r_0^3}E' = \frac{c_0}{k_H^{N_2} r_0^3}E', \quad m^i = R_0^3 c_0 m^{i\prime}, \quad p = \frac{c_0}{k_H^{N_2}}p' + p_0$$

For this problem, $c_0 \coloneqq c_0^{N_2}$ and $p_0 \coloneqq c_0^{N_2}/k_H^{N_2}$ are the initial concentration and partial pressure of nitrogen in the tissue respectively. The system of equations (2.3.1), (2.3.4) and (2.3.11) that govern the model are written,

$$\frac{\partial c^{i\prime}}{\partial t'} = \frac{\tau D}{r_0^2}\left(\frac{\partial^2 c^{i\prime}}{\partial x'^2} + \frac{\partial^2 c^{i\prime}}{\partial y'^2}\right) \tag{2.3.12}$$

with initial and boundary conditions,

$$c^{i\prime}(x', y', 0) = \frac{c_0^i - c_0^i}{c_0} = 0 \tag{2.3.13}$$

$$c^{i\prime}(0, y', t') = c^{i\prime}(x', 0, t') = \frac{k_H^i}{k_H^{\mathrm{N_2}}}\big(p'(t') + 1\big) - \frac{c_0^i}{c_0} \tag{2.3.14}$$

$$c^{i\prime}(x', y', t') = \frac{k_H^i}{k_H^{\mathrm{N_2}}}\big(p_b'(t') + 1\big) - \frac{c_0^i}{c_0},\ \forall\,(x', y') \in B_b \tag{2.3.15}$$

Equation (2.3.11) becomes,

$$\frac{d}{dt'}\left[\left(\left(\frac{c_b^{\mathrm{N_2}\prime}}{k_H^{\mathrm{N_2}}} + \frac{c_b^{\mathrm{He}\prime}\alpha^{\mathrm{N_2}}}{k_H^{\mathrm{He}}\alpha^{\mathrm{He}}} + \frac{c_b^{\mathrm{O_2}\prime}\alpha^{\mathrm{N_2}}}{k_H^{\mathrm{O_2}}\alpha^{\mathrm{O_2}}}\right)\frac{p_0' + \frac{2\sigma'}{R_b'} + \frac{4\pi}{3}E'R_b^{3\prime}}{\frac{c_b^{\mathrm{N_2}\prime}}{k_H^{\mathrm{N_2}}} + \frac{c_b^{\mathrm{He}\prime}}{k_H^{\mathrm{He}}} + \frac{c_b^{\mathrm{O_2}\prime}}{k_H^{\mathrm{O_2}}}}\right)\frac{R_b^{3\prime}}{3}\right] = R_b^{2\prime}\frac{\tau D\alpha^{\mathrm{N_2}}k_H^{\mathrm{N_2}}}{r_0^2}\left.\frac{\partial\left(c_b^{\mathrm{tot}\prime}\right)}{\partial r'}\right|_{r'=R_b'} \tag{2.3.16}$$

From this equation the characteristic time is,

$$\tau = \frac{r_0^2}{D\alpha^{\mathrm{N_2}}k_H^{\mathrm{N_2}}}$$

Using this characteristic time in the dimensionless equations (2.3.12) to (2.3.16) results in, having dropped primes for clarity,

$$\frac{\partial c^i}{\partial t} = \frac{1}{\alpha^{\mathrm{N_2}}k_H^{\mathrm{N_2}}}\left(\frac{\partial^2 c^i}{\partial x^2} + \frac{\partial^2 c^i}{\partial y^2}\right) \tag{2.3.17}$$

with initial and boundary conditions,

$$c^i(x, y, 0) = 0 \tag{2.3.18}$$

$$c^i(0, y, t) = c^i(x, 0, t) = \frac{k_H^i}{k_H^{\mathrm{N_2}}}\big(p(t) + 1\big) - \frac{c_0^i}{c_0} \tag{2.3.19}$$

$$c^i(x, y, t) = \frac{k_H^i}{k_H^{\mathrm{N_2}}}\big(p_b(t) + 1\big) - \frac{c_0^i}{c_0},\ \forall\,(x, y) \in B_b \tag{2.3.20}$$

and the bubble's equation of motion and its initial condition are,

$$\frac{d}{dt}\left[\left(\left(\frac{c_b^{\mathrm{N_2}}}{k_H^{\mathrm{N_2}}} + \frac{c_b^{\mathrm{He}}\alpha^{\mathrm{N_2}}}{k_H^{\mathrm{He}}\alpha^{\mathrm{He}}} + \frac{c_b^{\mathrm{O_2}}\alpha^{\mathrm{N_2}}}{k_H^{\mathrm{O_2}}\alpha^{\mathrm{O_2}}}\right)\frac{p_0 + \frac{2\sigma}{R_b} + \frac{4\pi}{3}ER_b^3}{\frac{c_b^{\mathrm{N_2}}}{k_H^{\mathrm{N_2}}} + \frac{c_b^{\mathrm{He}}}{k_H^{\mathrm{He}}} + \frac{c_b^{\mathrm{O_2}}}{k_H^{\mathrm{O_2}}}}\right)\frac{R_b^3}{3}\right] = R_b^2\left.\frac{\partial\left(c_b^{\mathrm{tot}}\right)}{\partial r}\right|_{r=R_b} \tag{2.3.21}$$

$$R_b(0) = \frac{r_0}{r_0} = 1 \tag{2.3.22}$$

The equation (2.3.8) for the rate of change of the mass of gas inside the bubble is,

$$\frac{dm^i}{dt} = \frac{4\pi R^2}{k_H^{\mathrm{N_2}}\alpha^{\mathrm{N_2}}} \left.\frac{\partial c^i}{\partial r}\right|_{r=R} \tag{2.3.23}$$

Equation (2.3.21) is solved for $\dot{R}$ where the "dot" denotes differentiation with respect to time. Once an expression for $\dot{R}$ is obtained, a relationship between ambient pressure, the concentration of each gas in the bubble and the rate of change of the radius of the bubble has been derived. Thus, remembering that both concentration and ambient pressure are functions of time,

$$\frac{dR_b}{dt} = \frac{f\big(R_b, p, c_b^{\mathrm{N_2}}, c_b^{\mathrm{He}}, c_b^{\mathrm{O_2}}\big)}{g\big(R_b, p, c_b^{\mathrm{N_2}}, c_b^{\mathrm{He}}, c_b^{\mathrm{O_2}}\big)} \tag{2.3.24}$$

where the functions $f\big(R_b, p, c_b^{\mathrm{N_2}}, c_b^{\mathrm{He}}, c_b^{\mathrm{O_2}}\big)$ and $g\big(R_b, p, c_b^{\mathrm{N_2}}, c_b^{\mathrm{He}}, c_b^{\mathrm{O_2}}\big)$ are,

$$\begin{aligned}
&f\big(R_b, p, c_b^{\mathrm{N_2}}, c_b^{\mathrm{He}}, c_b^{\mathrm{O_2}}\big) = \\
&-\Bigg(R_b\Bigg(3\Big(k_H^{\mathrm{N_2}}\Big)^2\Big(k_H^{\mathrm{O_2}}\Big)^2\alpha^{\mathrm{O_2}}\Big(c_b^{\mathrm{He}}\Big)^2\Bigg(\alpha^{\mathrm{N_2}}R_b\frac{dp}{dt} - 3\alpha^{\mathrm{He}}\left.\frac{\partial c_b^{\mathrm{tot}}}{\partial r}\right|_{r=R_b}\Bigg) + k_H^{\mathrm{He}}k_H^{\mathrm{N_2}}k_H^{\mathrm{O_2}}c_b^{\mathrm{He}}\times \\
&\Bigg(\Big(6\sigma + 3R_bp + 4\pi ER_b^4\Big)\Bigg(k_H^{\mathrm{O_2}}\big(\alpha^{\mathrm{He}} - \alpha^{\mathrm{N_2}}\big)\alpha^{\mathrm{O_2}}\frac{dc_b^{\mathrm{N_2}}}{dt} + k_H^{\mathrm{N_2}}\alpha^{\mathrm{N_2}}\big(\alpha^{\mathrm{He}} - \alpha^{\mathrm{O_2}}\big)\frac{dc_b^{\mathrm{O_2}}}{dt}\Bigg) \\
&+ 3k_H^{\mathrm{O_2}}\alpha^{\mathrm{O_2}}c_b^{\mathrm{N_2}}\Bigg(\big(\alpha^{\mathrm{He}} + \alpha^{\mathrm{N_2}}\big)R_b\frac{dp}{dt} - 6\alpha^{\mathrm{He}}\left.\frac{\partial c_b^{\mathrm{tot}}}{\partial r}\right|_{r=R_b}\Bigg) + 3k_H^{\mathrm{N_2}}c_b^{\mathrm{O_2}}\times \\
&\Bigg(\alpha^{\mathrm{N_2}}\big(\alpha^{\mathrm{He}} + \alpha^{\mathrm{O_2}}\big)R_b\frac{dp}{dt} - 6\alpha^{\mathrm{He}}\alpha^{\mathrm{O_2}}\left.\frac{\partial c_b^{\mathrm{tot}}}{\partial r}\right|_{r=R_b}\Bigg)\Bigg) + k_H^{\mathrm{He}}\Bigg(3k_H^{\mathrm{He}}\Big(k_H^{\mathrm{O_2}}\Big)^2\alpha^{\mathrm{He}}\alpha^{\mathrm{O_2}}\Big(c_b^{\mathrm{N_2}}\Big)^2\times \\
&\Bigg(R_b\frac{dp}{dt} - 3\left.\frac{\partial c_b^{\mathrm{tot}}}{\partial r}\right|_{r=R_b}\Bigg) + k_H^{\mathrm{N_2}}c_b^{\mathrm{O_2}}\Bigg(-k_H^{\mathrm{O_2}}\Big(6\sigma + 3R_bp + 4\pi ER_b^4\Big)\Big(k_H^{\mathrm{N_2}}\alpha^{\mathrm{N_2}}\big(\alpha^{\mathrm{He}} - \alpha^{\mathrm{O_2}}\big)\frac{dc_b^{\mathrm{He}}}{dt} \\
&+ k_H^{\mathrm{He}}\alpha^{\mathrm{He}}\big(\alpha^{\mathrm{N_2}} - \alpha^{\mathrm{O_2}}\big)\frac{dc_b^{\mathrm{N_2}}}{dt}\Bigg) + 3k_H^{\mathrm{He}}k_H^{\mathrm{N_2}}\alpha^{\mathrm{He}}c_b^{\mathrm{O_2}}\Bigg(\alpha^{\mathrm{N_2}}R_b\frac{dp}{dt} - 3\alpha^{\mathrm{O_2}}\left.\frac{\partial c_b^{\mathrm{tot}}}{\partial r}\right|_{r=R_b}\Bigg)\Bigg) \\
&+ k_H^{\mathrm{N_2}}k_H^{\mathrm{O_2}}c_b^{\mathrm{N_2}}\Bigg(-\Big(6\sigma + 3R_bp + 4\pi ER_b^4\Big)\Bigg(k_H^{\mathrm{O_2}}\alpha^{\mathrm{O_2}}\big(\alpha^{\mathrm{He}} - \alpha^{\mathrm{N_2}}\big)\frac{dc_b^{\mathrm{He}}}{dt} \\
&+k_H^{\mathrm{He}}\alpha^{\mathrm{He}}\big(\alpha^{\mathrm{O_2}} - \alpha^{\mathrm{N_2}}\big)\frac{dc_b^{\mathrm{O_2}}}{dt}\Bigg) + 3k_H^{\mathrm{He}}\alpha^{\mathrm{He}}c_b^{\mathrm{O_2}}\Bigg(\big(\alpha^{\mathrm{N_2}} + \alpha^{\mathrm{O_2}}\big)R_b\frac{dp}{dt} - 6\alpha^{\mathrm{O_2}}\left.\frac{\partial c_b^{\mathrm{tot}}}{\partial r}\right|_{r=R_b}\Bigg)\Bigg)\Bigg)\Bigg)\Bigg)
\end{aligned}$$

and,

$$\begin{aligned}
g\big(R_b, p, c_b^{\mathrm{N_2}}, c_b^{\mathrm{He}}, c_b^{\mathrm{O_2}}\big) = &\Bigg(3\Big(k_H^{\mathrm{N_2}}k_H^{\mathrm{O_2}}c_b^{\mathrm{He}} + k_H^{\mathrm{He}}k_H^{\mathrm{O_2}}c_b^{\mathrm{N_2}} + k_H^{\mathrm{He}}k_H^{\mathrm{N_2}}c_b^{\mathrm{O_2}}\Big)\times \\
&\Bigg(k_H^{\mathrm{N_2}}k_H^{\mathrm{O_2}}\alpha^{\mathrm{N_2}}\alpha^{\mathrm{O_2}}c_b^{\mathrm{He}} + k_H^{\mathrm{He}}\alpha^{\mathrm{He}}\Big(k_H^{\mathrm{O_2}}\alpha^{\mathrm{O_2}}c_b^{\mathrm{N_2}} + k_H^{\mathrm{N_2}}\alpha^{\mathrm{N_2}}c_b^{\mathrm{O_2}}\Big)\Bigg)\big(4\sigma + 3R_bp + 8\pi ER_b^4\big)\Bigg)
\end{aligned}$$

2.3.4 Numerical modelling

The model is now fully described by equations (2.3.17) and (2.3.24) with initial and boundary conditions on the tissue given in (2.3.18) to (2.3.20) and the initial condition on the bubble radius as equation (2.3.22).

Numerical solutions of the differential equations are now required and this is carried out using a finite difference method. A forward difference equation and central difference equation are used to discretise time and space respectively. At each time-step s, and spatial-steps j and k in the x and y directions respectively, the derivatives are approximated by,

$$\begin{aligned}
\frac{\partial c}{\partial t} &\approx \frac{c_{j,k,s+1} - c_{j,k,s}}{\delta t} \\
\frac{\partial^2 c}{\partial x^2} &\approx \frac{c_{j+1,k,s} - 2c_{j,k,s} + c_{j-1,k,s}}{(\delta x)^2} \\
\frac{\partial^2 c}{\partial y^2} &\approx \frac{c_{j,k+1,s} - 2c_{j,k,s} + c_{j,k-1,s}}{(\delta y)^2} \\
\frac{dR}{dt} &\approx \frac{R_{s+1} - R_s}{\delta t} \\
\frac{dp}{dt} &\approx \frac{p_s - p_{s-1}}{\delta t} \\
\frac{dc_b}{dt} &\approx \frac{c_{b(s)} - c_{b(s-1)}}{\delta t}
\end{aligned}$$

Finite steps taken in x, y and time dimensions have also been defined as δx, δy and δt respectively, thus the tissue is divided into X and Y steps in the x and y directions and T time-steps. Consequently, the size of the tissue is $X\delta x \times Y\delta y$ and the total simulation time is $T\delta t$. The finite difference scheme is calculated at each time-step for every point in the tissue that is not contained within a bubble. Explicitly, the concentration at time $s+1$ at point (j,k) for gas i is given by inserting the finite difference approximations into equation (2.3.17) and solving for $c^i_{j,k,s+1}$,

$$c^i_{j,k,s+1} = \frac{\delta t}{\alpha^{\mathrm{N}_2} k_H^{\mathrm{N}_2}} \left(\frac{c^i_{j+1,k,s} - 2c^i_{j,k,s} + c^i_{j-1,k,s}}{(\delta x)^2} + \frac{c^i_{j,k+1,s} - 2c^i_{j,k,s} + c^i_{j,k-1,s}}{(\delta y)^2} \right) + c^i_{j,k,s} \tag{2.3.25}$$

shown schematically in figure 2.1.

Moreover, the diffusive flux in a spherically symmetric domain across the bubble boundary at the closest point to its edge r, where the actual boundary is a distance Δ from the next point in the grid, is calculated to second order error as,

$$\left.\frac{\partial c}{\partial r}\right|_{r=R} \approx \frac{-(1+2\Delta)c_{r,s} + (1+\Delta)^2 c_{r+1,s} - \Delta^2 c_{r+2,s}}{\Delta(1+\Delta)\delta r}$$

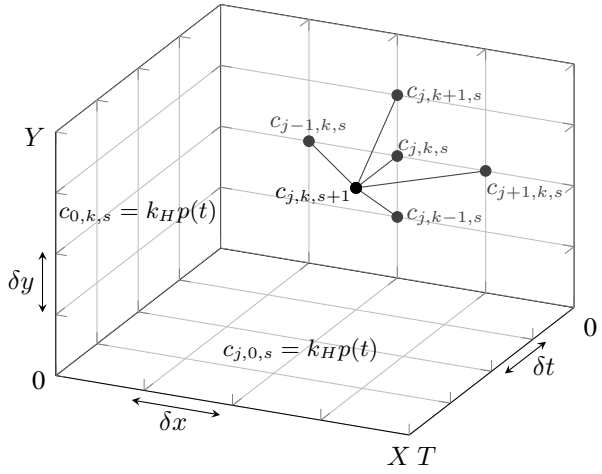

Figure 2.1: The finite difference scheme for the tissue-bubble diffusion model.

When the distance between the bubble and the next node is very small, the finite difference scheme can become inaccurate so the flux is calculated starting at point $r + 1$.

Since it has been assumed that the bubble is spherically symmetric but the tissue gas concentration around it is not, the flux for each gas is approximated by using the points in the grid, $\overset{+}{r}$ and $\overset{-}{r}$, closest to the bubble edge in a particular axis direction,

$$\begin{aligned}\left.\frac{\partial c}{\partial r}\right|_{r=R} \approx \frac{1}{4\Delta(1+\Delta)} \Bigg(& \frac{-(1+2\Delta)c_{\overset{+}{r},r,s} + (1+\Delta)^2 c_{\overset{+}{r}+1,r,s} - \Delta^2 c_{\overset{+}{r}+2,r,s}}{\delta x} \\ & + \frac{-(1+2\Delta)c_{\overset{-}{r},r,s} + (1+\Delta)^2 c_{\overset{-}{r}-1,r,s} - \Delta^2 c_{\overset{-}{r}-2,r,s}}{\delta x} \\ & + \frac{-(1+2\Delta)c_{r,\overset{+}{r},s} + (1+\Delta)^2 c_{r,\overset{+}{r}+1,s} - \Delta^2 c_{r,\overset{+}{r}+2,s}}{\delta y} \\ & + \frac{-(1+2\Delta)c_{r,\overset{-}{r},s} + (1+\Delta)^2 c_{r,\overset{-}{r}-1,s} - \Delta^2 c_{r,\overset{-}{r}-2,s}}{\delta y} \Bigg)\end{aligned}$$

shown schematically in figure 2.2. At each time point, the tissue diffusion equation (2.3.17) is updated throughout the tissue and the values for c^i around each bubble are used to calculate the flux, which is then inserted into equation (2.3.24) to update the values of $R_b(t)$ for each bubble. The values for the flux of each gas into and out of the bubble can in turn be used to update the mass of the gas inside the bubble using equation (2.3.23), which can be discretised into an explicit finite difference format using the same methodology as before. This new value of the mass of gas i is used to update the concentration of gas inside the bubble using Henry's law (2.3.4) and the ideal gas law (2.3.6),

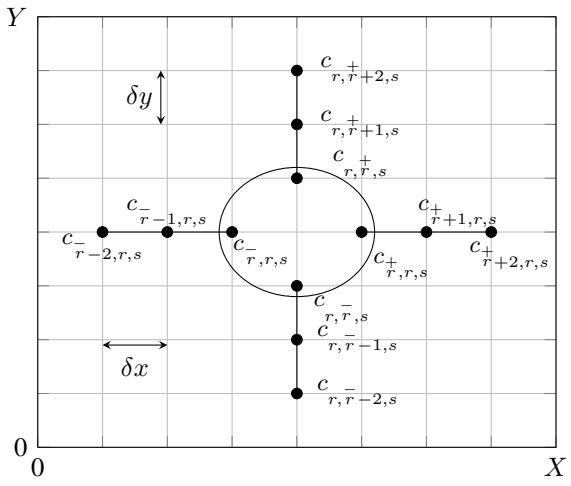

Figure 2.2: The finite difference scheme for calculating the bubble gas flux.

$$c_b^i = \frac{m^i \alpha^i k_H^i}{\frac{4\pi}{3} R_b^3} \tag{2.3.26}$$

which is the new boundary condition on bubble b. This computation is repeated for each bubble in the tissue. Then the entire finite difference calculation is looped over each time-step until $s = T$ and the total time has elapsed.

Furthermore, the numerical scheme must satisfy the von Neumann stability conditions after non-dimensionalisation,

$$\frac{\delta t}{\alpha^{\mathrm{N}_2} k_H^{\mathrm{N}_2}} \left(\frac{1}{(\delta x)^2} + \frac{1}{(\delta y)^2} \right) < \frac{1}{2}$$

It was found that once stable, varying δx, δy and δt had little effect on the results of the simulation.

Additionally, nucleation is not modelled per se. Instead, it is assumed that there already exist stable microbubble nuclei randomly distributed throughout the tissue from which it is possible for a bubble to grow. The mechanisms by which stabilisation is achieved are not investigated but could include the effects of surfactants and hydrophobicity of various sites in the body (Blatteau et al., 2006). It is important to note that for the purposes of this model, the number of nuclei remains constant and only one bubble can form at each. Consequently, to account for the stability of the nuclei in the model, an additional constraint on the bubble radius for $t \geq 0$ is,

$$R_b(t) \geq R_b(0), \; \forall \, b = 1, \ldots, N \tag{2.3.27}$$

2.3.5 Bubble coalescence and tissue boundary impacts in the numerical scheme

Although bubble coalescence is not modelled explicitly, care must be taken when two bubbles meet during the simulation. Since at least two points are needed outside of the bubble to calculate the gas flux, if two bubble edges are within two grid points of each other, they are deemed to have touched. In keeping with the assumptions, coalescence occurs instantly; the mass of the new bubble is equal to the sum of the masses of the two old bubbles and its new location is along a line that connects the centres of the old bubbles at a position that is in a ratio with the sizes of the two old bubbles. The reasoning behind this latter assumption was that a large bubble coalescing with a smaller one would not move very far from its initial position, whereas two bubbles of equal size could form one bubble located exactly equidistant between their centres.

In the case when the bubble impacts the tissue boundary, since it is assumed neither bubble nor tissue deforms, the centre of the bubble is moved one grid point away from the boundary. Again, as two grid points are needed to calculate the flux in a given direction, the bubble is deemed to have impacted the boundary when there are fewer than two grid points between it and the edge.

2.4 Results

The equations (2.3.17) to (2.3.20), (2.3.22) to (2.3.24) and (2.3.27) are solved using the parameters in table C.1 for various pressure and gas profiles. The initial investigation focuses on the growth of bubbles within the tissue for different dive profiles and gas mixtures. These profiles were obtained from a team of technical divers and classified as “conservative”, “normal” and “aggressive” for dives performed to different depths, and are explained in more detail in Appendix A. Although the divers questioned claimed that a particular dive was more aggressive – and by consequence more dangerous – than another, this claim is investigated using the tissue-bubble model, observing whether larger bubbles are predicted to appear for a less conservative dive profile. The characteristics of the more aggressive dives tend to be longer bottom times (BT) and fewer deep decompression stops.

For the purpose of bubble density in tissue, Van Liew and Burkard (1993) suggested that a density of 10^4 bubbles/ml is “very high”. This value is scaled for a two dimensional tissue as $\left(10^4\right)^{2/3}$ bubbles/cm^2. In addition, the bubbles’ positions were initially chosen at random but subsequently kept constant for subsequent simulations using the same number of bubbles.

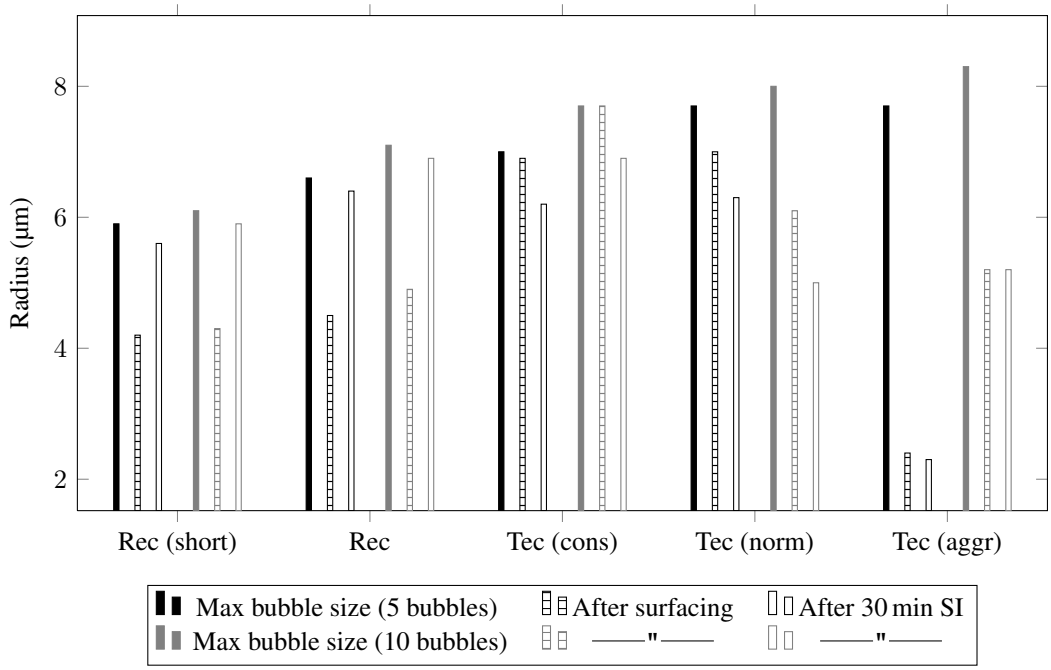

Figure 2.3: Size of the maximum bubble in the tissue at any point during the dive, immediately on surfacing and after a 30 minute surface interval (SI). This is shown for recreational (rec) dives and technical (tec) dives for conservative (cons), normal (norm) and aggressive (aggr) dive profiles on air. This data can be found in table A.1.

2.4.1 Air dives

The profiles for dives modelled where the breathing gas was air for the entire dive are presented in Appendix A.1. As well as decompression dives that were classified as conservative, normal and aggressive, recreational dives – where no decompression stops are required – are modelled, planned using the standard PADI Recreational Dive Planner. The results from the simulations for the dives performed on air are presented in figure 2.3.

The first visible trend is that the dives with longer bottom dives and/or were considered more aggressive lead to larger bubbles appearing in the tissue during the dive. This supports the hypothesis that it is the size of bubbles within the tissue that increases the risk of DCS during or after a dive. The other interesting trend is that increasing the number of bubbles in the tissue leads to a greater maximum bubble size over the course of the dive. This seems to contradict the intuitive belief that the more bubbles in the tissue, the smaller they would be since they are competing for a finite amount of gas. One possible explanation is that the bubbles "store" gas on the ascent which causes some of them to grow larger. When they are fewer in number, the off-gassing takes place more rapidly and efficiently, allowing the bubbles to shrink more easily.

In addition, after the recreational dives, the bubbles in the tissue continue to grow for approximately 30 minutes after surfacing. This is in contrast to the technical dives that are carried out to a deeper depth and require decompression stops, where the bubbles are shrinking on surfacing and continue to shrink further. This suggests that there is still a significant amount of gas in the tissue after a recreational dive, despite the 3 minute safety stop at 5 metres in the recreational dive profile recommended by PADI. On the other hand, the decompression stops during the technical dives allow sufficient gas to leave the tissue that the bubbles are no longer growing on surfacing. Consequently, a longer safety stop and/or a slower ascent is needed to reduce bubble growth on the surface after a recreational dive.

This latter point was further explored by Mroz (2012) who used this model and investigated the effects of varying the length of the dive and the nature of the decompression stops for dives to 45 m. It was found that the deep stops did have a small and positive effect in reducing bubble size. However, it was the presence of longer, shallow stops that had the greatest effect on bubble size, particularly in tissue with a relatively low bubble concentration. Those dives simulated with no stops led to the largest bubbles and also the largest total bubble volume. This particular study supports the hypothesis that aggressive dives with longer bottom times, no deep stops or less decompression do lead to larger microbubbles and with them, a potential increase in the risk of DCS.

Another interesting conclusion of Mroz's study was that there seemed to be a particular number density of bubbles that would lead to maximum bubble growth: too few bubbles and the gas can easily diffuse out of the tissue during the decompression stops; too many bubbles and the gas cannot diffuse into the tissue in order for the bubbles to grow. This is also reflected in the results here for the simulation of air dives.

The conclusion from the air dive modelling supports the dual-phase models such as VPM and RGBM that aim to minimise bubble size and free-phase gas volume by using deep stops. Furthermore, the model also supports the use of shallow safety stops in recreational diving to improve safety.

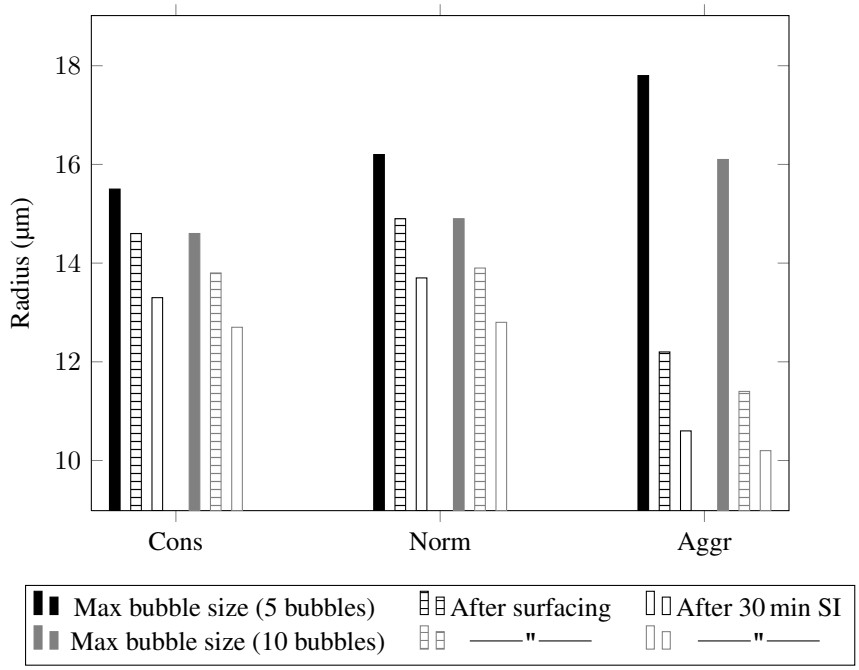

Figure 2.4: Size of the maximum bubble in the tissue at any point during the dive, immediately on surfacing and after a 30 minute surface interval (SI). This is shown for conservative (cons), normal (norm) and aggressive (aggr) dive profiles to 80 metres using trimix. This data can be found in table A.2.

2.4.2 Trimix dives

The profiles of dives modelled using trimix gases are presented in Appendix A.2. Dives to 80 m and 120 m in depth are simulated for different profiles. Furthermore, the 120 m dives are modelled for closed-circuit as well as open-circuit breathing apparatuses. Traditional open-circuit SCUBA gear expels all exhaled gas into the water. However, in a closed-circuit system, the exhaled air is recycled and any carbon dioxide "scrubbed out" and more oxygen injected if required. This means that, rather than being limited by the gas mixes in their cylinders, the diver has more freedom over the choice of gases during a dive. This generally leads to longer bottom times as well as shorter and/or fewer decompression stops. The results for the 80 m dive simulations are presented in figure 2.4 and the results for the 120 m dives on open- and closed-circuit breathing apparatuses are presented in figure 2.5.

In contrast with the results of the air dives in Section 2.4.1, the results of these simulations suggest that a greater number of bubbles in the tissue leads to a smaller maximum size during the dive. This change in behaviour may be because, as a result of a longer dive time, the gas has sufficient time to diffuse throughout the tissue and the bubbles now compete with each other for the available gas: the more bubbles in the tissue, the less gas available for each

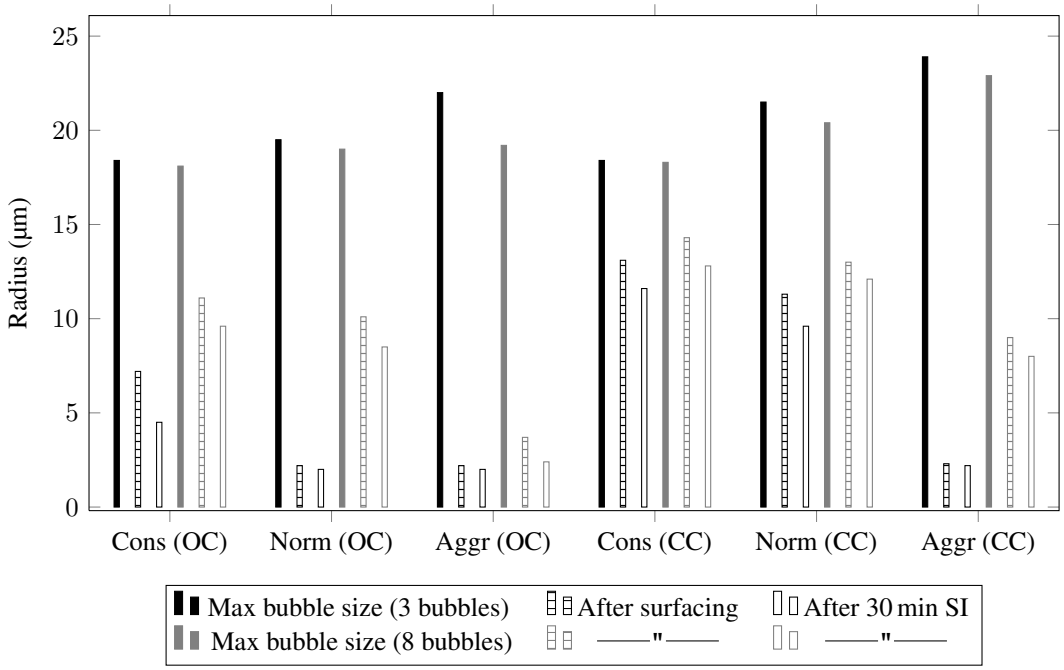

Figure 2.5: Size of the maximum bubble in the tissue at any point during the dive, immediately on surfacing and after a 30 minute surface interval (SI). This is shown for conservative (cons), normal (norm) and aggressive (aggr) dive profiles to 120 metres using trimix. The dives are also modelled for the use of open-circuit (OC) and closed-circuit (CC) breathing apparatuses. This data can be found in table A.3.

individual bubble. Furthermore, increased depth and bottom time leads to larger bubbles, once again suggesting that this could be a physiological reason why these profiles are riskier. On the other hand, the size of the bubbles on surfacing decreases as the risk of the dives increases. This is because the increased decompression times involved, particularly the long, shallow stops, allow the bubbles to shrink considerably before the diver exits the water. Whether the risk of these dives is due to the larger bubbles during the dive or some other physiological mechanism that has not been modelled is still an open question.

Additionally, there appears to be little difference between using open- and closed-circuit systems on the maximum size of the bubble. The longer bottom times modelled suggest that the increased flexibility in the diver's breathing gas when using a closed-circuit system has a small but noticeable effect on the rate of off-gassing and the size of the bubbles.

Moreover, the simulations suggest that gas changes under water do not have a significant effect on bubble growth, in contrast to the divers' belief that this could be a risk. In the same vein, it is observed that breathing gas with higher fractions of oxygen does lead bubbles to dissolve faster. Consequently, breathing 100% oxygen on return to the surface is a sensible option for the diver.

One further trend that can be drawn from this model is that the deeper dives lead to larger bubbles in the tissue. For the deepest dives modelled, these bubbles reach a size many times larger than a capillary, suggesting occlusion could be a dangerous risk for the diver, which in turn could be a contributing factor to DCS. Nevertheless, it must be stressed that these were dives that the divers considered sufficiently safe, suggesting there may be other risks to the safety of the diver that are not presently modelled.

2.5 Summary

In this chapter a tissue-bubble diffusion model is developed and presented that attempts to simulate bubble growth in a two-dimensional tissue for slow ambient pressure changes. A diffusion model is solved throughout the tissue and the concentration flux across bubble boundaries calculated by applying Boyle's and Henry's laws. Unlike previous models, this research accounts for multiple bubbles within the same block of tissue and their effects on each other as gas diffuses into and out of them. Within the human body, this represents a more realistic simulation of the processes occurring since bubbles would not occur in isolation.

Having neglected the convection term in the diffusion equation, this model is only applicable in situations where pressure changes are gradual and bubble wall velocities small. Furthermore, nucleation and coalescence have been approximated in a simple manner that does not reflect the full underlying physics. However, it is argued that coalescence phenomena occur on a timescale that is much faster than the pressure changes and can be reasonably ignored. The assumption that there exist microbubble nuclei from which bubbles grow is reasonable and fits with experimental data.

Moreover, the assumption that the gas concentration in the blood supplying the tissue instantly equilibrates with the breathing gas fails to take into account the time it takes for the gas to be transported to the tissue from the lungs. Since the pressure changes are slow relative to the time it takes for blood to circulate the body, it is not expected that this would have a significant impact on the results of the model. On the other hand, gas transported from other tissues could affect bubble growth in a different part of the body, particularly in areas that are less well supplied with blood. Highly vascular tissue such as the brain are less likely to be affected by this phenomenon.

The model is applied to realistic recreational and technical dives using different breathing gas mixes. Results suggest that deeper dives with more aggressive profiles lead to larger

bubbles in the tissue but after lengthy decompression, they are smaller on surfacing. This leads to a number of different possible scenarios with regards to the risks of DCS:

1. Since these bubbles are modelled to grow within tissue and never enter the blood stream, these large bubbles may never be at risk of causing occlusions and DCS.

2. The assumptions that the bubbles remain within the tissue is incorrect and in reality they escape into the blood stream where they dissolve more rapidly before they reach a dangerous size.

3. It is the number, as well as the size of bubbles, that increases the risks of DCS.

4. Large bubbles coalesce with each other, increasing the chance of DCS.

5. The real danger of aggressive dives is outside of the tissue, something that has hitherto not been modelled.

The problem of modelling bubble growth in tissue during a dive is an extremely complex one. Nevertheless, qualitatively, the results here support some hypotheses about the danger of certain dive profiles relating to bubble size, but how DCS arises is still an open question.

The main conclusion of these simulations is that dives that are traditionally considered more dangerous because they have longer bottom times, fewer deep stops and/or shorter decompression schedules do lead to larger bubbles, potentially increasing the risk of DCS. This validates the divers' intuition as well as their current diving algorithms and practices.

Other conclusions that can be drawn from the simulations are that bubble growth is fastest close to the blood vessel. This implies that deep stops (also known as "Pyle stops") would have less of an effect on bubbles in tissue with poor blood circulation such as in cartilage and joints, areas of the body traditionally associated with long-term damage in deep divers. In the same vein, shallow stops do have a significant effect on bubble size on surfacing and it could be concluded from these simulations that PADI should increase the recommended length of the safety stop during recreational dives. Having said that, since the bubbles are smaller, any continued increase in bubble size on surfacing may not significantly increase the risk of DCS.

Furthermore, the number of bubbles in the tissue affects their growth rate and maximum size. Echoing Mroz's results, there appears to be a number density of bubbles in the tissue that leads to the largest growth: fewer bubbles allows the gas to diffuse out of the tissue easily; more bubbles leads to competition for gas between them and limits their growth.

Additionally, breathing gas with a high concentration of oxygen encourages bubble elimination and should continue to be breathed on surfacing to reduce sudden bubble growth particularly after deep dives, whereas gas changes during a dive have little effect on bubble size.

In future, it would be helpful to model more bubble concentrations and different tissue types by varying the model parameters in table C.1. However, the computational nature of the model meant that further investigation was not possible.

Having considered the quasi-static growth of a bubble population in tissue, the next chapter investigates time-dependent effects of ultrasound on an individual lipid-coated microbubble. To account for the effect of gas diffusion into and out of the bubble on its behaviour, three diffusion equations for the air, perfluorocarbon and surfactant dissolved in the bulk liquid are solved simultaneously with an equation of motion for the microbubble oscillations. Since the bubble wall velocities in this situation are large, the convection term cannot be ignored and the equations become coupled.

CHAPTER 3

MICROBUBBLE DYNAMICS AND SURFACTANT SHEDDING

In Chapter 2, the problem of bubble growth in tissue undergoing slow pressure changes was modelled. In this chapter, the time-dependent behaviour of lipid-coated microbubbles undergoing ultrasound excitation is investigated, including diffusion and lipid shedding effects.

Uncoated microbubbles would dissolve in a few tenths or hundredths of a second (Epstein and Plesset, 1950) as a result of the effects of both surface tension and gas concentration gradient unless the liquid is saturated. This creates a pressure gradient across the boundary and drives gas out. Contrast agents used in biomedical applications on the other hand, must be able to survive for seconds or minutes in order to reach a desired imaging site in the body after injection. As a result, they have some form of stabilising coating, such as a protein or phospholipid. Since the most widely used microbubble contrast agents SonoVue® and Definity® are lipid-coated, this research focuses on the effects of these lipids on bubble behaviour.

Each lipid molecule on the microbubble surface is made up of a hydrophilic head and hydrophobic tail; thermodynamically, the most stable arrangement is for the head of the lipid to remain in the liquid and for the tail to sit inside the bubble. The effect of the resulting monolayer is to both reduce the surface tension that drives the dissolution of the bubble as well as inhibiting the diffusion of gas across the boundary.

Both of these effects lead to longer contrast agent survival times. Furthermore, the presence of surfactants also leads to changes in the microbubble's behaviour under insonation. The main changes are increased nonlinearity in the bubble oscillation, leading to higher levels of sub- and higher harmonics in the scattered signal. Models have been proposed to account for the effect of surfactants on bubble behaviour and their radial oscillations, primarily de Jong, Cornet and Lancee (1994); Church (1995); Hoff, Sontum and Hovem (2000); Sarkar

et al. (2005) and Marmottant et al. (2005). Whilst these have had varying degrees of success in modelling microbubble behaviour and introducing the aforementioned dynamics into the physics, they all assume that the bubble remains unchanged post-insonation. In particular, they all assume that the surfactant mass on the surface of the bubble is constant.

However, it has been shown by Borden et al. (2005) and Viti et al. (2011) that multiple insonations of the same contrast agent microbubble do not always result in the same response. Bubbles much smaller or larger than resonance remained relatively stable, whereas those close to resonance exhibited the greatest changes. The most notable was a reduction in bubble radius accompanied by variations in the harmonic content of the scattered signal. Fyrillas and Szeri (1994, 1995, 1996) modelled the effect of surfactant-dependent diffusivity on gas diffusion into and out of the bubble and theoretically derived the thresholds required for rectified diffusion to occur. This was shown to take place on the timescale of the transport of gas molecules through the liquid, which is much longer than the timescale of a microbubble oscillation at medical ultrasound frequencies (i.e. MHz), thus could not account for changes in bubble size.

Additionally, the experimental evidence by Borden et al. (2005) and Viti et al. (2011) using high-speed camera images showed not only microbubble shrinkage, but also that it eventually reached a stable size. Moreover, Borden et al.'s images showed material shedding during or after the pulse. Since the only material present on the bubble is the surfactant coating, this suggests that surfactant shedding can take place under certain circumstances, thus violating the assumption of constant surfactant mass made in the bubble models mentioned previously.

The other surprising result of Viti et al.'s work (2011) was changes in microbubble oscillation during subsequent pulses, between compression- and expansion-only. Whereas Marmottant et al.'s (2005) and Stride's (2008) nonlinear surface tension models explain some of this behaviour, they cannot account for dynamic changes in oscillation during an experiment.

Since these effects are of particular importance in medical ultrasound and have hitherto not been modelled, this chapter incorporates a new nonlinear surface tension model as well as a gas diffusion and surfactant shedding mechanism into an equation of motion for a lipid-coated microbubble. Consequently, the shrinking of a microbubble both during and after insonation, together with compression- and expansion-only behaviour during the course of multiple can be accounted for[1].

[1]Published in O'Brien, Ovenden and Stride (2011a)

3.1 Overview of free-bubble dynamics models

The radial motion of a spherical bubble as a function of time is $R(t)$. The model parameters are the equilibrium rest radius R_0, the external pressure p, the interior bubble pressure p^{int} as well as the density of the liquid ρ. The basic model is the Rayleigh model (1917),

$$\rho R\ddot{R} + \frac{3}{2}\rho\dot{R}^2 = p^{\text{int}} - p$$

When the liquid viscosity μ_l and surface tension σ are taken into account, Plesset (1949) assumed an adiabatic process with polytropic index γ to show,

$$\rho R\ddot{R} + \frac{3}{2}\rho\dot{R}^2 = \left(\frac{2\sigma}{R_0} + p_0 - p_v\right)\left(\frac{R_0}{R}\right)^{3\gamma} + p_v - p_0 - \frac{2\sigma}{R} - \frac{4\mu_l\dot{R}}{R} - p(t)$$

The Keller-Miksis model (Keller and Miksis, 1980) incorporates sound radiation from the oscillating bubble and features a retarded time $(t - R/\mathcal{C})$. To first order in $\mathcal{C}^{-1}$, it was shown by Prosperetti (1984) and Parlitz et al. (1990) that this model is equivalent to,

$$\left(1-\frac{\dot{R}}{\mathcal{C}}\right)R\ddot{R}+\frac{3}{2}\left(1-\frac{\dot{R}}{3\mathcal{C}}\right)\dot{R}^2 = \frac{1}{\rho}\left(1+\frac{\dot{R}}{\mathcal{C}}+\frac{R}{\mathcal{C}}\frac{d}{dt}\right)\left(p_0^{\text{int}}\left(\frac{R_0}{R}\right)^{3\gamma}-\frac{2\sigma}{R}-4\mu_l\frac{\dot{R}}{R}-p_0-p(t)\right)$$

Another model by Gilmore (1952) also included sound radiation by modelling the surface of the bubble as a loudspeaker. For strong oscillations, Löfstedt, Barber and Putterman (1993) extended the model to account for a non-compressible volume of the inert gas inside the bubble by using a van der Waals hard core law.

The other main model including sound radiation is the Herring equation (Herring, 1941; Trilling, 1952),

$$\left(1-\frac{2\dot{R}}{\mathcal{C}}\right)R\ddot{R}+\frac{3}{2}\left(1-\frac{4\dot{R}}{3\mathcal{C}}\right)\dot{R}^2 = \frac{1}{\rho}\left(1+\frac{R}{\mathcal{C}}\frac{d}{dt}\right)\left(p_0^{\text{int}}\left(\frac{R_0}{R}\right)^{3\gamma}-\frac{2\sigma}{R}-4\mu_l\frac{\dot{R}}{R}-p_0-p(t)\right)$$

The Herring and Keller-Miksis equations were derived rigorously by Prosperetti and Lezzi (1986) and shown to be equivalent to within an arbitrary constant. However, it was not determined which of the two equations is the most accurate.

3.2 Overview of encapsulated bubble dynamics models

Models for encapsulated bubbles have evolved along two paths. One approach is to model the coating as a non-Newtonian liquid layer of finite thickness characterised by viscoelastic parameters (Avetisyan, 1977) and derive a Rayleigh-Plesset type equation from first principles. Assuming a spherical bubble immersed in an infinite liquid, Church (1995) rigorously derived,

$$R_1\ddot{R}_1\left(1+\left(\frac{\rho_l-\rho_S}{\rho_S}\right)\frac{R_1}{R_2}\right)+\dot{R_1}^2\left(\frac{3}{2}+\left(\frac{\rho_l-\rho_S}{\rho_S}\right)\left(\frac{4R_2^3-R_1^3}{2R_2^3}\right)\frac{R_1}{R_2}\right)=$$
$$\frac{1}{\rho_S}\left(p_0^{\text{int}}\left(\frac{R_{10}}{R_1}\right)^{3\gamma}-\frac{2\sigma_1}{R_1}-\frac{2\sigma_2}{R_2}-4\mu_l\frac{R_1^2\dot{R}_1}{R_2^3}-p_0-p(t)+3\int_{R_1}^{R_2}\frac{\tau_{rr}^{(S)}(r,t)}{r}\mathrm{d}r\right)$$

where R_1 and R_2 are the inner and outer radii of the bubble shell respectively; ρ_l and ρ_S are the densities of the liquid and shell; σ_1 and σ_2 are the surface tension coefficients for the gas-shell and shell-liquid interfaces respectively; $\tau_{rr}^{(S)}$ is the radial component of the stress tensor of the shell. This can be simplified by assuming a small, but finite thickness ϵ of shell with shear modulus η_S and shear viscosity μ_s, as done by Hoff, Sontum and Hovem (2000), and using the Kelvin-Voigt law to model the stress,

$$R\ddot{R}+\frac{3}{2}\dot{R}^2=\frac{1}{\rho}\left(p_0^{\text{int}}\left(\frac{R_0}{R}\right)^{3\gamma}-\frac{2\sigma}{R}-4\mu_l\frac{\dot{R}}{R}-p_0-p(t)-12\eta_S\frac{\epsilon R_0^2}{R^3}\left(1-\frac{R_0}{R}\right)-12\mu_\text{s}\frac{\epsilon R_0^2}{R^3}\frac{\dot{R}}{R}\right)$$

The other approach to modelling encapsulated bubbles is to include the effects of encapsulation into a Rayleigh-Plesset equation in a heuristic manner based on empirical observations. To account for a shell with elasticity and friction parameters S_p and S_f respectively, de Jong, Cornet and Lancee (1994) proposed the following modification,

$$R\ddot{R}+\frac{3}{2}\dot{R}^2=\frac{1}{\rho}\left(p_0^{\text{int}}\left(\frac{R_0}{R}\right)^{3\gamma}+p_v-\frac{2\sigma}{R}-p_0-p(t)-\delta\omega\rho R\dot{R}-2S_p\left(\frac{1}{R_0}-\frac{1}{R}\right)-\frac{S_f\dot{R}}{4\pi R^2}\right)$$

Expressions for the damping coefficient δ are given by Medwin (1977), although different expressions can be used (Church, 1995). The Church model is sometimes compared with the de Jong model by saying the former was derived for a shell of finite thickness whereas the latter was derived with an infinitesimal shell thickness. Consequently, it is claimed the Church model is more suitable for albumin-shelled bubbles with a shell thickness of approximately 20 nm whereas the de Jong model is more suitable for lipid-coated bubbles whose shell thickness is approximately 2 nm. Reassuringly, Doinikov and Bouakaz (2011) showed that in the limit of the shell thickness tending to zero and linear oscillations, the shell terms in the Church model are identical to the de Jong model.

Another approach to developing a dynamic surface tension model that accounts for the effect of a surfactant coating on the bubble surface was taken by Fox and Herzfeld (1954), who proposed a purely elastic membrane on the bubble surface characterised by its Young's modulus and Poisson's ratio. Glazman (1983) subsequently derived a model in which the properties of the elastic membrane arise as a result of the interfacial variation of adsorbed molecules. This approach was extended by Marmottant et al. (2005) who assumed that: there exists a lower limit of the radius R_{buck} below which the shell buckles; an upper radius limit $R_{\text{break-up}}$ before the shell breaks; a rupturing radius R_{rupt} above which the shell is ruptured. The shell elasticity and friction parameters of the de Jong model are replaced by $\chi = S_p/2$ and $\mu_{\text{s}} = S_f/16\pi$ and a nonlinear surface tension $\sigma(R)$ defined by assuming a constant surfactant mass on the bubble surface,

$$\sigma(R) = \begin{cases} 0 & \text{if } R \leq R_{\text{buck}}, \\ \chi\left(\dfrac{R^2}{R_{\text{buck}}^2} - 1\right) & \text{if } R_{\text{buck}} \leq R \leq R_{\text{break-up}}, \\ \sigma_0 & \text{if ruptured/broken and } R \geq R_{\text{rupt}}. \end{cases} \tag{3.2.1}$$

According to this model, the elastic regime holds for small bubble oscillations, but above and below this range, the bubble either breaks-up or buckles leading to a maximum or minimum surface tension on the bubble boundary. The "break-up" surface tension $\sigma_{\text{break-up}}$ when the radius is $R_{\text{break-up}}$, can be higher than σ_0 because "any polymer component confers more cohesion to the shell, and shifts the break-up to higher tensions" (Marmottant et al., 2005, p. 3501).

Other models that have been developed, based on the Church and de Jong models, are the Chatterjee-Sarkar model (Sarkar et al., 2005), Doinikov model (Doinikov, Haac and Dayton, 2009), Tsiglifis-Pelekasis model (Tsiglifis and Pelekasis, 2008) and the Paul model (Paul et al., 2010).

Since this thesis focuses on the behaviour of lipid-coated microbubbles, a new equation of motion describing their behaviour is developed based on the de Jong model. The effects of diffusion along with surfactant shedding and a surface tension that depends on the surfactant surface concentration are included in the next section. The model for surface tension is based on the Marmottant model since it is particularly successful in replicating experimentally observed SonoVue® bubble oscillations and sub-harmonic content in the scattered signal.

3.3 Diffusion problem

In this section, a mathematical model for the dynamics of a lipid-coated microbubble incorporating the effects of gas and lipid diffusion is presented. There are in fact two diffusion problems to consider: one is the diffusion of gas between the bubble and the bulk liquid; the other is the diffusion of surfactant from the bubble surface into and throughout the bulk liquid. An analytical approach was explored by Fyrillas and Szeri (1994, 1995, 1996) where a multiple scales method was used. Briefly, concentration of the gas $c(r,t)$ in the liquid is modelled by the usual convection-diffusion equation and the boundary condition on the bubble stating that the rate of change of mass of gas inside the bubble m is equal to the flux of gas through its boundary, where the diffusivity $D(\Gamma)$ is a function of the surface concentration $\Gamma(t)$,

$$\frac{\partial c}{\partial t} + \frac{R^2\dot{R}}{r^2}\frac{\partial c}{\partial r} = \frac{D}{r^2}\frac{\partial}{\partial r}\left(r^2\frac{\partial c}{\partial r}\right) \tag{3.3.1}$$

$$\frac{dm}{dt} = 4\pi R^2 D(\Gamma)\frac{\partial c(r=R,t)}{\partial r} \tag{3.3.2}$$

The dynamics of the microbubble oscillations in a static pressure field p_0 and driving pressure $p(t)$ are modelled using a Rayleigh-Plesset equation for the partial pressures of air and perfluorocarbon (PFC) inside the bubble p_b^{air} and p_b^{PFC} and it is assumed that the shell surface viscosity μ_s is constant,

$$R\ddot{R} + \frac{3\dot{R}^2}{2} = \frac{1}{\rho}\left(\left(p_b^{\text{air}} + p_b^{\text{PFC}}\right)\left(\frac{R_0}{R}\right)^{3\gamma} + p_v - \frac{2\sigma(\Gamma)}{R} - \frac{4\mu_l\dot{R}}{R} - \frac{4\mu_\text{s}\dot{R}}{R^2} - p_0 - p(t)\right) \tag{3.3.3}$$

The partial pressure exerted by a dissolved gas is proportional to its concentration in the mixture and Henry's constant k_H,

$$c = k_H p$$

which, by assuming constant temperature and gas pressure throughout the bubble, gives a value for the concentration of gas to use as a boundary condition at $c(0,t)$. Assuming ideal gas behaviour, the partial pressure in a bubble of volume V containing n moles of gas with molar mass M at a temperature T is related to the mass of gas using the ideal gas law,

$$\begin{aligned} pV &= nGT \\ &= \frac{mGT}{M} \\ &= m\alpha \end{aligned}$$

where G is the universal gas constant and $\alpha \coloneqq GT/M$. The Rayleigh-Plesset can now be rewritten,

$$R\ddot{R}+\frac{3\dot{R}^2}{2}=\frac{1}{\rho}\left(\frac{1}{V}\left(m^{\text{air}}\alpha^{\text{air}}+m^{\text{PFC}}\alpha^{\text{PFC}}\right)\left(\frac{R_0}{R}\right)^{3\gamma}+p_v-\frac{2\sigma(\Gamma)}{R}-\frac{4\mu_l\dot{R}}{R}-\frac{4\mu_{\text{s}}\dot{R}}{R^2}-p_0-p(t)\right) \tag{3.3.4}$$

Since the rate of change of the mass of gas is given by equation (3.3.2), it is a simple process of calculating the flux given the results of the diffusion equation (3.3.1) and using that to update the mass of gas inside the bubble, whereupon equation (3.3.4) is solved using the 4$^{\text{th}}$-order Runge-Kutta method to model its behaviour.

Similarly, the diffusion equations governing the surfactant behaviour with bulk diffusivity D_{s} are formulated using a kinetic expression for the surfactant Φ,

$$\frac{\partial C}{\partial t}+\frac{R^2\dot{R}}{r^2}\frac{\partial C}{\partial r}=\frac{D_{\text{s}}}{r^2}\frac{\partial}{\partial r}\left(r^2\frac{\partial C}{\partial r}\right) \tag{3.3.5}$$

$$\frac{d\Gamma}{dt}+2\frac{\dot{R}}{R}\Gamma=\Phi\big(\Gamma,C(r=R,t)\big) \tag{3.3.6}$$

$$D_{\text{s}}\frac{\partial C(r=R,t)}{\partial r}=\Phi\big(\Gamma,C(r=R,t)\big) \tag{3.3.7}$$

The differential equation governing the surfactant concentration over a microbubble's surface area A is,

$$\frac{d(A\Gamma)}{dt}=\Phi\big(\Gamma,C(r=R,t)\big) \tag{3.3.8}$$

The above equations are solved by first splitting the problem into smooth and oscillatory parts and then using a method of multiple scales approach. On the one hand, the oscillation of the bubble is occurring on a fast timescale whilst the diffusion process takes place on a much longer timescale, hence the problem lends itself well to using a slow and fast timescale.

Fyrillas and Szeri (1994, 1995, 1996) found a series expansion for large values of the gas and surfactant Péclet numbers $Pe=R_0^2\omega/D$ and $Pe_{\text{s}}=R_0^2\omega/D_{\text{s}}$ for typical values of the radius R_0 and frequency ω. In this current research, the Péclet numbers are large since $R_0\sim10^{-6}$ m, $\omega\sim10^6$ Hz, $D\sim10^{-9}$ m^2/s and $D_{\text{s}}\sim10^{-12}$ m^2/s, hence $Pe\sim10^3$ and $Pe_{\text{s}}\sim10^6$ and consequently their research is applicable in this work. Importantly, the order of Pe suggests that diffusion becomes important on the timescale of milliseconds, or a pulse repetition frequency of 1 kHz.

The crucial difference in this work, however, is the treatment of the boundary condition, i.e. Φ above. In Fyrillas and Szeri's work, there was no mechanism for surfactant shedding to

occur. To account for this, Morris et al.'s (2001) collapsing film model (initially developed to model the effect of DPPC adsorption and diffusion in the bulk on a microbubble) is used and coupled with a bubble dynamics equation. To understand its behaviour, the shedding model is analysed using a multiple scales approach.

3.4 Collapsing film model

To begin, it is assumed different regimes of boundary condition behaviour exist depending on the surface concentration at a particular time.

Firstly, the surfactant surface concentration on the microbubble $\Gamma(t)$ is assumed to be governed by Langmuir adsorption at concentrations close to equilibrium. There exists a maximum surface concentration Γ^* that can be achieved by increasing the bulk surfactant concentration C_∞ to the saturation concentration C_{sat} and once reached, the surfactant is assumed to become insoluble on the bubble surface. Furthermore, there is said to exist a maximum concentration Γ_{max} that the bubble surface can support. Above this concentration, the surfactant film "collapses" and material is ejected from the bubble. Consequently, the boundary conditions (3.3.8) on the surface of the microbubble are modified,

$$\frac{d\big(A(t)\Gamma(t)\big)}{dt} = A(t)D_{\text{s}}\left.\frac{\partial C(r,t)}{\partial r}\right|_{r=R} \tag{3.4.1}$$

$$\frac{d(A\Gamma)}{dt} = \begin{cases} A\left[a_1 C(R,t)\left(\Gamma^* - \Gamma\right) - a_2\Gamma\right] & \text{if } \Gamma < \Gamma^*, \\ 0 & \text{if } \Gamma^* < \Gamma < \Gamma_{\text{max}}, \\ \Gamma_{\text{max}}\dfrac{dA}{dt} & \text{if } \Gamma_{\text{max}} < \Gamma. \end{cases} \tag{3.4.2}$$

Here, the Langmuir adsorption and desorption coefficients, a_1 and a_2 respectively, are allowed to reduce to zero linearly as Γ^* is approached in order to avoid a numerical artefact that Morris et al. (2001) call "pseudo-film collapse". Consequently a_i, for $i = 1, 2$, are written as functions of Γ,

$$a_i(\Gamma) = \begin{cases} a_i & \Gamma < 0.96 \times \Gamma^*, \\ 25a_i\left(1 - \dfrac{\Gamma}{\Gamma^*}\right) & 0.96 \times \Gamma^* < \Gamma < \Gamma^*, \\ 0 & \Gamma > \Gamma^*. \end{cases} \tag{3.4.3}$$

This is unphysical but will be used in this research for consistency with their work and since it is not anticipated to have a large impact on the results.

Equation (3.4.2) is used to obtain the value of the equilibrium surface concentration Γ_{eq} at $t = 0$,

$$\Gamma_{\text{eq}} = \frac{\Gamma^* a_1 C_\infty}{a_1 C_\infty + a_2} \tag{3.4.4}$$

This model is further extended by using Marmottant et al.'s model (2005) for surface tension that depends on the surfactant concentration on the bubble. At small oscillations, the shell is elastic for a narrow surface area range. For large compressions, the shell buckles at a radius of R_{buck} and the surface tension reaches a minimum σ_{min}. For large expansions, the shell ruptures at a radius of R_{rupt}, at which point the surfactant molecules are sufficiently far apart that they do not have an effect on the surface tension and the value is that of the uncoated bubble σ_0. These conditions can be formulated in terms of the surface concentration since $\Gamma = m_{\text{s}}/(4\pi R^2)$ and adapting equation (3.2.1), the surface tension is,

$$\sigma(\Gamma) = \begin{cases} \sigma_0 & \text{if } \Gamma < \Gamma_{\text{rupt}}, \\ \sigma_{\text{min}} + \chi\left(\dfrac{\Gamma_{\text{buck}}}{\Gamma} - 1\right) & \text{if } \Gamma_{\text{rupt}} < \Gamma < \Gamma_{\text{buck}}, \\ \sigma_{\text{min}} & \text{if } \Gamma_{\text{buck}} < \Gamma. \end{cases} \tag{3.4.5}$$

To avoid discontinuities in the Marmottant surface tension model, equation (3.4.5) is replaced by a smooth sigmoid curve. The relationship between surface concentration and surface tension using coefficients Q, U, W and Y are fitted to the discontinuous model,

$$\sigma(\Gamma) = \sigma_0 + \frac{\sigma_{\text{min}} - \sigma_0}{\Big(1 + Q\exp\big(-U(\Gamma - W)\big)\Big)^{1/Y}} \tag{3.4.6}$$

To determine the parameter values, equation (3.3.3) is solved using a 4$^{\text{th}}$-order Runge-Kutta method and compared to Viti et al.'s experimental data (unpublished). The sigmoidal surface tension coefficients determined by choosing $\Gamma_{\text{eq}} = \Gamma_{\text{buck}}$, $\chi = 0.5$ N/m and $\sigma_{\text{min}} = 0.001$ N m (Morris et al., 2001) in equation (3.4.5) and fitting (3.4.6) using MATLAB®'s *fit* function are presented in table C.2 and figure 3.1. The result of using these values and $\mu_{\text{s}} = 4 \times 10^{-9}$ kg/s in equation (3.3.3) is shown in figure 3.2 for the insonation of a 1.4 µm radius bubble at 2 MHz.

It is also assumed that diffusivity through the bubble surface is a function of surfactant concentration. A linear dependence between surface concentration and diffusivity is used, as shown in figure 3.3. However, since it has been noted (Mulvana et al., 2010, 2012) that SonoVue® microbubbles are stable to the extent that they will survive for hours or even days,

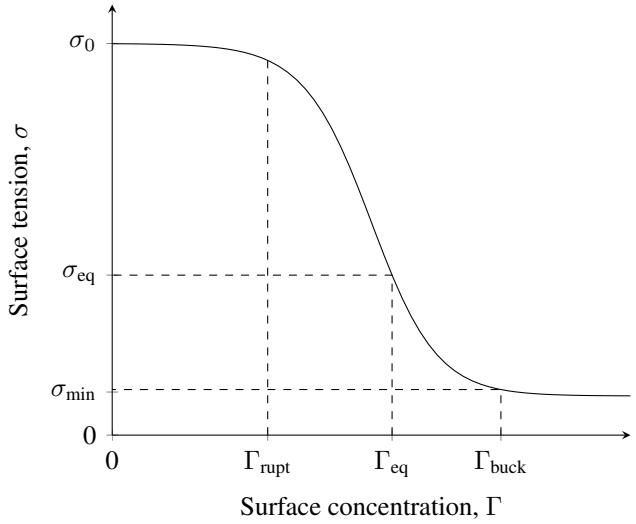

Figure 3.1: The model of the behaviour of surface tension, σ, versus surface concentration, Γ, using a general sigmoid function (3.4.6) fitted to Marmottant et al.'s surface tension model (2005) using $R_0 = R_{\text{buck}}$ and $\chi = 0.5\,\text{N/m}$ in equation (3.2.1).

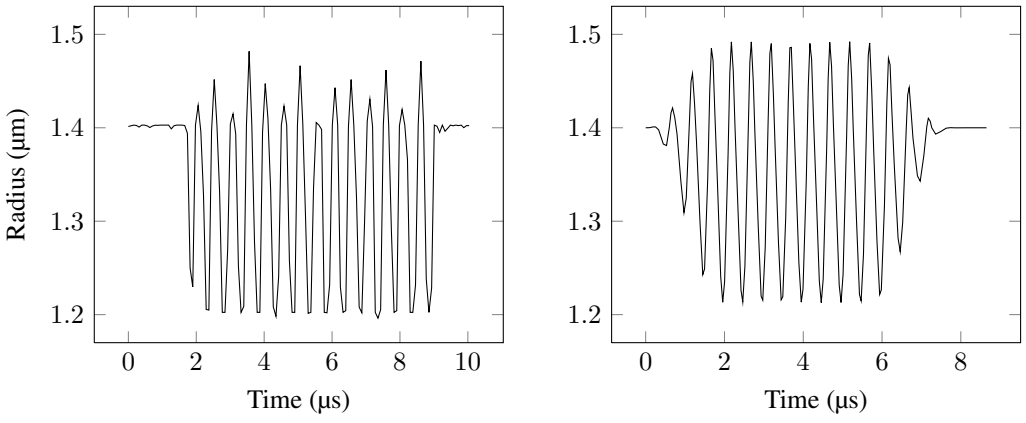

(a) Experimental data

(b) Rayleigh-Plesset simulation

Figure 3.2: Microbubble insonation at 2 MHz and 70 kPa peak negative pressure: (a) high-speed camera microscopy data of Viti et al. (unpublished data) sampled at 12 MHz; (b) the numerical solution of equation (3.3.3) using the sigmoidal surface tension function (3.4.6) and coefficients in table C.2.

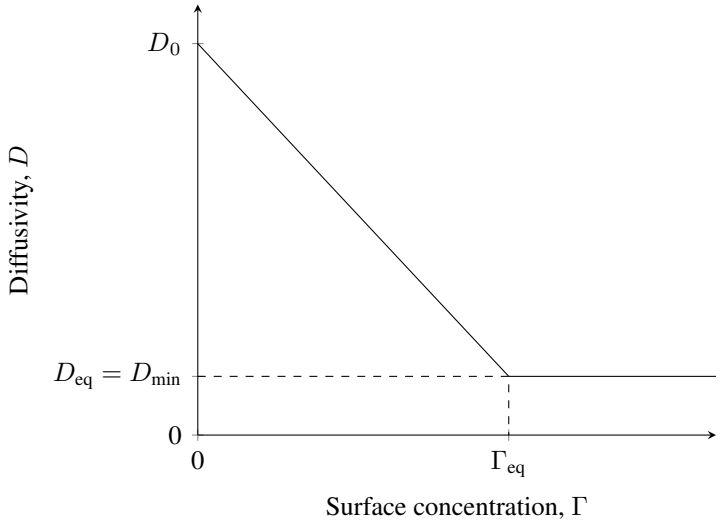

Figure 3.3: Relationship between diffusivity and surface concentration of surfactant. Since microbubble contrast agents are stable at Γ_{eq}, it is assumed that $D = D_{\text{min}}$ at that point.

the effect of gas diffusing out must be small at equilibrium. Consequently, it is assumed that the diffusivity D is equal to some minimum value D_{min} at $\Gamma = \Gamma_{\text{eq}}$ in order to replicate these observations. In the limit of surface concentration tending to zero, the clean-surface diffusivity constant D_0 is recovered.

The shell surface viscosity μ_{s} on the other hand is assumed to be constant at all times. It is likely that this parameter also depends on the concentration of surfactant on the bubble surface but a model for this effect is not incorporated for the sake of simplicity.

3.4.1 Non-dimensional boundary conditions

The boundary condition is analysed assuming that the saturation concentration C_{sat} is sufficiently larger than the bulk concentration at infinity C_∞ that all surfactant ejected from the bubble surface dissolves into the fluid outside the microbubble. Thus the boundary conditions on the bubble are given by flux conditions for the rate of change of mass of surfactant adsorbed.

Equation (3.4.2) is non-dimensionalised using the frequency of the incident pulse ω, initial bubble radius R_0, maximum surface concentration attainable through adsorption processes alone Γ^*, concentration of surfactant in the bulk at infinity C_∞ and a characteristic concentration $\widehat{C}$,

$$\begin{aligned} t &= \omega^{-1} t', & r &= R_0 r', & R &= R_0 R', \\ C &= \widehat{C} C' + C_\infty, & \Gamma &= \Gamma^* \Gamma', & Pe_{\text{s}} &= \frac{R_0^2 \omega}{D_{\text{s}}}. \end{aligned} \tag{3.4.7}$$

Inserting into equation (3.4.2) and dropping the primes for clarity leads to,

$$\left.\frac{\partial C}{\partial r}\right|_{r=R} = \begin{cases} \dfrac{R_0\Gamma^*}{\widehat{C}D_\mathrm{s}}\Big(a_1\big(\widehat{C}C(R,t)-C_\infty\big)(1-\Gamma)-a_2\Gamma\Big) & \Gamma<1, \\ 0 & 1<\Gamma<\dfrac{\Gamma_\mathrm{max}}{\Gamma^*}, \\ \dfrac{2\Gamma_\mathrm{max}R_0\omega}{\widehat{C}D_\mathrm{s}}\dfrac{1}{R}\dfrac{dR}{dt} & \Gamma>\dfrac{\Gamma_\mathrm{max}}{\Gamma^*}. \end{cases}$$

Using a non-dimensional version of (3.4.4) and rearranging, this is written as,

$$\left.\frac{\partial C}{\partial r}\right|_{r=R} = \begin{cases} \dfrac{R_0\Gamma^*a_1}{D_\mathrm{s}}C(R,t)\big(1-\Gamma\big)+\dfrac{R_0\Gamma^*\big(a_1C_\infty+a_2\big)}{\widehat{C}D_\mathrm{s}}\big(\Gamma_\mathrm{eq}-\Gamma\big) & \Gamma<1, \\ 0 & 1<\Gamma<\dfrac{\Gamma_\mathrm{max}}{\Gamma^*}, \\ \dfrac{2\Gamma_\mathrm{max}R_0\omega}{\widehat{C}D_\mathrm{s}}\dfrac{1}{R}\dfrac{dR}{dt} & \Gamma>\dfrac{\Gamma_\mathrm{max}}{\Gamma^*}. \end{cases}$$

Choosing $\widehat{C}=\big(R_0\Gamma^*(a_1C_\infty+a_2)\big)/D_\mathrm{s}$,

$$\left.\frac{\partial C}{\partial r}\right|_{r=R} = \begin{cases} \dfrac{R_0\Gamma^*a_1}{D_\mathrm{s}}C(R,t)\big(1-\Gamma\big)+\big(\Gamma_\mathrm{eq}-\Gamma\big) & \Gamma<1, \quad \text{(3.4.8a)} \\ 0 & 1<\Gamma<\dfrac{\Gamma_\mathrm{max}}{\Gamma^*}, \quad \text{(3.4.8b)} \\ \dfrac{2\omega}{(a_1C_\infty+a_2)}\dfrac{\Gamma_\mathrm{max}}{\Gamma^*}\dfrac{1}{R}\dfrac{dR}{dt} & \Gamma>\dfrac{\Gamma_\mathrm{max}}{\Gamma^*}. \quad \text{(3.4.8c)} \end{cases}$$

Typical values (Morris et al., 2001) for the constants in equation (3.4.8) are $\omega\sim10^6\,\mathrm{Hz}$, $R_0\sim10^{-6}\,\mathrm{m}$, $\Gamma^*\sim10^{-8}\,\mathrm{kg/m^2}$, $C_\infty\sim1\,\mathrm{kg/m^3}$, $D_\mathrm{s}\sim10^{-12}\,\mathrm{m^2/s}$, $a_1\sim1\,\mathrm{m^3/(kg\,s)}$ and $a_2=0.01a_1=0.01\,\mathrm{s^{-1}}$.

Using these values, it can be seen that the first term in (3.4.8a) is of the order of 10^{-2} and the term in (3.4.8c) is of the order of 10^6. A value for the Péclet number can also be determined from (3.4.7) as $Pe_\mathrm{s}\sim10^6$.

In the absence of contrary experimental data, it is assumed that the first term in equation (3.4.8a) is $\mathcal{O}\left(Pe_\mathrm{s}^{-1/2}\right)$ and a_1 is $\mathcal{O}(1)$ (Morris et al., 2001). Furthermore, it is also assumed that the term in (3.4.8c) is of the order of the Péclet number Pe_s and, additionally, $\Gamma_\mathrm{max}/\Gamma^*$ is $\mathcal{O}(1)$.

3.4.2 Multiple scales

Similar to Fyrillas and Szeri (1994, 1995, 1996), the behaviour of the system is investigated by a multiple scales analysis. It was noted that, as a result of the effect of diffusion, the concentration of gas and surfactant will vary slowly throughout the bulk liquid. In addition, the effect of the bubble oscillation causes the concentration gradient at the bubble surface to increase and decrease with each cycle. Thus a multiple scales approach seems useful.

Moreover, the time-dependent nature of the boundary condition (3.4.2) renders the problem more difficult. To proceed, the governing convection-diffusion equations for the surfactant through the bulk is written, after non-dimensionalisation, as,

$$\frac{\partial C}{\partial t} = \frac{1}{Pe_{\mathrm{s}}}\frac{\partial}{\partial \zeta}\left(\left(3\zeta + R^3\right)^{4/3}\frac{\partial C}{\partial \zeta}\right) \tag{3.4.9}$$

where the equation has been transformed into Lagrangian coordinates $\zeta = \frac{1}{3}\left(r^3 - R^3\right)$. Writing $\mathcal{A}$ and $\mathcal{B}$ to account for variations in the scaling and assuming both are $\mathcal{O}\left(1\right)$, the boundary conditions are,

$$\left.\frac{\partial C}{\partial \zeta}\right|_{\zeta=0} = \begin{cases} \dfrac{1}{R^2}\left(\left(\Gamma_{\mathrm{eq}} - \Gamma\right) + \dfrac{\mathcal{A}}{Pe_{\mathrm{s}}^{1/2}}C(0,t)\left(1-\Gamma\right)\right) & \Gamma < 1, \quad \text{(3.4.10a)} \\ 0 & 1 < \Gamma < \dfrac{\Gamma_{\max}}{\Gamma^*}, \quad \text{(3.4.10b)} \\ Pe_{\mathrm{s}}\mathcal{B}\dfrac{1}{R^3}\dfrac{dR}{dt} & \Gamma > \dfrac{\Gamma_{\max}}{\Gamma^*}. \quad \text{(3.4.10c)} \end{cases}$$

The concentration field is split into smooth and oscillatory parts $C = C_{\mathrm{sm}} + C_{\mathrm{osc}}$. From the linearity of the diffusion equation, both processes are governed by equation (3.4.9). To simplify the problem, it is assumed that there is a single shedding event that occurs during the compression phase of the first pulse. The time at which Γ first equals $\Gamma_{\max}$ and shedding begins is denoted t_0. Subsequent bubble expansion begins at time t_1 and causes Γ to decrease.

3.4.2.1 Initial compression

After substituting the length scale $s = Pe_{\mathrm{s}}^{1/2}\zeta$ and nonlinear time $\tilde{t} = \int_0^t R^4(\theta)\mathrm{d}\theta$ into (3.4.9) and (3.4.10), the governing equation is,

$$\frac{\partial C}{\partial \tilde{t}} = \frac{\partial}{\partial s}\left(R^4\left(\frac{3s}{Pe_{\mathrm{s}}^{1/2}}R^3 + 1\right)^{4/3}\frac{\partial C}{\partial s}\right) \tag{3.4.11}$$

and the boundary condition becomes,

$$Pe_{\mathrm{s}}^{1/2}\left.\frac{\partial C}{\partial s}\right|_{s=0} = \begin{cases} \dfrac{1}{R^2}\left(\left(\Gamma_{\mathrm{eq}}-\Gamma\right)+\dfrac{\mathcal{A}}{Pe_{\mathrm{s}}^{1/2}}C\left(0,\tilde{t}\right)\left(1-\Gamma\right)\right) & \Gamma<1, \quad (3.4.12a) \\ 0 & 1<\Gamma<\dfrac{\Gamma_{\max}}{\Gamma^*}. \quad (3.4.12b) \end{cases}$$

This implies that there is a non-zero contribution to the concentration field around the bubble of $\mathcal{O}\left(Pe_{\mathrm{s}}^{-1/2}\right)$ in a boundary layer $s\sim\mathcal{O}\left(Pe_{\mathrm{s}}^{-1/2}\right)$. Since the initial compression occurs on a short timescale, the concentration C is expanded in powers of $Pe_{\mathrm{s}}^{-1/2}$,

$$C\left(s,\tilde{t}\right)=\frac{1}{Pe_{\mathrm{s}}^{1/2}}C^1\left(s,\tilde{t}\right)+\frac{1}{Pe_{\mathrm{s}}}C^2\left(s,\tilde{t}\right)+\ldots \quad (3.4.13)$$

Using equation (3.4.9) and the new scalings, the governing equation for C^1 is,

$$\frac{\partial C^1}{\partial\tilde{t}}=\frac{\partial^2 C^1}{\partial s^2} \quad (3.4.14)$$

with boundary and initial conditions,

$$\left.\frac{\partial C^1}{\partial s}\right|_{s=0} = \begin{cases} \dfrac{1}{R^2}\left(\Gamma_{\mathrm{eq}}-\Gamma\right) & \Gamma<1, \quad (3.4.15a) \\ 0 & 1<\Gamma<\dfrac{\Gamma_{\max}}{\Gamma^*}. \quad (3.4.15b) \end{cases}$$

$$C^1\left(s,\tilde{t}=0\right)=0 \quad (3.4.16)$$

$$C^1\left(s\to\infty,\tilde{t}\right)\to 0 \quad (3.4.17)$$

3.4.2.2 Shedding

Between times t_0 and t_1 the bubble is shedding surfactant into the bulk. The length and nonlinear timescales $s=Pe_{\mathrm{s}}^{1/2}\zeta$ and $\tilde{t}=\int_0^t R^4(\theta)\mathrm{d}\theta$ are used again, leading to the same governing equation (3.4.11) but where the boundary condition is now,

$$\left.\frac{\partial C}{\partial s}\right|_{s=0}=Pe_{\mathrm{s}}^{1/2}\mathcal{B}R\frac{dR}{d\tilde{t}} \quad (3.4.18)$$

This implies that the solution for the concentration field around the bubble takes the form,

$$C\left(s,\tilde{t}\right)=Pe_{\mathrm{s}}^{1/2}C^{-1}\left(s,\tilde{t}\right)+C^0\left(s,\tilde{t}\right)+\frac{1}{Pe_{\mathrm{s}}^{1/2}}C^1\left(s,\tilde{t}\right)+\ldots \quad (3.4.19)$$

where C^1 has a contribution from the initial compression phase discussed previously.

3.4.2.3 Periodic oscillation

There is now assumed to be continuous, periodic insonation of the bubble. At time t_1, the concentration profile has the form,

$$C\big(s,\tilde{t}=\tilde{t}_1\big) = Pe_{\mathrm{s}}^{1/2}C^{-1}\big(s,\tilde{t}=\tilde{t}_1\big) + C^0\big(s,\tilde{t}=\tilde{t}_1\big) + \frac{1}{Pe_{\mathrm{s}}^{1/2}}C^1\big(s,\tilde{t}=\tilde{t}_1\big) + \dots$$

which implies that the final concentration field also has the form,

$$C(\zeta,t) = Pe_{\mathrm{s}}^{1/2}C^{-1}(\zeta,t) + C^0(\zeta,t) + \frac{1}{Pe_{\mathrm{s}}^{1/2}}C^1(\zeta,t) + \dots \tag{3.4.20}$$

The problem is approached by splitting the solution into "oscillatory" and "smooth" parts that account for the fast and slow timescales respectively, which is perfectly valid since the governing equations are linear. On the short length scale where $s = Pe_{\mathrm{s}}^{1/2}\zeta$ and nonlinear time $\tilde{t} = \int_0^t R^4(\theta)\mathrm{d}\theta$, the governing equation and boundary conditions of the oscillatory problem are given by equations (3.4.11) and (3.4.12). To account for slow changes in the concentration, a slow timescale $\tau = Pe_{\mathrm{s}}^{-1}t$ is defined leading to a governing equation for the smooth problem of the form,

$$\frac{\partial C_{\mathrm{sm}}}{\partial t} + \frac{1}{Pe_{\mathrm{s}}}\frac{\partial C_{\mathrm{sm}}}{\partial \tau} = \frac{1}{Pe_{\mathrm{s}}}\frac{\partial}{\partial \zeta}\left(\left(3\zeta + R^3\right)^{4/3}\frac{\partial C_{\mathrm{sm}}}{\partial \zeta}\right) \tag{3.4.21}$$

where now $C_{\mathrm{sm}} = C_{\mathrm{sm}}(\zeta,t,\tau)$. Following Fyrillas and Szeri's analysis (1994), an average with respect to the nonlinear time $\tilde{t}$ over a period T is defined as,

$$\big\langle f\big(\zeta,\tilde{t}\big)\big\rangle_{\tilde{t}} \equiv \frac{1}{\tilde{t}(T)}\int_0^{\tilde{t}(T)} f\big(\zeta,\tilde{t}\big)\mathrm{d}\tilde{t} = \frac{1}{\int_0^T R^4(t)\mathrm{d}t}\int_0^T f(\zeta,t)R^4(t)\mathrm{d}t$$

To simplify the calculation of the average, it is assumed that $\Gamma^* = \Gamma_{\max}$ and the boundary condition (3.4.12) is rewritten by adding and subtracting the smooth part to highlight the splitting technique,

$$\begin{aligned}\left.\frac{\partial C}{\partial \zeta}\right|_{\zeta=0} =& \frac{\Gamma_{\mathrm{eq}}-\Gamma}{R^2} + \frac{\mathcal{A}}{Pe_{\mathrm{s}}^{1/2}}C\big(0,\tilde{t}\big)\left(\frac{1-\Gamma}{R^2}\right) + \left(\left\langle\frac{\Gamma_{\mathrm{eq}}-\Gamma}{R^2}\right\rangle_{\tilde{t}} - \left\langle\frac{\Gamma_{\mathrm{eq}}-\Gamma}{R^2}\right\rangle_{\tilde{t}}\right)\\ &+ \frac{\mathcal{A}}{Pe_{\mathrm{s}}^{1/2}}C_{\mathrm{sm}}(0,t,\tau)\left(\left\langle\frac{1-\Gamma}{R^2}\right\rangle_{\tilde{t}} - \left\langle\frac{1-\Gamma}{R^2}\right\rangle_{\tilde{t}}\right)\\ &+ \frac{\mathcal{A}}{Pe_{\mathrm{s}}^{1/2}}\left(\left\langle\frac{(1-\Gamma)C_{\mathrm{osc}}\big(0,\tilde{t}\big)}{R^2}\right\rangle_{\tilde{t}} - \left\langle\frac{(1-\Gamma)C_{\mathrm{osc}}\big(0,\tilde{t}\big)}{R^2}\right\rangle_{\tilde{t}}\right)\end{aligned} \tag{3.4.22}$$

Since the oscillatory part occurs on the fast timescale and recalling that $C = C_{\mathrm{sm}} + C_{\mathrm{osc}}$, the corresponding boundary condition from equation (3.4.22) is,

$$\left.\frac{\partial C_{\text{osc}}}{\partial \zeta}\right|_{\zeta=0} = \frac{\Gamma_{\text{eq}}-\Gamma}{R^2} + \frac{\mathcal{A}}{Pe_{\text{s}}^{1/2}}\Big(C_{\text{osc}}\big(0,\tilde{t}\big) + C_{\text{sm}}(0,t,\tau)\Big)\left(\frac{1-\Gamma}{R^2}\right) - \left\langle \frac{\Gamma_{\text{eq}}-\Gamma}{R^2}\right\rangle_{\tilde{t}} - \frac{\mathcal{A}}{Pe_{\text{s}}^{1/2}}\left(C_{\text{sm}}(0,t,\tau)\left\langle\frac{1-\Gamma}{R^2}\right\rangle_{\tilde{t}} + \left\langle\frac{\big(1-\Gamma\big)C_{\text{osc}}\big(0,\tilde{t}\big)}{R^2}\right\rangle_{\tilde{t}}\right) \tag{3.4.23}$$

where in effect, the smooth part has been subtracted from the boundary condition. On the slow timescale, the smooth boundary condition is written as,

$$\left.\frac{\partial C_{\text{sm}}}{\partial \zeta}\right|_{\zeta=0} = \left\langle \frac{\Gamma_{\text{eq}}-\Gamma}{R^2}\right\rangle_{\tilde{t}} + \frac{\mathcal{A}}{Pe_{\text{s}}^{1/2}}\left(C_{\text{sm}}(0,t,\tau)\left\langle\frac{1-\Gamma}{R^2}\right\rangle_{\tilde{t}} + \left\langle\frac{\big(1-\Gamma\big)C_{\text{osc}}\big(0,\tilde{t}\big)}{R^2}\right\rangle_{\tilde{t}}\right) \tag{3.4.24}$$

Whether $\mathcal{A}\sim 1$ or $\mathcal{A}\sim Pe_{\text{s}}^{1/2}$, to leading order the governing equation and boundary condition of the oscillatory problem are,

$$\frac{\partial C_{\text{osc}}^{-1}}{\partial \tilde{t}} = \frac{\partial^2 C_{\text{osc}}^{-1}}{\partial s^2} \tag{3.4.25}$$

$$\left.\frac{\partial C_{\text{osc}}^{-1}}{\partial s}\right|_{s=0} = \mathcal{O}\left(Pe_{\text{s}}^{-1/2}\right) \tag{3.4.26}$$

implying no significant amount of surfactant (to leading order) is adsorbed back onto the bubble surface over the fast timescale. In other words, an $\mathcal{O}\left(Pe_{\text{s}}^{1/2}\right)$ concentration diffuses away in an $\mathcal{O}\left(1\right)$ time. On the slow timescale, this implies $C_{\text{sm}}^{-1}\equiv 0$ by mass conservation.

At the next order, if $\mathcal{A}\sim Pe_{\text{s}}^{1/2}$, the governing equation and boundary condition of the oscillatory problem are,

$$\frac{\partial C_{\text{osc}}^{0}}{\partial \tilde{t}} = \frac{\partial^2 C_{\text{osc}}^{0}}{\partial s^2} + \frac{4}{R^3}\frac{\partial}{\partial s}\left(s\frac{\partial C_{\text{osc}}^{-1}}{\partial s}\right) \tag{3.4.27}$$

$$\left.\frac{\partial C_{\text{osc}}^{0}}{\partial s}\right|_{s=0} = \frac{\mathcal{A}}{R^2}C_{\text{osc}}^{-1}\big(0,\tilde{t}\big)\big(1-\Gamma\big) \tag{3.4.28}$$

Since $(1-\Gamma)>0$, equation (3.4.28) implies that there is a positive flux of surfactant back onto the surface of the bubble at this order, if the adsorption coefficient is large enough. On the longer timescale, the governing equation and boundary condition for the smooth problem obtained from equations (3.4.21) and (3.4.24) are,

$$\frac{\partial C_{\text{sm}}^{0}}{\partial t} = 0 \tag{3.4.29}$$

$$\left.\frac{\partial C_{\text{sm}}^{0}}{\partial \zeta}\right|_{\zeta=0} = \left\langle \frac{\Gamma_{\text{eq}}-\Gamma}{R^2}\right\rangle_{\tilde{t}} + \frac{\mathcal{A}}{Pe_{\text{s}}^{1/2}}C_{\text{sm}}^{0}(0,t,\tau)\left\langle\frac{1-\Gamma}{R^2}\right\rangle_{\tilde{t}} + \mathcal{A}\left\langle\frac{\big(1-\Gamma\big)C_{\text{osc}}^{-1}\big(0,\tilde{t}\big)}{R^2}\right\rangle_{\tilde{t}} + \frac{\mathcal{A}}{Pe_{\text{s}}^{1/2}}\left\langle\frac{\big(1-\Gamma\big)C_{\text{osc}}^{0}\big(0,\tilde{t}\big)}{R^2}\right\rangle_{\tilde{t}} \tag{3.4.30}$$

Equation (3.4.29) implies that the smooth solution at this order does not depend on the fast time t. In addition, the third averaged term of (3.4.30) becomes negligible on the long timescale. If $\mathcal{A} \sim 1$, only the first term of (3.4.30) acts at this order. Since shedding has occurred, $(\Gamma_{\text{eq}} - \Gamma)$ is positive on average and there is a net surfactant flux onto the bubble surface which causes $\Gamma \to \Gamma_{\text{eq}}$ as $t \to \infty$. If $\mathcal{A} \sim Pe_{\text{s}}^{1/2}$, the other terms in equation (3.4.30) also contribute a positive surfactant mass flux accelerating the rate at which $\Gamma \to \Gamma_{\text{eq}}$. In other words, all the surfactant returns to the bubble in an $\mathcal{O}(1)$ timescale. However, since gas diffusion occurs on a faster timescale of $\mathcal{O}(Pe)$, as discussed in Section 3.3, the bubble will shrink faster than the surfactant is re-adsorbed.

During initial insonation, transient oscillations are exhibited before the microbubble reaches periodic behaviour (Leighton, 1989). To investigate the importance of this, the rate of change of the mass of surfactant m_{s} on the bubble surface is non-dimensionalised,

$$\frac{d(m_{\text{s}})_{\text{osc}}}{d\tilde{t}} = \frac{(a_1 C_\infty + a_2)}{\omega} \left.\frac{\partial C_{\text{osc}}}{\partial \zeta}\right|_{\zeta=0} \approx Pe_{\text{s}}^{-1} \left.\frac{\partial C_{\text{osc}}}{\partial \zeta}\right|_{\zeta=0}$$

For $t > t_1$, equation (3.4.26) suggests that to leading order,

$$\frac{d(m_{\text{s}})_{\text{osc}}}{d\tilde{t}} \approx 0$$

At longer times, the boundary layer of lipid around the bubble diffuses away into an $\mathcal{O}(1)$ concentration and so the effect of transience is concluded to be negligible.

3.4.3 Analysis

It is interesting to note in this section that the presence of sudden surfactant shedding in the boundary condition leads to a term of $\mathcal{O}\left(Pe_{\text{s}}^{1/2}\right)$ in both oscillatory and smooth boundary conditions and thus a characteristic scale of $\mathcal{O}\left(Pe_{\text{s}}^{1/2}\right)$ for this shedding to take place. In a thin boundary layer around the bubble, the ejected surfactant is $\mathcal{O}\left(Pe_{\text{s}}^{1/2}\right)$ and diffuses away in a time of $\mathcal{O}(1)$. However, on a longer timescale, all the surfactant will be re-adsorbed. Compared to gas diffusion, this process is much slower and it is likely that $\Gamma \to \Gamma_{\text{eq}}$ as the bubble shrinks due to gas loss rather than surfactant returning to its surface. If the adsorption coefficient is extremely large such that $\mathcal{A} \sim Pe_{\text{s}}$ then surfactant is re-adsorbed on a faster timescale and little escapes the boundary layer.

It has also been shown that the effects of transience are negligible, which is an important consideration in multiple short-pulsed microbubble excitations. Most pertinently, the faster

shedding timescale would explain sudden bubble size changes that have been seen in experiments during or after insonation of surfactant-coated microbubbles.

Whilst the problem is similar to the one investigated by Fyrillas and Szeri (1996), the analysis in this section is more complicated. Their choice of kinematic boundary condition ensured that the right-hand side of equation (3.4.10a) is $\mathcal{O}\left(Pe_{\mathrm{s}}\right)$. It was then possible to split the problem more easily into oscillatory and smooth parts since the partial derivative was negligible to leading order. Furthermore, the non-trivial initial condition that arises from the shedding in this analysis complicates the averaging process. Nevertheless, the analysis presented above does provide some important insights into the behaviour of the surfactant in this situation.

3.5 Obtaining a value for the maximum packing concentration

A value for the maximum packing concentration Γ_{max} is needed in the model, which is the maximum concentration that the bubble surface can support before surfactant is shed. Unpublished data kindly provided by David Thomas, U. Edinburgh, allow this parameter to be estimated and used in the numerical modelling to follow.

Thomas placed a Definity® bubble against a glass plate and took consecutive high speed camera footage as it was insonated by progressively higher pressure pulses (see Appendix D.1). From these data, it is possible to determine the initial and final bubble size as well as the amplitude of the oscillations. It is assumed that when the bubble radius decreased by at least 5%, lipid shedding has taken place and thus the maximum packing concentration was reached at some point during oscillation.

The surfactant concentration could be calculated using $\Gamma = m_{\mathrm{s}}/4\pi R^2$ if the surfactant mass was known. Alternatively, since the radial oscillations are known, the ratio of initial surface concentration to the maximum surface concentration reached during the insonation is found by $\Gamma_0/\Gamma_{\mathrm{max}} = R^2_{\mathrm{min}}/R^2_0$ where "max" and "min" refer to the maximum and minimum values during the oscillation. Figure 3.4 plots this ratio against the final radius R_{T} as a ratio of the initial bubble size. Taking averages of these two data sets results in an estimate for the upper and lower bounds for the maximum packing concentration Γ_{max} as a ratio of the initial concentration.

The results suggest that the maximum packing concentration lies between $\Gamma_0/0.39$ and $\Gamma_0/0.55$. It must be noted however, that it has been assumed that the bubble oscillations

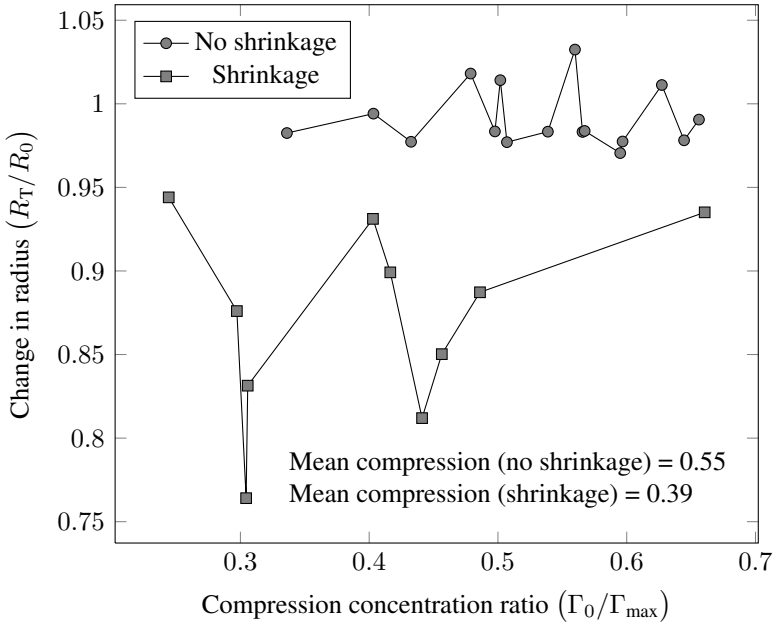

Figure 3.4: Estimating the maximum packing concentration by taking the mean of the compression concentration ratio, calculated as the initial concentration Γ_0 divided by the maximum concentration achieved during oscillation Γ_{max}. Data obtained from David Thomas, U. Edinburgh (unpublished).

during the experiments were spherical. Since the bubble was floating against a glass plate, its oscillations may have contained additional modes leading to less accurate values for the minimum radius and hence the maximum packing concentration. However, it is shown later in this chapter that this estimate leads to reasonable results. Furthermore, it is assumed that the microbubble was at equilibrium between each insonation. Since the pulse repetition frequency used was 1 kHz, it is concluded from previous analysis that this was sufficient time for the bubble to return to equilibrium between insonations.

3.6 Numerical modelling

Further analytical progress cannot be made easily, as was noted by Fyrillas and Szeri (1996), so the problem must be tackled using numerical tools. Morris et al.'s approach (2001) is used to model the gas diffusion equation (3.3.1) relative to the moving interface $x(t) = r - R(t)$,

$$\frac{\partial c(x,t)}{\partial t} + \boldsymbol{u}_{\text{rel}} \frac{\partial c(x,t)}{\partial x} = \frac{D}{(x+R)^2} \frac{\partial}{\partial x} \left[(x+R)^2 \frac{\partial c(x,t)}{\partial x} \right] \tag{3.6.1}$$

$$= \frac{D}{(x+R)} \left(2 \frac{\partial c(x,t)}{\partial x} + (x+R) \frac{\partial^2 c(x,t)}{\partial x^2} \right) \tag{3.6.2}$$

where the relative velocity is,

$$\boldsymbol{u}_{\text{rel}} = \left[\left(\frac{R}{x+R}\right)^2 - 1\right]\dot{R}$$

which is then solved using an explicit finite difference scheme where time and space are discretised into finite steps as $t = \{0, \delta t, \ldots, s\delta t, \ldots, T\delta t\}$ and $x = \{0, \delta x, \ldots, j\delta x, \ldots, X\delta x\}$ respectively whilst derivatives are approximated by,

$$\begin{aligned}
\frac{\partial c(x,t)}{\partial t} &\approx \frac{c_{j,s+1} - c_{j,s}}{\delta t} \\
\frac{\partial c(x,t)}{\partial x} &\approx \frac{c_{j+1,s} - c_{j-1,s}}{2\delta x} \\
\frac{\partial^2 c(x,t)}{\partial x^2} &\approx \frac{c_{j+1,s} - 2c_{j,s} + c_{j-1,s}}{(\delta x)^2}
\end{aligned}$$

at time point s and spatial point j. The finite difference scheme for equation (3.6.2) is given by,

$$\begin{aligned}
c_{j,s+1} \approx & \frac{D\delta t}{\big(j\delta x + R(s)\big)}\left(\frac{c_{j+1,s} - c_{j-1,s}}{\delta x} + \big(j\delta x + R(s)\big)\frac{c_{j+1,s} - 2c_{j,s} + c_{j-1,s}}{(\delta x)^2}\right) \\
& - \left[\left(\frac{R(s)}{j\delta x + R(s)}\right)^2 - 1\right]\dot{R}(s)\delta t\frac{c_{j+1,s} - c_{j-1,s}}{2\delta x} + c_{j,s}
\end{aligned} \tag{3.6.3}$$

and the calculation is looped over all spatial points and for all time points respectively. The boundary condition on the bubble is given by equation (3.3.2) and it is assumed that the concentration at infinity c_∞ remains constant.

Since the problem is identical for both gases, this is repeated simultaneously for air and PFC diffusion equations with concentrations through the bulk of c^{air} and c^{PFC} respectively. A similar computation is used for the surfactant problem C except that the boundary condition on the bubble is replaced by equations (3.4.1) and (3.4.2).

The results of these computations are used to calculate the flux of gas and surfactant and by consequence, the change in the mass of gas inside the bubble by using equation (3.3.2) and the change in surfactant concentration on its surface in (3.4.1), which are then used in the Rayleigh-Plesset equation (3.3.4), solved using the 4^{th}-order Runge-Kutta method at each time-step s. Not only does the surface tension σ depend on the surface concentration Γ but so does the diffusivity of the gas D. Hence any changes in the surfactant concentration has an effect on the flux of gases at the boundary.

If shedding occurs, surfactant dissolves into the liquid around the bubble and the concentration C must be updated. Ideally, an ejection speed and rate for the lipid would be calculated which would enable the distance that the molecules travel to be calculated. Thus the concentration in the liquid around the bubble could be adjusted accordingly. Unfortunately, the processes that control this are complicated. For instance, the binding energy of the surfactant molecules, the activation energy required for shedding to occur and exactly how the molecules are ejected, whether individually or in larger "buds", are difficult to ascertain. The phenomena are complicated further by the presence of different types of molecules on the surface of the bubble and their interaction also affects the dynamics. Additionally, the distribution of these molecules is unlikely to be homogeneous across the bubble surface, further complicating the analysis. Whilst the precise physicochemical processes that occur during shedding are difficult to predict, experiments using a fluorescence marker on the lipid molecules and imaging the luminescence after insonation have been carried out and show a bright region around the bubble. For instance, images from Gelderblom et al. (2010) suggest that the lipid is ejected within $1\,\mu$m of the bubble. For the purpose of this work, a heuristic assumption is made that surfactant is shed uniformly within a volume outside of the bubble within $0.6\,\mu$m of its surface.

The four equations – the diffusion equations for the two gases and surfactant, as well as the ODE modelling the behaviour of the microbubble – are coupled and solved together. As the pulse passes the bubble, the radial velocity can become so large that instabilities appear in the diffusion equations (3.3.1) and (3.3.5). To avoid this, a smaller time-step is used when the bubble is being insonated by the pulse and its oscillations are likely to be large, but a longer time-step at other times in order to reduce computation time. The values chosen for the parameters in the model are shown in table C.2.

3.7 Results

The results of the numerical computation of the surfactant shedding model presented in this chapter are compared with the optical results from Viti et al. (2011) including unpublished data. Their experiments investigated the behaviour of an individual contrast agent microbubble when repeatedly insonated and are described in more detail in Appendix D.1. This was conducted by sending a series of pulses at $70\,$kPa at varying pulse repetition frequencies (PRF) and imaging the oscillating bubble. The frequencies for the incident pulses that were used were either all $2\,$MHz or a Frequency Modulation (FM) sequence consisting of 2, 2.5, 3, 3.5 and

4 MHz pulses cycled sequentially from low to high before starting at the lowest frequency again. The contrast agent used was Definity® and it was imaged using the Brandaris high-speed camera.

Initial simulations using a microbubble containing a perfluorocarbon (PFC) gas and no air led to an initial growth in bubble size as air diffuses into the bubble from the bulk. This behaviour was not observed in the experiments – although it has been seen in other studies (Kwan and Borden, 2010; Mulvana et al., 2012) – and it is suspected that this is because by the time they were insonated, the contrast agent microbubbles had reached an equilibrium with the bulk and no more gas would diffuse in. Consequently, the first numerical simulations that are compared to experiment are for a bubble that contains exclusively air and no PFC. This simulates the scenario that sufficient time has elapsed between the preparation of the contrast agent and imaging to allow it to equilibrate with the bulk solution. This is a reasonable assumption since in medical cases, the bubbles could be in the body for seconds or minutes, during which time they would equilibrate in this way. Subsequent investigation using the model examines the behaviour of a newly created contrast agent microbubble containing only PFC gas and its response to different ultrasound pulses.

3.7.1 Air microbubble: 2 MHz

In this experiment, a series of 2 MHz 12-cycle pulses with a PRF of 62.5 Hz was used to insonify the bubble. Individual bubbles were imaged using a sampling frequency of 12 MHz and one optical recording was made every five pulses, which is the limit of the high-speed camera.

The experimental data in figure 3.5 illustrate a number of interesting phenomena, primarily bubble shrinkage and eventual stabilisation. Firstly, there were large reductions in bubble radius that appear to be sudden and on the timescale of the pulse. Secondly, the bubble reached a stable radius of 1.4 μm after which it no longer shrank despite being repeatedly hit with ultrasound.

A third interesting feature of the behaviour was the change in oscillation amplitude and symmetry. During this experiment when the bubble was around 1.8 μm, the oscillations were initially approximately symmetric. However, after a certain amount of time, although it had not appreciably changed in size, the behaviour favoured compression-only oscillations, where the amplitude of the expansion phase was reduced and the compression phase larger.

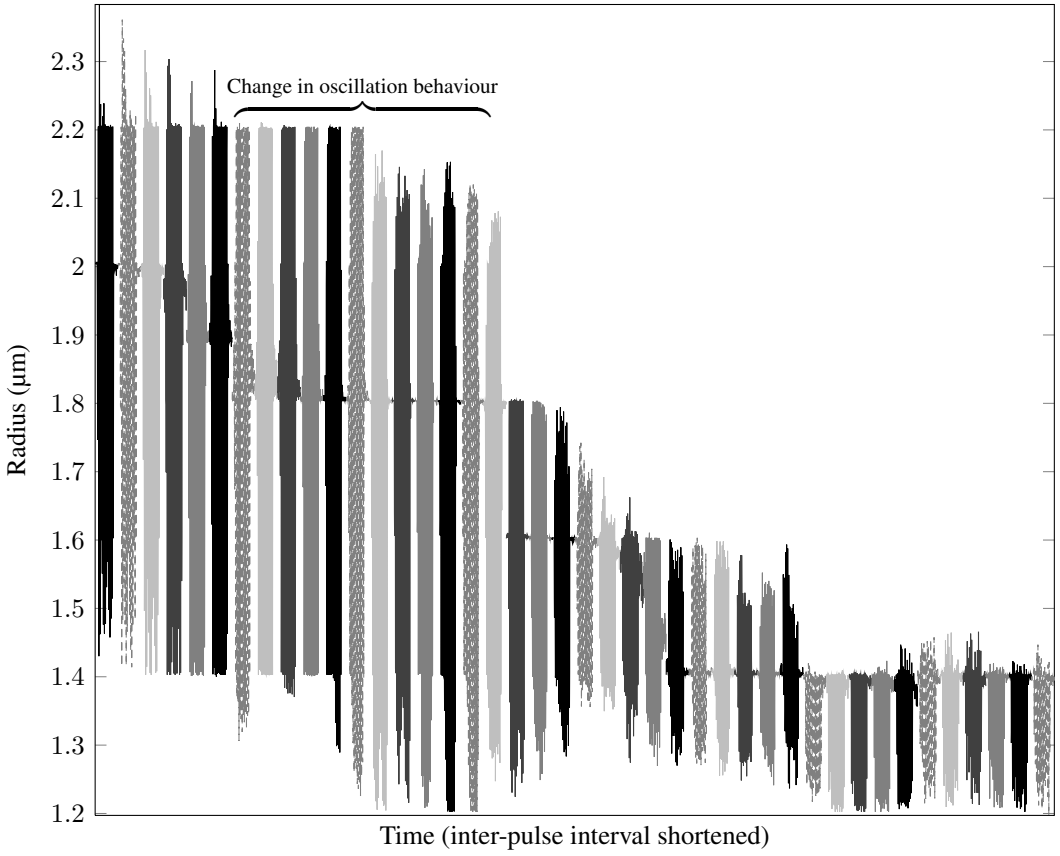

Figure 3.5: Experimental optical experiments for the insonation of a single lipid-coated microbubble using a PRF of 62.5 Hz and peak negative pressure of 70 kPa, sampled at 12 MHz. Every fifth pulse was optically recorded and $R_0 = 2\,\mu$m. Data provided by Viti et al., (unpublished).

These results are compared to the numerical solution of the surfactant shedding model using the same pulse sequence except at a higher PRF of 1 kHz for the sake of computational speed. The numerical results are presented in figure 3.6 where every fifth pulse is plotted in order to make the plot clearer. Firstly, the model simulates sudden bubble shrinkage as a result of surfactant loss, as visible in the first pulse. This phenomenon only occurs when the bubble is sufficiently close to its resonant size that its oscillations are large enough to cause shedding. Smaller or larger bubbles remain stable, in agreement with experimental results.

Secondly, the model also suggests that the bubble reaches a stable radius size between 1.4 μm and 1.5 μm, close to the experimental results. The reason for this behaviour is that, as the bubble size moves away from resonance, its oscillations are no longer large enough to cause shedding and consequently, a reduction in radius. Moreover, since the surface tension and diffusivity tend towards σ_{min} and D_{min} as gas diffuses out, the rate of diffusion slows, further reducing the shrinkage rate.

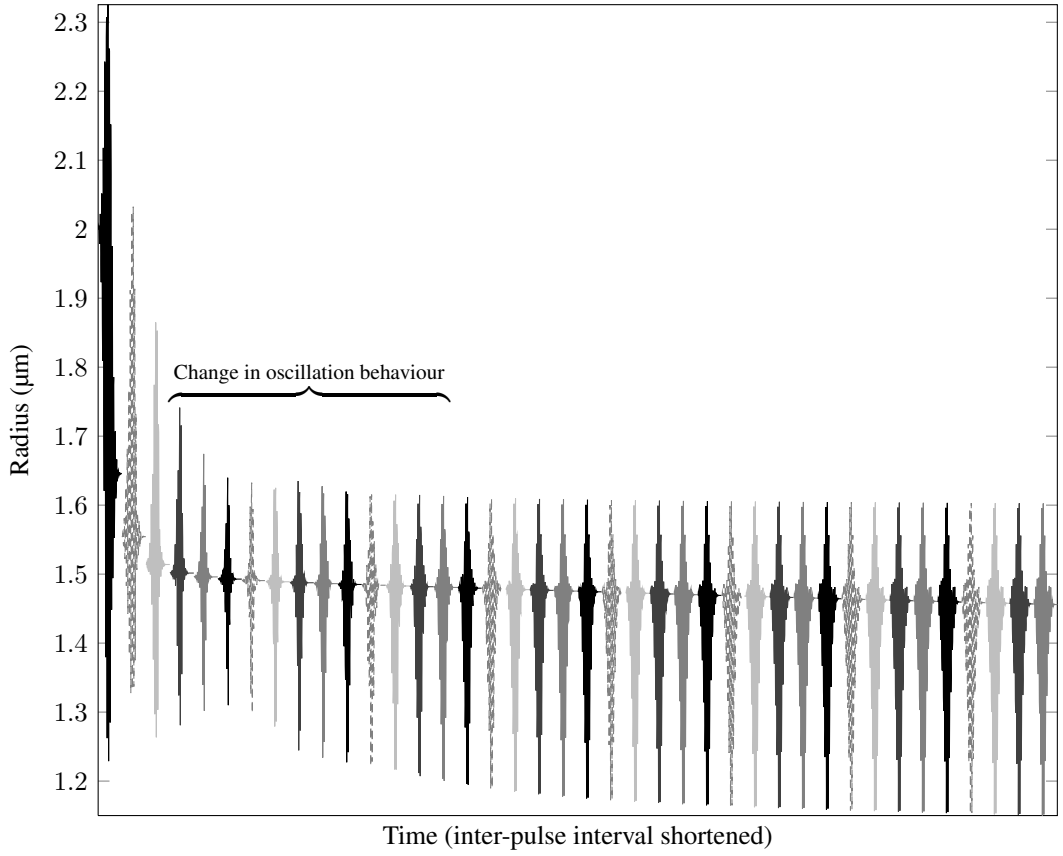

Figure 3.6: Numerical simulation of the lipid-shedding microbubble model initially containing air, including gas and surfactant diffusion in the bulk, using a PRF of 1 kHz and a frequency of 2 MHz at a peak negative pressure of 70 kPa. Every fifth pulse is displayed and $R_0 = 2\,\mu$m.

Thirdly, the change in oscillation behaviour is replicated with the shedding model. At approximately $1.5\,\mu$m, the bubble initially demonstrates symmetrical oscillations. However, as gas diffuses out, it shrinks slightly and the surface concentration increases. Eventually, the surface tension tends to the minimum ruptured regime and the microbubble exhibits behaviour favouring compression-only oscillations. This is similar to the experimental results and supports the theory that gas diffusion does have an effect on the behaviour of the contrast agent microbubble on the long timescale.

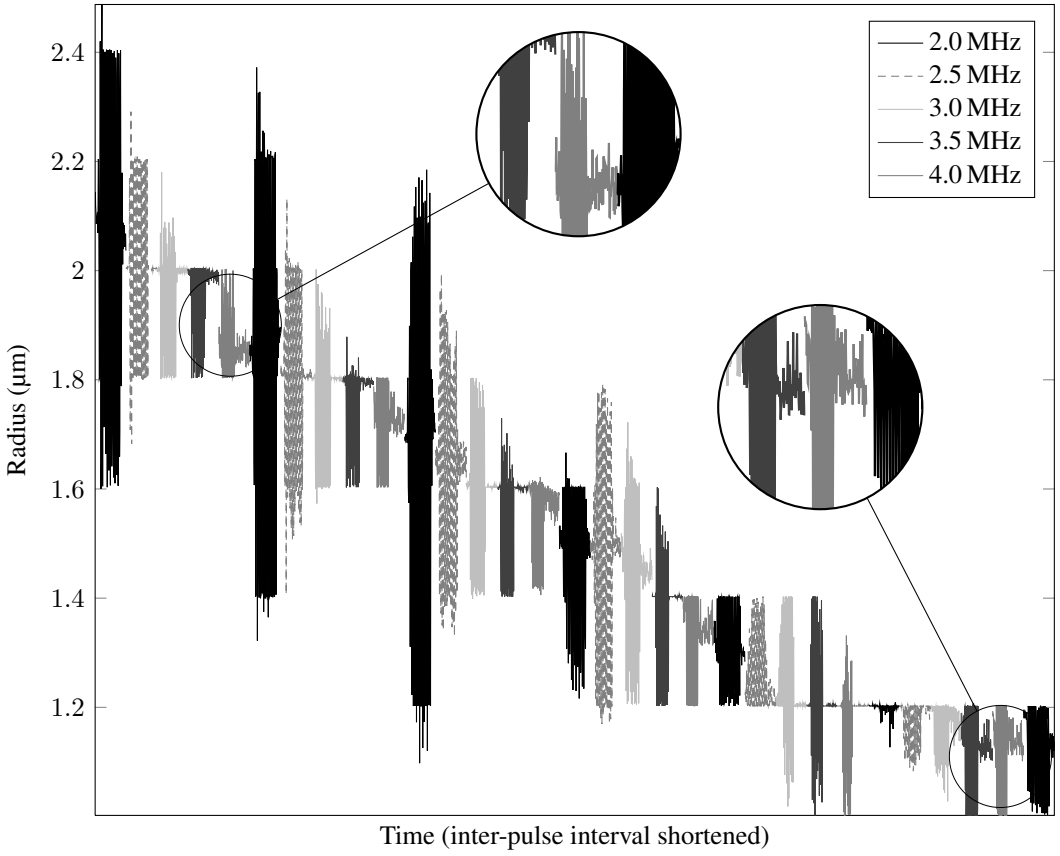

Figure 3.7: Experimental optical data for the insonation of a single lipid-coated microbubble where a PRF of 325 Hz and a pulse sequence of 2, 2.5, 3, 3.5 and 4 MHz at a peak negative pressure of 70 kPa was used, sampled at 12 MHz. Every 26 pulses was recorded optically and $R_0 = 2.15\,\mu$m. Data provided by Viti et al., (unpublished).

3.7.2 Air bubble: FM cycle

In this section, the results of the FM experiment are examined where the microbubble was excited using pulses of 2, 2.5, 3, 3.5 and 4 MHz at a PRF of 325 Hz. Individual bubbles images were sampled at 12 MHz and one optical recording was made every 26 pulses.

There are four trends that are visible in the experimental data of figure 3.7. Firstly, sudden bubble shrinkage taking place either during or soon after a pulse is observed. For instance the very first pulse in the plot shows a reduction in radius from 2.15 µm to 2 µm. As expounded earlier in this chapter, this sudden shrinkage cannot be explained solely by gas diffusion and so suggests some form of surfactant shedding is occurring. This only occurred when the bubble was sufficiently close to its resonant size that its oscillations were large enough to cause shedding.

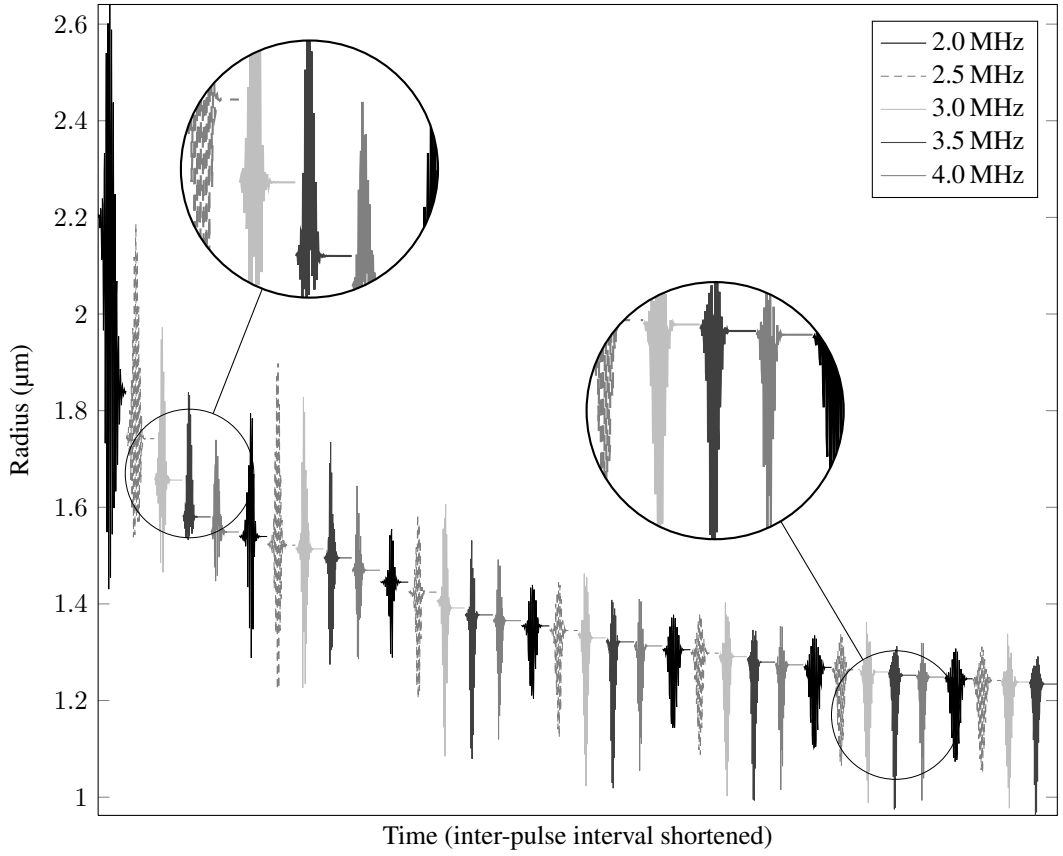

Figure 3.8: Numerical simulation of the lipid-shedding microbubble model initially containing air, including gas and surfactant diffusion in the bulk, using a PRF of 1 kHz and a pulse sequence 2, 2.5, 3, 3.5 and 4 MHz at a peak negative pressure of 70 kPa. Only every sixth pulse is displayed and $R_0 = 2.2\,\mu$m.

Secondly, after a suspected shedding event, the bubble exhibited expansion-only behaviour, as highlighted in the first zoom window. Thirdly, after sufficient time and/or further insonations, the bubble returned to its equilibrium state, albeit at a smaller size, and exhibited compression-only behaviour, as highlighted in the second zoom window.

Fourthly, after multiple insonations, the microbubble eventually reached a stable radius and stopped shrinking. In this experiment, the stable radius was around $1.2\,\mu$m.

Again, the numerical simulations are conducted using the same pulse sequence except at a higher PRF of 1 kHz for the sake of computational speed. The numerical results in figure 3.8 show only every sixth pulse in order to make the plot clearer. Figure 3.8 demonstrates that the surfactant shedding model replicates the bubble behaviours observed in experiments. Firstly, sudden bubble shrinkages occur as a result of surfactant shedding as seen in the first pulse on the plot, where the initial bubble radius is $2.2\,\mu$m and $1.85\,\mu$m after exposure to ultrasound.

Secondly, the first zoom window shows expansion-only behaviour after a shedding event. Referring to the surface tension model in figure 3.1, when surfactant has been lost, the monolayer is said to be ruptured and the surface tension is close to or at the clean surface value. On compression, the bubble will pass through the elastic regime to the buckled regime, causing the surface tension to fall to its minimum and discouraging the bubble from compressing further, leading to expansion-only behaviour.

However, after sufficient time, gas has diffused out of the bubble causing it to shrink and the surfactant concentration to return to its equilibrium value. The second zoom window shows that this results in a return to compression-only behaviour.

Furthermore, the bubble eventually reaches a stable radius of around $1.2\,\mu\text{m}$ at which point it no longer compresses sufficiently to shed more surfactant.

Although the model does seem to explain a number of experimental phenomena, it does not replicate the exact microbubble oscillations. First of all, the compression-only behaviour in the experimental data is more pronounced, with virtually no expansion towards the end of the experiments. Secondly, shedding events were smaller and occurred more often in the experiments. This is believed to be due to uncertainty in the parameter values used in the model, particularly the maximum packing concentration and the exact form of the surface tension model. Moreover, the optical data are misleading because only one plane of the bubble was visible and it was against an elastic boundary, thus a perfect fit with a spherical bubble model is practically impossible. Nevertheless, with more accurate inputs derived from further experiments, it is expected that the theory would better replicate experiments.

3.7.3 PFC microbubble: $2\,\text{MHz}$

The behaviour of a recently created contrast agent microbubble containing only PFC gas in an ultrasound field, assuming it has not had time to equilibrate with the gases in the bulk liquid, was simulated. The results of the $2\,\text{MHz}$ pulsed excitation is presented where as before, the PRF is $1\,\text{kHz}$ and for the sake of readability, only every fourth pulse is plotted in figure 3.9.

It can be seen from figure 3.9 that sudden bubble shrinkage does occur due to surfactant shedding when it is close to resonance. The oscillation amplitudes also change during the simulation, as a result of not only shedding, but changes in bubble size due to gas diffusion. The primary effect of having an initial interior gas of PFC is that air dissolved in the bulk solution diffuses into the bubble faster than the PFC gas diffuses out since the diffusivity

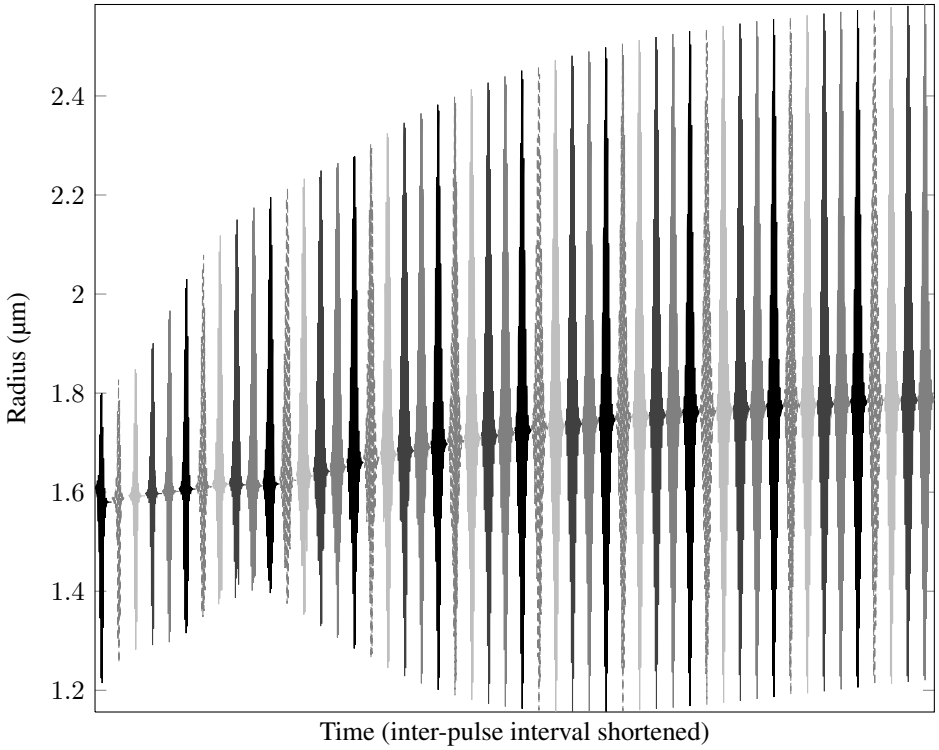

Figure 3.9: Numerical simulation of the lipid-shedding microbubble model including gas and surfactant diffusion in the bulk, using a PRF of 1 kHz. The incident pulse frequency and peak negative pressure are 2 MHz and 70 kPa respectively. The initial bubble gas is PFC and $R_0 = 1.6\,\mu$m. Only every fourth pulse is displayed.

of PFC is smaller, resulting in a positive total gas flux and bubble growth. After sufficient time, the rate of growth slows and a stable size is reached. It can be assumed that, on a longer timescale, the PFC gas would have sufficient time to diffuse out of the bubble until it contained only air. In that case, the analysis of Section 3.7.1 would be relevant and the microbubble would behave accordingly.

3.7.4 PFC microbubble: FM cycle

The results of the multi-frequency (FM) pulse cycle are presented in this section, where the bubble was insonated with 2, 2.5, 3, 3.5 and 4 MHz pulses in cycle at a PRF of 1 kHz. Only every sixth pulse of the simulation is plotted.

Figure 3.10 shows that sudden bubble size changes do still take place when it is close to resonance as a result of surfactant shedding. This initially results in oscillations that favour expansion-only behaviour. Again however, instead of shrinking, air dissolved in the bulk diffuses in at a faster rate than the PFC diffuses out, causing the bubble to grow. Eventually a larger stable size is reached where its oscillations are approximately symmetric. It can be

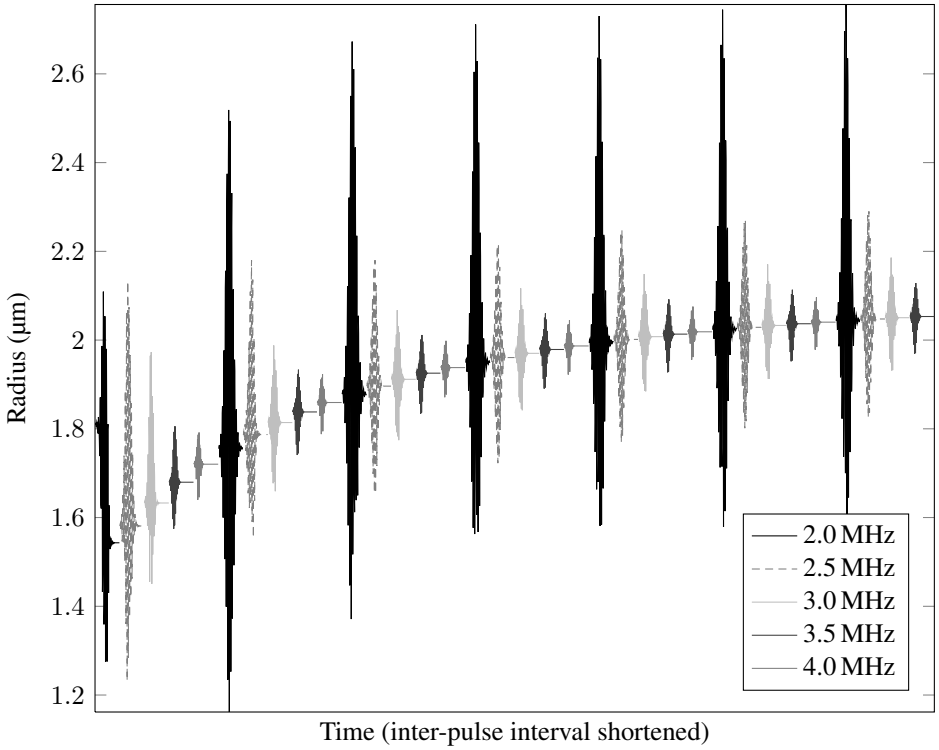

Figure 3.10: Numerical simulation of the lipid-shedding microbubble model including gas and surfactant diffusion in the bulk, using a PRF of 1 kHz. The FM pulse cycle is used and the peak negative pressure is 70 kPa. The initial bubble gas is PFC and $R_0 = 1.8\,\mu$m. Only every sixth pulse is displayed.

assumed that further diffusion of PFC gas would take place, albeit on a much slower timescale because the diffusivity is much lower, until the PFC gas inside the bubble has been entirely replaced with air. It is expected that the microbubble would subsequently behave as in Section 3.7.2.

Consequently, it is important for clinical and modelling applications to be aware of the contents of the contrast agents and specifically how long it has been in the vial prior to injection. If quickly administered, it would contain mainly PFC; on the other hand, if given sufficient time to equilibrate, it would contain mainly air and behave differently. The effects of growth post-creation would alter the harmonic content of the signal as microbubble behaviour changes between symmetric, compression- and expansion-only, affecting any quantitative modelling and imaging algorithms.

3.8 Summary

In this chapter, a novel model is presented coupling gas and surfactant diffusion equations to a Rayleigh-Plesset type equation, including a surfactant shedding condition on the boundary of the contrast agent microbubble as well as nonlinear models for the diffusivity and surface tension that depend on the surface concentration of surfactant. These equations are analysed mathematically using a multiple scales approach and in particular the implication of the shedding condition is investigated. It is found that the shedding mechanism causes surfactant to be lost on a much faster timescale than the timescale of diffusion, which would explain the sudden bubble size changes observed in experiments.

Since no further analytical progress can be made, the equations are solved numerically using explicit finite difference schemes and the 4^{th}-order Runge-Kutta method using parameters derived from experiments or found in other peer-reviewed papers.

It is found that the model successfully replicates certain experimental phenomena that have been hitherto not well understood. These phenomena are:

- Sudden shrinkage during or soon after a pulse when the bubble size is sufficiently close to resonance, as a result of surfactant shedding causing the surface tension to increase, forcing it to shrink.

- The tendency for the microbubble to exhibit compression-only behaviour is altered to expansion-only behaviour after a shedding event. The ruptured surfactant layer and the tendency for the surface tension to decrease on compression, discourages bubble shrinkage during oscillation.

- The microbubble eventually returns to its previous compression-only behaviour. The higher surface tension leads to a larger concentration gradient, causing the gas to diffuse out of the bubble faster. It then shrinks and the surface concentration rises until it has returned to its equilibrium state, albeit at a smaller size.

- A stable microbubble size is eventually reached. After sufficient shedding and subsequent gas diffusion, the bubble is small enough that it is no longer close to resonance and its oscillations are not large enough to cause further shedding to occur.

However, there are discrepancies between the model and experimental data. For instance, the model does not replicate the bubble oscillations precisely. In addition, there tended to be

fewer, larger shedding events in the numerical simulations compared with experiment. It is believed that both of these issues can be improved upon with further experiments, particularly to obtain more accurate values for the maximum packing concentration and the nonlinear surface tension model. Since only one plane of the bubble is visible and it was imaged against an elastic boundary, an exact fit with a spherical bubble model is practically impossible.

Modelling of the behaviour of a newly created lipid-coated microbubble assuming it contains only PFC gas suggests that the above behaviours are still present. However, the lower diffusivity of PFC compared to air causes a net flux of gas into the bubble leading to growth in the early stages. In clinical applications, this would have an effect on the behaviour of the contrast agent as well as the harmonic content of ultrasound waves propagated through the bubbly medium. Since the diffusivity of PFC is around ten times smaller than air (Sarkar, Katiyar and Jain, 2009), using the analysis of Section 3.3, it is concluded that the effects of PFC diffusion could become important on the timescales of tenths of seconds to seconds. This is relevant because it results in longer contrast agent survival times – useful when it takes seconds to minutes for the microbubbles to arrive at the imaging site – but it does also mean that care must be taken when modelling to account for any changes in the size distribution that may have occurred after creation.

In conclusion, the hypothesis that rapid microbubble size changes can be explained by lipid shedding which occurs on a much faster timescale than diffusion is supported by this work. This is particularly relevant when its size is close to resonance: bubbles much smaller or larger do not exhibit sufficiently large oscillations to cause shedding, in agreement with experimental evidence. However, on the longer timescales relevant to therapeutic medical applications and targeted imaging, diffusion plays an important role in altering the behaviour of the microbubbles, forcing them to return to an equilibrium. Despite the good agreement with experimental data, further experiments are necessary to obtain more accurate values for the parameters, in particular the maximum packing concentration, as well as the behaviour of the nonlinear surfactant-dependant surface tension and diffusivity. The model could be further extended by using a non-constant shell surface viscosity that could, for instance, also depend on the concentration of surfactant on the bubble surface.

Having proposed a new model describing the behaviour of a single lipid-coated microbubble in an ultrasound field, the next chapter examines theories for the propagation of ultrasound waves through a bubbly mixture and the effect of scattering interactions between the bubbles.

CHAPTER 4

SCATTERING THEORIES

The work of Chapter 3 focused on the time-dependent response of a single lipid-coated microbubble in an ultrasound field. It is also important to understand the behaviour of a cloud of microbubbles in a similar situation. Crucially, the way in which the bubbles interact as they scatter sound is vital to accurate and reliable quantitative imaging techniques. Consequently, this chapter contains a summary of existing scattering theories, both linear and nonlinear. Subsequently in Section 4.4, a new implementation of a scattering theory designed to increase computational efficiency is investigated and regimes of validity for different pressures, concentrations and bubble sizes are established.

4.1 Overview of scattering theories

Theories of wave scattering in bubbly liquids have their origins in Lord Rayleigh's work in the 19^{th} century on light scattering (Strutt, 1871) which explains, amongst other things, why the sky is blue. Scattering of acoustic waves can also be traced back to work by Rayleigh (1896) and to Sewell (1911) who investigated the propagation of sound through fog. These early theories focused on obtaining analytical solutions to the relevant wave equations whereas subsequent work has been driven to a larger extent by tractable computation. Overall, scattering theories can be roughly classified into two broad groups; those based on fluid dynamical principles and those based on multiple scattering approaches. A "genealogy" of theories is presented in figure 4.1.

The first fluid dynamical theories, developed from Sewell's approach, were by Urick (1947) and Urick and Ament (1949) based on earlier work by Herzfeld (1930), and aimed to determine the adiabatic compressibility of small particles by suspending them in a liquid and measuring the speed of sound as it passed through the mixture. Epstein (1941) considered a

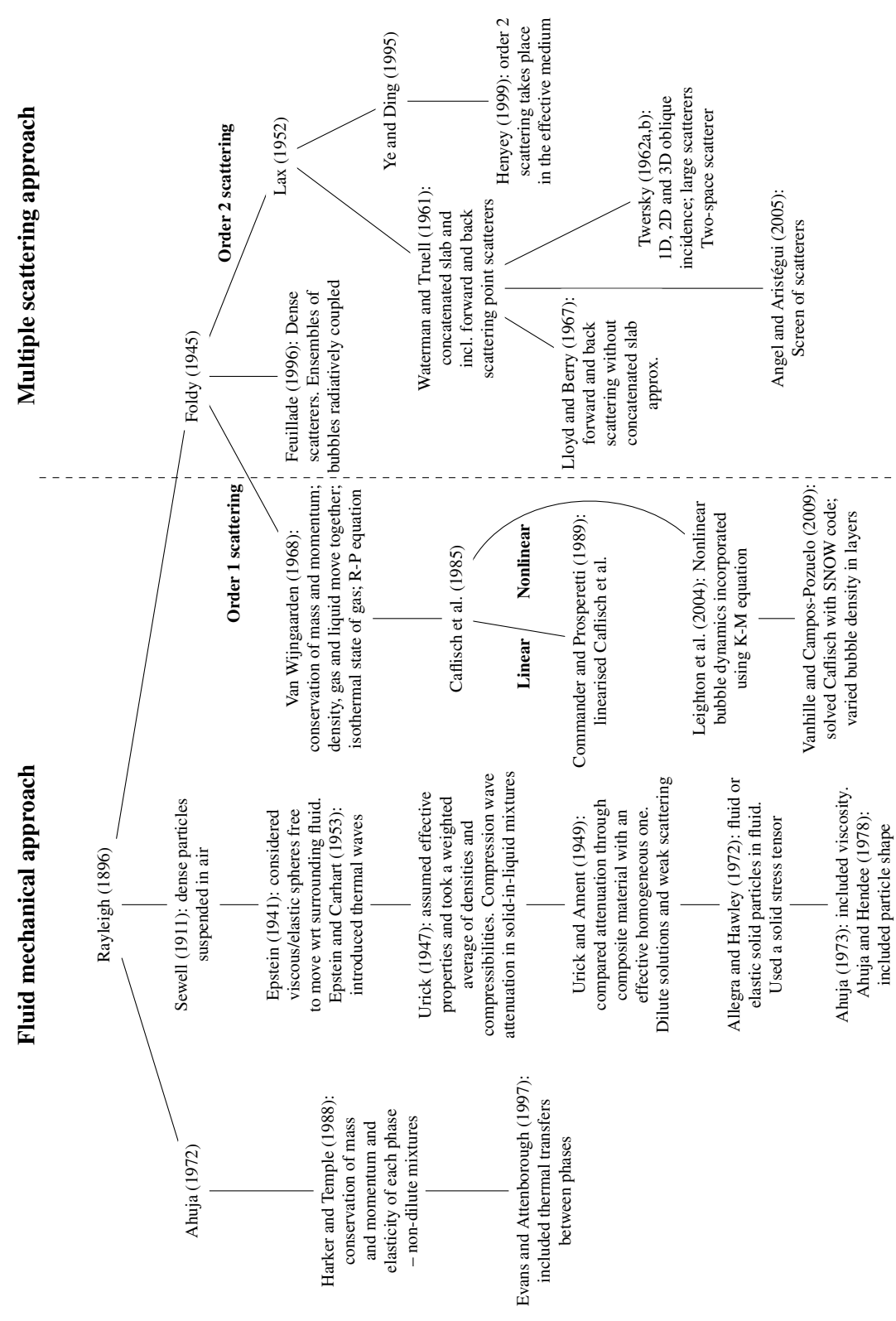

Figure 4.1: A "genealogy" of scattering theories from Lord Rayleigh to more recent nonlinear theories including Leighton.

similar problem, but one in which viscous or elastic spheres were free to move in the liquid; Epstein and Carhart (1953) also included thermal waves in their considerations. The main theory in this branch, however, can be attributed to Allegra and Hawley (1972), who extended the theory to both elastic and solid spheres that are free to move. In all these models, the authors concentrated on the response from isolated particles with negligible interaction.

An alternative route was taken by Ahuja (1972, 1973), expanding on earlier work by Biot (1956a,b, 1962a,b), who considered the momentum transfer between the two phases of particles and the surrounding medium within the mixture before Ahuja and Hendee (1978) included particle shape. Using this analysis, Harker and Temple (1988) derived an expression for the effective wavenumber for the mixture which was subsequently extended by Evans and Attenborough (1997) to include thermal effects in the transfer. This effective wavenumber can be interpreted as the effective complex propagation constant in the medium, where the real part represents the wavenumber $2\pi/\lambda$ given a wavelength λ, and the imaginary part represents the attenuation in a homogeneous medium with the same propagation characteristics as the inhomogeneous one.

Multiple scattering theories, on the other hand, are based on an attempt to find a closed-form solution to the acoustic field by keeping track of all the scattered waves in the mixture. Waves that have been scattered once are said to be part of the "first-order scattered field"; waves that are subsequently scattered again by a different scatterer are then said to represent the "second-order scattered field", and so on *ad infinitum*. Unfortunately, applying a technique to calculate these scattered fields explicitly is computationally unwieldy and usually impossible since, in practical applications, the precise positions of the scatterers are often unknown. However, exact solutions for spherical scatterers have been developed by Gaunaurd, Huang and Strifors (1995) and Skaropoulos, Yagridou and Chrissoulidis (2003).

To circumvent the above difficulties, Foldy (1945) was the first to consider how the average field behaves over all possible configurations of objects, by assuming that each scatterer behaves independently and that the incident wave is only scattered once by each scatterer; an assumption only valid in dilute liquids i.e. for low scatterer volume fractions. From this, it was possible to close the model and derive the effective wavenumber of the mixture. This approach was then extended by Lax (1952), who included the next order of the scattered field in the series, and also by Feuillade (1996), who modelled bubble clusters acting together in dense mixtures, both of which are discussed in Sections 4.2.2.4 and 4.2.3 respectively.

The aforementioned theories require certain, quite severe, simplifying assumptions to be made in order to derive a closed-form solution. Firstly, the scatterers are assumed to behave linearly, a situation that is rarely the case with the use of bubbles in medicine. Secondly, the interactions between scatterers are assumed to be negligible, which is only applicable in the case of dilute mixtures. Van Wijngaarden (1968) was the first author to present a model that took into account fully nonlinear bubble oscillations by matching the pressure and momentum changes between the liquid and the bubble. The rigorous derivation of this theory is examined in Section 4.3 and was implemented numerically by Stride and Saffari (2005) amongst others. A second distinct nonlinear theory can be attributed to Leighton, Meers and White (2004) who developed a method for inverting the wave problem to determine the bubble population distribution in the case of air bubbles in the ocean.

4.2 Multiple scattering theories

4.2.1 Scattering series approach

This approach was used by Gaunaurd, Huang and Strifors (1995) for wave scattering by two objects and subsequently extended by Skaropoulos, Yagridou and Chrissoulidis (2003) to the problem of scattering by an arbitrary number of objects. The method is to formulate the problem as an infinite series that represents all the modes of oscillation of the bubble. Addition theorems for the spherical harmonics are then used to construct the multiple scattering effects, providing an exact treatment of the situation, applicable to a wide range of frequencies and bubble sizes. However, these approaches are complicated and incorporating other effects such as damping is difficult. Moreover, the calculation of these series is computationally intense, even for the case of just two bubbles and assumes that their locations are known.

Nevertheless, this is the approach reviewed first, in the belief that an understanding of the *exact* solution would enhance the understanding of the effective medium model and other approximations that are used in multiple scattering problems.

4.2.1.1 Wave description

An acoustic wave described by a scalar function $u(\boldsymbol{r}, t)$ travelling in an unbounded medium satisfies the linear wave equation,

$$\mathcal{C}_0^2 \nabla^2 u(\boldsymbol{r}, t) = \frac{\partial^2 u(\boldsymbol{r}, t)}{\partial t^2}$$

and the velocity potential ψ subsequently satisfies the Helmholtz equation $\nabla^2\psi + k_0^2\psi = 0$, where $k_0 = \omega/\mathcal{C}_0$ is the wavenumber in the liquid, ω is the frequency and $\mathcal{C}_0$ is the wavespeed in the medium.

The total field in the medium is a sum of the incident field and the field scattered by the N objects in the medium $\psi = \psi^{\text{inc}} + \psi^{\text{sca}}$, where both left and right sides of the equation satisfy the Helmholtz equation.

Without loss of generality, the incident wave is assumed to have unit amplitude and thus written as $\psi^{\text{inc}} = e^{ik_0\boldsymbol{j}\cdot\boldsymbol{r}}$, or alternatively as a sum of n^{th}-order spherical Bessel functions $j_n(r)$ and spherical harmonics $Y_n^m(\theta,\phi) = P_n^m(\cos\theta)e^{im\phi}$, where $P_n^m(x)$ is the Legendre polynomial of degree n and order m,

$$\psi^{\text{inc}} = \sum_{n=0}^{\infty}\sum_{m=-n}^{n} a_{mn} j_n(k_0 r) Y_n^m(\theta,\phi) \tag{4.2.1}$$

In addition, the incident plane wave amplitude coefficients are defined as,

$$a_{mn} = i^n(2n+1)\frac{(n-m)!}{(n+m)!}P_n^m(\cos\theta^{\text{inc}}) \tag{4.2.2}$$

Furthermore, the objects' scattered wave can be expressed with respect to their own coordinate system $(O_p; r_p\theta_p\phi_p)$, where $p = 1,\ldots,N$ is the bubble identification index. Since $\boldsymbol{r} = \boldsymbol{r}_p + \boldsymbol{d}_p$, where $\boldsymbol{d}_p$ is the vector from the origin to the centre of the p^{th} scatterer and $\boldsymbol{r}_p$ is the vector from the centre of the p^{th} scatterer to the observer, the incident wave can be written as $\psi^{\text{inc}} = e^{ik_0\boldsymbol{j}\cdot\boldsymbol{r}_p}e^{ik_0\boldsymbol{j}\cdot\boldsymbol{d}_p}$ and thus, writing $a_{mnp} = a_{mn}e^{ik_0\boldsymbol{j}\cdot\boldsymbol{d}_p}$,

$$\psi^{\text{inc}} = \sum_{n=0}^{\infty}\sum_{m=-n}^{n} a_{mnp} j_n(k_0 r_p) Y_n^m(\theta_p,\phi_p) \tag{4.2.3}$$

Each bubble in the population contributes a scattered wave of unknown amplitude b_{mnp} written in terms of an n^{th}-order spherical Hankel function of the first kind $h_n^{(1)}(x)$ and spherical harmonics,

$$\psi_p^{\text{sca}} = \sum_{n=0}^{\infty}\sum_{m=-n}^{n} b_{mnp} h_n^{(1)}(k_0 r_p) Y_n^m(\theta_p,\phi_p) \tag{4.2.4}$$

The function $h_n^{(1)}(x)$ obeys the radiation condition (Abramowitz and Stegun, 1965) since as $x\to\infty$, $h_n^{(1)}(x) \approx (-i)^n e^{ix}/(ix)$, which is a spherical wave emanating outwards from the origin. To account for all the interactive multiple scattering between the objects, the scattered fields from each are summed,

$$\begin{aligned}\psi^{\text{sca}} &= \psi_1^{\text{sca}} + \ldots + \psi_N^{\text{sca}} \\ &= \sum_{p=1}^{N}\sum_{n=0}^{\infty}\sum_{m=-n}^{n} b_{mnp} h_n^{(1)}(k_0 r_p) Y_n^m(\theta_p, \phi_p)\end{aligned} \tag{4.2.5}$$

Since each ψ_p^{sca} satisfies the radiation condition at infinity, their sum ψ^{sca} also does.

In order to close the problem, it is necessary to describe the waves inside the objects of the cluster. This is done using the same logic as before, noting that the field in the interior ψ^{int} satisfies the Helmholtz equation $\nabla^2\psi_p^{\text{int}} + k_p^2\psi_p^{\text{int}} = 0$, where $k_p = \omega/\mathcal{C}_p$ is the wavenumber inside the p^{th} object. Therefore the interior field can be written in terms of an unknown internal wave amplitude c_{mnp},

$$\psi_p^{\text{int}} = \sum_{n=0}^{\infty}\sum_{m=-n}^{n} c_{mnp} j_n(k_p r_p) Y_n^m(\theta_p, \phi_p) \tag{4.2.6}$$

4.2.1.2 Determining the wave amplitudes by applying the boundary conditions

To obtain expressions for the unknown amplitudes b_{mnp} and c_{mnp}, boundary conditions stating that the acoustic pressure and the normal of the boundary velocity are continuous at the boundary are applied.

The acoustic pressure across the surface of the q^{th} object must be continuous, implying $(\psi^{\text{ext}} - \psi_q^{\text{int}})_{r_q = R_q} = 0$. Writing r_{pq}, θ_{pq} and ϕ_{pq} as the coordinates of the q^{th} object relative to the p^{th} object's coordinate system centred on O_p and $z_n(x)$ can equal $j_n(x)$ or $h_n^{(1)}(x)$, the addition theorem for spherical harmonics expressed in terms of the Wigner 3–j symbols (see Appendix of Gaunaurd and Huang, 1995) is,

$$\begin{aligned}z_n(kr_0)Y_n^m(\theta_q, \phi_q) = &\sum_{\nu=0}^{\infty}\sum_{\mu=-\nu}^{\nu}\begin{pmatrix} j_\nu(kr_p) \\ h_\nu^{(1)}(kr_p)\end{pmatrix} Y_\nu^\mu(\theta_p, \phi_p)(-1)^\mu i^{\mu-n}(2\mu+1) \\ &\times \sum_{l=|n-\nu|}^{n+\nu} i^l \sqrt{\frac{(n+m)!|(\nu-\mu)|!|(l-m+\mu)|!}{|(n-m)|!(\nu+\mu)!|(l+m-\mu)|!}} \\ &\times \begin{pmatrix} n & \nu & l \\ 0 & 0 & 0\end{pmatrix}\begin{pmatrix} n & \nu & l \\ m & -\mu & -m+\mu\end{pmatrix} \\ &\times \begin{pmatrix} h_\nu^{(1)}(kr_p) \\ j_\nu(kr_p)\end{pmatrix} Y_l^{m-\mu}(\theta_{pq}, \phi_{pq}), \qquad \text{for } \begin{pmatrix} r_p \le r_{pq} \\ r_p > r_{pq}\end{pmatrix}.\end{aligned}$$

Subsequently by adding equations (4.2.3) and (4.2.5) and subtracting (4.2.6), one obtains for the q^{th} object,

$$\begin{aligned}\psi^{\text{inc}} + \psi^{\text{sca}} - \psi_q^{\text{int}} =& \sum_{n=0}^{\infty}\sum_{m=-n}^{n}[a_{mnq}j_n(k_0R_q) - c_{mnq}j_n(k_qR_q)]Y_n^m(\theta_q,\phi_q) \\ &+ \sum_{p=1}^{N}\sum_{n=0}^{\infty}\sum_{m=-n}^{n} b_{mnp}h_n^{(1)}(k_0R_p)Y_m^n(\theta_p,\phi_p) \\ =& \sum_{n=0}^{\infty}\sum_{m=-n}^{n}[a_{mnq}j_n(k_0R_q) + b_{mnq}h_n^{(1)}(k_0R_q) \\ &\qquad - c_{mnq}j_n(k_qR_q)]Y_n^m(\theta_q,\phi_q) \\ &+ \sum_{\substack{p=1\\p\neq q}}^{N}\sum_{n=0}^{\infty}\sum_{m=-n}^{n} b_{mnp}h_n^{(1)}(k_0R_p)Y_m^n(\theta_p,\phi_p) = 0 \end{aligned} \tag{4.2.7}$$

where the $p = q$ term has been removed from the scattered wave and inserted into the first sum. Defining $Q_{mn\mu\nu}(r,\theta,\phi)$ by[1],

$$\begin{aligned} Q_{mn\mu\nu}(r,\theta,\phi) =& (2\nu+1)(-1)^{-m}\sum_{l=|n-\nu|}^{n+\nu} i^{l+\nu-n}(2l+1) \\ &\times \sqrt{\frac{(n+|m|)!\,|(\nu-|\mu|)|!\,|(l-|m-\mu|)|!}{|(n-|m|)|!\,(\nu+|\mu|)!\,|(l+|m-\mu|)|!}} \\ &\times \begin{pmatrix} n & \nu & l \\ 0 & 0 & 0 \end{pmatrix}\begin{pmatrix} n & \nu & l \\ m & -\mu & -m+\mu \end{pmatrix} \\ &\times h_l^{(1)}(kr)Y_l^{m-\mu}(\theta,\phi) \end{aligned}$$

and applying the addition theorem for spherical harmonics to equation (4.2.7) leads to,

$$\begin{aligned}&\sum_{n=0}^{\infty}\sum_{m=-n}^{n}[a_{mnq}j_n(k_0R_q) + b_{mnq}h_n^{(1)}(k_0R_q) - c_{mnq}j_n(k_qR_q)]Y_n^m(\theta_q,\phi_q) \\ &\qquad + \sum_{\substack{p=1\\p\neq q}}^{N}\sum_{n=0}^{\infty}\sum_{m=-n}^{n} b_{mnp}\sum_{\nu=0}^{\infty}\sum_{\mu=-\nu}^{\nu} Q_{mn\mu\nu}(r_{pq},\theta_{pq},\phi_{pq})j_\nu(k_0R_q)Y_\nu^\mu(\theta_q,\phi_q) = 0\end{aligned} \tag{4.2.8}$$

Taking advantage of the orthogonality of the spherical harmonics enables both sides of equation (4.2.8) to be multiplied by the complex conjugate of the spherical harmonic $\overline{Y_l^k(\theta_q,\phi_q)}$ and integrating over the surface of the object S_q,

[1]Modulus signs are inserted under the square root in order to ensure accurate resolution when coding. This is required as whenever the relevant factorials are negative, the multiplying Wigner–3j symbols are equal to zero although MATLAB® still produces an error unless modulus signs are in place.

$$a_{klq}j_l(k_0R_q) + b_{klq}h_l^{(1)}(k_0R_q) - c_{klq}j_l(k_qR_q) + j_l(k_0R_q)\sum_{\substack{p=1\\p\neq q}}^{N}\sum_{n=0}^{\infty}\sum_{m=-n}^{n} b_{mnp}Q_{mnkl}(r_{pq},\theta_{pq},\phi_{pq}) = 0 \tag{4.2.9}$$

Subsequently applying the condition that the normal component of the boundary wall is continuous on the surface of the object $\left(\rho_0^{-1}\partial\psi^{\text{ext}}/\partial r_q - \rho_q^{-1}\partial\psi_q^{\text{int}}/\partial r_q\right)_{r_q=R_q} = 0$ and by using the same logic used to derive equation (4.2.9),

$$a_{klq}j_l'(k_0R_q) + b_{klq}h_l'^{(1)}(k_0R_q) - \frac{k_q\rho_0}{k_0\rho_q}c_{klq}j_l'(k_qR_q) + j_l'(k_0R_q)\sum_{\substack{p=1\\p\neq q}}^{N}\sum_{n=0}^{\infty}\sum_{m=-n}^{n} b_{mnp}Q_{mnkl}(r_{pq},\theta_{pq},\phi_{pq}) = 0 \tag{4.2.10}$$

where the prime denotes differentiation with respect to the argument. Writing $\xi_q = k_q\rho_0/k_0\rho_q$, constants $C_l(k_0, k_q, \xi_q, R_q)$ are defined as,

$$C_l(k_0,k_q,\xi_q,R_q) = -\frac{j_l'(k_0R_q)j_l(k_qR_q) - \xi_q j_l'(k_qR_q)j_l(k_0R_q)}{h_l'^{(1)}(k_0R_q)j_l(k_qR_q) - \xi_q h_l^{(1)}(k_0R_q)j_l'(k_qR_q)} \tag{4.2.11}$$

and the c_{mnq} terms in the above expressions can be eliminated by multiplying equation (4.2.9) by $j_l'(k_qR_q)k_q\rho_0$ and (4.2.10) by $j_l(k_qR_q)k_0\rho_q$, then subtracting one from the other,

$$b_{klq} = C_l(k_0,k_q,\xi_q,R_q)\times\left[a_{klq} + \sum_{\substack{p=1\\p\neq q}}^{N}\sum_{n=0}^{\infty}\sum_{m=-n}^{n} b_{mnp}Q_{mnkl}(r_{pq},\theta_{pq},\phi_{pq})\right] \tag{4.2.12}$$

In the limit of the density of each sphere ρ_q tending to zero or infinity, equations (22) and (25) from Gaunaurd, Huang and Strifors (1995) are recovered for the soft and hard sphere coefficients respectively.

The full solution to equation (4.2.5), as found by Gaunaurd, Huang and Strifors (1995), has been shown, and in theory it is possible to describe the scattered wave completely using this technique when the exact locations of the N objects are known.

4.2.2 Foldy's theory

Foldy (1945) attempted to negotiate the computational difficulties inherent in having an infinite sum representing the scattering series by considering how the average field behaves for all configurations of scatterers.

To that end, the scattered field of a wave impinging on N disjoint objects B_i located at $\boldsymbol{r}_1, \ldots, \boldsymbol{r}_N$ is considered. The total field ψ in the system is the sum of the incident field ψ^{inc} and the field scattered by each of the objects in the set ψ_j^{sca},

$$\psi = \psi^{\text{inc}} + \sum_{j=1}^{N} \psi_j^{\text{sca}} \tag{4.2.13}$$

Furthermore, the exciting field on any scatterer ψ_j^{ex} is the field impinging on it from both the incident wave and all the other scatterers in the configuration,

$$\psi_j^{\text{ex}} = \psi - \psi_j^{\text{sca}} = \psi^{\text{inc}} + \sum_{\substack{i=1 \\ i \neq j}}^{N} \psi_i^{\text{sca}} \tag{4.2.14}$$

As has been demonstrated, it is sometimes possible to solve equation (4.2.13) exactly. However, for the case of bubbly liquids, the computation time required to obtain ψ exactly would be prohibitive and in any event, the locations of the bubble centres are usually unknown, hence solving exactly becomes an impossible task. Instead, the average properties of ψ with respect to changes in the arrangement of scatterers are calculated and to do so requires some form of statistical averaging.

4.2.2.1 Ensemble average

One can begin by assuming there are on average $n(\boldsymbol{r}, s)\mathrm{d}s$ scatterers per unit volume with scattering properties lying between s and $s + \mathrm{d}s$ and the probability of the scatterers having a particular arrangement is $p(\boldsymbol{r}_1, \ldots, \boldsymbol{r}_N, s_1, \ldots, s_N)\mathrm{d}V_1 \cdots \mathrm{d}V_N \mathrm{d}s_1 \cdots \mathrm{d}s_N$ whereby the first scatterer is at the point $\boldsymbol{r}_1$ in the volume element $\mathrm{d}V_1$ and so on for all N objects. Furthermore, the probability distribution $p(\boldsymbol{r}_1, \ldots, \boldsymbol{r}_N, s_1, \ldots, s_N)$ is normalised over all configurations to unity. In the case of bubbly liquids, it is assumed that each bubble is indistinguishable from another so that the order of the arrangement is irrelevant. In addition, for the case of bubbly liquids in an unbounded medium, a valid assumption is that the location of each bubble is independent of the others and so the probability distribution is,

$$p(\boldsymbol{r}_1, \ldots, \boldsymbol{r}_N, s_1, \ldots, s_N) = p(\boldsymbol{r}_1, s_1) \cdots p(\boldsymbol{r}_N, s_N)$$

The normalisation of the probability requires that,

$$\int\!\!\int_V n(\boldsymbol{r}, s)\mathrm{d}V\mathrm{d}s = N$$

where the integration volume V contains the bubbles. This implies,

$$Np(\boldsymbol{r}_j, s_j) = n(\boldsymbol{r}_j, s_j) \tag{4.2.15}$$

since each scatterer is equally likely to occupy the volume $\mathrm{d}V_j$. The total number of scatterers per unit volume in the neighbourhood of $\boldsymbol{r}$ is,

$$n(\boldsymbol{r}) = \int n(\boldsymbol{r}, s)\mathrm{d}s$$

For a function $f(\boldsymbol{r}, s)$, the ensemble average is defined as the average over the ensemble of possible configurations,

$$\big\langle f(\boldsymbol{r}, s)\big\rangle = \int_V \cdots \int_V \int \cdots \int f(\boldsymbol{r}, s)p(\boldsymbol{r}_1, \ldots, \boldsymbol{r}_N, s_1, \ldots, s_N)\mathrm{d}s_1 \cdots \mathrm{d}s_N \mathrm{d}V_1 \cdots \mathrm{d}V_N \tag{4.2.16}$$

Similarly, by taking an ensemble average over the configuration with one scatterer held fixed by using an appropriate conditional probability gives,

$$\big\langle f(\boldsymbol{r}, s \mid \boldsymbol{r}_1, s_1)\big\rangle = \int_V \cdots \iint_V \cdots \int f(\boldsymbol{r}, s)p(\boldsymbol{r}_2, \ldots, s_2, \ldots \mid \boldsymbol{r}_1, s_1)\mathrm{d}s_2 \cdots \mathrm{d}s_N \mathrm{d}V_2 \cdots \mathrm{d}V_N \tag{4.2.17}$$

4.2.2.2 Foldy's method

To proceed with this problem, Foldy (1945) considered isotropic point scatterers. Such an assumption is applicable to small bubbles impinged by medical ultrasound since their diameter is typically two orders of magnitude smaller than the wavelength. This implies that, for an unknown scattering amplitude A_j, the scattered field in the neighbourhood of the j^{th} scatterer can be described by the free-space Green's function $G(\boldsymbol{r})$,

$$\psi_j^{\text{sca}} = A_j G(\boldsymbol{r} - \boldsymbol{r}_j)$$

and the Green's function in three dimensions can be written for the external, homogeneous medium with wavenumber k as,

$$G(\boldsymbol{r}) = \frac{e^{ik|\boldsymbol{r}|}}{4\pi|\boldsymbol{r}|}$$

The scattering amplitude of a scatterer is characterised by,

$$A_j = g_j u_j^{\text{ex}}(\boldsymbol{r}_j)$$

In other words, the strength of the scattered wave is proportional to the external field acting on it, where $g = g(s, \omega)$ is referred to as the "scattering coefficient" of the object and ω is the frequency of the scattered wave. These definitions are inserted into equation (4.2.13) to obtain,

$$\psi = \psi^{\text{inc}} + \sum_{j=1}^{N} g_j \psi_j^{\text{ex}}(\boldsymbol{r}_j) G(\boldsymbol{r} - \boldsymbol{r}_j) \tag{4.2.18}$$

Observing that $\langle \psi^{\text{inc}}(\boldsymbol{r}) \rangle = \psi^{\text{inc}}(\boldsymbol{r})$ since the incident wave is unaffected by the arrangement of the scatterers, the ensemble averaging of (4.2.16) is applied to equation (4.2.18) by multiplying both sides by $p(\boldsymbol{r}_1, \ldots, \boldsymbol{r}_N, s_1, \ldots, s_N)\mathrm{d}V_1 \cdots \mathrm{d}V_N \mathrm{d}s_1 \cdots \mathrm{d}s_N$ and integrating,

$$\begin{aligned}\langle \psi(\boldsymbol{r}) \rangle =& \psi^{\text{inc}}(\boldsymbol{r}) \\ &+ \sum_{j=1}^{N} \int_V \cdots \int_V \int \cdots \int p(\boldsymbol{r}_1, \ldots, s_N) g_j \psi_j^{\text{ex}}(\boldsymbol{r}_j) G(\boldsymbol{r} - \boldsymbol{r}_j) \mathrm{d}s_1 \cdots \mathrm{d}s_N \mathrm{d}V_1 \cdots \mathrm{d}V_N\end{aligned}$$

But,

$$p(\boldsymbol{r}_1, \ldots, \boldsymbol{r}_N, s_1, \ldots, s_N) = p(\boldsymbol{r}_j, s_j) p(\boldsymbol{r}_1, \ldots, \boldsymbol{r}_{j-1}, \boldsymbol{r}_{j+1}, \ldots, s_1, \ldots, s_{j-1}, s_{j+1}, \ldots | \boldsymbol{r}_j)$$

and using this in equation (4.2.17) along with the indistinguishability of the scatterers,

$$\langle \psi(\boldsymbol{r}) \rangle = \psi^{\text{inc}}(\boldsymbol{r}) + N \int_V \int p(\boldsymbol{r}_j, s_j) g_j \langle \psi_j^{\text{ex}}(\boldsymbol{r} | \boldsymbol{r}_j) \rangle G(\boldsymbol{r} - \boldsymbol{r}_j) \mathrm{d}s_j \mathrm{d}V_j \tag{4.2.19}$$

Finally, inserting equation (4.2.15) in (4.2.19) and defining $F(\boldsymbol{r}) = \int n(\boldsymbol{r}, s) g(s, \omega) \mathrm{d}s$, the well-known expression for the ensemble average of the wave function is,

$$\langle \psi(\boldsymbol{r}) \rangle = \psi^{\text{inc}}(\boldsymbol{r}) + \int_V \langle \psi_j^{\text{ex}}(\boldsymbol{r} | \boldsymbol{r}_j) \rangle F(\boldsymbol{r}_j) G(\boldsymbol{r} - \boldsymbol{r}_j) \mathrm{d}V_j \tag{4.2.20}$$

It is possible to calculate the ensemble average of the exciting field using equation (4.2.18) by holding one scatterer fixed and multiplying (4.2.14) by,

$$\begin{aligned}&p(\boldsymbol{r}_1, \ldots, \boldsymbol{r}_{j-1}, \boldsymbol{r}_{j+1}, \ldots, \boldsymbol{r}_N, s_1, \ldots, s_{j-1}, s_{j+1}, \ldots, s_N | \boldsymbol{r}_j) = p(\boldsymbol{r}_k | s_k) \times \\ &p(\boldsymbol{r}_1, \ldots, \boldsymbol{r}_{j-1}, \boldsymbol{r}_{j+1}, \ldots, \boldsymbol{r}_{k-1}, \boldsymbol{r}_{k+1}, \ldots, s_1, \ldots, s_{j-1}, s_{j+1}, \ldots, s_{k-1}, s_{k+1}, \ldots | \boldsymbol{r}_k, \boldsymbol{r}_j)\end{aligned}$$

before integrating using equation (4.2.17) and using a similar logic as before, obtaining,

$$\langle \psi_j^{\text{ex}}(\boldsymbol{r} | \boldsymbol{r}_j) \rangle = \psi^{\text{inc}} + (N-1) \int_V \int p(\boldsymbol{r}_k | \boldsymbol{r}_j) g_k \langle \psi_k^{\text{ex}}(\boldsymbol{r} | \boldsymbol{r}_j, \boldsymbol{r}_k) \rangle G(\boldsymbol{r} - \boldsymbol{r}_k) \mathrm{d}V_k \mathrm{d}s_k \tag{4.2.21}$$

This illustrates the inherent problem of multiple scattering theories: the exciting field with j scatterers fixed is expressed in terms of the exciting field with $j+1$ scatterers held fixed. One could carry on like this reducing each equation to the next level of scattering with more scatterers held fixed and obtain a set of integral equations, but when N is large, solving this is too computationally expensive. Therefore an approximation is required to break this hierarchy at some point where the problem is still tractable.

4.2.2.3 Foldy's assumption

In the case of dilute solutions, Foldy (1945) assumed that the exciting field on the j^{th} scatterer is the same as the total field at that point if the scatterer is removed. Physically, this implies that waves scattered by the objects are small relative to the exciting fields *felt* by other scatterers. Mathematically this means,

$$\left\langle \psi_j^{\text{ex}}(\boldsymbol{r}|\boldsymbol{r}_j) \right\rangle = \left\langle \psi(\boldsymbol{r}) \right\rangle + \mathcal{O}\left(\frac{1}{N}\right)$$

Assuming N is large, the error is small and using this approximation in equation (4.2.20) by ignoring terms $\mathcal{O}\left(N^{-1}\right)$, an integral equation for $\langle \psi(\boldsymbol{r}) \rangle$ that can be solved exactly is,

$$\left\langle \psi(\boldsymbol{r}) \right\rangle = \psi^{\text{inc}}(\boldsymbol{r}) + \int_V \left\langle \psi(\boldsymbol{r}) \right\rangle F(\boldsymbol{r}_j) G(\boldsymbol{r} - \boldsymbol{r}_j) \mathrm{d}V_j \tag{4.2.22}$$

To see the significance of equation (4.2.22), the operation $\nabla^2 + k^2$ is applied to both sides, where ∇^2 is the usual Laplacian operator,

$$\nabla^2 \left\langle \psi(\boldsymbol{r}) \right\rangle + k_{\text{eff}}^2 \left\langle \psi(\boldsymbol{r}) \right\rangle = 0 \tag{4.2.23}$$

$$k_{\text{eff}}^2 = k^2 + 4\pi F(\boldsymbol{r}) \tag{4.2.24}$$

Thus the ensemble averaged wave function satisfies the wave equation in a homogeneous medium with effective wavenumber k_{eff}.

4.2.2.4 Lax's assumption

In the case where multiple scatterings between objects cannot be ignored and the scattered waves of one object do contribute to the exciting field of other scatterers, Lax (1952) suggested breaking the hierarchy at the next level in equation (4.2.21), known as the Quasi-Crystalline Approximation (QCA). Physically, this means that waves scattered by an object from the incident wave (known as first-order scattered waves) impinge on other objects, but subsequent re-scatterings (known as n^{th}-order scattered waves, where there have been n re-scatterings)

are too weak to have an effect on the exciting fields of other scatterers. Such an approximation should be valid for more concentrated solutions of bubbles. Mathematically, this means,

$$\langle \psi_k^{\text{ex}}(\boldsymbol{r}|\boldsymbol{r}_j, \boldsymbol{r}_k)\rangle \approx \langle \psi_j^{\text{ex}}(\boldsymbol{r}|\boldsymbol{r}_j)\rangle$$

Writing $\upsilon(\boldsymbol{r}_j) = \langle \psi_j^{\text{ex}}(\boldsymbol{r}|\boldsymbol{r}_j)\rangle$, this results in two sets of Lax's integral equations from (4.2.20) and (4.2.21),

$$\big\langle \psi(\boldsymbol{r})\big\rangle = \psi^{\text{inc}}(\boldsymbol{r}) + \int_V \upsilon(\boldsymbol{r}_j) F(\boldsymbol{r}_j) G(\boldsymbol{r} - \boldsymbol{r}_j) \mathrm{d}V_j \tag{4.2.25}$$

$$\upsilon(\boldsymbol{r}) = \psi^{\text{inc}}(\boldsymbol{r}) + (N-1) \int_V p(\boldsymbol{r}_k|\boldsymbol{r}_j) g(s_k, \omega) \upsilon(\boldsymbol{r}_k) G(\boldsymbol{r} - \boldsymbol{r}_k) \mathrm{d}V_k \mathrm{d}s_k \tag{4.2.26}$$

Thus (4.2.26) must be solved first for $\upsilon(r)$ and subsequently used to solve equation (4.2.25). Before proceeding, it is necessary to specify a suitable conditional probability consistent with the normalisation condition and taking into account that no object can overlap, known as the "hole correction". Using the Heaviside function $H(\boldsymbol{r})$ a simple choice for the case of bubbles of diameter $2a$ would be, for $b \geq 2a$,

$$p(\boldsymbol{r}_1|\boldsymbol{r}_2) = q_0 H\big(|\boldsymbol{r}_2 - \boldsymbol{r}_1| - b\big)$$

In addition, q_0 is a constant that can be determined from the normalisation condition and the fact that the scatterers are independent (see Martin, 2006).

Solving equations (4.2.25) and (4.2.26) in general is much more involved than the equivalent Foldy integral equations and often impossible. However progress has been made over the years in specific instances, as described in the following section.

4.2.2.5 Semi-infinite region

An infinite medium of uniform density ρ and constant wavespeed $\mathcal{C}$ in which are randomly distributed many identical scatterers in the $z > 0$ region is considered. A time-harmonic wave with constant wavenumber $k = \omega/\mathcal{C}$ impinges on the scatterers. The problem is to find an ensemble averaged solution to determine the average field using the QCA.

Waterman and Truell (1961) were the first to tackle this problem assuming that there are an infinite number of point scatterers (objects whose radius is much smaller than the incident wavelength). They approximated the scattering region as an infinite number of concatenated slabs and summed the scattered contributions in the form of an integral, in terms of the forward

and backward scattering amplitude from each scatterer. The boundaries of the region had to be treated with care using this method and it was later shown that their result was incorrect. Twersky (1962a) tackled the same problem but this time by considering large scatterers in 1, 2 and 3 dimensions. He tried to overcome the stratification problem of Waterman and Truell by introducing the concept of a two-space scatterer (Twersky, 1962b). On the microscopic scale, the scattered waves travel in k-space whereas the macroscopic internal field travels in k_{eff}-space. To extend his formulation to dense scatterers, he attempted to write the scattering amplitude in terms of these two wave parameters rather than in terms of the microscopic wavenumbers only. However Twersky's results, which also depended on the angle of incidence, were shown to be accurate only to first order.

In fact it was Lloyd and Berry (1967) who first answered the semi-infinite problem correctly in a nuclear physics formulation. Linton and Martin (2005) have since derived the *Lloyd-Berry* formula in more conventional acoustics terminology. The result obtained was,

$$k_{\text{eff}}^2 = k^2 + 4\pi n_0 f(0) + \frac{4\pi^2 n_0^2}{k^2}\left[-f(0)^2 + f(\pi)^2 - \int_0^\pi \frac{1}{\sin(\theta/2)}\frac{df(\theta)^2}{d\theta}\mathrm{d}\theta\right] \qquad (4.2.27)$$

where $f(0)$ and $f(\pi)$ are the forward and back-scattering amplitudes respectively and n_0 is the number of scatterers per unit volume. To first order, Foldy's famous result (4.2.24) is recovered, which is obtained if there is a small volume fraction whereby the scattering amplitudes are very small i.e. $f(\theta) \ll 1$. Subsequently, Angel and Aristégui (2005) have extended this theory to propagation through a screen of scatterers of finite thickness.

4.2.2.6 Henyey's correction

In the case of a uniform density of identical scatterers, Henyey (1999) derived a correction to Foldy's expression (4.2.24) that included second-order scattering. In summary, Henyey's correction factor only becomes important when the factor $n_0 A/k^2$ is not small, where n_0 is the constant scatterer density, A is the constant scattering amplitude and k is the wavenumber in the liquid. In other words, Henyey's correction is applicable when the average spacing of bubbles is such that the scattered wave felt by other bubbles is not negligible. In this instance, Henyey's effective wavenumber is,

$$k_{\text{eff}}^2 = k^2 + 4\pi n_0 \frac{A}{1 - iA(k_{\text{eff}} - k)}$$

Equivalently, using equation (4.2.24), Henyey wrote the effective wavenumber in terms of the *effective scattered amplitude* of one scatterer A_{eff},

$$k_{\text{eff}}^2 = k^2 + 4\pi n_0 A + 16\pi i n_0^2 A \frac{A_{\text{eff}}^2}{k_{\text{eff}} - k} \tag{4.2.28}$$

In the two equations above, for n_0 and/or A small, Foldy's expression is an adequate approximation. It is also worth noting that the correction term is of the order A^3, which agrees with Ye and Ding's expression (1995) in a similar setting, although theirs is inaccurate when $\frac{k_{\text{eff}}}{k} \gg 1$.

4.2.3 Dense population of bubbles

Both Foldy's and Lax's approximations are not applicable in mixtures with a high concentration of bubbles as in these situations, the multiple scattering between objects becomes too important to ignore, particularly at the resonance frequency of the bubbles. The reason why a new model was required is that the classic theory of Foldy (see equation (4.2.24)) overestimates the level of acoustic attenuation in dense mixtures of bubbles at the resonance frequency. Feuillade (1996) thus developed a much-debated linear theory to better model this situation which is outlined and reviewed in this section.

Feuillade started with two assumptions: the bubbles can be treated as monopole sources (a valid assumption when the bubbles are very small compared to the incident wavelength) and bubbles in close proximity oscillate in phase with each other as an ensemble and "the scattered sound from each of them to all the others couples them radiatively together". This contrasts with the classic theory of Foldy which "assumes ... that bubbles always oscillate independently of each other, even when they resonate strongly and are closely spaced" (Feuillade, 1996, p. 3413) which is certainly incorrect.

4.2.3.1 Resonance scattering by a single bubble

To begin, an equation of motion for the monopole mode of a spherical model was first formulated by Minnaert (1933). This was further developed by Devin (1959) who included radiation, thermal and viscous damping processes. For a wave with driving pressure and frequency P and ω respectively, the ordinary differential equation modelling the difference in volume ν between a bubble's equilibrium value and the value at that instant, in a fluid of density ρ and ambient pressure p_0, with specific gas ratio γ is,

$$m\ddot{\nu} + b\dot{\nu} + \kappa\nu = -Pe^{i\omega t} \tag{4.2.29}$$

where $m = \rho/4\pi R$ is the "inertial mass" of the bubble, $\kappa = 3\gamma p_0/4\pi R^3$ is the adiabatic stiffness and b is the damping coefficient.

Writing Minnaert's resonance frequency (derived in Appendix B.3) as ω_{N} and assuming a harmonic solution $\nu = \bar{\nu}\exp[i\omega t]$ to (4.2.29),

$$\bar{\nu} = \frac{-P}{\kappa - \omega^2 + i\omega b} = \frac{-P/\left(m\omega^2\right)}{\left(\frac{\omega_{\mathrm{N}}^2}{\omega^2} - 1\right) + i\frac{b}{m\omega}} \tag{4.2.30}$$

The term $b/m\omega$ is the damping term and is identified with radiative, thermal and viscous damping in the form $b/m\omega = \delta_r + \delta_t + \delta_\mu = \delta$ although the exact forms of the damping are not discussed here. In addition, the pressure at a distance r from the bubble is given by,

$$p(r) = \frac{\rho e^{-ikr}}{4\pi r}\ddot{\nu}$$

4.2.3.2 An ensemble of bubbles

Using a similar logic as that used to derive (4.2.13) and (4.2.14), a set of coupled differential equations for the whole system of N bubbles, where the centres of the j^{th} and i^{th} bubbles are a distance r_{ij} apart and each bubble's motion is described by (4.2.29), can be expressed by,

$$\begin{aligned} m\ddot{\nu}_1 + b\dot{\nu}_1 + \kappa\nu_1 &= -P_1 e^{i(\omega t+\varphi_1)} - \sum_{j=2}^{N} \frac{\rho e^{-ikr_{j1}}}{4\pi r_{j1}}\ddot{\nu}_j \\ &\cdots\cdots \qquad\qquad \cdots\cdots \\ m\ddot{\nu}_N + b\dot{\nu}_N + \kappa\nu_N &= -P_N e^{i(\omega t+\varphi_N)} - \sum_{j=1}^{(N-1)} \frac{\rho e^{-ikr_{jN}}}{4\pi r_{jN}}\ddot{\nu}_j \end{aligned} \tag{4.2.31}$$

The system of equations (4.2.31) is written in matrix form $M\boldsymbol{\nu} = p$ where $\boldsymbol{\nu} = \{\bar{\nu}_1, \ldots, \bar{\nu}_N\}$, $p = \{-p_1, \ldots, -p_N\} = \{-P_1 e^{i\varphi_1}, \ldots, -P_N e^{i\varphi_N}\}$ and M is the coupling matrix whose diagonal elements describe the individual bubble dynamics and the off-diagonal elements characterise the coupling between bubbles,

$$M_{ij} = \begin{cases} \kappa_j - \omega^2 m_j + i\omega b_j & \text{if } i = j, \\ \dfrac{-\omega^2 \rho e^{-ikr_{ji}}}{4\pi r_{ji}} & \text{if } i \neq j. \end{cases}$$

Although the matrix includes information about all modes of coupling, it would be computationally expensive and virtually impossible to solve. Consequently, Foldy's notion of an ensemble average to find the *average scattered field* is used.

4.2.3.3 Eigenvalue problem

The answer to the problem is thus $\langle \boldsymbol{\nu} \rangle = \langle M^{-1} \rangle p$. Calculating $\langle M^{-1} \rangle$ is numerically possible but Feuillade (1996) described an analytical solution by considering "collective modes". In the case of symmetric modes, where the bubbles oscillate in phase with each other, they dominate over the anti-symmetric modes, since these latter modes are excited by gradients in pressure across the bubble, which in the case of small bubbles where $k_0 R \ll 1$, are very small indeed. Hence it is assumed that all anti-symmetric modes can be neglected in the long wavelength limit.

The next step is to decompose the matrix M into its eigenvalues $\{\lambda_j\}$ and eigenvectors. Since M is symmetric, the set of complex eigenvectors $\{x_1, \ldots, x_N\}$ can be found by solving the eigenvalue equations,

$$M x_j = \lambda_j x_j \tag{4.2.32}$$

Thus,

$$\boldsymbol{\nu} = \sum_{j=1}^{N} c_j x_j$$

and assuming that the eigenvector representing the symmetric mode x_1 dominates over all other modes, without loss of generality $|c_1| \gg |c_j|,\ j \neq 1$. Putting these facts into the matrix equation $M\boldsymbol{\nu} = p$,

$$p = M\boldsymbol{\nu} = \sum_{j=1}^{N} c_j M x_j = \sum_{j=1}^{N} c_j \lambda x_j \approx c_1 \lambda_1 x_1 \tag{4.2.33}$$

Using the orthogonality relationship of the eigenvectors, both sides of equation (4.2.33) are multiplied by x_1^T to obtain,

$$c_1 = \frac{x_1^T p}{\lambda_1}$$

The problem of finding $\langle M^{-1} \rangle$ is thus reduced to,

$$\langle \boldsymbol{\nu} \rangle \approx \langle c_1 x_1 \rangle = \left\langle \frac{x_1^T p x_1}{\lambda_1} \right\rangle \tag{4.2.34}$$

Therefore the problem now involves finding the eigenvalue λ_1 and eigenvector x_1 of the symmetric modes. To do this, it is argued that in the long wavelength limit, the distance between bubbles is very small, thus the difference in phase and moduli of the waves scattered by the objects is small since they are roughly oscillating in phase, and can be assumed to be equal. In this case,

$$x_1 = \frac{1}{\sqrt{N}}[1, \ldots, 1]^T \tag{4.2.35}$$

The eigenvalue is subsequently obtained from equation (4.2.32) leading to $\lambda_1 = x_1^T M x_1$ and with (4.2.35), writing the distance between the j^{th} bubble and its k^{th} nearest neighbour as $r_j^{(k)}$, this gives,

$$\lambda_1 = \kappa - \omega^2 m + i\omega b - \omega^2 \rho \left[\frac{1}{N} \left(\sum_{j=1}^{N-1} \frac{e^{-ikr_j^{(1)}}}{4\pi r_j^{(1)}} + \ldots + \sum_{j=1}^{N-1} \frac{e^{-ikr_j^{(N)}}}{4\pi r_j^{(N)}} \right) \right] \tag{4.2.36}$$

When N is large, each summation is an average within the ensemble and assuming that there are n_0 bubbles per unit volume with the probability that a bubble's n^{th} nearest neighbour lies between a and $a + \mathrm{d}a$ being $p_n(a)\mathrm{d}a$, equation (4.2.36) becomes,

$$\lambda_1 = \kappa - \omega^2 m + i\omega b - \omega^2 \rho \left[\sum_{j=1}^{N} \int_0^\infty \frac{e^{-ikr}}{4\pi r} p_j(r) \mathrm{d}r \right]$$

On interchanging the order of the summation and the integration, the eigenvalue,

$$\lambda_1 = \kappa - \omega^2 m + i\omega b - \omega^2 \rho n_0 \int_0^\infty r e^{-ikr} \mathrm{d}r \tag{4.2.37}$$

is obtained and using (4.2.35) and (4.2.37) in equation (4.2.34) leads to an approximate ensemble average for $\langle \boldsymbol{\nu} \rangle$ given by,

$$\langle \bar{\nu}_j \rangle = \frac{-\sum p_j / N}{\kappa - \omega^2 m + i\omega b - \omega^2 \rho n_0 \int_0^\infty r e^{-ikr} \mathrm{d}r} \tag{4.2.38}$$

where $\sum p_j / N$ is interpreted as the average pressure P felt by the bubbles in the ensemble. Then finally, an expression for the effective wavenumber in a bubbly liquid with dense scatterers of different radius sizes R is arrived at,

$$k_{\text{eff}}^2 = k^2 + \left(\left(\int_0^\infty \frac{4\pi R n(R) \mathrm{d}R}{\left(\frac{\omega_{\text{N}}}{\omega}\right)^2 - 1 + i\delta} \right)^{-1} - \int_0^\infty r e^{-ikr} \mathrm{d}r \right)^{-1} \tag{4.2.39}$$

and an expression for the compressibility of an effective medium and its wavespeed was used, given the compressibility of bubbles φ_g and the external medium (water) $\varphi_l = \left(\rho \mathcal{C}^2\right)^{-1}$,

$$\begin{aligned} \frac{1}{\rho \mathcal{C}_{\text{eff}}^2} \approx \varphi_{\text{eff}} &= \varphi_g + \varphi_l \\ \varphi_g &= \frac{n_0 \langle \bar{\nu} \rangle}{P} \end{aligned} \tag{4.2.40}$$

The approximation $\rho_{\text{eff}} \approx \rho_l$ is valid since the density of air is much less than water. Combining this together with equation (4.2.38) leads to Feuillade's expression (4.2.39) for the effective wavenumber.

4.2.3.4 Criticisms

As already alluded to, the results of Feuillade have been much contested particularly by Henyey (1999, 2002). Henyey's objections centred around the fact that, due to Feuillade not adequately defining what he means by the wavenumber k in his system of equations (4.2.31), he is in fact counting waves twice and thus arriving at an inaccurate value for the effective wavenumber. He argued that if one uses the effective wavenumber, then the results simply reduce to Foldy's result (4.2.24).

Feuillade (2002) retorted that it is not important what the exact definition of k is and moreover, Henyey's perturbation analysis of his equations of the previous section was inappropriate since Henyey considered dilute solutions only, whereas the theory presented by Feuillade was for non-dilute mixtures.

Henyey also alleged that Feuillade was inconsistent with his definition of what he was treating as the *total field* and what as the *incident field*. During Feuillade's discussion, Henyey claims that Feuillade switched from the total pressure in Feuillade's equation (7) to total pressure in equation (29) (here equations (4.2.40) and (4.2.38) respectively). Feuillade's response to this criticism was that Henyey misinterpreted his work and that p referred to the incident field throughout, whilst interactive scatterings were incorporated in the matrix M.

A further criticism was provided by Skaropoulos, Yagridou and Chrissoulidis (2003) who modelled the scattering from two and three bubbles exactly. Their results suggested that, like Feuillade's previous results, the resonance frequency is shifted downwards in a configuration of three identical bubbles. Feuillade used this result when deriving the eigenvector (4.2.35) and assumed that this pattern of downward-shifting of frequency was present in populations of different sized bubbles. However, it was shown that this does not appear to be the case and the response of the bubbles is dominated by the largest bubble in the ensemble. It seems therefore that Feuillade's assumption that different sized bubbles oscillate in phase with each other is inaccurate in the case of non-identical bubbles. Ultimately, this argument was not resolved satisfactorily and it seems there are too many potential issues with Feuillade's work to be confident in its validity.

4.3 Nonlinear approaches to scattering

Rather than tackle the problem by searching for a linear closed-form solution, authors (van Wijngaarden, 1968; Caflisch et al., 1985; Leighton, Meers and White, 2004) have spoken of the need for nonlinear theories because of the inadequacies of linear models to describe microbubble behaviour as they approach resonance. Van Wijngaarden (1968) in particular was the first author to present a model that took into account fully nonlinear bubble oscillations. His results were subsequently rigorously proved by Caflisch et al. (1985) and the theory was linearised for the case of small bubble oscillations by Commander and Prosperetti (1989) to obtain an effective wavenumber for the solution that agreed with Foldy's result, valid when the wavelength is large compared with the bubble radius.

4.3.1 A model of nonlinear scattering

Van Wijngaarden (1968) formulated a set of equations matching the macroscopic behaviour of a bubbly mixture with the microscopic nonlinear behaviour of an individual bubble by equating the pressure changes that occur between the two. It was assumed that the mixture was sufficiently dilute that the influence of radiation from individual bubbles upon their nearest neighbours was small compared with that of the total acoustic field. However, the argument was presented in a heuristic manner and it was not until Caflisch et al. (1985) derived the equations rigorously, that the range of validity for the model could be fully determined. This derivation is investigated in this section in order to be used later.

The equations for the conservation of mass and momentum of the fluid of density ρ, given velocity $\boldsymbol{u}$ and pressure p, writing subscripts l and g to refer to the liquid and gas phases, are,

$$\frac{\partial \rho}{\partial t} + \nabla \cdot (\rho \boldsymbol{u}) = 0 \tag{4.3.1}$$

$$\rho \left(\frac{\partial \boldsymbol{u}}{\partial t} + \boldsymbol{u} \cdot \nabla \boldsymbol{u} \right) = -\nabla p \tag{4.3.2}$$

applied to N bubbles with centres located at $\boldsymbol{r}_1, \ldots, \boldsymbol{r}_N$ and bubble radii $R_1(t), \ldots, R_N(t)$. The necessary boundary conditions for continuity of pressure and the normal velocity on each bubble surface, given a surface tension σ and liquid viscosity μ_l, are,

$$\frac{dR_j}{dt} = \boldsymbol{u} \cdot \hat{\boldsymbol{n}}_j \tag{4.3.3}$$

$$p = p_{g_j} - \frac{4\mu_l \dot{R}_j}{R_j} - \frac{2\sigma}{R_j} \tag{4.3.4}$$

for $j = 1, \ldots, N$ where $\hat{\boldsymbol{n}}$ is a unit normal to the bubble surface and the superscript "dot" denotes differentiation with respect to time.

The equation of state for the gas in the j^{th} bubble of mass M_j with polytropic index γ is, defining κ to be the ratio of specific heats,

$$p_{g_j} = \kappa \left(\frac{M_j}{\frac{4}{3}\pi R_j^3} \right)^{\gamma} \tag{4.3.5}$$

Furthermore, the mass of each bubble is assumed to be constant in time, i.e. there is no diffusion, coalescence or destruction of bubbles.

To close the model, an equation describing the nonlinear motion of the bubble wall due to the influence of the imposed sound field is required and the most commonly used is the Rayleigh-Plesset equation (Plesset and Prosperetti, 1977). Here, the effects of surface tension and fluid viscosity are additionally included since these effects are particularly significant in the case of bubbles in water. The Rayleigh-Plesset equation, as derived in Appendix B, is,

$$p_g - p = \rho_l \left(R\ddot{R} + \tfrac{3}{2}\dot{R}^2 \right) + \frac{4\mu_l \dot{R}}{R} + \frac{2\sigma}{R} \tag{4.3.6}$$

One further point is that typical scenarios of interest occur when the total number of bubbles is very large and, by taking a suitable limit as N tends to infinity, an average density $n(\boldsymbol{r})$ can be defined, which is the average number of scatterers per unit volume in the region of $\boldsymbol{r}$. For any continuous function $\phi(\boldsymbol{r})$ this limit leads to the relation,

$$\lim_{N\to\infty} \frac{1}{N} \sum_{j=1}^{N} \phi(\boldsymbol{r}_j) = \int \phi(\boldsymbol{r}) n(\boldsymbol{r}) \mathrm{d}\boldsymbol{r} \tag{4.3.7}$$

It is necessary to scale the equations to derive non-dimensional effective equations that describe the fluid behaviour. The following dimensionless parameters are formulated using a typical bubble radius R_0, a specified volume V of the whole mixture containing N bubbles and the incident wavelength λ,

$$\epsilon = \frac{1}{\lambda} \left(\frac{V}{N} \right)^{1/3} \tag{4.3.8a}$$

$$\delta = \frac{R_0}{\lambda} \tag{4.3.8b}$$

$$\beta = \frac{1}{V} \frac{4}{3} \pi R_0^3 N = \frac{4}{3} \pi \left(\frac{\delta}{\epsilon} \right)^3 \tag{4.3.8c}$$

Here ϵ can be described as the non-dimensional bubble separation distance, δ as the non-dimensional bubble radius and β as the gas volume fraction. In addition, velocities are scaled with respect to $\bar{C}$, a characteristic sound speed for the medium, and time is scaled with respect to the frequency ω associated with the effective medium. The ambient pressure is p_0 and

the typical mass of a single bubble is also defined as m_0. As a result, the following non-dimensional scalings, denoted by primes, are defined:

$$\boldsymbol{r}' = \lambda^{-1}\boldsymbol{r}, \qquad t' = \omega t, \qquad \rho' = \rho_l^{-1}\rho,$$
$$R' = R_0^{-1}R = \delta^{-1}\lambda^{-1}R, \qquad p' = p_0^{-1}(p - p_0), \qquad \boldsymbol{u}' = \bar{\mathcal{C}}^{-1}\delta^{-2}\boldsymbol{u} = R_0^{-1}\omega^{-1}\delta^{-1}\boldsymbol{u}.$$

Here, the non-dimensionalisation of pressure is different to Caflisch et al.'s method (1985) and this has been done for simplicity later. The effective equations are subsequently derived by taking the limit $\delta \to 0$ and assuming a solution in the form of an asymptotic expansion in orders of δ.

First, equation (4.3.1) is expanded and using the facts that $\partial p/\partial\rho = \mathcal{C}^2$ and $\rho \approx \rho_l$ since the gas density is small,

$$\frac{1}{\rho_l \mathcal{C}_l^2}\left(\frac{\partial p}{\partial t} + \boldsymbol{u}\cdot\nabla p\right) + \nabla\cdot\boldsymbol{u} = 0$$

For constant ρ_l and $\mathcal{C}_l$, this is non-dimensionalised to give,

$$\xi C^{-2}\left(\frac{\partial p'}{\partial t} + \delta^2\boldsymbol{u}'\cdot\nabla' p'\right) + \nabla'\cdot\boldsymbol{u}' = 0 \tag{4.3.9}$$

where two further non-dimensional parameters are defined as,

$$C = \frac{\mathcal{C}_l}{\bar{\mathcal{C}}}$$
$$\xi = \frac{p_0}{\delta^2\rho_l\bar{\mathcal{C}}^2}$$

It has been suggested that the equations could have been non-dimensionalised with respect to the wavespeed in the liquid and the extra parameter C dispensed with, but it is kept here for consistency with the original paper. Similarly for equation (4.3.2),

$$\frac{\partial \boldsymbol{u}'}{\partial t} + \delta^2\boldsymbol{u}'\cdot\nabla'\boldsymbol{u}' + \xi\nabla' p' = 0 \tag{4.3.10}$$

From equations (4.3.3) and (4.3.4), the non-dimensional boundary conditions are,

$$\delta^{-1}\frac{dR_j'}{dt} = \boldsymbol{u}'\cdot\hat{\boldsymbol{n}}_j \tag{4.3.11}$$
$$p' = \left(\frac{m_j'}{R_j'^3}\right) = F_j(R_j') \tag{4.3.12}$$

and the initial conditions, written with a tilde, are given as,

$$p'(0,\boldsymbol{r}_j) = \widetilde{p}(\boldsymbol{r}_j), \qquad \boldsymbol{u}'(0,\boldsymbol{r}_j) = \widetilde{\boldsymbol{u}}(\boldsymbol{r}_j), \qquad m'_j = \widetilde{m}(\boldsymbol{r}_j),$$
$$R'_j(0) = \widetilde{R}_j(\boldsymbol{r}_j), \qquad \frac{dR'(0)}{dt} = \frac{d\widetilde{R}(\boldsymbol{r}_j)}{dt}.$$

4.3.2 Derivation of the effective equations

It is now assumed that velocity is an irrotational field and so can be written as a scalar potential of the form $\boldsymbol{u} = \nabla\psi$. Inserting this into equation (4.3.10) gives an expression for the pressure in terms of the potential, where "primes" are henceforth dropped for clarity,

$$\begin{aligned} &\nabla\frac{\partial\psi}{\partial t} + \frac{\delta^2}{2}\nabla(\nabla\psi)^2 + \xi\nabla p = 0 \\ \implies &\nabla\left(\frac{\partial\psi}{\partial t} + \frac{\delta^2}{2}(\nabla\psi)^2 + p\xi\right) = 0 \\ \implies &\frac{\partial\psi}{\partial t} + \frac{\delta^2}{2}(\nabla\psi)^2 + p\xi = 0 \end{aligned} \tag{4.3.13}$$

where as $r \to \infty$, $\psi =$ const and $p = 0$. Solving for the pressure in (4.3.13) and inserting the expression into (4.3.9) gives an equation for the velocity potential alone,

$$-\xi\left(\xi^{-1}\left[\frac{\partial^2\psi}{\partial t^2} + \frac{\delta^2}{2}\frac{\partial(\nabla\psi)^2}{\partial t}\right] + \xi^{-1}\left[\delta^2\nabla\psi\cdot\nabla\left(\frac{\partial\psi}{\partial t} + \frac{\delta^2}{2}(\nabla\psi)^2\right)\right]\right) + C^2\nabla^2\psi = 0$$

$$\implies \frac{\partial^2\psi}{\partial t^2} + 2\delta^2\nabla\psi\cdot\nabla\frac{\partial\psi}{\partial t} + \delta^4(\nabla\psi\cdot\nabla\psi)\nabla\nabla\psi - C^2\nabla^2\psi = 0 \tag{4.3.14}$$

The boundary conditions on the surface of the j^{th} bubble (4.3.11), (4.3.12) and the initial conditions, using (4.3.13), similarly become,

$$\frac{\partial\psi}{\partial n_j} = \delta^{-1}\frac{dR_j}{dt}, \tag{4.3.15a}$$

$$\frac{\partial\psi}{\partial t} + \frac{\delta^2}{2}(\nabla\psi)^2 = -\xi F_j(R_j), \tag{4.3.15b}$$

$$\psi(0,\boldsymbol{r}_j) = \widetilde{\psi}(\boldsymbol{r}_j), \tag{4.3.16a}$$

$$\nabla\widetilde{\psi}(0,\boldsymbol{r}_j) = \widetilde{u}(\boldsymbol{r}_j), \tag{4.3.16b}$$

$$\frac{\partial\psi(0,\boldsymbol{r}_j)}{\partial t} = -\xi\widetilde{p}(\boldsymbol{r}_j) - \frac{1}{2}\delta^2(\nabla\widetilde{\psi})^2. \tag{4.3.16c}$$

To continue, one can multiply equation (4.3.14) by a "test function" $G(t,\boldsymbol{r})$, where $G(t,\boldsymbol{r})$ is the Green's function for the effective wave equation $\partial^2 G/\partial t^2 - C^2\nabla^2 G = \delta(\boldsymbol{r})\delta(t)$. Then, using Green's first identity and Gauss' formula, the problem can be transformed into an integral wave equation by integrating both over time and over the entire volume of liquid with the

bubbles removed, defined as $\Omega^N(t) = \Re^3 - \bigcup_{j=1}^{N} B_j$, where B_j is the volume occupied by the j^{th} bubble. On integrating,

$$\int_{\Omega^N}\int_0^t \frac{\partial^2\psi(\tau,\boldsymbol{s})}{\partial\tau^2}G(t-\tau,\boldsymbol{r}-\boldsymbol{s})\mathrm{d}\tau\mathrm{d}V = C^2\int_{\Omega^N}\int_0^t G(t-\tau,\boldsymbol{r}-\boldsymbol{s})\nabla^2\psi(\tau,\boldsymbol{s})\mathrm{d}\tau\mathrm{d}V$$
$$-\delta^2\int_{\Omega^N}\int_0^t G(t-\tau,\boldsymbol{r}-\boldsymbol{s})\left(2\nabla\psi(\tau,\boldsymbol{s})\nabla\frac{\partial\psi(\tau,\boldsymbol{s})}{\partial\tau}+\delta^2(\nabla\psi\cdot\nabla\psi)\nabla\nabla\psi\right)\mathrm{d}\tau\mathrm{d}V$$

Now integrating the left-hand side in time by parts and using Green's first identity on the first term of the right-hand side,

$$\int_{\Omega^N}\left(\left[G(t-\tau,\boldsymbol{r}-\boldsymbol{s})\frac{\partial\psi(\tau,\boldsymbol{s})}{\partial\tau}\right]_0^t-\int_0^t\frac{\partial\psi(\tau,\boldsymbol{s})}{\partial\tau}\frac{\partial G(t-\tau,\boldsymbol{r}-\boldsymbol{s})}{\partial\tau}\mathrm{d}\tau\right)\mathrm{d}V =$$
$$-\delta^2\int_{\Omega^N}\int_0^t G(t-\tau,\boldsymbol{r}-\boldsymbol{s})\left(2\nabla\psi(\tau,\boldsymbol{s})\nabla\frac{\partial\psi(\tau,\boldsymbol{s})}{\partial\tau}+\delta^2(\nabla\psi\cdot\nabla\psi)\nabla\nabla\psi\right)\mathrm{d}\tau\mathrm{d}V$$
$$+C^2\int_0^t\left(\oint G(t-\tau,\boldsymbol{r}-\boldsymbol{s})\nabla\psi(\tau,\boldsymbol{s})\cdot\hat{\boldsymbol{n}}\mathrm{d}S-\int_{\Omega^N}\nabla G(t-\tau,\boldsymbol{r}-\boldsymbol{s})\cdot\nabla\psi(\tau,\boldsymbol{s})\mathrm{d}V\right)\mathrm{d}\tau$$

Then repeating the same analysis by integrating by parts on the left-hand side and using Green's first identity on the right-hand side,

$$\int_{\Omega^N}\left[\psi(0,\boldsymbol{s})\frac{\partial G(t,\boldsymbol{r}-\boldsymbol{s})}{\partial t}-G(t,\boldsymbol{r}-\boldsymbol{s})\frac{\partial\psi(0,\boldsymbol{s})}{\partial t}+\int_0^t\psi(\tau,\boldsymbol{s})\frac{\partial^2G(t-\tau,\boldsymbol{r}-\boldsymbol{s})}{\partial\tau^2}\mathrm{d}\tau\right]\mathrm{d}V =$$
$$-\delta^2\int_{\Omega^N}\int_0^t G\left(2\nabla\psi\nabla\frac{\partial\psi}{\partial\tau}+\delta^2(\nabla\psi\cdot\nabla\psi)\nabla\nabla\psi\right)\mathrm{d}\tau\mathrm{d}V+C^2\int_0^t\oint G(t-\tau,\boldsymbol{r}-\boldsymbol{s})\nabla\psi(\tau,\boldsymbol{s})\cdot\hat{\boldsymbol{n}}\mathrm{d}S\mathrm{d}\tau$$
$$+C^2\int_0^t\left[\int_{\Omega^N}\psi(\tau,\boldsymbol{s})\nabla^2G(t-\tau,\boldsymbol{r}-\boldsymbol{s})\mathrm{d}V-\oint\psi(\tau,\boldsymbol{s})\nabla G(t-\tau,\boldsymbol{r}-\boldsymbol{s})\cdot\hat{\boldsymbol{n}}\mathrm{d}S\right]\mathrm{d}\tau$$

Rearranging,

$$\int_0^t\int_{\Omega^N}\psi(\tau,\boldsymbol{s})\left[\frac{\partial^2G(t-\tau,\boldsymbol{r}-\boldsymbol{s})}{\partial\tau^2}-C^2\nabla^2G(t-\tau,\boldsymbol{r}-\boldsymbol{s})\right]\mathrm{d}V\mathrm{d}\tau =$$
$$-\delta^2\int_{\Omega^N}\int_0^t G\left(2\nabla\psi\nabla\frac{\partial\psi}{\partial\tau}+\delta^2(\nabla\psi\cdot\nabla\psi)\nabla\nabla\psi\right)\mathrm{d}\tau\mathrm{d}V$$
$$+C^2\int_0^t\oint\Big(G(t-\tau,\boldsymbol{r}-\boldsymbol{s})\nabla\psi(\tau,\boldsymbol{s})\cdot\hat{\boldsymbol{n}}-\psi(\tau,\boldsymbol{s})\nabla G(t-\tau,\boldsymbol{r}-\boldsymbol{s})\cdot\hat{\boldsymbol{n}}\Big)\mathrm{d}S\mathrm{d}\tau$$
$$+\int_{\Omega^N}\left[G(t,\boldsymbol{r}-\boldsymbol{s})\frac{\partial\psi(0,\boldsymbol{s})}{\partial t}-\psi(0,\boldsymbol{s})\frac{\partial G(t,\boldsymbol{r}-\boldsymbol{s})}{\partial t}\right]\mathrm{d}V$$

Using the fact that $G(\boldsymbol{r},t)$ is the Green's function to the wave equation in the integral on the left-hand side and the assumption that the bubbles do not interact in order to turn the surface integral into a sum over the surfaces of each bubble, this becomes, for $\boldsymbol{s}\in\Omega^N(t)$ and $t>0$,

$$\begin{aligned}\psi(t,\boldsymbol{r}) =& -\delta^2\int\limits_{\Omega^N}\int_0^t G\left(2\nabla\psi\nabla\frac{\partial\psi}{\partial\tau}+\delta^2(\nabla\psi\cdot\nabla\psi)\nabla\nabla\psi\right)\mathrm{d}\tau\mathrm{d}V\\ &+C^2\int_0^t\sum_{j=1}^N\oint_{\partial B_j}\Big(G(t-\tau,\boldsymbol{r}-\boldsymbol{s})\nabla\psi(\tau,\boldsymbol{s})\cdot\hat{\boldsymbol{n}}-\psi(\tau,\boldsymbol{s})\nabla G(t-\tau,\boldsymbol{r}-\boldsymbol{s})\cdot\hat{\boldsymbol{n}}\Big)\mathrm{d}S\mathrm{d}\tau\\ &+\int\limits_{\Omega^N}\left[G(t,\boldsymbol{r}-\boldsymbol{s})\frac{\partial\psi(0,\boldsymbol{s})}{\partial t}-\psi(0,\boldsymbol{s})\frac{\partial G(t,\boldsymbol{r}-\boldsymbol{s})}{\partial t}\right]\mathrm{d}V\end{aligned}\tag{4.3.17}$$

Terms of order δ^2 or higher are ignored in equation (4.3.17) and each term in the surface integral is calculated separately. It is at this point that the theory ties in with Foldy's assumption (1945) that the field incident upon a particular bubble is the same as the field that would exist at that point if the bubble were removed from the ensemble. One can approximate $G(\boldsymbol{r})$ in the second term of the right-hand side of (4.3.17) at $\boldsymbol{r}_j$, by making an error of order δ and replacing $\nabla\psi\cdot\hat{\boldsymbol{n}}$ using (4.3.15a), whilst noting that ψ is of order unity to leading order. It is also assumed that the average bubble radius approaches the value of the radius in the effective medium $R(t,\boldsymbol{r}_j)$ in the limit of large N. Thus,

$$\begin{aligned}\psi(t,\boldsymbol{r}) =& 4\pi N\delta C^2\lim_{N\to\infty}\frac{1}{N}\sum_{j=1}^N\int_0^t G(t-\tau,\boldsymbol{r}-\boldsymbol{r}_j)R^2(\tau,\boldsymbol{r}_j)\frac{\partial R(\tau,\boldsymbol{r}_j)}{\partial\tau}\mathrm{d}\tau\\ &-\int\limits_V\left[G(t,\boldsymbol{r}-\boldsymbol{s})\xi\widetilde{p}(\boldsymbol{s})+\widetilde{\psi}(\boldsymbol{s})\frac{\partial G(t,\boldsymbol{r}-\boldsymbol{s})}{\partial t}\right]\mathrm{d}V\end{aligned}$$

Using a non-dimensional version of (4.3.7) then taking the limit, the integral form of the equation is found[2], by assuming $\chi\coloneqq NV^{-1}\lambda^3\delta$ is of the order unity,

$$\begin{aligned}\psi(t,\boldsymbol{r}) =& \chi C^2\int_0^t\int\limits_V G(t-\tau,\boldsymbol{s})\frac{\partial}{\partial\tau}\left(\frac{4\pi}{3}R^3(\tau,\boldsymbol{s})n(\boldsymbol{s})\right)\mathrm{d}V\mathrm{d}\tau\\ &-\int\limits_V\left[G(t,\boldsymbol{r}-\boldsymbol{s})\xi\widetilde{p}(\boldsymbol{s})+\widetilde{\psi}(\boldsymbol{s})\frac{\partial G(t,\boldsymbol{r}-\boldsymbol{s})}{\partial t}\right]\mathrm{d}V\end{aligned}\tag{4.3.18}$$

From this integral representation, the effective equations for the velocity potential that characterise the bubbly liquid can be derived by applying the operator $C^{-2}\frac{\partial^2}{\partial t^2}-\nabla^2$,

[2]Caflisch et al. (1985) started their analysis by multiplying by $\partial G/\partial t$ instead, consequently resulting in a different integral equation. The present method was chosen for the purpose of this thesis as it was considered easier to follow and the result more straightforward to interpret.

$$C^{-2}\frac{\partial^2\psi}{\partial t^2} - \nabla^2\psi + \frac{\partial}{\partial t}\left(\frac{4}{3}\pi R^3 n\chi\right) = 0, \tag{4.3.19}$$

$$\nabla\psi(0,\boldsymbol{r}) = \widetilde{u}(\boldsymbol{r}), \qquad \frac{\partial\psi(0,\boldsymbol{r})}{\partial t} = -\xi\widetilde{p}(\boldsymbol{r}), \tag{4.3.20}$$

where, noting that $p = -\xi^{-1}\partial\psi/\partial t$, the behaviour of the bubble is given by the Rayleigh-Plesset equation (4.3.6) and the equation of state,

$$R\ddot{R} + \tfrac{3}{2}\dot{R}^2 + \frac{4\mu_l\dot{R}}{R} + \frac{2\sigma}{R} = \xi\big(F(R) - p\big),$$
$$F(R) = \left(\frac{m}{R^3}\right)^{\gamma},$$
$$R(0,\boldsymbol{r}) = \widetilde{R}(\boldsymbol{r}), \qquad \dot{R}(0,\boldsymbol{r}) = \frac{d\widetilde{R}(\boldsymbol{r})}{dt}.$$

Equations (4.3.19) and (4.3.20) can be presented in a form that is similar to that of van Wijngaarden (1968) by rewriting them in terms of fluid velocity and pressure instead of the velocity potential, which leads to equations (4.1) and (4.2) of Caflisch et al. (1985),

$$\xi C^{-2}\frac{\partial p}{\partial t} + \nabla\cdot\boldsymbol{u} = \frac{\partial}{\partial t}\left(\frac{4}{3}\pi R^3 n\chi\right), \tag{4.3.21}$$

$$\frac{\partial\boldsymbol{u}}{\partial t} + \xi\nabla p = 0, \tag{4.3.22}$$

$$p(0,\boldsymbol{r}) = \widetilde{p}(\boldsymbol{r}), \qquad \bar{\boldsymbol{u}}(0,\boldsymbol{r}) = \widetilde{\boldsymbol{u}}(\boldsymbol{r}). \tag{4.3.23}$$

A full determination of the exact parameter regimes for which these equations are valid is given in Caflisch et al. (1985). In summary, the above equations are an accurate approximation for propagation in a bubbly liquid if all of the following are true:

$$\beta \ll 1, \qquad \delta \ll 1, \qquad \chi = \frac{\delta}{\epsilon^3} \leq \mathcal{O}\left(1\right). \tag{4.3.24}$$

In addition, accuracy also requires that ξ and C are independent of δ and ϵ and the magnitude of the fluid velocity is small enough to ignore convection. These assumptions imply that the bubbly liquid is dilute to the extent that the distances between bubbles are sufficiently large that any interaction between them can be ignored.

4.3.3 Linearisation

An alternative model for bubble behaviour that takes into account the compressibility of the host medium is given by Keller and Miksis (1980). A linear form of this equation along with equations (4.3.21) to (4.3.23) above were used by Commander and Prosperetti (1989)

to obtain an effective wave equation for the propagation of small amplitude waves through a dilute mixture of small bubbles.

The equations used in dimensional variables, derived from Caflisch et al. (1985), are,

$$\frac{1}{\rho \mathcal{C}^2}\frac{\partial p}{\partial t} + \nabla \cdot \boldsymbol{u} = \frac{\partial \beta}{\partial t} \tag{4.3.25}$$

$$\rho \frac{\partial \boldsymbol{u}}{\partial t} + \nabla p = 0 \tag{4.3.26}$$

where $\beta \coloneqq \frac{4}{3}\pi \int R^3(R_0, \boldsymbol{r}, t) n(\boldsymbol{r}, R_0) \mathrm{d}R_0$ is the volume fraction of bubbles present in the liquid and $n(\boldsymbol{r}, R_0)$ is the size distribution of bubbles in the mixture. Assuming the distribution is homogeneous across the volume, elimination of $\boldsymbol{u}$ from (4.3.25) and (4.3.26) gives,

$$\frac{1}{\mathcal{C}^2}\frac{\partial^2 p}{\partial t^2} - \nabla^2 p = 4\pi\rho \int_0^\infty \left[R^2 \frac{\partial^2 R}{\partial t^2} + 2R \left(\frac{\partial R}{\partial t} \right)^2 \right] n(R_0) \mathrm{d}R_0 \tag{4.3.27}$$

and, using the linear approximation $R = R_0(1 + X(t))$ where $|X|$ is small, this reduces to,

$$\frac{1}{\mathcal{C}^2}\frac{\partial^2 p}{\partial t^2} - \nabla^2 p = 4\pi\rho \int_0^\infty R_0^2 \frac{\partial^2 X}{\partial t^2} n(R_0) \mathrm{d}R_0 \tag{4.3.28}$$

The relationship between pressure, temperature T and velocity at the boundary of the bubble is obtained (Prosperetti, Crum and Commander, 1988) from the enthalpy equation and the equation of state of a perfect gas with thermal conductivity K, along with the energy equation for a gas with specific heat at constant pressure C_p,

$$\dot{p} = \frac{3}{R}\left((\gamma - 1) K \left(\frac{\partial T}{\partial r} \right)_{r=R} - \gamma p \dot{R} \right) \tag{4.3.29}$$

$$\rho C_p \frac{DT}{Dt} - \dot{p} = \nabla \cdot (K \nabla T) \tag{4.3.30}$$

Equations (4.3.29) and (4.3.30) are solved in the linear regime by assuming that pressure changes, along with changes in radius, are small as before. If the temperature changes across the boundary of the bubble are negligible, i.e. $\partial T / \partial r \ll 1$, then from equation (4.3.29), the adiabatic condition used in Caflisch et al. (1985) is recovered.

The Keller-Miksis equation used to describe bubble oscillation allows for compressible fluid regions and is thus valid for larger amplitude oscillations, unlike the Rayleigh-Plesset equation. It does, however, assume spherical oscillations of the bubble, although this assumption is reasonable in the regime where bubble size is small compared with the incident wavelength. The equation is,

$$\left(1-\frac{\dot{R}}{\mathcal{C}}\right)R\ddot{R}+\frac{3}{2}\left(1-\frac{\dot{R}}{3\mathcal{C}}\right)\dot{R}^2=\frac{1}{\rho}\left(1+\frac{\dot{R}}{\mathcal{C}}+\frac{R}{\mathcal{C}}\frac{d}{dt}\right)\left(p_0^{\text{int}}\left(\frac{R_0}{R}\right)^{3\gamma}-\frac{2\sigma}{R}-4\mu_l\frac{\dot{R}}{R}-p_0-p(t)\right)$$

The solution to the linear Keller-Miksis equation along with the linearised pressure solution to (4.3.29) and (4.3.30), is substituted into the wave equation (4.3.28) to obtain an effective wavenumber in terms of the natural frequency of a single bubble ω_{N} and a damping coefficient δ representing the effects of viscous, thermal and acoustic radiation damping,

$$k_{\text{eff}}^2=k^2+4\pi\omega^2\int_0^\infty\frac{R_0n(R_0)\text{d}R_0}{\omega_{\text{N}}^2-\omega^2+2i\delta\omega} \tag{4.3.31}$$

In the case of a monodisperse bubble population, where $n(R_0)=n_0\delta(R_0-\widehat{R}_0)$ and $\widehat{R}_0$ is the equilibrium radius of a single bubble, the effective wavenumber is given by,

$$k_{\text{eff}}^2=k^2+4\pi\omega^2\frac{n_0\widehat{R}_0}{\omega_{\text{N}}^2-\omega^2+2i\delta\omega} \tag{4.3.32}$$

Kargl (2002) subsequently argued that the Keller-Miksis equation for the bubble dynamics should be written in terms of the effective medium. As a result, the wavenumber equivalent to that obtained by Commander and Prosperetti in (4.3.31) becomes,

$$k_{\text{eff}}^2=k^2+4\pi\omega^2\int_0^\infty\frac{R_0n(R_0)\text{d}R_0}{\omega_{\text{N}_{\text{eff}}}^2-\omega^2+2i\delta_{\text{eff}}\omega} \tag{4.3.33}$$

where $\omega_{\text{N}_{\text{eff}}}$ and δ_{eff} are the natural frequency and the damping coefficient of a single bubble evaluated in the effective medium respectively, using the substitutions $\mathcal{C}\rightarrow\mathcal{C}_{\text{eff}}$, $\rho\rightarrow\rho_{\text{eff}}$ and $\mu_l\rightarrow\mu_{\text{eff}}$ in the Keller-Miksis equation. In a dilute mixture, Kargl claimed that one can still use $\mathcal{C}$, ρ and μ_l instead, as "the mixture laws for density and viscosity suggest [the presence of bubbles] would have negligible effect" (Kargl, 2002, p. 170). The equivalent of (4.3.33) for a monodisperse population is obtained by replacing the bubble density function with the Dirac-delta function, $n(R_0)\rightarrow n_0\delta(R_0-\widehat{R}_0)$, as before.

4.4 Homogeneous sheet approximation

The accurate modelling of wave propagation through a bubbly liquid is important to the successful development of therapeutic ultrasound devices. A numerical scheme for such propagation derived from Caflisch et al. (1985) and Commander and Prosperetti (1989), as examined in Sections 4.3.1 and 4.3.3, was proposed by Hamilton and Blackstock (1998). The scheme involves solving an inhomogeneous wave equation for the pressure p travelling through a liq-

uid with wavespeed $\mathcal{C}$ and density ρ, where the forcing term models the average response of an effective medium composed of a population of $n(R_0)$ bubbles with initial and current radius size R_0 and $R = R(R_0, t)$ respectively,

$$\frac{1}{\mathcal{C}^2}\frac{\partial^2 p}{\partial t^2} - \nabla^2 p = 4\pi\rho \int_0^\infty \left[R^2 \frac{\partial^2 R}{\partial t^2} + 2R\left(\frac{\partial R}{\partial t}\right)^2 \right] n\big(R_0\big)\mathrm{d}R_0 \tag{4.4.1}$$

This equation can be discretised in space j and time s, by space- and time-steps of length Δx and Δt respectively, for each bubble of size R_k out of a total of N discrete bubble sizes in the population, using an explicit finite difference scheme that is accurate to second-order,

$$\begin{aligned} p_{j,s} = 2p_{j,s-1} - p_{j,s-2} + \mathcal{C}^2\Delta t^2 \frac{p_{j+1,s-1} - 2p_{j,s-1} + p_{j-1,s-1}}{\Delta x^2} \\ + 4\pi\rho\mathcal{C}^2\Delta t^2 \sum_{k=1}^{N} n(R_k)\Big[2R_k\dot{R}_k^2 + R_k^2\ddot{R}_k\Big]_{j,s-1} \end{aligned} \tag{4.4.2}$$

writing $\dot{R}(t)$ and $\ddot{R}(t)$ as the bubble radial velocities and accelerations respectively.

Computational complexity arises when modelling a polydisperse bubble population. In equation (4.4.2), the bubble response in the sum must be computed for each bubble size R_k. For large N this is computationally intensive. Consequently, an approximation was proposed by Hibbs et al. (2007) whereby there is only one bubble at each point in the mesh. The size of this bubble is chosen randomly according to a probability distribution defined by the size distribution $n(R)$ and fixed at the start of the simulation. Consequently it is possible to reduce the complexity of the problem by a factor of N and equation (4.4.2) is simplified to give,

$$p_{j,s} = 2p_{j,s-1} - p_{j,s-2} + \mathcal{C}^2\Delta t^2\left(\frac{p_{j+1,s-1} - 2p_{j,s-1} + p_{j-1,s-1}}{\Delta x^2} + 4\pi\rho n\Big[2R\dot{R}^2 + R^2\ddot{R}\Big]_{j,s-1}\right) \tag{4.4.3}$$

The remainder of this chapter is devoted to investigating the accuracy and range of validity of this "homogeneous sheet" (HS) approximation. If it can be shown that this yields valid results in certain parameter regimes then it could greatly simplify the computational complexity, leading to improvements in modelling and eventually, diagnostic and therapeutic applications.

4.4.1 Transmission coefficient analogy

To begin, equation (4.4.3) is equivalent to approximating the effective medium as a series of "sheets" of monodisperse bubbles. As a result, the propagation of waves through a layered structure is considered. For notational convenience, a function for a wave propagating a distance x through a medium with wavenumber k_j is defined,

$$W_j(x) = \exp\left[-ik_j x\right]$$

neglecting the time component of the wave for simplicity since it cancels out in the final calculation.

Next, a series of $n+1$ layers of equal width s with density ρ_j are considered. The 0^{th} and n^{th} layers are assumed to be semi-infinite with a rightward travelling wave propagating along the x-direction from $-\infty$ to $+\infty$ at right-angles to the layers. Consequently, the first boundary is located at $x = 0$ and the final boundary is at $x = (n-1)s$. Due to the change in density between the layers, there will be a reflected wave created at the boundaries. The transmission and reflection coefficients in the j^{th} layer are T_j and L_j respectively, such that the total wave is,

$$P = \sum_{j=0}^{n} T_j W_j(k_j s) + L_j W_j(-k_j s)$$

By ensuring that the pressure and particle velocity are continuous at each boundary, $2n$ simultaneous equations for the transmission and reflection coefficients are obtained and can be solved exactly,

$$\begin{aligned} T_j W_j(js) + L_j W_j(js) &= T_{j+1} W_{j+1}(js) + L_{j+1} W_{j+1}(js) \\ \frac{\partial}{\partial x}\big(T_j W_j(x) + L_j W_j(x)\big)\Big|_{x=js} &= \frac{\partial}{\partial x}\big(T_{j+1} W_{j+1}(x) + L_{j+1} W_{j+1}(x)\big)\Big|_{x=js} \end{aligned}$$

for all $j = 0, \ldots, n-1$.

For instance, with three layers in which the wavespeed and density in the j^{th} medium are $\mathcal{C}_j$ and ρ_j respectively, and the acoustic impedance is defined as $Z_j = \rho_j \mathcal{C}_j$,

$$\begin{aligned} 1 + L_0 &= T_1 + L_1 \\ T_1 W_1(s) + L_1 W_1(-s) &= T_2 W_2(s) \\ \frac{1}{Z_0}(1 - L_0) &= \frac{1}{Z_1}(T_1 - L_1) \\ \frac{1}{Z_1}\big(T_1 W_1(s) - L_1 W_1(-s)\big) &= \frac{T_2}{Z_2} W_2(s) \end{aligned}$$

It has also been assumed that $T_0 = 1$ and $L_2 = 0$, implying the incident amplitude equals 1 and there is no reflected wave after the final layer. Solving for T_2,

$$T_2 = \frac{4 W_1(s) W_2(-s) Z_1 Z_2}{W_1(2s)(Z_0 - Z_1)(Z_1 - Z_2) + (Z_0 + Z_1)(Z_1 + Z_2)} \tag{4.4.4}$$

Unfortunately it is not simple to prove a relationship between T_n in the n and the $n+1$ layer models since by adding a layer, another reflected wave is created that then affects all the previous transmission and reflection coefficients calculated previously due to the coupled nature of the problem. However, by looking at a succession of solutions for T_n, a general form is deduced,

$$T_n = \left(2^n \left(\prod_{i=1}^{n-1} W_i(s) Z_i\right) W_n\big((n-1)s\big)^{-1} Z_n\right) \Bigg/ \left(\sum_{x\in\mathcal{P}(S)} \left[\prod_{i\in x} W_i(2s) \prod_{j=1}^{n} \left(Z_{j-1} + (-1)^{f[j]} Z_j\right)\right]\right) \tag{4.4.5}$$

where $\mathcal{P}(S)$ is the *power set* of the set $S = \{1, \ldots, n\}$, and the function $f[j]$ is defined as,

$$f[j] = \begin{cases} 1 & \text{if } j \in i \text{ and } j-1 \notin i, \\ 0 & \text{otherwise.} \end{cases}$$

To make progress, linearisation about the value of the wavenumber in water k is conducted in order to understand the behaviour of the transmission coefficient for small perturbations of the medium. Therefore, the subsequent analysis is valid for dilute mixtures containing linearly behaving bubbles. For simplicity, it is also assumed that there are only two bubble types in the population and that the layers alternate from one type to the other. To correspond with clinical uses, it is also assumed that the two semi-infinite layers at the beginning and end of the layered structure are water. Consequently, the two wavenumbers for the bubbly layers given perturbations $\epsilon_1,\ \epsilon_2 \in \mathbb{C}$ and $|\epsilon_1| \ll 1, |\epsilon_2| \ll 1$, are,

$$\begin{aligned} k_1 &= k + \epsilon_1 \\ k_2 &= k + \epsilon_2 \end{aligned} \tag{4.4.6}$$

Using equation (4.3.31) for the effective wavenumber, denoting the resonance frequency and damping term for the j^{th} bubble in the population as ω_j and δ_j respectively,

$$k_{\text{eff}}^2 = k^2 + 4\pi\omega^2 \int_0^\infty \frac{R_j n(R_j) \mathrm{d}R_j}{\omega_j^2 - \omega^2 + 2i\delta_j\omega} \tag{4.4.7}$$

it is deduced that,

$$k_{\text{eff}} \approx k + \frac{\epsilon_1 + \epsilon_2}{2} + \frac{(\epsilon_1 - \epsilon_2)^2}{8k} + \mathcal{O}\left(\epsilon_1^3, \epsilon_1^2\epsilon_2, \epsilon_1\epsilon_2^2, \epsilon_2^3\right) \tag{4.4.8}$$

and from the definition of acoustic impedance, assuming that for low bubble concentrations $\rho_i \approx \rho$,

$$\begin{aligned} Z_1 = \rho_1 \mathcal{C}_1 &= \rho_1 \frac{\omega}{k_1} \\ &= \rho\omega \left(\frac{1}{k} - \frac{\epsilon_1}{k^2} + \frac{\epsilon_1^2}{k^3} \right) + \mathcal{O}\left(\epsilon_1^3\right) \\ &\approx Z \left(1 - \frac{\epsilon_1}{k} + \frac{\epsilon_1^2}{k^2} \right) \end{aligned} \tag{4.4.9a}$$

and similarly,

$$Z_2 = Z \left(1 - \frac{\epsilon_2}{k} + \frac{\epsilon_2^2}{k^2} \right) + \mathcal{O}\left(\epsilon_2^3\right) \tag{4.4.9b}$$

as well as,

$$Z_{\text{eff}} = Z \left(1 - \frac{\epsilon_1 + \epsilon_2}{2k} + \frac{1}{8k^2} \left(\epsilon_1^2 + 6\epsilon_1\epsilon_2 + \epsilon_2^2 \right) \right) + \mathcal{O}\left(\epsilon_1^3, \epsilon_1^2\epsilon_2, \epsilon_1\epsilon_2^2, \epsilon_2^3\right) \tag{4.4.9c}$$

An effective medium of length $D = (n-1)s$ composed of two bubble sizes such that their wavenumbers and impedances are given as above, is considered. By inserting $k_1 = k_{\text{eff}}$ and $Z_1 = Z_{\text{eff}}$ from (4.4.7) and (4.4.9c) into equation (4.4.4) and expanding about ϵ_1 and ϵ_2,

$$\begin{aligned} T_2 = 1 - \frac{iD}{2}(\epsilon_1 + \epsilon_2) + \frac{1}{16k^2} \left(\exp[-2iDk] - (1 + 2D^2k^2) \right) (\epsilon_1 + \epsilon_2)^2 - \frac{iD}{8k}(\epsilon_1 - \epsilon_2)^2 \\ + \mathcal{O}\left(\epsilon_1^3, \epsilon_1^2\epsilon_2, \epsilon_1\epsilon_2^2, \epsilon_2^3\right) \end{aligned} \tag{4.4.10}$$

Comparing this to the HS approach where alternating homogeneous layers of monodisperse layers are considered and substituting equations (4.4.6), (4.4.9a) and (4.4.9b) into (4.4.5), then expanding about ϵ_1 and ϵ_2, noting that the denominator of (4.4.5) is $\mathcal{O}\left(\epsilon_1^2, \epsilon_1\epsilon_2, \epsilon_2^2\right)$,

$$T_n = 1 - \frac{iD}{2}(\epsilon_1 + \epsilon_2) + \mathcal{O}\left(\epsilon_1^2, \epsilon_1\epsilon_2, \epsilon_2^2\right) \tag{4.4.11}$$

Unfortunately the denominator is too complicated to be able to arrive at an expression for the higher order term in the expression, but to first order, equations (4.4.10) and (4.4.11) are equal.

This linearisation work does, therefore, suggest that the homogeneous sheet method is a good approximation to the effective medium method when the mixture is dilute and the bubbles are much smaller than the incident wavelength, thus behaving linearly. Nevertheless, further numerical investigations are carried out to ascertain whether this conclusion is valid in the linear regime.

4.4.2 Numerical analysis of the transmission coefficient

It is useful to simulate equation (4.4.5) for different numbers of layers n, as well as varying the propagation distance. By analysing the magnitude of the transmission coefficient and comparing it to the value obtained by calculating (4.4.4) with $k_1 = k_{\text{eff}}$ and $Z_1 = Z_{\text{eff}}$, a value for the error involved in using the HS approximation is found.

For clinical applications of ultrasound contrast agents, representative parameters to use in the analysis are 2 MHz and a concentration of 4×10^{10} bubbles/m^3 (Gorce, Arditi and Schneider, 2000). For simplicity, the bubbles are assumed to be uncoated since the various coating models described in Section 3.2 could lead to the following analysis being too specific to a particular theory.

In the case of linearly behaving bubbles, figure 4.2 shows the magnitude of the transmission coefficient calculated using equation (4.4.5) for a population containing equal numbers of bubble sizes, 1 μm and 1.2 μm. There is little attenuation of the wave since the transmission coefficient is very close to 1. Additionally, there is agreement to within 4 decimal places between the HS and effective medium in figure 4.2(b). This figure also shows that the magnitude of the coefficient is decreasing on the long length scale but that there are small oscillations on the short length scale. Furthermore, using the HS approximation induces larger dips in the transmission coefficient suggesting a slight shielding effect in the bubbly medium. This phenomenon has been documented for the case of bubbles inside a sphere (Ye and Hsu, 2001) but has not been published elsewhere in the literature. With regards to modelling the full effective medium, this suggests that there may well be layer/distance parameter regimes for which the HS approximation underestimates the amplitude of the propagated wave and thus would be a very poor approximation. Overall though, agreement to within 4 decimal places does suggest an accurate approximation for linearly behaving bubbles.

Progressing to the case of a population containing equal numbers of bubbles of size 1.5 μm and 1.9 μm, where the 1.9 μm bubble is close to resonance, figure 4.3 shows that the difference between the two approaches is much greater. There does appear to be some small qualitative agreement at short propagation distances, but as the width of the bubbly medium is increased, the value of the transmission coefficient bears no resemblance to the effective medium value and it can be concluded that the HS approximation is poor when there is a large proportion of resonant bubbles in the population.

(a) Transmission coefficient ratio

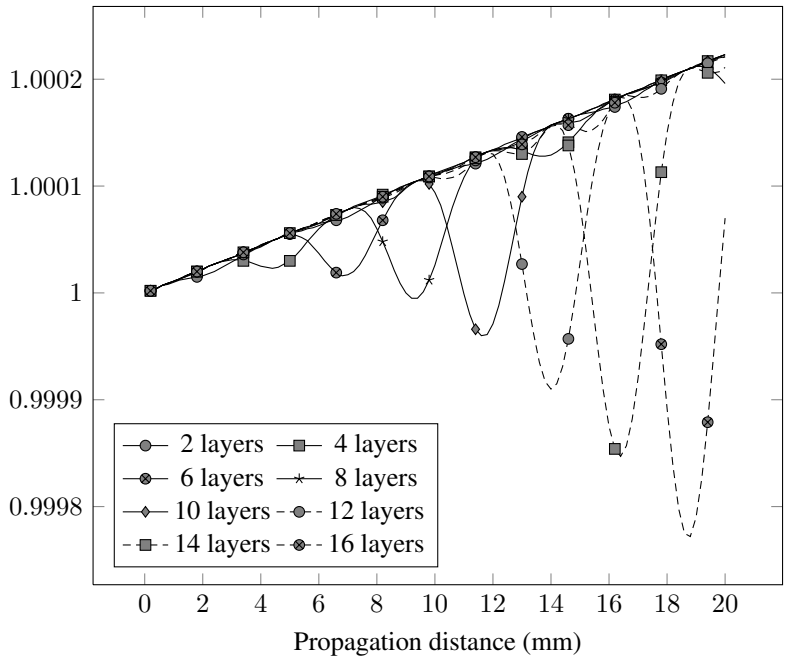

(b) Transmission coefficient

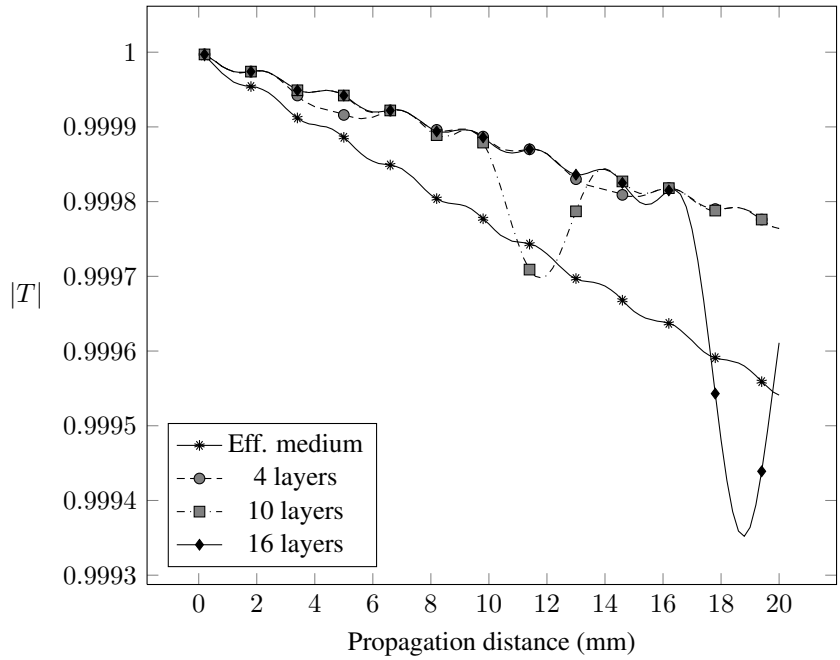

Figure 4.2: The amplitude of the transmission coefficient plotted against propagation distance through the bubbly medium, for bubble sizes $1\,\mu$m and $1.2\,\mu$m and concentration 4×10^{10} bubbles/m^3. Not all points have been marked and the oscillatory behaviour is as shown here. Subfigure (a) shows the ratio between the HS approximation and the effective medium approach: a value of 1 would indicate perfect agreement. In subfigure (b), the absolute value of the coefficients is plotted. Agreement between the two approaches to four decimal places suggests that the HS approximation is valid for linearly behaving bubbles.

(a) Transmission coefficient ratio

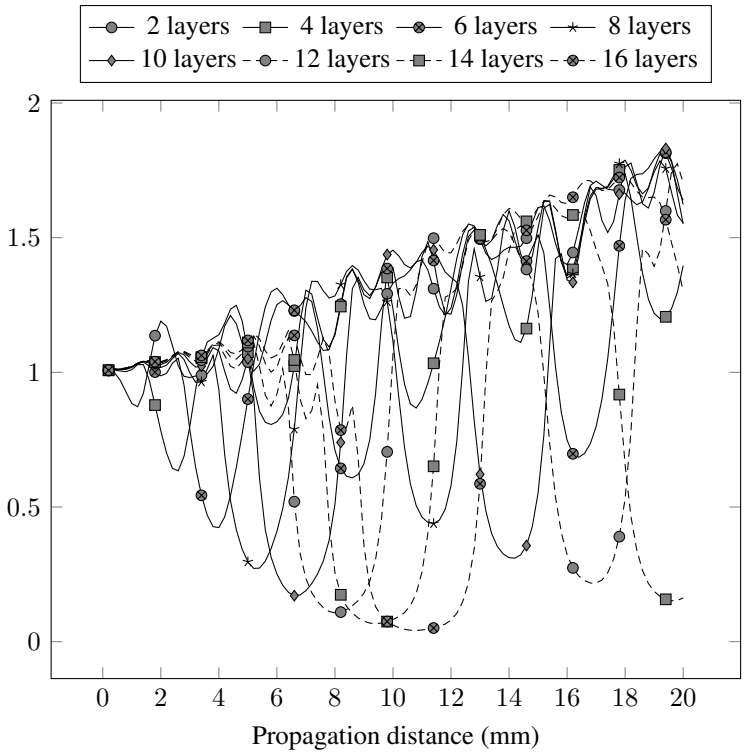

(b) Transmission coefficient

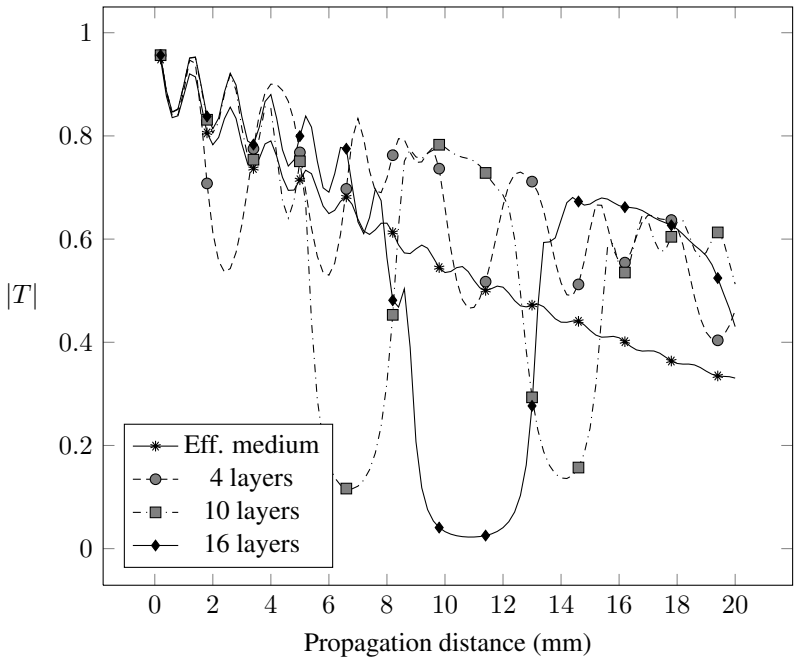

Figure 4.3: The amplitude of the transmission coefficient plotted against propagation distance through the bubbly medium, for bubbles of size $1.5\,\mu$m and $1.9\,\mu$m and concentration 4×10^{10} bubbles/m^3. Not all points have been marked and the oscillatory behaviour is as shown here. In subfigure (a), the error increases with distance and is larger than for linearly behaving bubbles. The oscillatory behaviour and dips in the transmission coefficient are present again in (b) but the deviation from the effective medium value is significantly greater.

(a) Transmission coefficient ratio

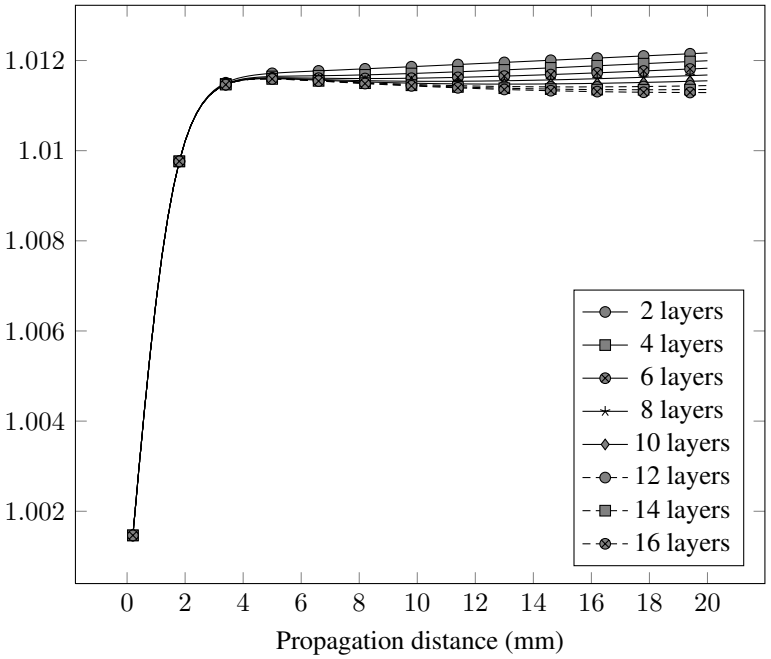

(b) Transmission coefficient

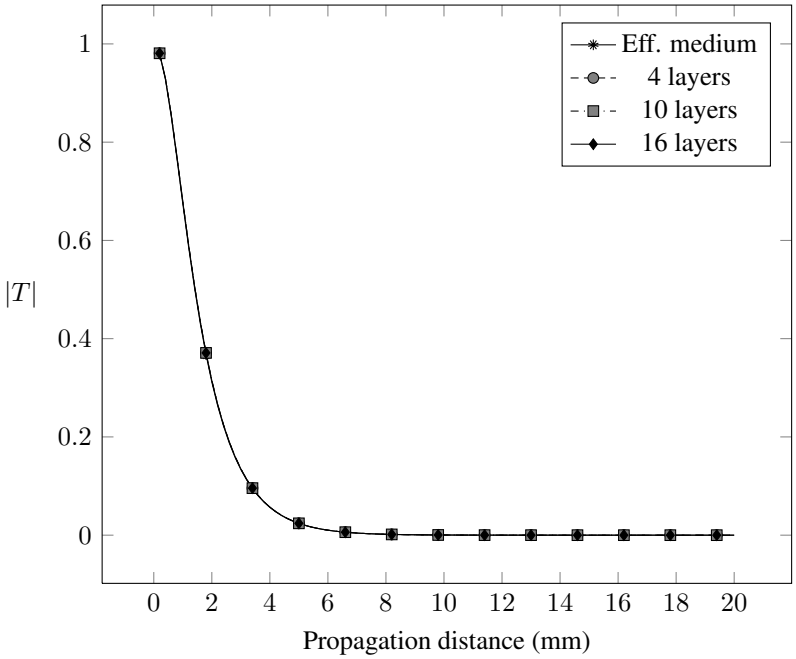

Figure 4.4: The amplitude of the transmission coefficient is plotted against propagation distance through the bubbly medium, for bubbles of size $3\,\mu$m and $4\,\mu$m and concentration 4×10^{10} bubbles/m^3. Not all points have been marked in the plot. Subfigure (b) shows high attenuation in this regime whilst (a) suggests that the HS approximation is accurate over long propagation distances.

In addition, the case of a bidisperse population containing equal numbers of $3\,\mu$m and $4\,\mu$m bubbles, which are larger than resonance, is investigated. In figure 4.4, the accuracy of the HS approach is much improved over the resonant bubble case considered previously. In fact, figure 4.4(a) suggests that the HS approach tends to a value that over-estimates the amplitude by 1% as the number of layers is increased. Despite the fact that the bubbles are unlikely to be oscillating linearly, it does suggest that the HS approximation is valid at bubble sizes far from resonance.

These results are now compared with the nonlinear propagation model given by the solution of equation (4.4.2). The aim is to validate the code with the analytical theory and to establish whether there could exist any high/low attenuation parameter regimes as seen in figures 4.2 to 4.4. To that end, figure 4.2 is replicated using the numerical scheme where the 12 layer approach has been used as well as the full homogeneous sheet approximation where at each point a bubble is chosen at random from the sample.

Firstly, there is good agreement in figure 4.5(a) to within 4 decimal places for the analytical calculations and within 3 decimal points for the numerical simulations in figure 4.5(b). The trend is for greater attenuation with distance in both instances, with a small oscillatory behaviour on the shorter length scale. Additionally, both suggest the layered medium underestimates attenuation compared with the effective medium. The full HS approach, where the bubble size at each mesh point is chosen at random from a probability distribution defined by the size distribution, leads to better agreement with the full summation although whether the approximation under- or over-estimates seems arbitrary and is likely due to the random selection of bubble sizes from the population. These results suggest that care must be taken when choosing bubbles at each point that the mesh is not in some way periodic. For the purposes of this simulation, there were approximately 2500 spatial points in the mesh and only 2 bubble sizes thus it can be assumed that not only was the bubble distribution well approximated, but that it is unlikely that there was any periodic behaviour that could lead to results such as in figure 4.5(a).

From the numerical analysis in this section, increasing the number of layers does not necessarily increase the accuracy of the HS approximation. In fact, the bubbles can form a *shield* to the propagation of the acoustic wave, a phenomenon that is not present in the effective medium case and is due to the interaction of the waves as they reflect off the various boundaries

(a) Analytical

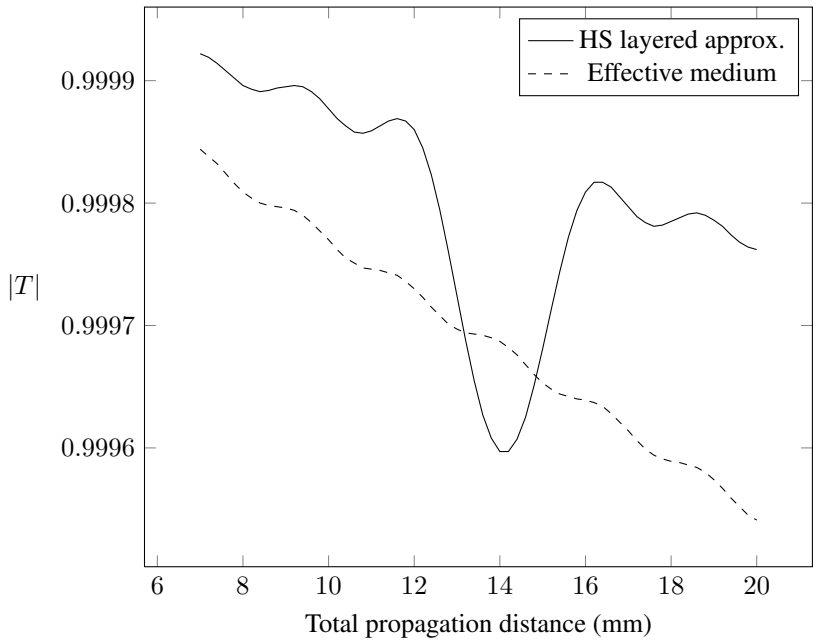

(b) Numerical

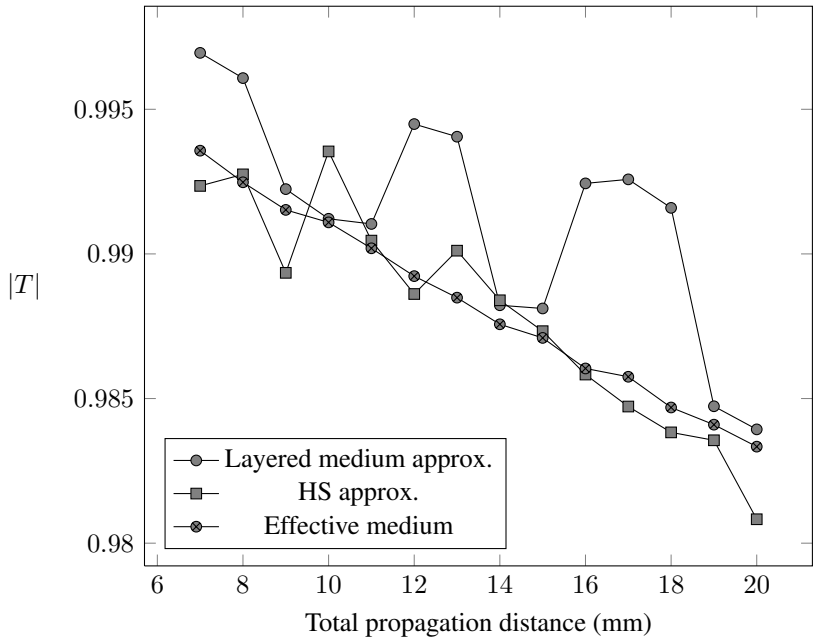

Figure 4.5: Comparison between the analytical approximation of equation (4.4.5) and the numerical approach of equations (4.4.2) and (4.4.3). In subfigure (a), the case of a population of 2 bubble sizes with radius 1 µm and 1.2 µm is simulated in the case where the medium is approximated as 12 layers. In subfigure (b) the same scenario is again considered but the numerical code is used. The *partially* homogeneous sheet approximation of 12 layers is also compared with the *fully* homogeneous case where the bubbles at each point in the mesh are chosen at random from a probability distribution defined by the size distribution.

in the medium. In the case of linearly oscillating bubbles, increasing the number of layers appears to increase the importance of this shielding effect whilst simultaneously requiring the wave to propagate further through the medium before this effect occurs. Furthermore, increasing the propagation distance did lead to worse agreement. Nevertheless, there was good numerical agreement and it can be concluded that the approximation is valid for a linearly behaving bubble population.

When the bubbles are larger than resonance, the attenuation effect is so great that there seems to be little difference between the two approaches, both when considering the number of layers and the propagation distance. However, when half the population is resonant, this analysis shows that the HS approximation does not accurately replicate the effective medium approach. Consequently, this scheme should not be used when there is a high proportion of resonant microbubbles in the population.

4.4.3 Numerical comparisons between homogeneous sheet and full summation

The linear analytical approach employed in the previous section is limited in the conclusions that can be drawn about the behaviour of the approximation scheme because in the majority of medical applications, the population is sufficiently polydisperse that there are some bubbles resonating. Furthermore, the approach employed by Hibbs et al. (2007) was to choose the bubble sizes at each point in the mesh from the distribution randomly, rather than specifying that they should alternate uniformly. Therefore, this section investigates by numerical comparison, agreement between the full summation and the HS approximation for different parameters. A regime of validity is established for certain parameters within which it is concluded that HS is a valid simplification of the full problem, and outside of which its accuracy is doubtful.

The parameter regimes investigated are relevant to medical applications. The incident pressures modelled vary from $0.1\,\mathrm{kPa}$ to $200\,\mathrm{kPa}$ for an 8-cycle sinusoid pulse at $2\,\mathrm{MHz}$ propagating $2\,\mathrm{cm}$ through the bubbly medium, whilst the concentration is varied from $10^{10}\,\mathrm{bubbles/m^3}$ to $10^{12}\,\mathrm{bubbles/m^3}$. Two types of bubble population are used: a bidisperse population containing two bubbles of different sizes to investigate the effect of resonance on accuracy; a SonoVue®-style bubble distribution where the number of bins used to simulate the population is varied in order to provide a lower bound for the bin number needed to accurately replicate SonoVue®.

The outputs compared are the values of the sub-, fundamental and second harmonics as well as the total energy in the propagated wave E calculated by integrating the total power P over the time of the pulse T across a surface area A which, without loss of generality equals one,

$$\begin{aligned} E &= \int_0^T P \mathrm{d}t \\ &= \int_0^T \frac{A(p-p_0)^2}{\rho \mathcal{C}} \mathrm{d}t \\ &= \frac{1}{\rho \mathcal{C}} \int_0^T (p-p_0)^2 \mathrm{d}t \end{aligned}$$

Good agreement between the full approach and any other approximation for all of these values would suggest a valid simplification of the problem. To establish this accuracy, a standard, "true", value is chosen to be the correct answer at any particular concentration and pressure. Thus, the percentage error in the output of the numerical approach test(p, x) at a particular concentration and pressure p for some value x, using true(p, X) as the "correct" answer, where X may or may not be kept constant, is calculated as,

$$\% \text{ error} = \left(\frac{\text{test}(p, x)}{\text{true}(p, X)} - 1 \right) \times 100$$

4.4.3.1 Bidisperse populations

Following on from the previous section, populations containing equal proportions of two bubble sizes are investigated, in which both bubbles are: smaller than resonance; one is close to resonance, the other smaller than resonance; larger than resonance. The aim is to establish general conclusions about the validity of the model when some bubbles are resonating.

Wave propagation using varying incident pressures through populations of different concentrations are simulated using both HS and full summations and the error ratio between the two approaches for the different size distributions $n(R)$ plotted,

$$\% \text{ error} = \left(\frac{\text{HS}\big(p, n(R)\big)}{\text{full}\big(p, n(R)\big)} - 1 \right) \times 100$$

Bubbles smaller than resonance

The population simulated has bubble sizes of $1\,\mu$m and $1.2\,\mu$m in equal proportion, which at an incident frequency of $2\,$MHz are below resonant size.

At low pressures, bubbles of this size should behave linearly and it may be expected that the two approaches would yield similar results. This is indeed the case at low concentrations where figures 4.6 and 4.7 show agreement to within a few percentage points for the energy content, sub-, fundamental and second harmonics of the propagated signal. Increasing the pressure of the incident wave does not have a large effect on the error in any of the measured quantities. On the other hand, at concentrations larger than 10^{11} bubbles/m^3, there is a large error between the HS and full methods. In fact, at the very highest concentration modelled, the propagated signal strength is particularly weak thus any discrepancy between the absolute values would greatly exaggerate the percentage error.

One size of bubble close to resonance

The bubble population simulated has equal numbers of $1.5\,\mu$m and $1.9\,\mu$m bubbles, which at 2 MHz means that the $1.9\,\mu$m bubble is close to resonance.

Where a large proportion of the bubbles within the population is resonant, there is much worse agreement between the two methods. Even at lower concentrations, figure 4.8(a) shows an error of about 30% between the two methods in the energy content of the signal. In addition, figure 4.9(a) shows particularly poor agreement in the fundamental content at higher concentrations in the mid-range of pressures modelled. However, this trend did not continue at higher pressures.

Bubbles larger than resonance

The bubble population in this simulation contains bubbles of $3\,\mu$m and $4\,\mu$m in equal number, which are larger than resonance.

When the bubbles are large relative to the resonant size, the result of good agreement at low concentrations is once again recovered in figures 4.10 and 4.11. However the error at higher concentrations is much worse than in the case of two bubbles smaller than resonance, which may be a symptom of the bubbles' nonlinearity. The errors in figures 4.10(a) and 4.11(a) at high concentration are in the order of hundreds of percent and the error in the second harmonic in figure 4.11(b) is above 10%. There does seem to be a trend in the sub- and second harmonic in figures 4.10(b) and 4.11(b) where agreement worsens with incident pressure, however this is not repeated in the analysis of the energy and fundamental frequency of the propagated signal.

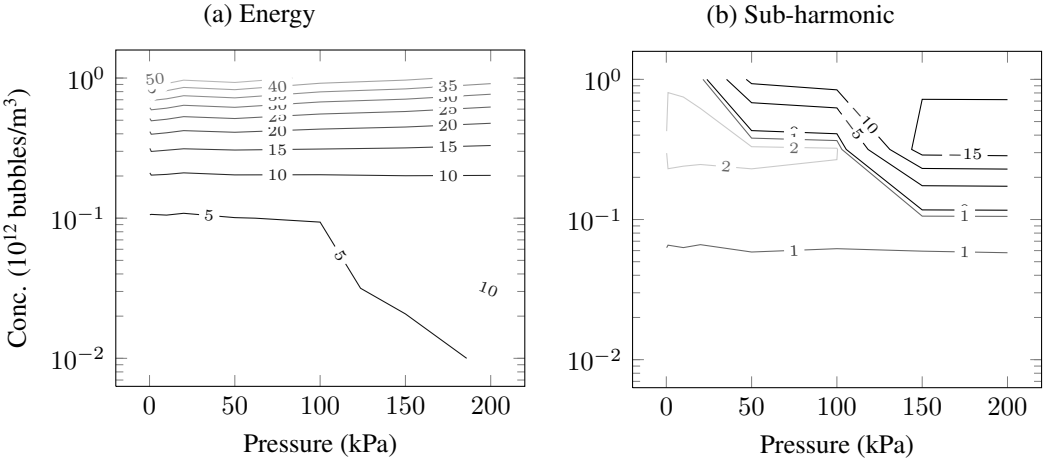

Figure 4.6: Comparison between HS and full summation methods where the contours show the percentage error between the two for the total energy and sub-harmonic content in the propagated signal. The population consists of 1 µm and 1.2 µm bubbles in equal number and the incident pulse is an 8-cycle Gaussian sinusoid at 2 MHz.

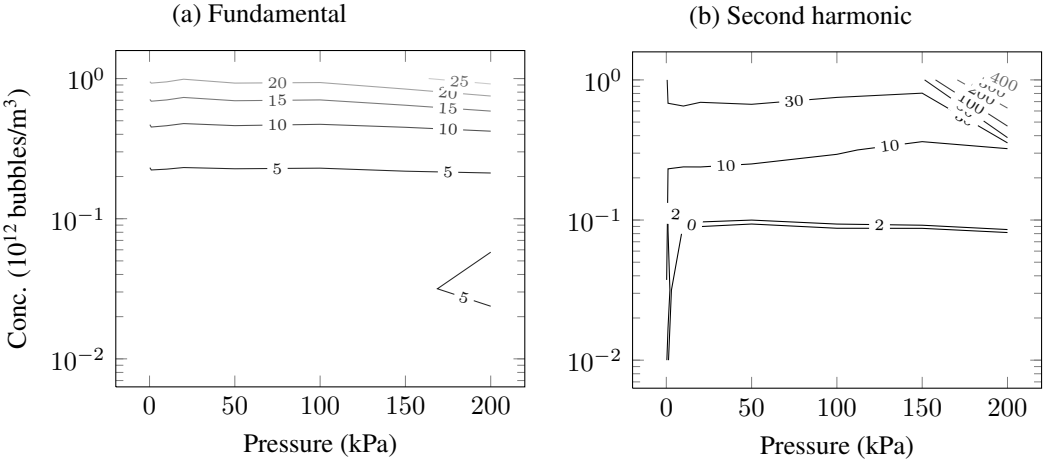

Figure 4.7: Comparison between HS and full summation methods where the contours show the percentage error between the two for the fundamental and second harmonic content in the propagated signal. The population consists of 1 µm and 1.2 µm bubbles in equal number and the incident pulse is an 8-cycle Gaussian sinusoid at 2 MHz.

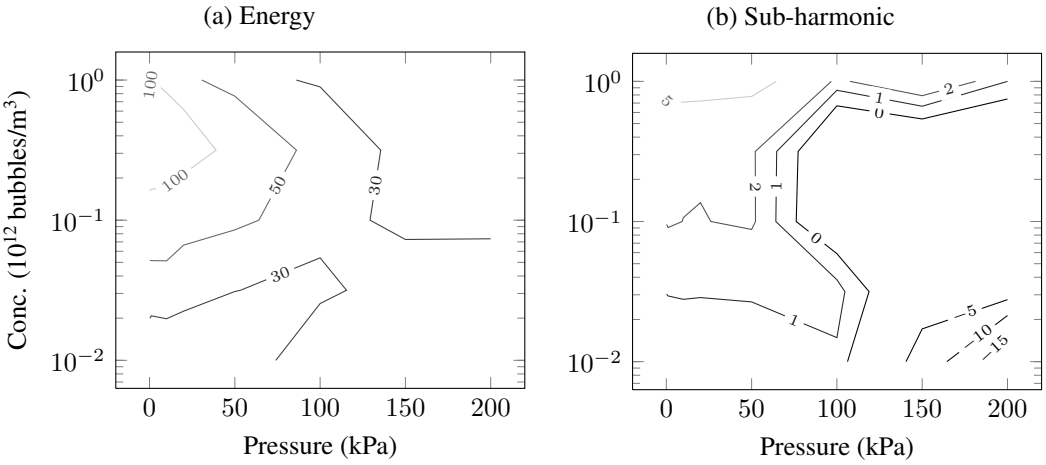

Figure 4.8: Comparison between HS and full summation methods where the contours show the percentage error between the two for the total energy and sub-harmonic content in the propagated signal. The population consists of 1.5 µm and 1.9 µm bubbles in equal number and the incident pulse is an 8-cycle Gaussian sinusoid at 2 MHz.

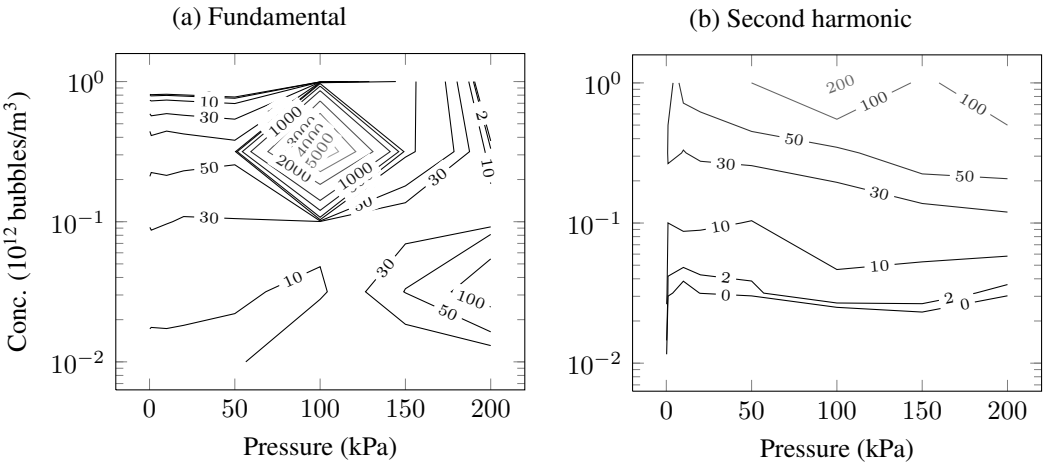

Figure 4.9: Comparison between HS and full summation methods where the contours show the percentage error between the two for the total fundamental and second harmonic content in the propagated signal. The population consists of 1.5 µm and 1.9 µm bubbles in equal number. For an 8-cycle Gaussian sinusoid at 2 MHz, the 1.9 µm bubble is close to resonance.

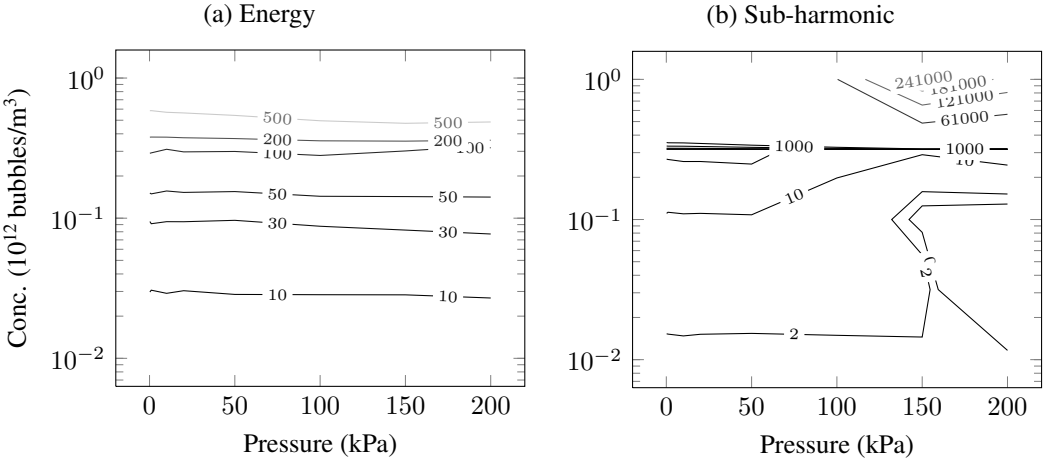

Figure 4.10: Comparison between HS and full summation methods where the contours show the percentage error between the two for the total energy and sub-harmonic content in the propagated signal. The population consists of 3 µm and 4 µm bubbles in equal number and the incident pulse is an 8-cycle Gaussian sinusoid at 2 MHz.

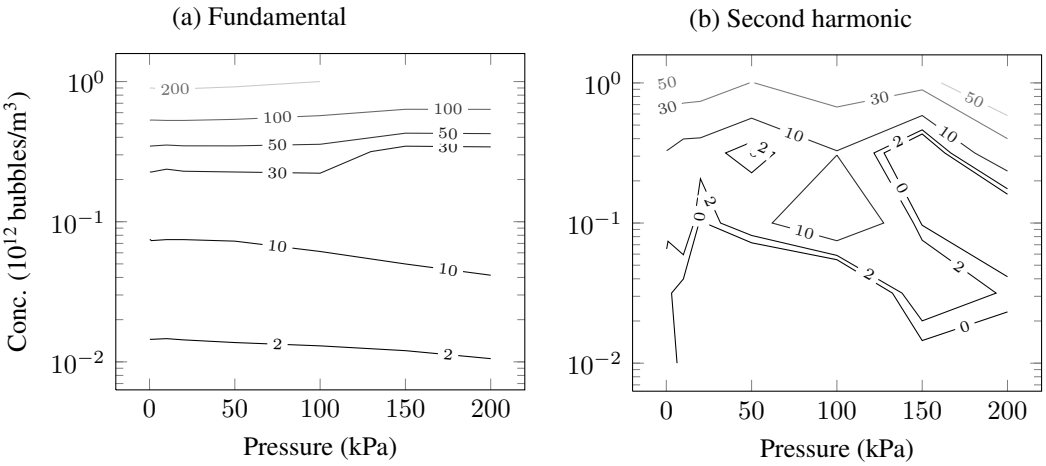

Figure 4.11: Comparison between HS and full summation methods where the contours show the percentage error between the two for the total fundamental and second harmonic content in the propagated signal. The population consists of 3 µm and 4 µm bubbles in equal number and the incident pulse is an 8-cycle Gaussian sinusoid at 2 MHz.

4.4.3.2 SonoVue® population

SonoVue® is a commercially available lipid-coated microbubble contrast agent. To ensure that this research is as applicable to clinical situations as possible, the HS approximation and full summation for this population are compared. The population distribution used in this work was obtained from Gorce, Arditi and Schneider (2000) and the parameters varied are the pressure, concentration and number of radius size "bins" used to discretise the distribution, corresponding to changing N in equation (4.4.2). The size of bubble in each layer of the HS approximation is chosen at random from the population. This section is particularly concerned with increasing numerical efficiency, so bin numbers used in the computation are 10, 15, 20, 25, 30 and 37. Not only is accuracy between HS and the full approach investigated, but also how few bins are required such that the full summation is of a reasonable accuracy. Obtaining results to both of these issues will help to improve computational efficiency.

The "true" value used is the result obtained modelling the SonoVue® population with the full summation and 37 radius bins. Thus, when conducting a test at a particular concentration, the percentage error using N bins to discretise the population is,

$$\% \text{ error} = \left(\frac{\text{test}(p, N)}{\text{true}(p, 37)} - 1 \right) \times 100$$

High concentration: 10^{12} bubbles/m^3

SonoVue® is prepared by mixing the solution and agitating. Typically, the concentrations at this point will be at least of the order of 10^{12} bubbles/m^3. Thus the simulation is run at this concentration using bin and pressure values discussed previously.

The total energy in the propagated wave when using the full summation is very close to the reference value, as long as the number of bins is greater than about 20. In fact, figure 4.12(a) demonstrates that agreement in this regime is within 1% of the reference value over a wide range of pressures and within 4% when using fewer bins.

Similarly, figure 4.13(a) shows the sub-harmonic content of the signal agrees well with the reference value, particular when the number of bins is greater than 20 once again. When using fewer bins, the error is still less than a few percent.

Agreement between the HS approximation and the reference value is not as consistent. Figure 4.12(b) shows the ratio between the energy propagated through the bubbly medium using the HS approach and using the full summation. Agreement with a small number of radius bins is particularly poor in this case and can be as different as 13% or more. There

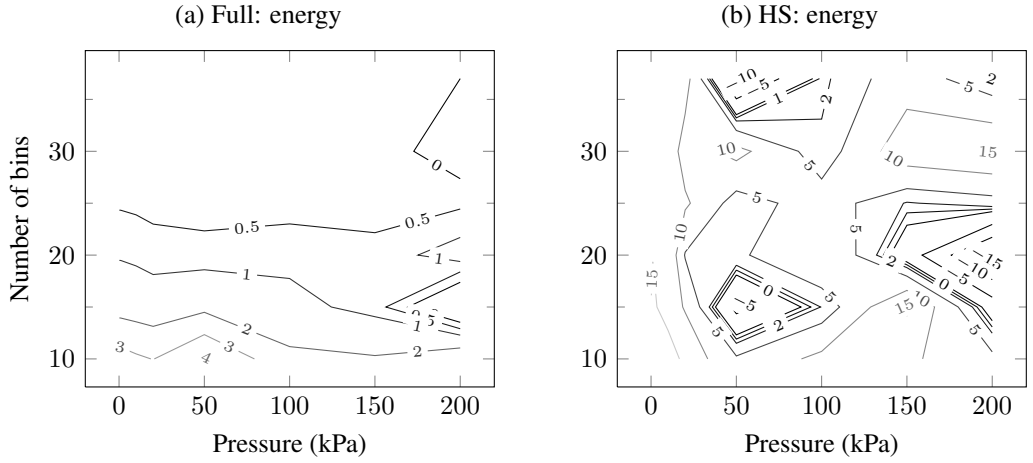

Figure 4.12: Comparison between the full summation approach in subfigure (a) and the homogeneous sheet approach in subfigure (b), with the full summation using 37 radius bins. The number of bins and incident pressure are varied and the percentage error in the total propagated energy plotted in the contours. Bubble concentration is 10^{12} bubbles/m^3 and the incident pulse is an 8-cycle Gaussian sinusoid at 2 MHz.

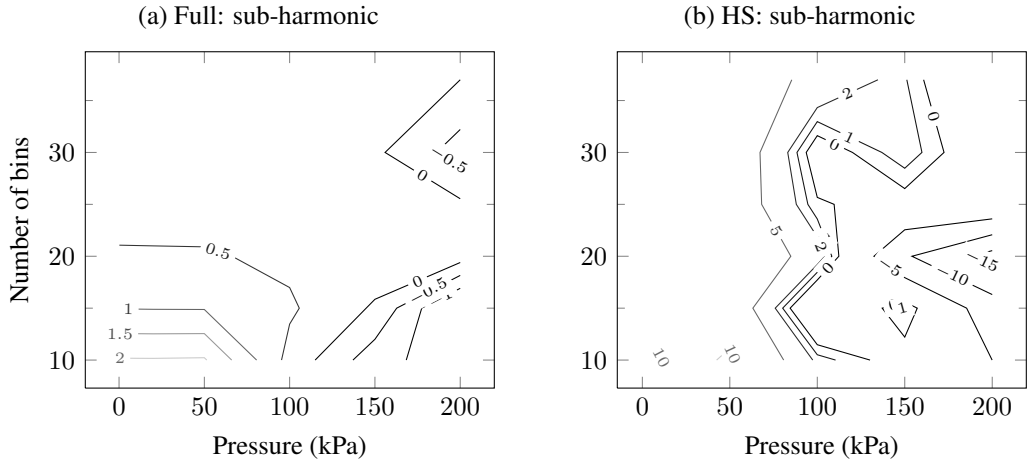

Figure 4.13: Comparison between the full summation approach in subfigure (a) and the homogeneous sheet approach in subfigure (b), with the full summation using 37 radius bins. The number of bins and incident pressure are varied and the percentage error in the sub-harmonic amplitude in the propagated wave plotted in the contours. Bubble concentration is 10^{12} bubbles/m^3 and the incident pulse is an 8-cycle Gaussian sinusoid at 2 MHz.

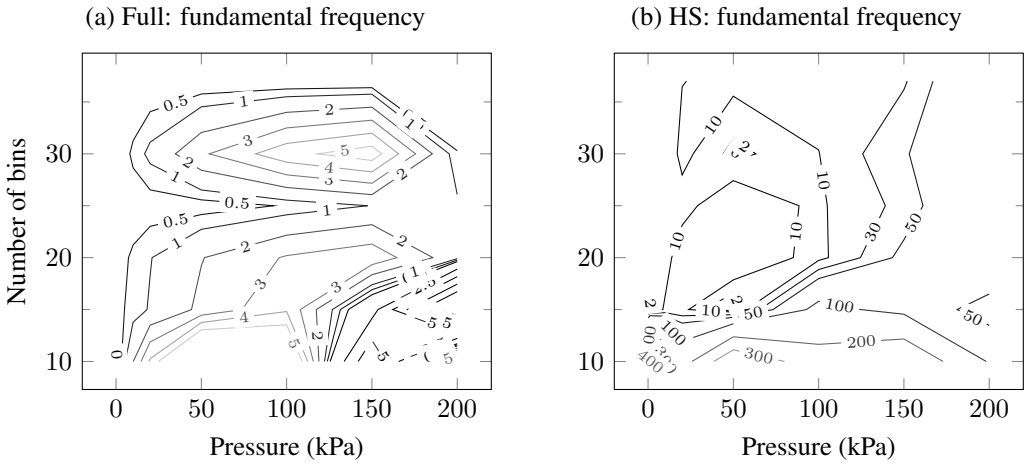

Figure 4.14: Comparison between the full summation approach in subfigure (a) and the homogeneous sheet approach in subfigure (b), with the full summation using 37 radius bins. The number of bins and incident pressure are varied and the percentage error in the amplitude of the fundamental frequency in the propagated wave plotted in the contours. Bubble concentration is 10^{12} bubbles/m^3 and the incident pulse is an 8-cycle Gaussian sinusoid at 2 MHz.

appears to be no consistent trend with increasing the number of bins although it does appear that increasing the pressure leads to a smaller error.

In the same vein, figure 4.13(b) shows a moderate improvement in the sub-harmonic error in the propagated signal as the number of bins is increased. Furthermore, unlike the signal energy, there appears to be a larger error at higher pressures and when using fewer bins.

Comparing the higher harmonics in the propagated signal when using the full summation, figure 4.14(a) shows better agreement in the fundamental frequency with the reference values as the number of bins is increased, being within 2% for most simulations. Additionally, increasing the pressure leads to a larger error, particularly at higher pressures.

A similar trend is apparent in the second harmonic content of the signal as visible in figure 4.15(a). Agreement is within a few percentage points when the number of bins is greater than about 25 and again, worsens as incident pressure increases.

Additionally, the HS approximation performs poorly compared with the reference values. The content of the fundamental frequency in figure 4.14(b) shows a very large error except at low pressures and a high bin number. Agreement is particularly poor when the pressure approaches and exceeds 100 kPa.

The trend is even more pronounced in the second harmonic content of the signal. In figure 4.15(b), the error in the HS approximation is more than 10% compared with the reference signal for all the trials except the smallest incident pressures.

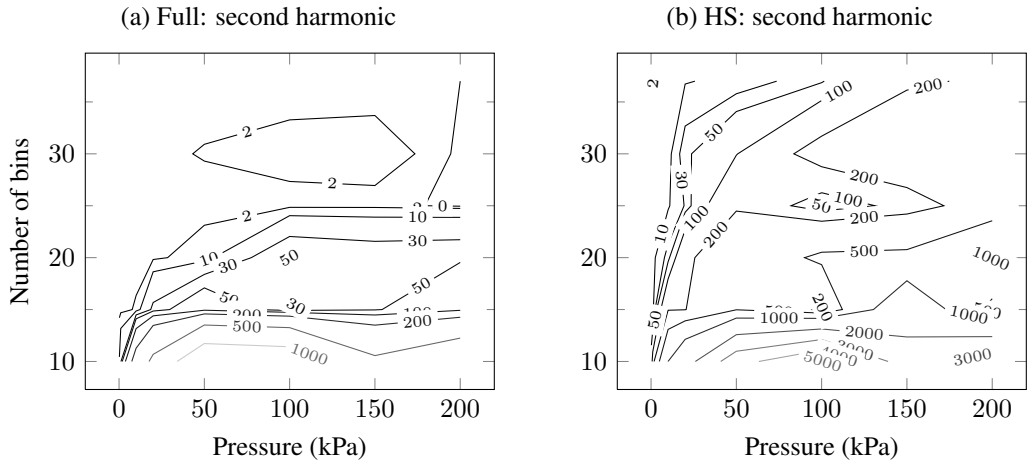

Figure 4.15: Comparison between the full summation approach in subfigure (a) and the homogeneous sheet approach in subfigure (b), with the full summation using 37 radius bins. The number of bins and incident pressure are varied and the percentage error in the amplitude of the second harmonic in the propagated wave was plotted in the contours. Bubble concentration is 10^{12} bubbles/m^3 and the incident pulse is an 8-cycle Gaussian sinusoid at 2 MHz.

Medium concentration: 10^{11} bubbles/m^3

After initial injection into the body, the concentration is likely to drop quickly as the contrast agent dilutes in the patient's blood. The results for simulations using a concentration of 10^{11} bubbles/m^3 are presented in this section.

At a lower concentration, the total propagated energy using the full summation is within 10% in figure 4.16(a) of the "true" value as long as more than about 30 bins are used to model the bubble population. Interestingly the accuracy improves as pressure increases.

In the same vein, the amplitude of the sub-harmonic in figure 4.17(a) is within 2% for a range of pressures and radius bins. This is encouraging although it has to be noted that there is very little sub-harmonic present in the propagated signal in these particular simulations.

On the other hand, the HS approximation performs much worse. For instance, the energy in the propagated wave is outside any reasonable range of accuracy as shown in figure 4.17(b). In fact, the error is never smaller than 60% for the parameter regimes investigated.

Conversely, the sub-harmonic content of the signal in the HS approximation is within 5% for a wide range of pressures and bin number, though it should be noted again that there is little sub-harmonic content in these pulses.

The error in the fundamental frequency amplitude in the propagated wave is particularly large even when using the full summation, as shown in figure 4.18(a). Using a relatively large

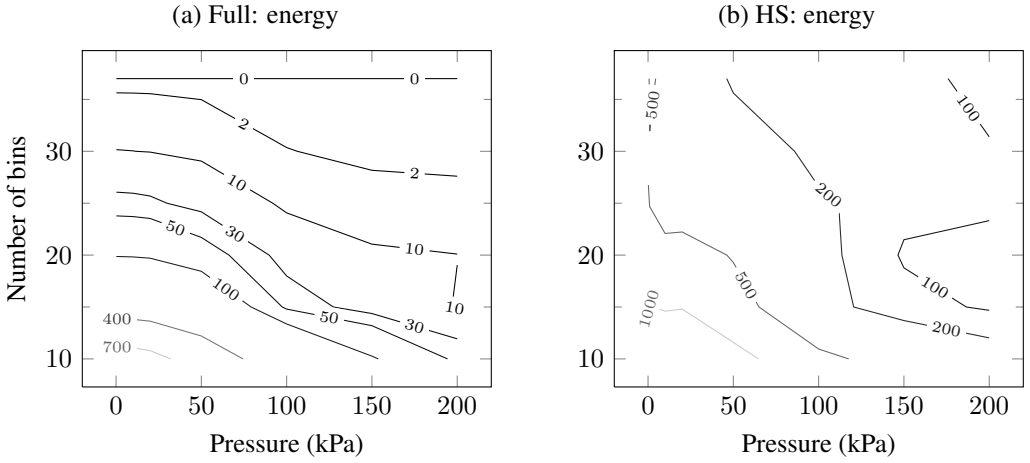

Figure 4.16: Comparison between the full summation approach in subfigure (a) and the homogeneous sheet approach in subfigure (b), with the full summation using 37 radius bins. The number of bins and incident pressure are varied and the percentage error in the total propagated energy plotted in the contours. Bubble concentration is 10^{11} bubbles/m^3 and the incident pulse is an 8-cycle Gaussian sinusoid at 2 MHz.

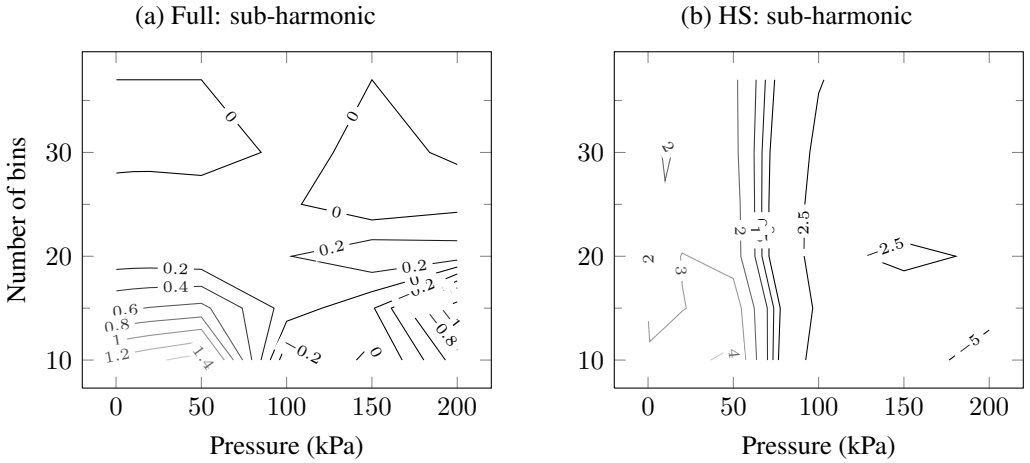

Figure 4.17: Comparison between the full summation approach in subfigure (a) and the homogeneous sheet approach in subfigure (b), with the full summation using 37 radius bins. The number of bins and incident pressure are varied and the percentage error in the sub-harmonic amplitude in the propagated wave plotted in the contours. Bubble concentration is 10^{11} bubbles/m^3 and the incident pulse is an 8-cycle Gaussian sinusoid at 2 MHz.

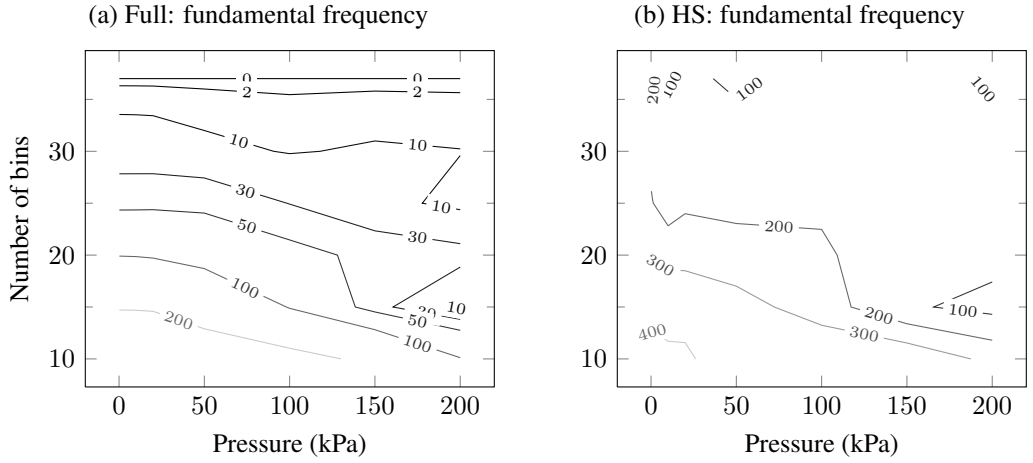

Figure 4.18: Comparison between the full summation approach in subfigure (a) and the homogeneous sheet approach in subfigure (b), with the full summation using 37 radius bins. The number of bins and incident pressure are varied and the percentage error in the fundamental amplitude in the propagated wave plotted in the contours. Bubble concentration is 10^{11} bubbles/m^3 and the incident pulse is an 8-cycle Gaussian sinusoid at 2 MHz.

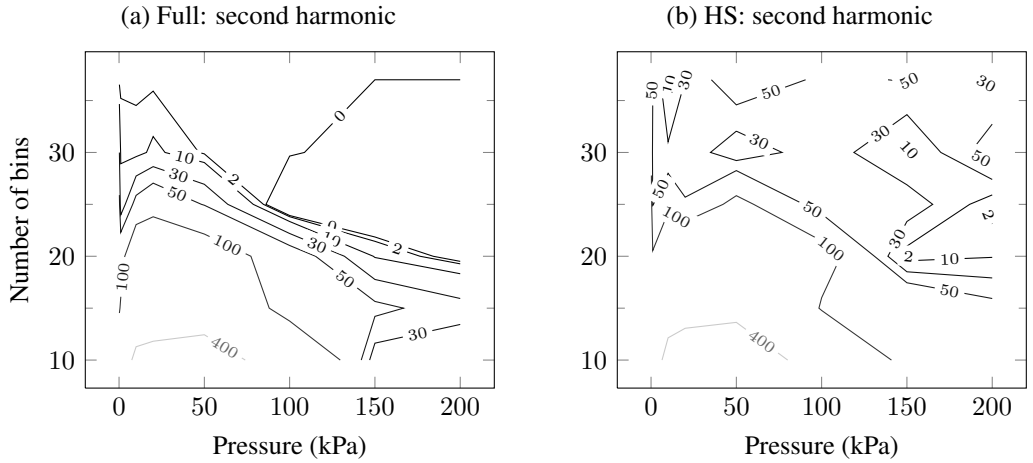

Figure 4.19: Comparison between the full summation approach in subfigure (a) and the homogeneous sheet approach in subfigure (b), with the full summation using 37 radius bins. The number of bins and incident pressure are varied and the percentage error in the second harmonic amplitude in the propagated wave plotted in the contours. Bubble concentration is 10^{11} bubbles/m^3 and the incident pulse is an 8-cycle Gaussian sinusoid at 2 MHz.

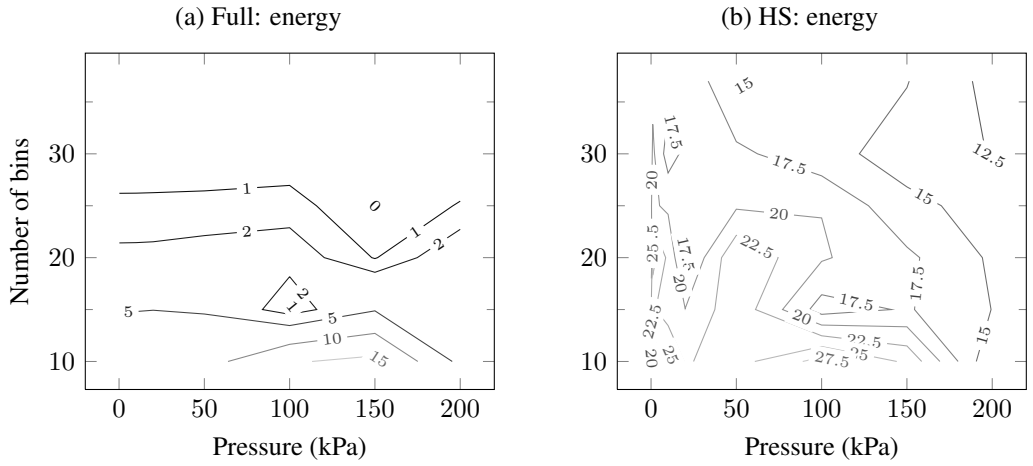

Figure 4.20: Comparison between the full summation approach in subfigure (a) and the homogeneous sheet approach in subfigure (b), with the full summation using 37 radius bins. The number of bins and incident pressure are varied and the percentage error in the total propagated energy plotted in the contours. Bubble concentration is 10^{10} bubbles/m^3 and the incident pulse is an 8-cycle Gaussian sinusoid at 2 MHz.

number of 30 bubble bins, the error is still around 20% at low pressures and 10% at higher pressures, compared with the reference value. Only when the number of bins is very close to the number used in the reference value can it be said that there is good agreement.

Conversely, the second harmonic in figure 4.19(a) shows much better agreement, particularly when the number of bubble bins used to model the distribution is about 30, leading to an error of less than 2%.

Again, the HS approximation performs poorly compared to the full summation, where the error in the fundamental frequency is of the order of 100% as seen in figure 4.18(b) and similarly the error is of the order 20%–50% in the second harmonic. The large errors in the signal components help to elucidate why the error in the total energy in figure 4.16(b) is so high. Clearly, if the energy within the main harmonics are different, then the total energy within the signal is also going to be different.

Low concentration: 10^{10} bubbles/m^3

Since the body contains approximately 5 litres of blood, once the contrast agent has had time to pass through the entire circulatory system, the concentration of microbubbles is likely to have dropped to at least 10^{10} bubbles/m^3. Hence further numerical analysis is conducted at this value.

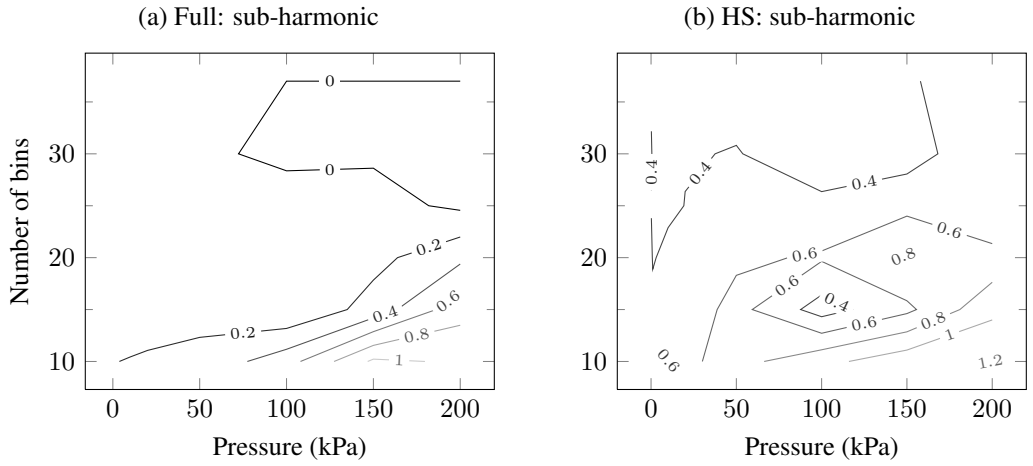

Figure 4.21: Comparison between the full summation approach in subfigure (a) and the homogeneous sheet approach in subfigure (b), with the full summation using 37 radius bins. The number of bins and incident pressure are varied and the percentage error in the sub-harmonic amplitude in the propagated wave plotted in the contours. Bubble concentration is 10^{10} bubbles/m^3 and the incident pulse is an 8-cycle Gaussian sinusoid at 2 MHz.

At a lower concentration, there is much better agreement in figure 4.20 between the energy in the propagated wave in the numerical tests and the reference value, compared with a concentration of 10^{11} bubbles/m^3 in figure 4.16. In fact, figure 4.20(a) shows the error is within 3% as long as at least about 20 radius bins are used in the full summation. The error also worsens as pressure increases particularly when using fewer bins, as one might expect, since nonlinearity has a greater effect on the propagated signal.

The HS approximation shows a similar improvement compared with the higher concentration, but the error is still particularly large at all pressures and bin numbers, as visible in figure 4.20(b). It is also interesting to note the way in which the error decreases as the pressure of the incident wave increases.

In both the full summation and HS approximation investigations, figure 4.21 shows agreement to within 1.5% at all pressures and bin numbers but again with the proviso that there is little sub-harmonic behaviour in these tests.

Once more, the error in the fundamental content of the propagated signal is much improved in figure 4.22, particularly in the full summation in figure 4.22(a) where the error across all pressures is less than 6% when the radius bin number is greater than about 20.

The smallest error apparent in the HS approximation is in the region of 10% even at low pressures, as seen in figure 4.22(b). Again the error improves as incident pressure increases.

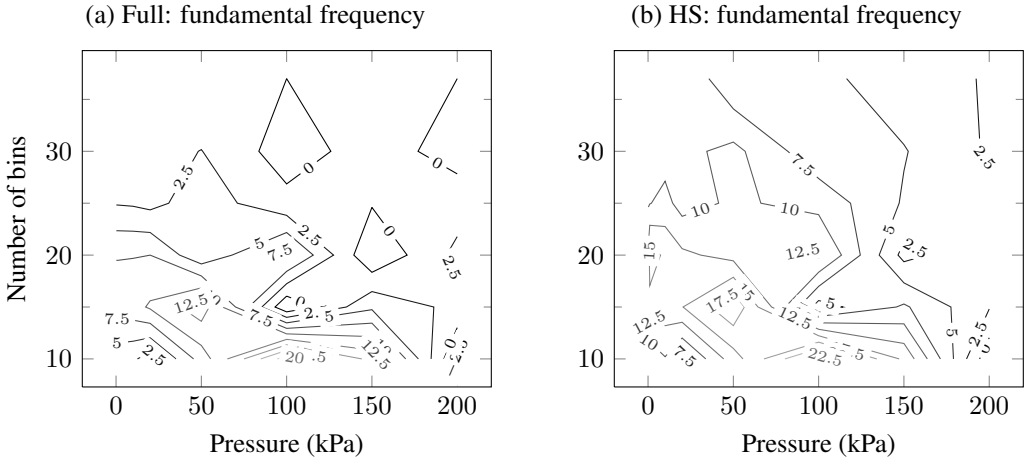

Figure 4.22: Comparison between the full summation approach in subfigure (a) and the homogeneous sheet approach in subfigure (b), with the full summation using 37 radius bins. The number of bins and incident pressure are varied and the percentage error in the fundamental frequency amplitude in the propagated signal plotted in the contours. Bubble concentration is 10^{10} bubbles/m^3 and the incident pulse is an 8-cycle Gaussian sinusoid at 2 MHz.

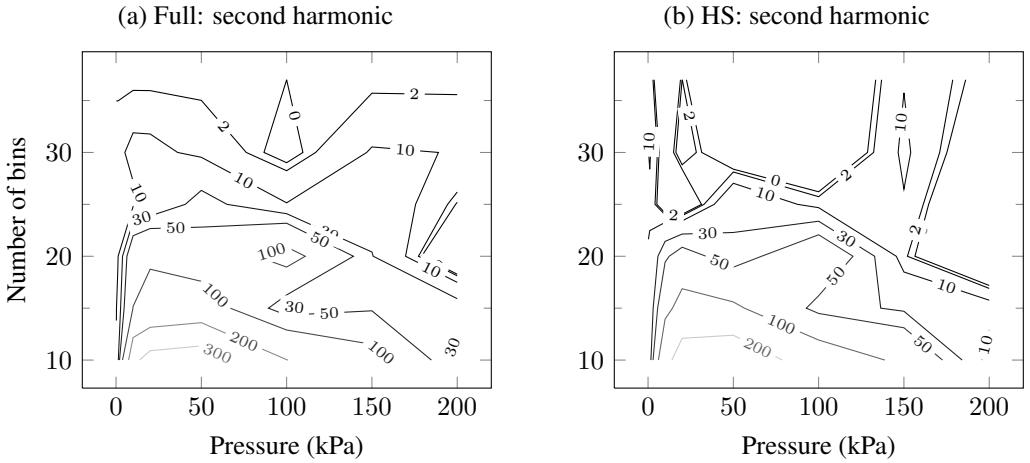

Figure 4.23: Comparison between the full summation approach in subfigure (a) and the homogeneous sheet approach in subfigure (b), with the full summation using 37 radius bins. The number of bins and incident pressure are varied and the percentage error in the second harmonic amplitude in the propagated wave plotted in the contours. Bubble concentration is 10^{10} bubbles/m^3 and the incident pulse is an 8-cycle Gaussian sinusoid at 2 MHz.

Furthermore, figure 4.23 shows that the full summation demonstrates particularly good agreement to within 10% in the second harmonic content when the number of bins used is greater than 30.

Moreover, there is also good agreement when using the HS approximation as noted in figure 4.22(b), when a bin number greater than about 25 leads to an error of less than 10%.

4.5 Summary

In this chapter, different scattering theories are examined and discussed. Particular attention is paid to the Caflisch nonlinear wave propagation model and its implementation with a finite difference scheme. This method is computationally expensive so ways of reducing its complexity are investigated, specifically the use of the homogeneous sheet approximation and varying the number of radius bins used to discretise a polydisperse bubble population.

The results of Section 4.4.3.1 suggest that when the bubble sizes are far from resonance, there is good agreement between the HS approximation and the full summation at the lower concentrations that would be found within the body after injection, specifically between 10^{10} and 10^{11} bubbles/m^3. However, if some of the population is resonant, agreement is poor.

This conclusion is supported by the results modelling SonoVue® in Section 4.4.3.2. The error in all quantities measured at low concentrations, apart from the sub-harmonic, is larger than 10% in most cases, even at the lowest pressures and when many radius bins are used to discretise the distribution. This seems surprising since perhaps only 10% of the population are resonant. However, this demonstrates the importance of the bubbles' behaviours within the population and how nonlinearity can negatively impact agreement between the two methods.

The results of varying the bin number in the full summation method, as investigated in Section 4.4.3.2, suggest that a minimum of around 30 bins should be used to obtain accuracy to within 10% for pressures in the range 0 to 200 kPa and concentrations from 10^{10} to 10^{12} bubbles/m^3. Naturally, the greater the number of bins used, the better the discretisation of the population and the more accurately it can be modelled. It is worth noting that there is more than one way in which to discretise a population of microbubbles. However, care was taken in this research to ensure a representative number of different bubble sizes are present, particularly resonant bubbles, even when using the fewest number of bins.

It appears that, by choosing only one bubble at each point, the HS approximation is failing to capture the full nonlinear interaction of the bubbles with the propagating wave. In particular,

when a sheet of bubbles is close to resonance, its behaviour interferes with neighbouring, potentially non-resonant, bubble sheets. This leads to unphysical behaviour and a deviation from the full summation method, ultimately causing poor performance between the two approaches.

In conclusion,

- The presence of resonant bubbles greatly reduces the accuracy of the HS approximation, even at low concentrations.
- Since the purpose of a contrast agent is to enhance echogenicity, particularly through the use of resonant bubbles, it seems that the HS approximation is a poor method of simplifying the computation in most cases.
- A minimum of 30 bins should be used in the full summation to ensure that the microbubble distribution is sufficiently discretised to accurately model the SonoVue® bubble population. This ensures reasonable accuracy across the range of pressures and concentrations tested in this work.

It is important to understand the computational challenges of modelling ultrasound propagation through bubble clouds and there have hitherto been no attempts to investigate the numerical efficiency of the nonlinear wave propagation model. The HS approximation has been used in published work but seen here to be an inaccurate approximation. Further work will unfortunately have to use the full summation method with a relatively fine discretisation of the size distribution, a numerically intensive task but one that ensures accurate modelling and with it, possible improvements in quantitative imaging techniques.

Having proposed a new model for the time-dependent behaviour of an individual contrast agent microbubble in an ultrasound field in Chapter 3, and investigated theories for the propagation of acoustic waves through bubbly media in this chapter, the following chapter combines these two ideas into a theory for modelling ultrasound wave propagation through a contrast agent suspension.

CHAPTER 5

NONLINEAR WAVE PROPAGATION MODEL INCLUDING DIFFUSION AND SURFACTANT SHEDDING

Chapter 4 introduced wave propagation theories that can be used to model an ultrasound pulse travelling through a bubbly mixture. For the purposes of modelling contrast agents, these models assume that the microbubbles' characteristics remain unchanged throughout the duration of the ultrasound scan. In light of the research in Chapter 3, it has been demonstrated that an individual lipid-coated microbubble's material properties are time-dependent, particularly when exposed to repeated ultrasound pulses. This contradicts the assumptions of a number of propagation models and is likely to impact the accuracy of quantitative imaging algorithms. Consequently, the final chapter of this thesis aims to combine the main themes and models explained previously to ultimately develop a nonlinear acoustic propagation model through a contrast agent suspension that includes gas diffusion into and out of the bubbles as well as a surfactant-shedding mechanism. The model is subsequently solved numerically and the results compared to experimental data.

5.1 Summary of the model

Since the constituent parts of the model have been explained and analysed in greater detail in previous chapters, only a brief summary of the model is presented here. The nonlinear propagation model for an acoustic wave travelling in a medium of density ρ with wavespeed $\mathcal{C}$ through a suspension of bubbles with size distribution $n(R)$, is that derived by Caflisch et al. (1985) in Section 4.3, viz.,

$$\frac{1}{\mathcal{C}^2}\frac{\partial^2 p}{\partial t^2} - \nabla^2 p = 4\pi\rho \int_0^\infty \left[R^2 \frac{\partial^2 R}{\partial t^2} + 2R\left(\frac{\partial R}{\partial t}\right)^2 \right] n(R_0)\mathrm{d}R_0 \tag{5.1.1}$$

where the radius of the bubble $R = R(R_0, t)$ containing air and PFC gas pressures p_b^{air} and p_b^{PFC} respectively, is found by simultaneously solving a Rayleigh-Plesset type equation using the surfactant-dependant surface tension $\sigma(\Gamma)$ from Section 3.4 and a constant shell viscosity μ_s,

$$R\ddot{R} + \frac{3\dot{R}^2}{2} = \frac{1}{\rho}\left(\left(p_b^{\text{air}} + p_b^{\text{PFC}}\right)\left(\frac{R_0}{R}\right)^{3\gamma} + p_v - \frac{2\sigma(\Gamma)}{R} - \frac{4\mu_l \dot{R}}{R} - \frac{4\mu_\text{s}\dot{R}}{R^2} - p_0 - p(t) \right) \tag{5.1.2}$$

These equations are solved jointly with convection-diffusion equations for the concentrations $c(r,t)$ of each gas and surfactant $C(r,t)$ in the bulk,

$$\frac{\partial c}{\partial t} + \frac{R^2\dot{R}}{r^2}\frac{\partial c}{\partial r} = \frac{D}{r^2}\frac{\partial}{\partial r}\left(r^2 \frac{\partial c}{\partial r}\right) \tag{5.1.3}$$

with the boundary condition for the concentration of gas on the bubble and rate of change of mass of gas m given by,

$$\frac{dm}{dt} = 4\pi R^2 D(\Gamma)\frac{\partial c(r=R,t)}{\partial r} \tag{5.1.4}$$

The concentration and mass of gas inside the bubble can be calculated knowing the volume of the bubble V using the ideal gas law and Henry's law with constant k_H,

$$pV = m\alpha \tag{5.1.5}$$

$$c = k_H p \tag{5.1.6}$$

where $\alpha \coloneqq GT/M$ for a gas of molar mass M at temperature T and the universal gas constant is G.

On the other hand, the differential equation governing the surfactant concentration $\Gamma(t)$ on the bubble surface with area A is,

$$\frac{d(A\Gamma)}{dt} = \Phi\big(\Gamma, C(r=R,t)\big) \tag{5.1.7}$$

with the boundary condition involving the kinetic expression for the surfactant Φ used previously in Section 3.4,

$$D_\text{s}\frac{\partial C(r=R,t)}{\partial r} = \Phi\big(\Gamma, C(r=R,t)\big) \tag{5.1.8}$$

$$\Phi\big(\Gamma, C(r=R,t)\big) = \begin{cases} A\left[a_1 C(r=R,t)\big(\Gamma^* - \Gamma\big) - a_2\Gamma\right] & \text{if } \Gamma < \Gamma^*, \\ 0 & \text{if } \Gamma^* < \Gamma < \Gamma_\text{max}, \\ \Gamma_\text{max}\dfrac{dA}{dt} & \text{if } \Gamma > \Gamma_\text{max}. \end{cases} \tag{5.1.9}$$

5.2 Numerical modelling

The equations (5.1.1) to (5.1.9) are solved simultaneously using an explicit finite difference scheme for the PDEs and a 4$^{\text{th}}$-order Runge-Kutta method for solving the Rayleigh-Plesset ODE, as described in Section 3.6 and equation (4.4.2). The derivatives are discretised in space j and time s using space- and time-lengths Δx and Δt respectively,

$$\begin{aligned}
\frac{\partial^2 p(x,t)}{\partial t^2} &\approx \frac{p_{j,s+1} - 2p_{j,s} + p_{j,s-1}}{(\Delta t)^2} \\
\frac{\partial^2 p(x,t)}{\partial x^2} &\approx \frac{p_{j+1,s} - 2p_{j,s} + p_{j-1,s}}{(\Delta x)^2} \\
\frac{\partial c(r,t)}{\partial t} &\approx \frac{c_{j,s+1} - c_{j,s}}{\Delta t} \\
\frac{\partial c(r,t)}{\partial r} &\approx \frac{c_{j+1,s} - c_{j-1,s}}{2\Delta r} \\
\frac{\partial^2 c(r,t)}{\partial r^2} &\approx \frac{c_{j+1,s} - 2c_{j,s} + c_{j-1,s}}{(\Delta r)^2}
\end{aligned}$$

The nonlinear wave equation (5.1.1) is approximated as,

$$\frac{p_{j,s+1} - 2p_{j,s} + p_{j,s-1}}{\mathcal{C}^2(\Delta t)^2} - \frac{p_{j+1,s} - 2p_{j,s} + p_{j-1,s}}{(\Delta x)^2} = 4\pi\rho \sum_{k=1}^{N} n(R_k)\Big[2R_k\dot{R}_k^2 + R_k^2\ddot{R}_k\Big]_{j,s-1} \tag{5.2.1}$$

for each bubble of size R_k in the population containing N initial bubble sizes. The convection-diffusion equation (5.1.3) is solved relative to the moving interface $x(t) = r - R(t)$,

$$\frac{\partial c(x,t)}{\partial t} + \boldsymbol{u}_{\text{rel}}\frac{\partial c(x,t)}{\partial x} = \frac{D}{(x+R)}\left(2\frac{\partial c(x,t)}{\partial x} + (x+R)\frac{\partial^2 c(x,t)}{\partial x^2}\right) \tag{5.2.2}$$

where the relative velocity is,

$$\boldsymbol{u}_{\text{rel}} = \left[\left(\frac{R}{x+R}\right)^2 - 1\right]\dot{R}$$

and discretised using the approximations above. To solve the equations, the next value at time point $s+1$ is found at each point j in the spatial grid using the Rayleigh-Plesset equation (5.1.2) to find the value of the bubble radius and surface velocity. These calculations are repeated until the end of the simulation time is reached; the parameters used are shown in table C.2.

Before proceeding, it is useful to check the scaling assumptions of equation (4.3.24) (Caflisch et al., 1985) to ensure that the nonlinear wave propagation model is appropriate.

These are,

$$\epsilon = \frac{1}{\lambda}\left(\frac{V}{N}\right)^{1/3}, \qquad \delta = \frac{R_0}{\lambda} \ll 1, \qquad \beta = \frac{4}{3}\pi\left(\frac{\delta}{\epsilon}\right)^3 \ll 1, \qquad \chi = \frac{\delta}{\epsilon^3} \leq \mathcal{O}(1).$$

At a concentration of 10^9 bubbles/m^3 and for a bubbly medium with propagation distance of 2 cm, medically relevant values of $\omega = 2.25$ MHz, $R_0 = 2 \times 10^{-6}$ m, $V = 8 \times 10^{-6}$ m^3 and $N = V \times 10^9 = 8 \times 10^3$ bubbles give scaling values of,

$$\epsilon = 1.5, \qquad \delta = 0.003, \qquad \beta = 3.4 \times 10^{-8}, \qquad \chi = 8.9 \times 10^{-4},$$

which are reasonably within the model scaling tolerances. At a higher concentration of 10^{11} bubbles/m^3, $N = 8 \times 10^5$ bubbles and,

$$\epsilon = 0.3, \qquad \delta = 0.003, \qquad \beta = 3.4 \times 10^{-6}, \qquad \chi = 0.09,$$

which again are within scaling tolerances. Despite the relatively small value of ϵ, the simulation was stable. At an even higher concentration of 10^{12} bubbles/m^3, $N = 8 \times 10^6$ bubbles and the scalings are,

$$\epsilon = 0.15, \qquad \delta = 0.003, \qquad \beta = 3.4 \times 10^{-5}, \qquad \chi = 0.9.$$

It was found that at this concentration, the simulation is unstable and this could be attributable to the fact that χ is approaching $\mathcal{O}(1)$ and ϵ is becoming much smaller than 1. This suggests that the mixture is no longer sufficiently dilute to assume that scattering between bubbles can be neglected.

5.3 Long pulse intervals

If the time between pulses is of the order of the Péclet number for the gas diffusion but less than the Péclet number for the surfactant diffusion, then the work in Chapter 3 suggests that the bubbles will have had sufficient time to return to equilibrium as gas diffusion occurs with the bulk, such that $\Gamma = \Gamma_{\text{eq}}$ but that surfactant adsorption is still negligible. Consequently, it is assumed that no lipid molecules adsorb onto the bubble surface in the interval between pulses. This allows the calculation of the new equilibrium radius R_0^{new} based on the amount of surfactant remaining on its surface after the pulse has passed using,

$$R_0^{\text{new}} = \sqrt{\frac{m_{\text{s}}}{4\pi\Gamma_{\text{eq}}}}$$

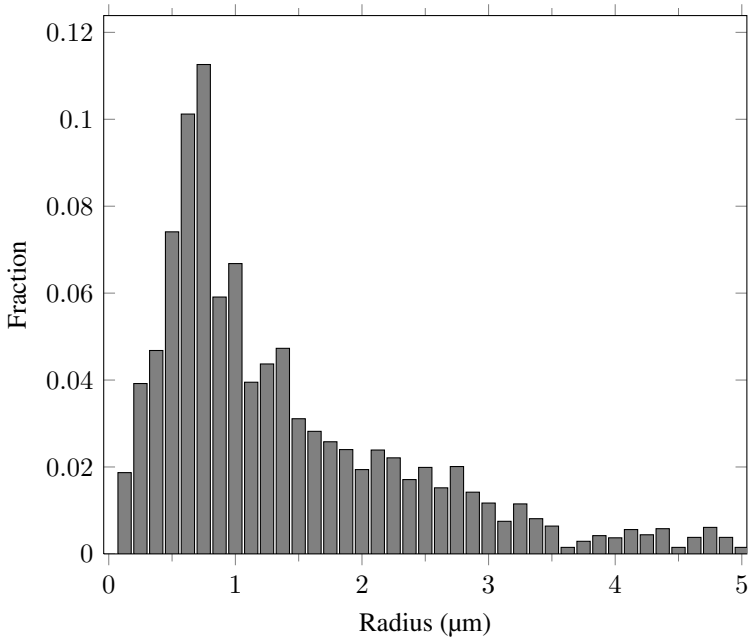

Figure 5.1: Size distribution for SonoVue® microbubbles (Sheetal Sanak, unpublished). The mean radius was approximately $1.4\,\mu$m.

Then, knowledge of the new microbubble size allows the mass of gas inside to be recalculated and the propagation simulation for one pulse can be repeated.

This approximation is used in order to reduce the computation of the problem by ignoring the explicit finite difference gas diffusion calculation during the interval between pulses. This is a realistic simplification since the timescales over which ultrasound scans are conducted are sufficient to allow the bubbles to equilibrate and this work demonstrates important changes in the suspension's response that occur.

5.4 Results

Simulations of different numbers of 8-cycle Gaussian sinusoids propagating through a SonoVue® suspension of different concentrations for a distance of 2 cm were carried out at pressures of 50, 100, 150 and 200 kPa. The interval between the pulses is assumed to be sufficiently long that the approximation outlined in Section 5.3 can be used. The size distribution was obtained from an experiment where optical microscopy was used to image and count a stock solution of the contrast agent (data kindly provided by Sheetal Sanak, U. Oxford). The distribution is shown in figure 5.1 and is discretised into $N = 40$ radius bins. Following any changes in radius, the bubbles are not redistributed amongst the radius bins for subsequent pulses but rather their final size is used for the start of the next insonation.

Section 5.4.1 investigates the attenuation of two 2.25 MHz pulses propagating through suspensions of 10^9, 10^{10} and 10^{11} bubbles/m^3 and which is subsequently compared to experimental results. In addition, further simulations involving six 2.25 MHz pulses propagating through the same suspension of 10^{11} bubbles/m^3 are carried out in Section 5.4.2 to examine the pulse-repetition dependence on the contrast agent behaviour. The evolution of the microbubble size distribution during these latter simulations is plotted to emphasise its role in the dynamic behaviour of the contrast agent. The six pulse simulations are repeated in Section 5.4.3 using a constant surface tension in equation (5.1.2) equal to the uncoated microbubble value and compared to previous results. Subsequently, the effect of incident pulse frequencies 1 MHz and 4 MHz on the calculated attenuation of the signal and the evolution of the size distribution is explored in Section 5.4.4.

To begin, the linear attenuation coefficient is calculated using equation (B.4.3) where the damping coefficient δ in a liquid with viscosity μ_l and constant shell viscosity μ_s is now,

$$\delta = \frac{4}{\rho R_0^2}\left(\mu_l + \frac{\mu_\mathrm{s}}{R_0}\right)$$

The attenuation for the discretised contrast agent population is calculated by,

$$a(\omega) = 10\log_{10}(e)\sum_{k=1}^{N}\Omega(R_k,\omega)n(R_k) \tag{5.4.1}$$

and using $\omega = 2.25$ MHz as well as the bubble distribution in figure 5.1, $a(\omega) = 5.4$ dB/cm at a concentration of 10^{11} bubbles/m^3 or 10^5 bubbles/ml. At concentrations of 10^3 and 10^4 bubbles/ml, $a(\omega) = 0.54$ dB/cm and $a(\omega) = 0.054$ dB/cm respectively.

In addition, the resonance frequency of a single lipid-coated microbubble can be calculated using equation (B.3.3). For incident frequencies of 1, 2.25 and 4 MHz, the resonant bubble sizes are 3.7, 1.8 and 1 µm respectively.

The fundamental and harmonic content of the simulated propagated pulses are subsequently extracted using a fast Fourier transform in MATLAB® and finding the peaks in the signal. The attenuation $a(\omega)$ of the signal over a 2 cm propagation distance d is calculated using the incident and propagated signals $P^{\mathrm{inc}}(\omega)$ and $P(\omega)$ respectively as follows,

$$a(\omega) = \frac{20}{d}\log_{10}\left(\frac{P^{\mathrm{inc}}(\omega)}{P(\omega)}\right)$$

5.4.1 Varying the suspension concentration

The results of the numerical simulations for two 8-cycle 2.25 MHz Gaussian sinusoids travelling through different concentrations of microbubbles are presented. In figure 5.2, the calculated attenuation of the fundamental component of the propagated signal at low pressures is close to 5 dB/cm, which is similar to the value obtained using the linearised attenuation model. At these pressures, it is expected that the microbubbles are behaving linearly and so the theory should be applicable. However, at higher pressures, this no longer holds. Looking at the figure, increasing the pressure of the incident pulse decreases the attenuation of the signal. Secondly, the calculated attenuation of the second pulse is generally lower than the first pulse for all concentrations. This is attributed to changes in the population's size distribution after the first pulse as a result of lipid shedding. One exception to this is at the lowest pressure when the bubbles' oscillation amplitudes are not sufficiently large for shedding to occur. Consequently, there is little change in the distribution, and thus the attenuation, for the second pulse.

The calculated attenuation of the second harmonic component of the propagated signal is plotted in figure 5.3. Again, at low pressures, there is little change in attenuation of the second harmonic because the oscillations of the microbubbles are insufficiently large to cause shedding and thus changes in the size distribution. At 100 kPa, there is a slight increase in the amount of second harmonic in the signal of the second pulse, implying that the population is behaving more nonlinearly. However, by increasing the pressure further, the amount of second harmonic decreases in the second pulse compared with the first, except at the lowest concentration. In the same vein as before, this phenomenon is attributable to changes in the contrast agent size distribution as a result of shedding events during the first pulse.

One interesting point is that the calculated attenuation of the second harmonic in the signal is not linearly proportional to the incident pressure. For a concentration of 10^5 bubbles/ml, the harmonic content increases as the incident pressure is raised from 50 kPa to 100 kPa however decreases at higher pressures, where the second pulse contains less harmonic content than the first. This suggests that the changes in the contrast agent population can have different effects on the signal depending on the incident pressures used.

For comparison, figure 5.4 shows experimental results (unpublished data kindly supplied by Sheetal Sanak, U. Oxford) for the propagation of acoustic waves with an incident frequency of 2.25 MHz through the same contrast agent population for a distance of 2 cm. A

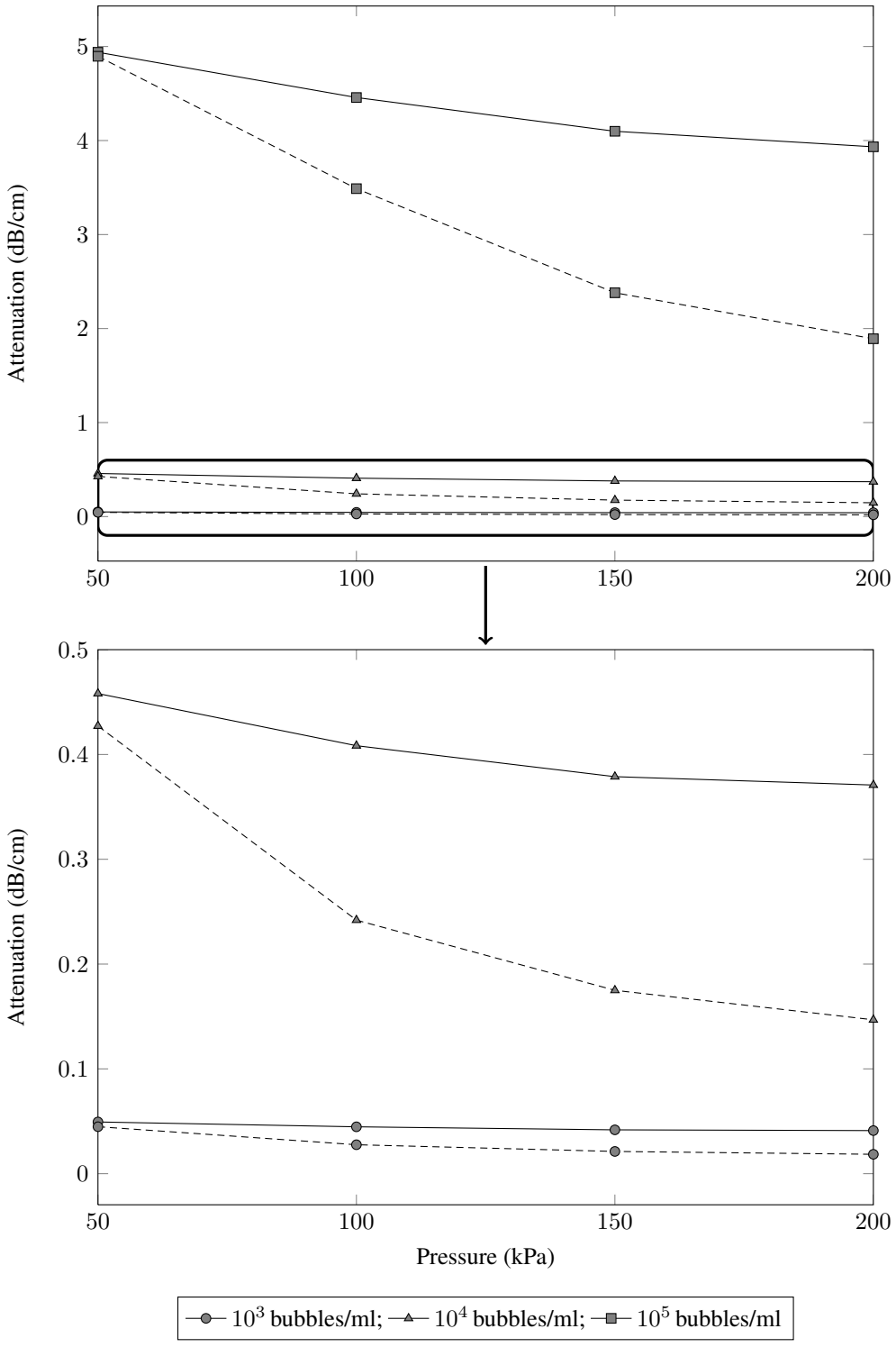

Figure 5.2: The calculated attenuation of the fundamental component of the signal in the numerical simulation of two 2.25 MHz pulses propagating through 2 cm of SonoVue® suspension. The solid line —— is the attenuation of the first pulse; the dashed line - - - is the attenuation of the second pulse.

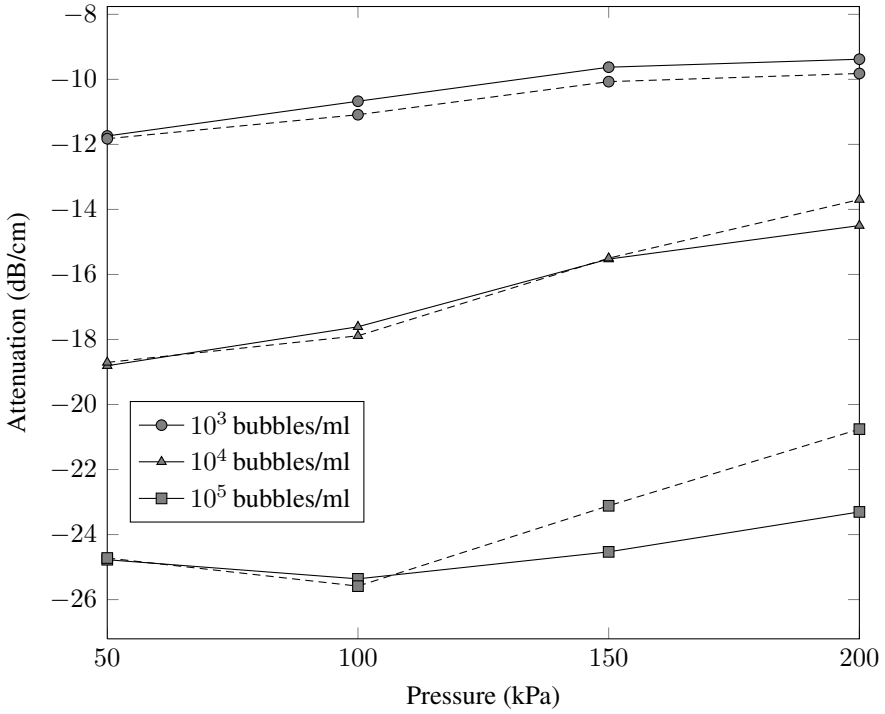

Figure 5.3: The calculated attenuation of the second harmonic component of the signal in the numerical simulation of two 2.25 MHz pulses propagating through 2 cm of SonoVue® suspension. The solid line —— is the attenuation of the first pulse; the dashed line - - - is the attenuation of the second pulse.

series of pulses were propagated through the bubbly mixture with a pulse repetition frequency of 1 kHz, described in more detail in Appendix D.2. The software used to capture the pulses took an average of the propagated pulses rather than recording each pulse separately. Nevertheless, the trends observed are similar to the numerical simulations presented before. Firstly, the measured attenuation of the fundamental component of the signal decreased with incident pressure, corresponding to the results of the numerical model in figure 5.2. Secondly, the measured attenuation of the second harmonic was not linearly proportional to the incident pressure. At 10^4 bubbles/ml, the simulation in figure 5.3 suggests a decrease in second harmonic in the propagated pulse as the pressure increases, whereas the experimental data show a slight increase at 100 kPa compared with 50 kPa. On the other hand, at 10^5 bubbles/ml, the numerical simulation does suggest an increase in second harmonic content at 100 kPa compared with 50 kPa. Furthermore, the attenuation measured at 50 kPa for a concentration of 10^5 bubbles/ml was smaller than the linear value obtained earlier. Stride and Saffari (2005) have shown that multiple scattering effects are observed at this concentration in experiments using Optison®. Since the models used to calculate the linear attenuation coefficient assume a sufficiently di-

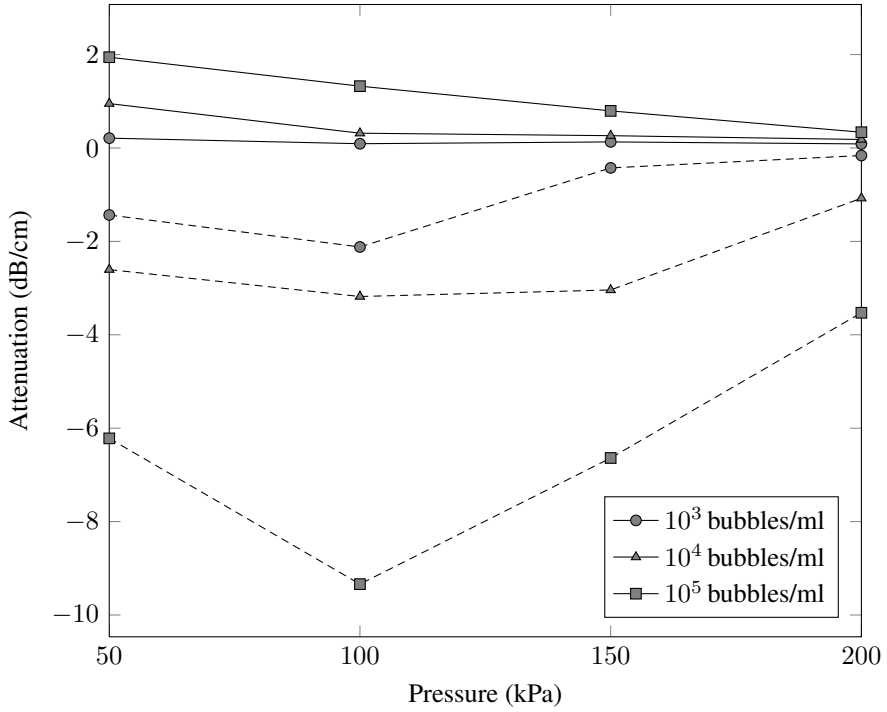

Figure 5.4: The attenuation of the fundamental and second harmonic component of the propagated signal in experimental data using an incident frequency of 2.25 MHz. The solid line —— is the attenuation of the fundamental signal component; the dashed line - - - is the attenuation of the second harmonic signal component.

lute mixture that multiple scattering effects can be ignored, it is possible that this could lead to a discrepancy with the linear theory. Further experimental work would help to elucidate the scattering effects that are occurring, but it is noteworthy that they play an important role even at the relatively low concentrations that are used clinically.

5.4.2 Six pulse insonations

Further simulations were carried out for six 8-cycle Gaussian-sinusoid 2.25 MHz pulses propagating 2 cm through a SonoVue® population of concentration 10^5 bubbles/ml. The aim is to investigate further the effect of multiple pulsed insonations on a contrast agent population and the propagated signal.

The changes in the fundamental and second harmonic content are shown in figure 5.5. Repeated insonation of the population causes a reduction in the calculated attenuation of the fundamental component of the propagated signal, except at the lowest incident pressure where there is little change. On the other hand, the nonlinear relationship between pulse number and attenuation of the second harmonic in the signal is again visible. For instance at 200 kPa, there is a decrease in second harmonic between the first and second pulses but an increase

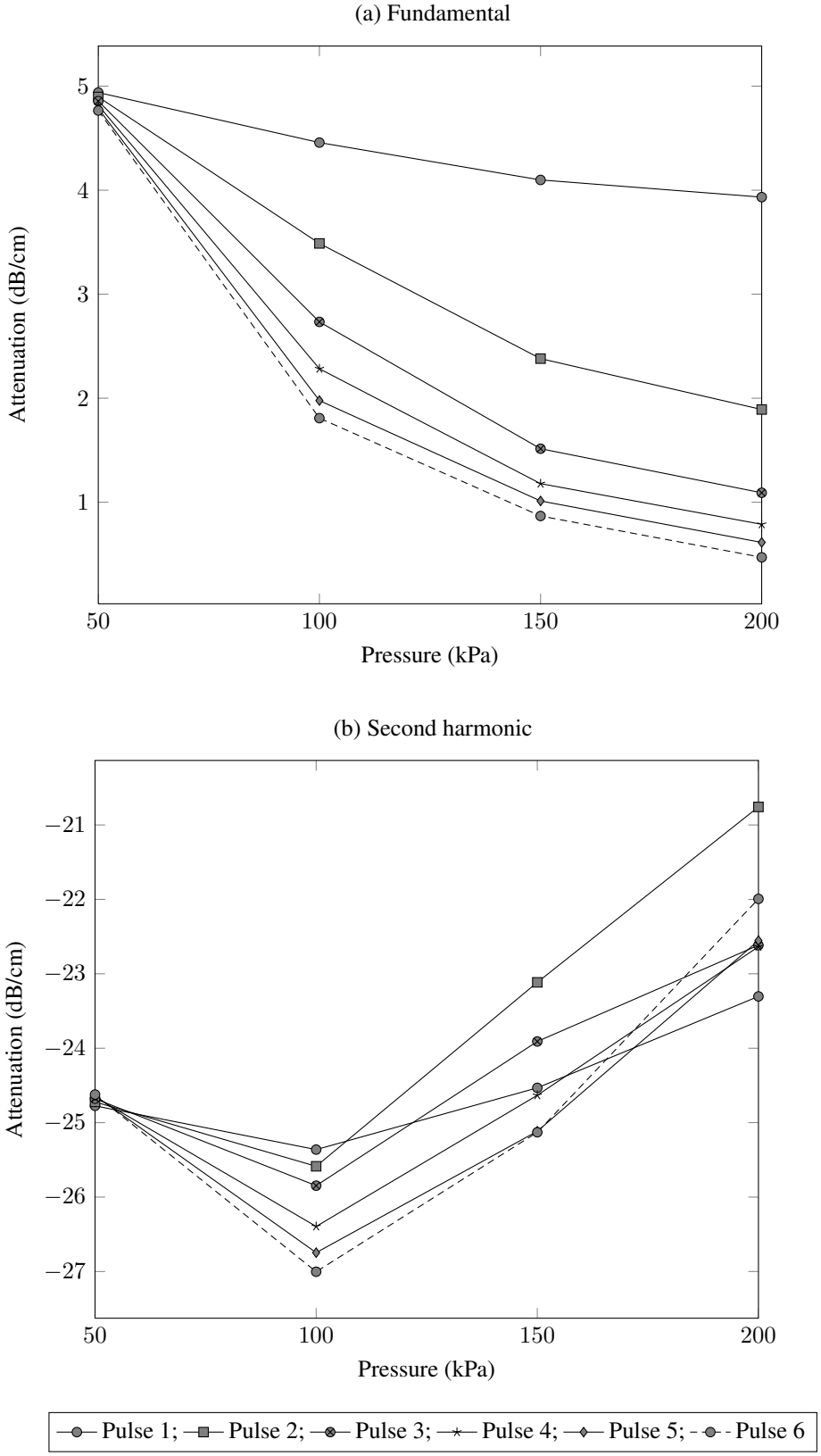

Figure 5.5: The calculated attenuation of the fundamental and second harmonic content of the signal for six 2.25 MHz pulses propagating 2 cm through a SonoVue® population distribution of concentration 10^5 bubbles/ml.

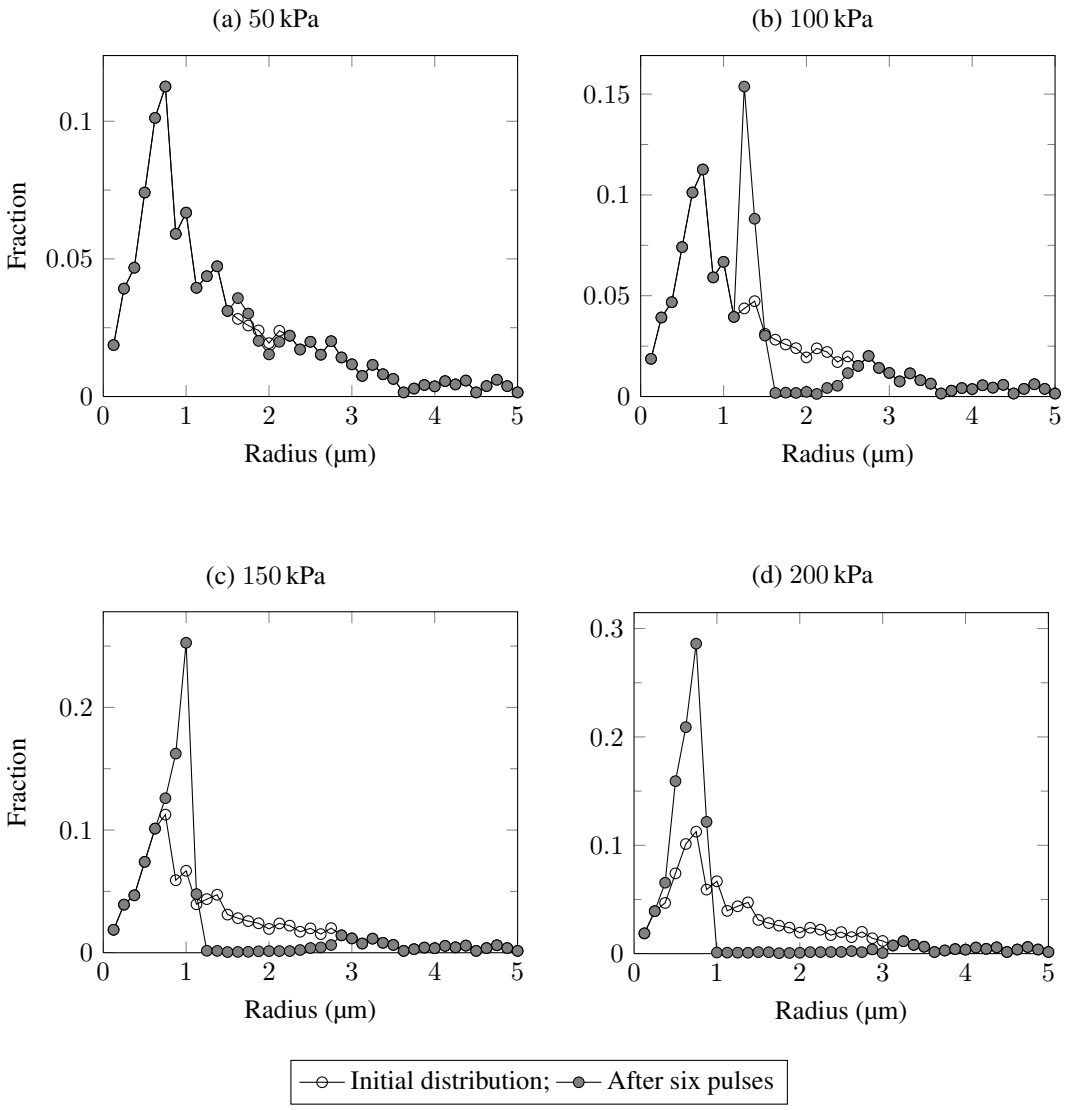

Figure 5.6: The changes in the SonoVue® size distribution after insonation by six 2.25 MHz pulses for different pressures at a concentration of 10^5 bubbles/ml. The mean radius after the sixth pulse is: (a) 1.4 μm; (b) 1.2 μm; (c) 1.1 μm; (d) 0.9 μm.

between the second and third pulses. This further emphasises the importance of the change in the contrast agent population size distribution during the course of the simulation and the effect that this can have on the characteristics of the bubbly medium.

According to the model of Chapter 3, it is the reductions in bubble size, and consequently changes in the contrast agent size distribution and shifts in the compression/expansion-only behaviour, that drives the changes in the harmonic content of the propagated pulse. To illustrate this, the evolution of the microbubble distribution is plotted in figure 5.6.

At the lowest incident pressure, the size distribution remains largely unchanged, as shown in figure 5.6(a). This explains the results of figure 5.5 which show that at the lowest pressures, there is little variation in calculated attenuation between consecutive pulses. Increasing the incident pressure to $100\,\text{kPa}$, however, does lead to alterations in the size distribution. The most notable change in figure 5.6(b) is a decrease in the proportion of bubbles with radii around $2\,\mu\text{m}$ – which corresponds to the resonant size of the distribution – and an increase in the proportion of bubbles with radii equal to $1.25\,\mu\text{m}$. This behaviour suggests that at this smaller, stable size, the microbubbles are far enough away from resonance that their oscillations are sufficiently small for no surfactant shedding to occur. Figures 5.6(c) and 5.6(d) demonstrate that this behaviour is replicated at higher pressures of $150\,\text{kPa}$ and $200\,\text{kPa}$, where the stable bubble size is $1\,\mu\text{m}$ and $0.75\,\mu\text{m}$ respectively. At higher pressures, they must shrink further in order to be sufficiently smaller than resonance such that shedding no longer occurs. Bubbles that are much smaller or larger than the resonant size do not shrink despite repeated insonations since their oscillations are not large enough to cause shedding. Finally at pressures higher than $50\,\text{kPa}$, it appears that after six pulses the population is beginning to stabilise since the changes in the harmonic content of the signal are no longer large.

5.4.3 Constant surface tension

The previous results are compared with the model using a constant surface tension term instead of the surfactant surface concentration-dependant sigmoidal function described in equation (3.4.6). A diffusivity dependent on surfactant surface concentration is still used and allows for the bubbles to remain stable at equilibrium but to shrink if surfactant is lost from their surface. The calculated attenuation for the propagation of six $2.25\,\text{MHz}$ 8-cycle Gaussian sinusoid pulses at pressures 50, 100, 150 and $200\,\text{kPa}$ through a suspension of SonoVue® for $2\,\text{cm}$ are plotted in figure 5.7.

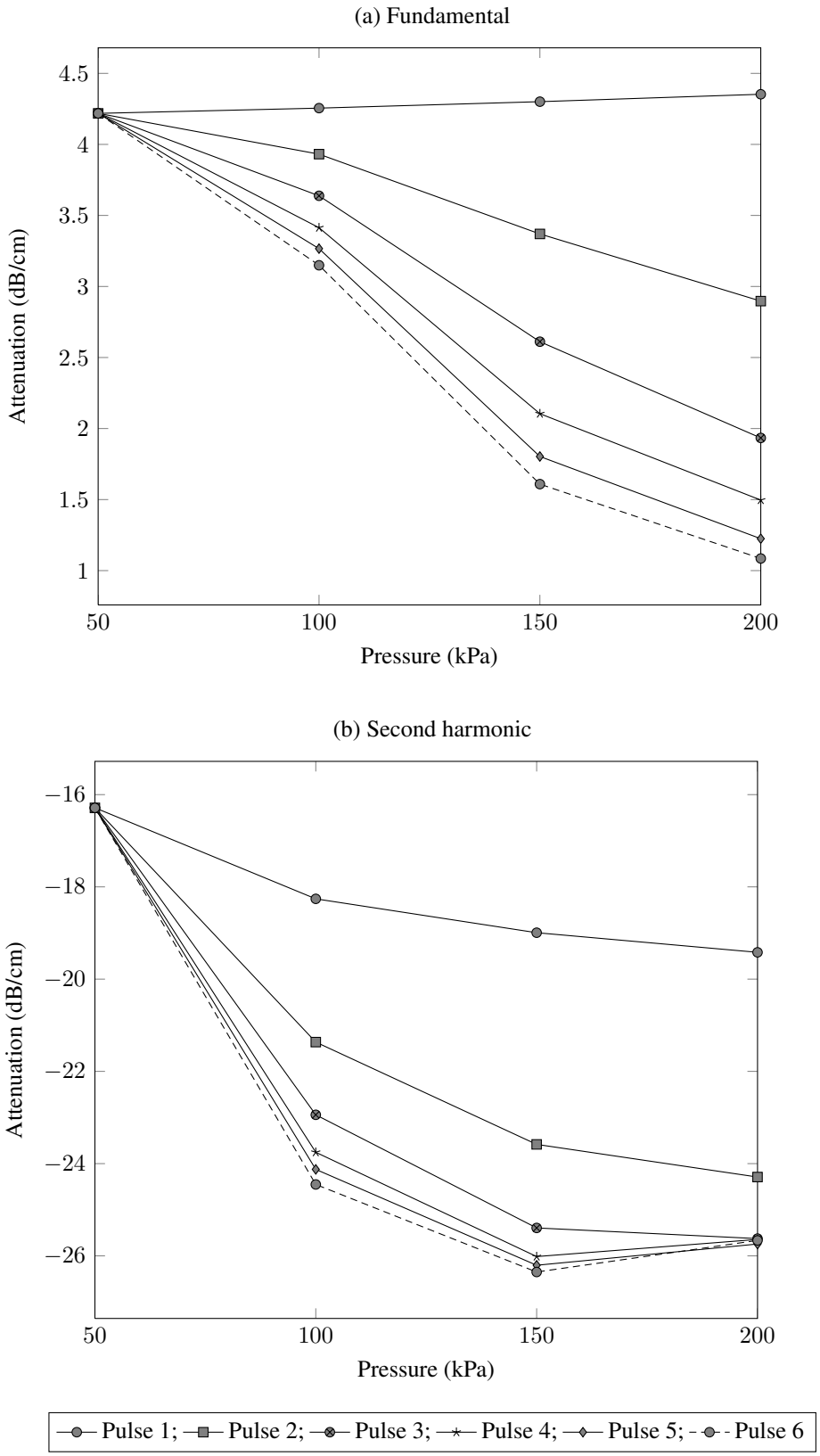

Figure 5.7: The calculated attenuation of the fundamental and second harmonic content of the signal for six 2.25 MHz pulses propagating 2 cm through a SonoVue® population distribution of concentration 10^5 bubbles/ml, using a constant surface tension in the bubble equation of motion.

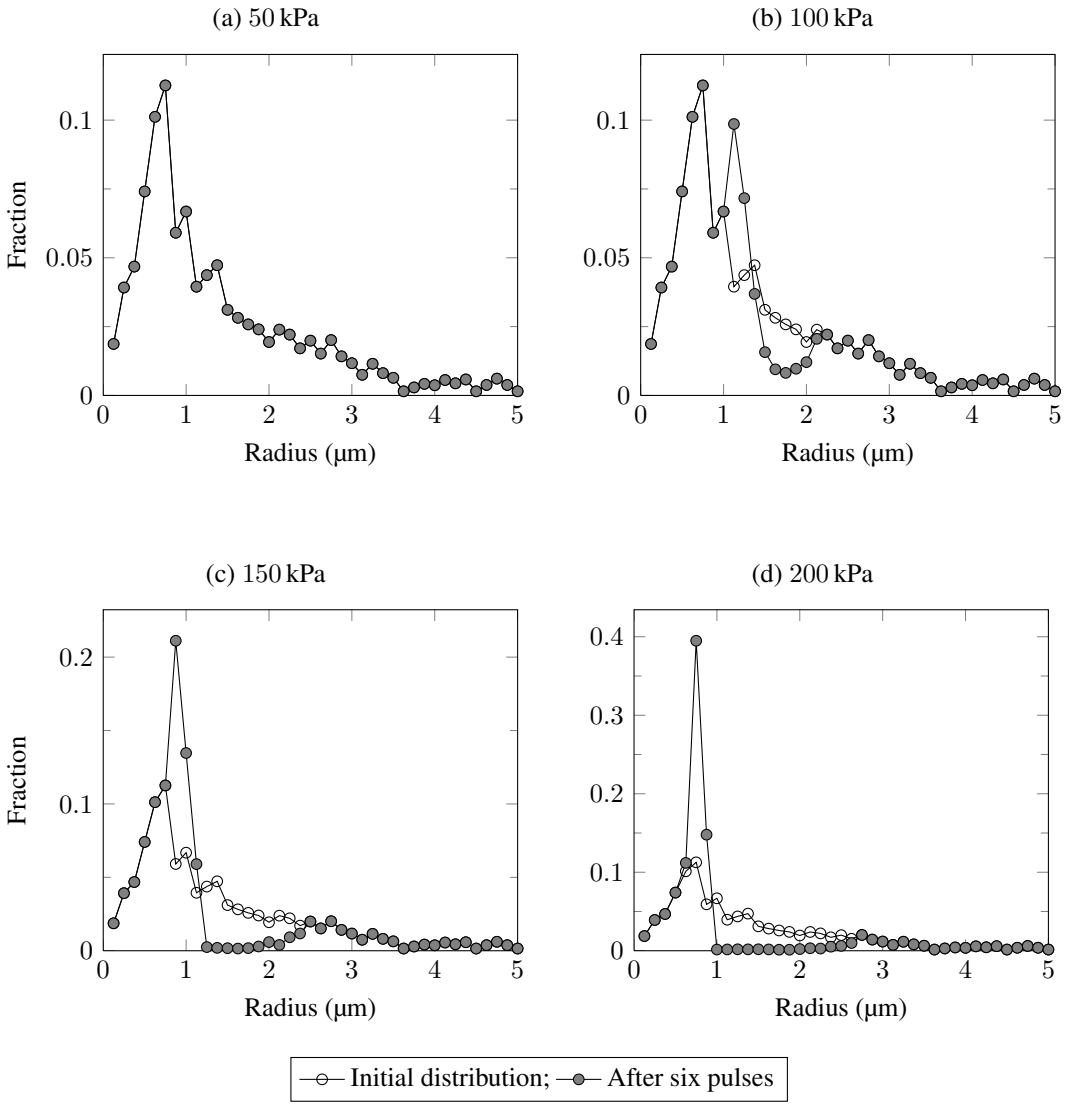

Figure 5.8: The changes in the SonoVue® size distribution after insonation by six 2.25 MHz pulses for different pressures at a concentration of 10^5 bubbles/ml using a constant surface tension. The mean radius after the sixth pulse is: (a) 1.4 μm; (b) 1.3 μm; (c) 1.2 μm; (d) 1.1 μm.

Comparing with figure 5.5, there is a trend of decreasing attenuation of the fundamental with increasing incident pressure. Except at the lowest pressures, the calculated attenuation decreases with each consecutive pulse. Once again, this is due to changes in the contrast agent size distribution, exhibiting trends similar to those shown in figure 5.6. When the bubble oscillations are insufficient to cause shedding, either because they were far from resonance or the incident pressure was too low, the bubbles do not shrink.

The calculated attenuation of the second harmonic in the propagated signal does not show a linear relationship with pressure. Furthermore, changes in the size distribution after consecutive pulses increase the harmonic content in the pulse. In particular at 150 kPa, the propagated pulse contains more second harmonic than at 200 kPa after the fourth pulse compared with the first three pulses, at which point the population appears to stabilise at the higher pressure. Until the bubble population reaches a stable size distribution, the harmonic content of the propagated signal continues to vary between pulses. Again at pressures higher than 50 kPa, it appears that after six pulses the population is stabilising since the changes in the harmonic content of the signal are no longer as large.

The evolution of the size distribution in figure 5.8 is similar to the simulations using a sigmoidal surface tension function. Bubbles close to resonance shrink, whereas those smaller and larger than this size do not. The size range of bubbles that reduce in size increases with pressure since this leads to larger oscillations and more bubbles shed surfactant. However, the harmonic content of the propagated signal is different. This suggests that the choice of surface tension model is important in determining the attenuation characteristics of the contrast agent.

5.4.4 Other incident frequencies

In this section, two simulations modelling the propagation of six 8-cycle Gaussian sinusoid pulses are presented: one series of pulses had an incident frequency of 1 MHz; the other, 4 MHz. The SonoVue® population modelled is shown in figure 5.1 and the concentration used is 10^5 bubbles/ml. Using equation (5.4.1), the linear attenuation values for these frequencies are 9.6 dB/cm and 2 dB/cm respectively.

At 1 MHz, figure 5.9 shows a calculated attenuation of 8.1 dB/cm at the lowest pressure during the first pulse where the bubbles are most likely to be behaving linearly, which is not particularly close to the theoretical value. Despite there being relatively fewer bubbles that are at the resonant size 3.7 μm, they contribute more to the scattered signal and consequently

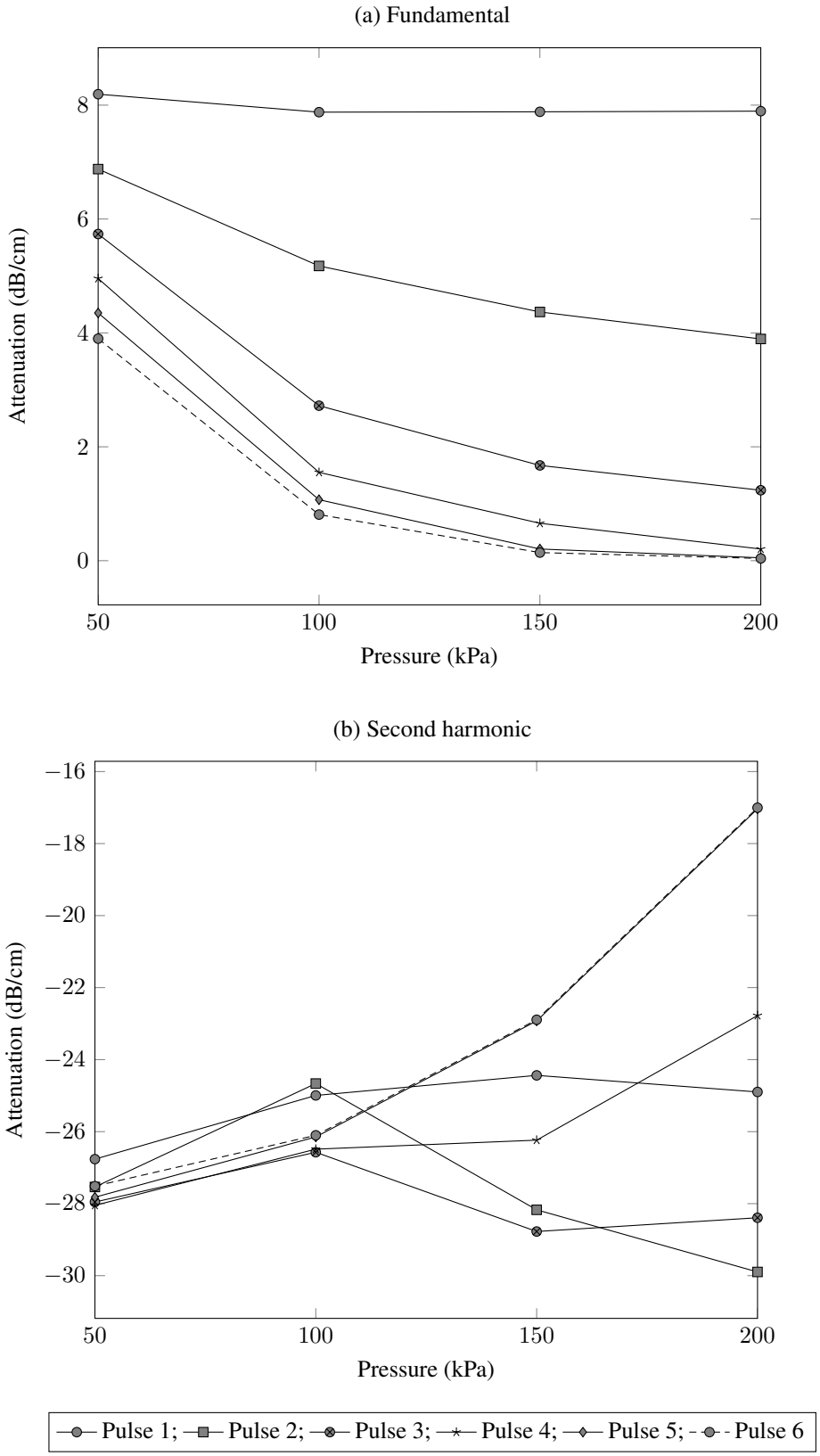

Figure 5.9: The calculated attenuation of the fundamental and second harmonic content of the signal for six 1 MHz pulses propagating 2 cm through a SonoVue® population distribution of concentration 10^5 bubbles/ml.

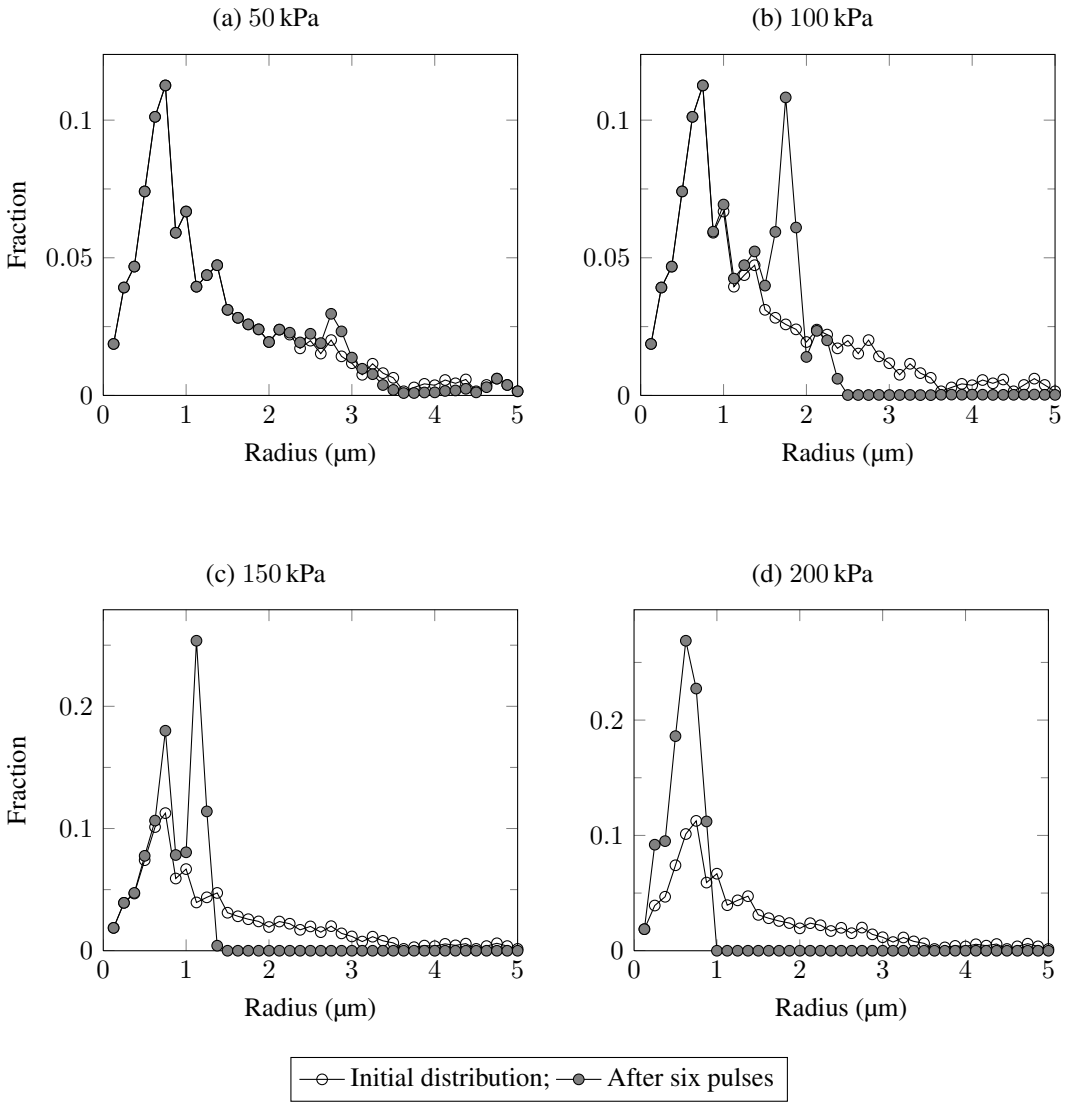

Figure 5.10: The changes in the SonoVue® size distribution after insonation by six 1 MHz pulses for different pressures at a concentration of 10^5 bubbles/ml. The mean radius after the sixth pulse is: (a) 1.4 μm; (b) 1.1 μm; (c) 0.9 μm; (d) 0.6 μm.

lead to greater nonlinearity in the propagated signal. The attenuation of the second harmonic corroborates this since there is a relatively large amount of nonlinearity in the signal. Consequently, the linear theory is less likely to be accurate.

In addition, after six 150 kPa or 200 kPa pulses there is very little calculated attenuation of the fundamental. On the other hand, the calculated attenuation of the second harmonic shows much more variation and is pulse-dependant. For instance, at 100 kPa, there is a slight decrease in the second harmonic content of the signal for the second pulse, compared with the first; at 150 kPa and 200 kPa, there is a relatively large increase. Not only does the calculated attenuation of the fundamental tend to zero, particularly at the highest pressures, the second harmonic content also stabilises after five to six pulses.

The evolution of the bubble distribution shown in figure 5.10 demonstrates important changes in the microbubbles' sizes. Using a lower frequency than previous simulations at 50 kPa causes the larger microbubbles to shed material and shrink, leading to an increase in bubbles with a radius of approximately 2.75 µm and almost no larger bubbles after six pulses as shown in figure 5.10(a). A higher incident pressure of 100 kPa results in a grouping of bubbles around 1.75 µm and similarly at 150 kPa around 1.1 µm. At the highest pressure of 200 kPa there are no bubbles of radius 1 µm or larger demonstrating considerable changes to the contrast agent size distribution in figure 5.10(d). The negligible changes in the calculated attenuation of the fundamental and second harmonic after six pulses, particularly at higher pressures, in figure 5.9 suggest that the population has stabilised.

At an incident frequency of 4 MHz, the calculated attenuation of the fundamental at 50 kPa is 1.9 dB/cm, as shown in figure 5.11. This is in better agreement with the value calculated using the linear analysis of equation (5.4.1) of 2 dB/cm and moreover, the numerical simulations suggest the propagated signal contains less nonlinearity. The resonant size at this frequency is 1 µm and whilst there are a greater number of bubbles close to this size, they contribute a smaller scattered signal compared to larger bubbles in the population.

Furthermore, at 50 kPa there is little change in the calculated attenuation of the fundamental and second harmonic in the propagated signal. At higher pressures, repeated pulses reduce the calculated attenuation of the fundamental but again, the attenuation of the second harmonic varies between consecutive insonations. For example, there is a decrease in the nonlinear component of the signal with subsequent pulses at 100 kPa but there can be an increase

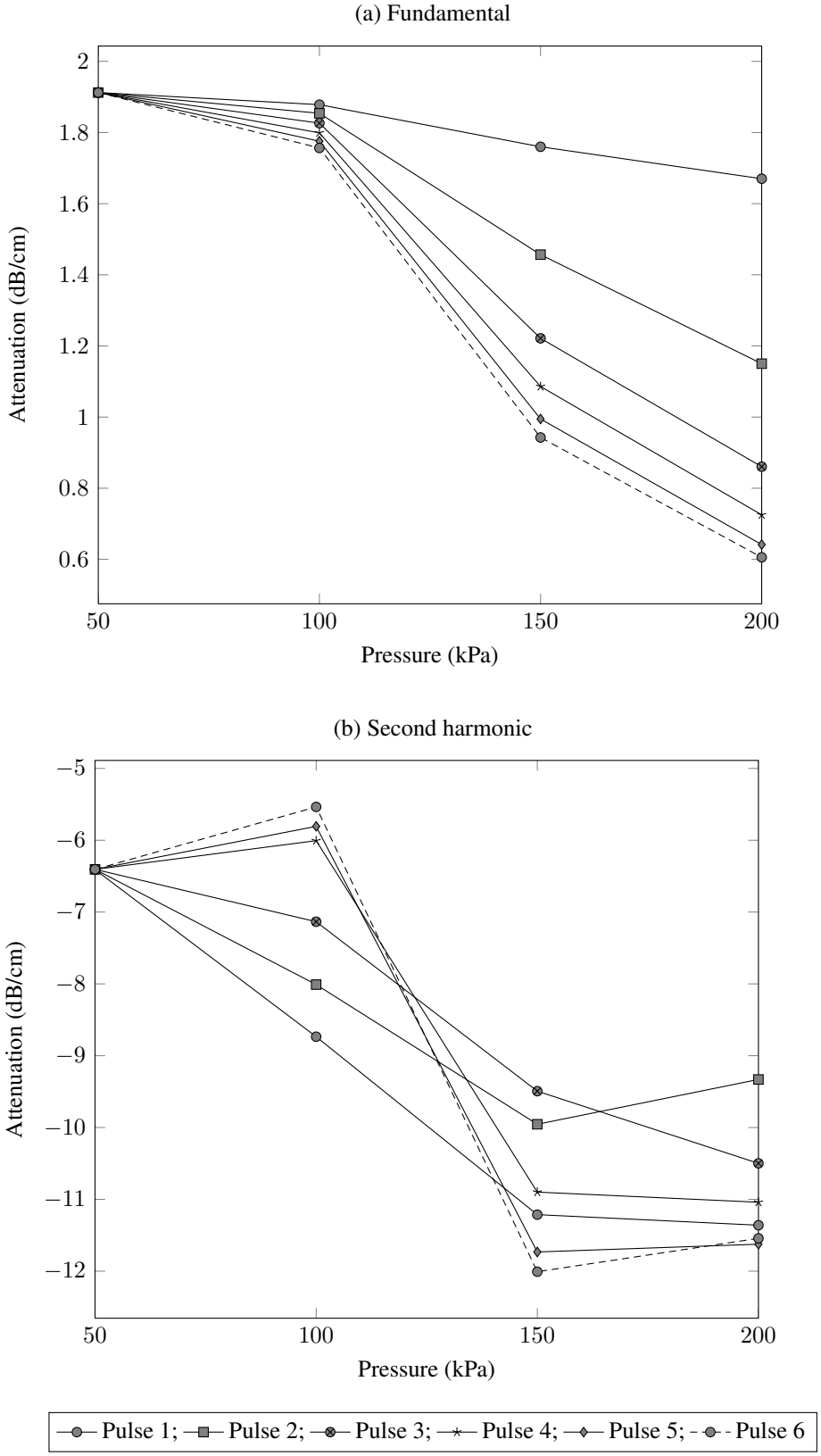

Figure 5.11: The calculated attenuation of the fundamental and second harmonic content of the signal for six 4 MHz pulses propagating 2 cm through a SonoVue® population distribution of concentration 10^5 bubbles/ml.

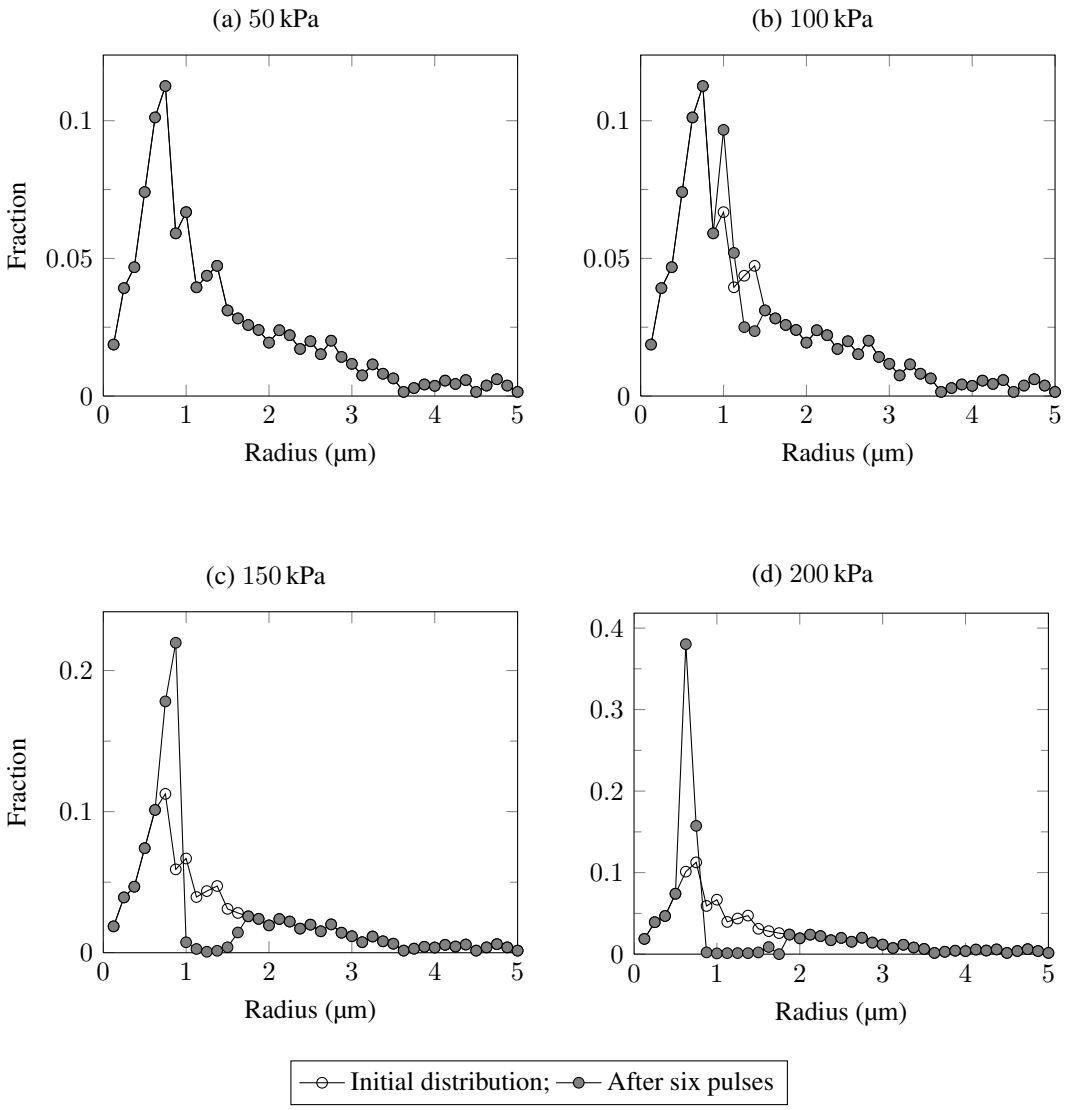

Figure 5.12: The changes in the SonoVue® size distribution following insonation by six 4 MHz pulses for different pressures at a concentration of 10^5 bubbles/ml. The mean radius after the sixth pulse is: (a) 1.4 μm; (b) 1.4 μm; (c) 1.3 μm; (d) 1.2 μm.

or decrease at $150\,\text{kPa}$ depending on the pulse number. After six pulses at pressures higher than $50\,\text{kPa}$, both the fundamental and second harmonic content of the signal appear to be stabilising suggesting that the population distribution is no longer undergoing large changes.

The evolution of the suspension size distribution in figure 5.12(a) shows that at the lowest pressure, there is no change in the microbubble population during the simulation explaining the consistent values for the calculated attenuation. Increasing the incident pressure leads to a decrease in the proportion of bubbles around $1.3\,\mu\text{m}$ as they shrink to a smaller size. Higher pressures result in a larger range of bubble sizes shrinking whilst those bubbles above and below this range do not undergo sufficiently large oscillations to cause lipid shedding. It is concluded that the downwards shift in a small range of bubble sizes around resonance in figure 5.12 is responsible for the changes in the calculated attenuation in figure 5.11.

5.5 Summary

This chapter combines the new equation of motion proposed in Chapter 3 with the nonlinear acoustic wave equation investigated in Chapter 4 to produce a novel time-dependent propagation model that accounts for changes in the lipid-coated microbubble population as a result of surfactant shedding. A SonoVue® size distribution is discretised into 40 radius bins and simulations of 8-cycle Gaussian sinusoid pulses travelling $2\,\text{cm}$ through the bubbly mixture are carried out at incident pressures of 50, 100, 150 and $200\,\text{kPa}$. The frequency spectrum of each propagated pulse is computed using a fast Fourier transform and the harmonic content compared. To reduce computational complexity, the time between pulses is assumed to be sufficiently long that the microbubbles have returned to equilibrium by the time the subsequent pulse passes through the suspension. This allows the diffusion calculation to be ignored during the interval between pulses.

To begin, two $2.25\,\text{MHz}$ pulses travelling through bubbly media of 10^3, 10^4 and 10^5 bubbles/ml are simulated and the results compared with experimental measurements. Further simulations for six pulses at the same frequency travelling through a 10^5 bubbles/ml suspension are conducted to elucidate the effects of multiple pulses on the behaviour of the bubble, and in particular, the evolution of the size distribution.

The results show that at $50\,\text{kPa}$, the microbubbles' oscillations are insufficiently large to cause shedding and the population to change. At higher pressures however, changes in the size distribution, and as a consequence, the propagated signal, do occur from one pulse to the next.

In particular, those bubbles close enough to resonance that their oscillations are sufficiently large to cause shedding, shrink until they reach a stable size. On the other hand, bubbles much smaller or larger than the resonant size demonstrate no shrinkage during the simulation.

This analysis is repeated using a constant surface tension value rather than the sigmoidal function introduced in Chapter 3, at a concentration of 10^5 bubbles/ml. Whilst the changes in bubble size distribution are similar, the nonlinear content of the propagated signal is different, suggesting that a realistic surface tension model is important to accurately capture the dynamics of the contrast agent microbubbles and their effect on the attenuation of an acoustic pulse.

In addition, the attenuation characteristics and changes in the bubble size distribution are significantly different when insonated using pulses of other frequencies at a concentration of 10^5 bubbles/ml. At 1 MHz, a far greater proportion of microbubble sizes oscillate sufficiently such that they shed surfactant. Consequently a larger fraction of bubbles shrink to a common smaller size. By comparison, at 4 MHz a much smaller fraction of bubbles shed surfactant and thus shrink. Nevertheless, there are still significant changes in the attenuation characteristics of the population. This suggests that those bubbles close to resonance, whose sizes change between pulses, have a much greater influence on the acoustic wave than others, which is what would be expected.

The changes in the harmonic content of the signal between pulses also hint at when the population is stabilising. At low pressures, the oscillations are insufficiently large to cause changes in the size distribution. However, at higher pressures this is not the case. At an incident frequency of 1 MHz, the population appears to have stabilised after six pulses since the harmonic content of the signal is no longer undergoing large changes between pulses. However, at 2.25 MHz and 4 MHz and pressures higher than 50 kPa, the harmonic content in the signal is still exhibiting small changes between pulses, suggesting that the population has yet to completely stabilise.

Unfortunately this model becomes unstable when the concentration of bubbles is higher than 10^5 bubbles/ml. Investigations at higher concentrations would require the use of a different wave propagation model, a problem that necessitates further work. Moreover it is suggested that multiple scattering effects could explain the lower attenuation values obtained in experiments compared to those predicted by the theory.

Nevertheless, the time-dependent behaviour of individual lipid-coated microbubbles modelled in Chapter 3 has demonstrated significant effects on the simulated behaviour of a contrast agent population. Current imaging algorithms assume the bubbles remain unchanged between pulses, in contradiction to experimental observations (Viti et al., 2011). In particular, the sudden changes in bubble size due to mechanisms such as lipid shedding as well as slower effects such as gas diffusion, should not be ignored in clinical applications. The results suggest it is important that future modelling work take this crucial behaviour into account.

CHAPTER 6

CONCLUSIONS AND FURTHER WORK

The aim of this thesis was to provide an improved description of the underlying physics of lipid-coated microbubble behaviour by including the time-dependent effects of gas diffusion and the properties of the coating, into a model describing microbubble oscillation. By improving qualitative and quantitative agreement between theory and experiment, it is believed that future improvements in the clinical implementation of microbubble contrast agents will be possible.

6.1 Conclusions

Chapter 2 considered the growth of bubbles in tissue under varying external pressure. The pressure changes, and by consequence the bubble wall velocities, were assumed to be sufficiently slow that convection can be ignored. A two-dimensional model for the tissue was used in which it is assumed there exists a constant number of stable micronuclei from which bubbles can grow. Separate diffusion equations for the concentration of nitrogen, oxygen and helium in the tissue were solved simultaneously using numerical methods and the flux across the boundary of each bubble in the tissue calculated by assuming the gas behaviour is ideal. This model was applied to the problem of decompression sickness (DCS) in diving for different depth and gas mixture profiles obtained from experienced divers. The results of the simulations suggest that deeper dives with fewer deep decompression stops lead to larger bubbles in the tissue and it is hypothesised that this could be a contributory factor in DCS.

Additionally, it is suggested that there exists a particular number density of bubbles in the tissue that is most favourable to maximum bubble growth: too many bubbles and they inhibit gas diffusion through the tissue as well as competing with each other for the available gas; too few and the gas can diffuse out of the tissue before the bubbles have time to grow.

In summary, the results of the decompression modelling validate current diving practices, particularly the use of deep decompression stops in order to inhibit bubble growth. Moreover, the practice of breathing gas with higher concentrations of oxygen during decompression does encourage bubble shrinkage in the simulations. It is further acknowledged that there are many other mechanisms that could cause injury that are not accounted for in the model such as: bubble growth and coalescence outside of tissue; bubble escape from the tissue into the venous system.

Subsequently, Chapter 3 incorporated the time-dependent effects of gas diffusion investigated in the previous chapter, including convection, into a revised equation for lipid-coated microbubble motion that also combined a time-dependent surface tension and diffusivity. The concentration of surfactant on the bubble surface was assumed to be governed by Langmuir adsorption for small oscillations around equilibrium, but at higher concentrations, the surfactant becomes insoluble. At high compressions, a "maximum packing concentration" is reached whereupon the surface cannot support any more molecules and surfactant is shed into the bulk liquid. In addition, the surface tension was assumed to be nonlinearly dependent on the concentration of surfactant on the bubble surface and fitted to a general sigmoid function where at low concentrations, the value of the surface tension is that of an uncoated microbubble; as the concentration increases, the surface tension tends to a minimum. The diffusivity of gas through the bubble surface was also assumed to be proportional to the concentration of surfactant to account for contrast agent stability, tending to a minimum at high concentrations and to the value for an uncoated microbubble at low concentrations.

The method of multiple scales was used to analyse the boundary condition on the surface of the bubble. Based on the timescale of an ultrasound pulse, the Péclet number Pe is large. Consequently, the timescale of diffusion $\mathcal{O}(Pe)$ is too slow to explain sudden bubble size changes that have been observed in experiments during ultrasound insonation. Crucially, the shedding of surfactant occurs on a faster timescale $\mathcal{O}\left(Pe_{\mathrm{s}}^{-1/2}\right)$, which could account for this phenomenon. Moreover, the effect of transience is shown to be negligible and so the theory is applicable to repeated short-pulse excitations of the microbubble. Despite similarities with published research, the problem in this work is more difficult due to the choice of boundary condition and the non-trivial initial condition that arises as a result of the shedding, which complicate the averaging process.

The model was then solved numerically and the behaviour of a lipid-coated microbubble undergoing repeated insonation with ultrasound pulses simulated. Comparing with experimental data, it was shown that the model successfully replicates aspects of lipid-coated microbubble behaviour that have hitherto remained unexplained. In particular, sudden microbubble shrinkage on the timescale of the pulse was observed. Furthermore, variations in the bubble oscillation symmetry over the longer timescale, from compression- to expansion-only and back, is attributed to the slow diffusion of gas out of the bubble after a shedding event and the behaviour of the nonlinear surface tension as the surfactant surface concentration changes. Additionally, the oscillations of bubbles much larger or smaller than resonance are insufficient for shedding – and by consequence, large, sudden changes in radius – to occur. After multiple shedding events and gas diffusion, the model suggests that the microbubble reaches a size at which shedding no longer occurs and the flux of gas across its surface is at a minimum, leading to size stability and behaviour witnessed in experiments.

Nevertheless, the experimental data were not replicated exactly. Firstly, since the microbubble was against an elastic boundary and only one plane was visible, an exact fit with a spherical bubble model is practically impossible. Secondly, more accurate values for the parameters and surface tension model require further experimental data to be obtained and it is believed that this would improve agreement with experiments.

An equation for nonlinear acoustic propagation through a population of microbubbles was examined in Chapter 4. It was noted that for polydisperse size distributions, the computation becomes highly intensive. Consequently, a method for simplifying the problem by approximating the medium as a series of sheets each containing homogeneous scatterers, which replicates the initial size distribution across the medium, was analysed. By calculating transmission and reflection coefficients between sheets, the case of a bidisperse population of uncoated bubbles alternating in size was linearised for small perturbations in the wavenumbers and densities of the layers. It is suggested that this so-called homogeneous sheet (HS) approximation is valid for a dilute solution of linearly oscillating bubbles: numerical solution of the problem and comparison with the full summation approach corroborated this finding. However, when a large proportion of the population contains resonant bubbles behaving nonlinearly, the HS method is a very poor approximation. Consequently, it is deemed an unsuitable method for reducing computational complexity for medical ultrasound purposes since contrast agents are designed to contain large numbers of bubbles that are likely to be at, or close to, resonance.

Varying the discretisation of the polydisperse population using the full summation in order to reduce computation time was also investigated. It was found that a relatively high number of radius bins is needed to accurately discretise the population. In conclusion, this research suggests that it is difficult to reduce the computational complexity of such a highly nonlinear problem.

The themes investigated previously in this thesis were combined in Chapter 5 into a nonlinear acoustic propagation model accounting for time-dependent lipid-coated microbubble behaviour. Numerical simulations of multiple ultrasound pulses travelling through a SonoVue® suspension were simplified by assuming that the interval between pulses is sufficiently long that the bubbles return to equilibrium before the next pulse, allowing the diffusion calculations to be approximated. The results suggest that the harmonic content of the propagated signal is significantly altered from one pulse to the next when changes in the size distribution of the contrast agent population resulting from surfactant shedding occur. Comparison with experimental data showed qualitative agreement, particularly in the nonlinearity of the second harmonic attenuation with incident pressure. However, a direct comparison was not possible because the experimental data available show only an average attenuation calculated over many pulses. Simulations using a constant surface tension term instead of the sigmoidal function introduced in Chapter 3 demonstrated similar changes in the bubble distribution. However, the attenuation of the signal was different suggesting that the collective behaviour of each microbubble in the suspension has a large impact on the attenuation characteristics of the medium. It is thus important to accurately model the behaviour of the surface tension. Variations in the incident frequency of the pulses also suggest that the resonant bubbles dominate the behaviour of the bubble suspension and its interaction with the acoustic wave.

Experiments have demonstrated that lipid-coated microbubbles do not always behave in the same manner when insonated with multiple ultrasound pulses. The processes that are likely to explain this phenomenon include changes in the nature or quantity of the bubble coating on the fast timescale, and gas diffusion on the slow timescale. By developing a novel model accounting for these behaviours in individual microbubbles, and combining with a model for the propagation of an acoustic wave through a suspension of scatterers, it has been shown that the contrast agent's characteristics are highly time-dependent. However, current imaging algorithms do not account for changes in the properties of the suspension after repeated ultra-

sound pulses. Consequently, significant improvements in medical diagnostic and therapeutic algorithms using contrast agents will only be possible once the results from this research are implemented.

6.2 Future work

There are many avenues for future research that could be explored as a result of the work in this thesis but some important ideas are highlighted below.

Extending the bubble diffusion model

The model presented in Chapter 2 simulating bubble growth in tissue under slow pressure variations required a number of simplifications to obtain a computationally tractable solution. It could be extended by modelling the problem in three-dimensions and solving the corresponding diffusion equations which would be a more realistic representation of tissue. The flux of gas through the bubble surface could be calculated by using more points around its boundary and the same numerical scheme accurate to second order employed in this thesis. It would then be useful to design an experiment in which a collagen tissue phantom was seeded with bubble micronuclei and placed in a pressure chamber, before being subjected to different decompression profiles. A viewing window in the chamber would allow the growth of the bubbles to be observed and recorded which could then be compared to the theoretical model developed in this work.

Developing the multiple scales analysis further

The convection-diffusion equations and boundary conditions on the bubble for the surfactant shedding model were analysed in Chapter 3 using a multiple scales analysis. It was found that the problem is more difficult than one investigated previously in the literature. It is possible that calculating higher order terms in the expansion may provide further insight into the problem. Furthermore, it is believed that using a smaller time-step during the initial shedding when the leading order term is $\mathcal{O}\left(Pe_{\mathrm{s}}^{1/2}\right)$, and subsequently lengthening the time-step, may provide additional computational efficiencies.

Theoretical properties of the shell

Currently, the effects of the lipid coating on a microbubble are poorly understood. This thesis has attempted to address this but there are still many open research questions. For instance, whilst surfactant shedding has been observed, the way in which this occurs is highly debated. A theoretical model that accounted for the physicochemical interactions of the molecules could enable the manner and speed of ejection to be estimated. This could in turn be used to update the concentration field around the bubble in the numerical calculations. Such a model could also help to understand the effects of a lipid-coating on the surface tension of a microbubble.

Further experiments on a single bubble

Whilst many optical studies have been carried out, further experiments could be carried that would provide more data for the model. For instance, fluorescently labelling and imaging the bubble during and after ultrasound insonation would provide evidence of surfactant shedding and support any model that might have been developed from the suggestion discussed previously.

In addition, the effect of the surfactant on the diffusivity of the gas through the bubble boundary has not been investigated. An experiment could be designed where a single lipid-coated microbubble was held in a laser trap and changes in its size recorded optically. Any changes in size could be attributed to gas diffusion and the rate at which the bubble shrank or grew could be fitted to a diffusivity model that depended on the surfactant concentration on the bubble's surface. This experiment could be repeated for bubbles of different sizes, ages, shell and gas compositions in order to provide further data.

Including more accurate multiple scattering effects in the propagation model

The results of Chapters 4 and 5 suggest that the model is only accurate and stable at low concentrations. To extend this research to suspensions of concentrations higher than 10^5 bubbles/ml, additional theoretical and experimental work is required to develop models valid in this regime. This includes accounting for multiple scattering interactions that are currently ignored in the nonlinear propagation model by including higher order scattering in the derivation. Additionally, the size of the bubbles is assumed to be much smaller than the incident wavelength. To accurately account for larger bubbles in the population, higher order terms must be retained in the derivation such that their presence results in a small correction in the final equation.

Computational efficiencies in the propagation model

The homogeneous sheet approach in Chapter 4 was an attempt to reduce the computational complexity of the nonlinear propagation model in a polydisperse bubble population. It was found that it is an unsuitable approximation for biomedical ultrasound purposes but the problem could still benefit from a more computationally efficient approach. One such approach could be a fast multipole method (Nishimura, 2002) where each scattering source in the system is described in terms of Green's functions which are expanded using a multipole expansion. In the far-field, sources in close proximity are approximated as acting from a single source thus significantly reducing the computational complexity of the problem.

APPENDIX A

DECOMPRESSION PROFILES AND RESULTS

Here, the decompression profiles that are used to simulate bubble growth in tissue during a dive in Section 2.4 are noted, as well as the results. Dives are simulated for different depths, "riskiness", gas mixtures and open- and closed-circuit devices. The majority of dives simulated are technical – they involve decompression stops and/or a breathing gas other than air is used – although recreational dives are also included for comparison.

A.1 Air dives

Even if the gas breathed throughout the dive is air, decompression stops might be necessary if the dive is sufficiently deep or long. A set of recreational dives – with no decompression stops – and technical dives on air were planned and the depth profiles are shown in figure A.1. Results for the maximum bubble radius size during, immediately on surfacing and after a 30 minute surface interval are displayed in table A.1.

The recreational dives were planned using the PADI Recreational Dive Planner and included a 3 minute "safety stop" at 5 meters, as recommended by PADI.

A.2 Trimix dives

Trimix is a form of breathing gas that is a mixture of helium, nitrogen and oxygen. The percentages of these gases can theoretically be varied in any way that the diver desires. Furthermore, multiple gases may be carried by the diver and used at various stages during decompression. This allows the diver to safely increase the rate of off-gassing from their body tissues by decreasing the amount of inert gas breathed in, or alternatively reduce the risk of oxygen toxicity by decreasing the partial pressure of oxygen in the breathing gas. Thus, not only is there a depth profile involving various decompression stages back to the surface, there is a breathing gas profile for the air breathed by the diver during the dive.

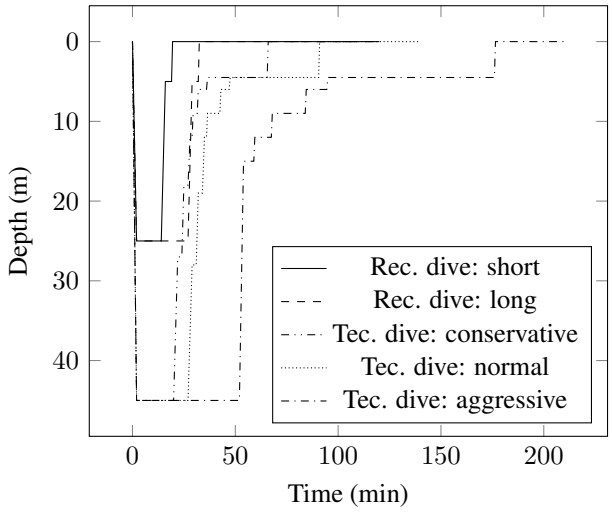

Figure A.1: Profiles for air dives used in numerical simulations including recreational (rec) and technical (tec) dives.

Dive (max depth – BT)	Characteristic	Max bubble radius (µm) **any time** / after surfacing / 30 min SI	
		5 bubbles in tissue	10 bubbles in tissue
25 m – 12 min	Recreational (short)	**5.9** / 4.2 / 5.6	**6.1** / 4.3 / 5.9
25 m – 25 min	Recreational	**6.6** / 4.5 / 6.4	**7.1** / 4.9 / 6.9
45 m – 18 min	Technical (conservative)	**7.0** / 6.9 / 6.2	**7.7** / 7.7 / 6.9
45 m – 20 min	Technical (normal)	**7.7** / 7.0 / 6.3	**8.0** / 6.1 / 5.0
45 m – 50 min	Technical (aggressive)	**7.7** / 2.4 / 2.3	**8.3** / 5.2 / 5.2

Table A.1: Maximum bubble size during decompression simulation of air dives comparing dives of varying maximum depth and bottom time (BT). The size is recorded at: any time during the simulation; immediately after surfacing; after a surface interval (SI) of 30 minutes.

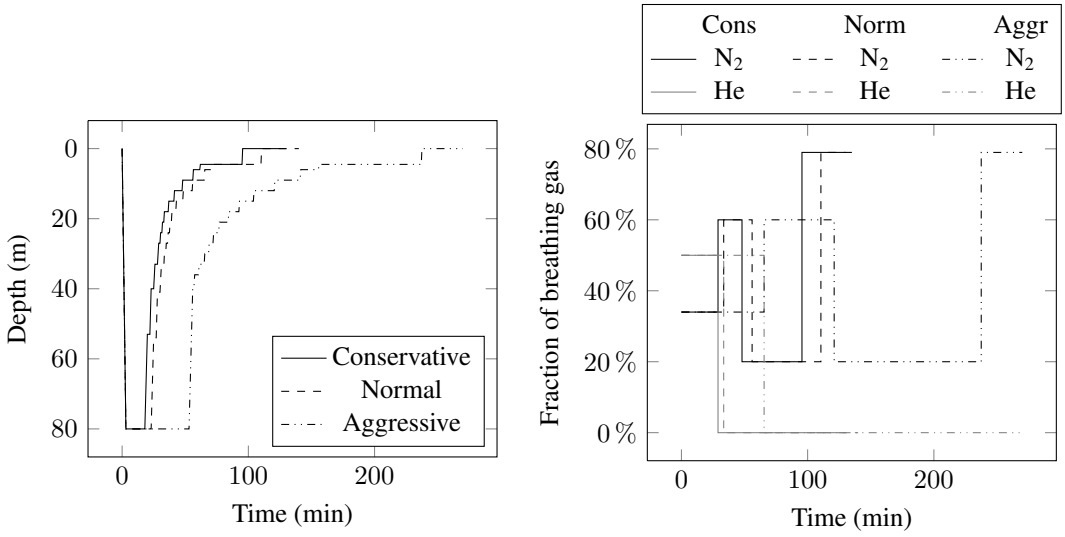

(a) Depth profile

(b) Gas mixture profile

Figure A.2: Dive and gas profiles for trimix dives to 80 m.

The depth and gas profiles used to simulate trimix dives to 80 metres are shown in figure A.2. Results for the maximum bubble radius size during, immediately on surfacing and after a 30 minute surface interval are displayed in table A.2.

An additional factor is that divers may choose to use a closed-circuit breathing apparatus as opposed to the more usual open-circuit device. In an open-circuit set-up, all exhaled gas is expelled whereas closed-circuit devices recycle the exhaled gas, scrubbing carbon dioxide out and injecting more oxygen if required. Hence this latter set-up allows more flexibility in the composition of the breathing gases since the diver is not restricted to what they are carrying in their bottles. Consequently open- and closed-circuit dives require different dive and gas profiles to be planned.

The decompression and gas profiles for deep dives to 120 metres on open-circuit are shown in figures A.3(a) and (b), and similar profiles for closed-circuit are shown in figures A.3(c) and (d). Results for the maximum bubble radius size during, immediately on surfacing and after a 30 minute surface interval are displayed in table A.3.

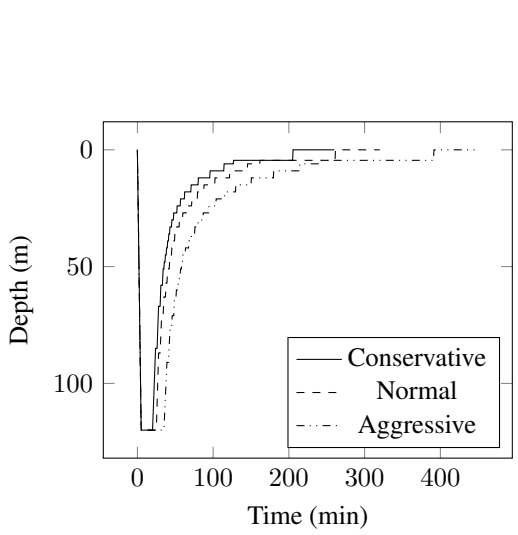

(a) Depth profile: OC

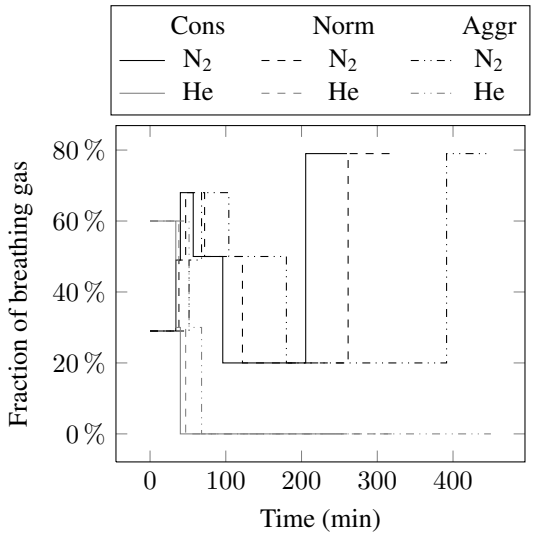

(b) Gas mixture profile: OC

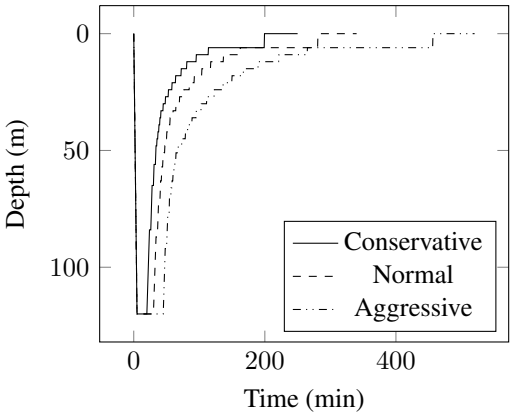

(c) Depth profile: CC

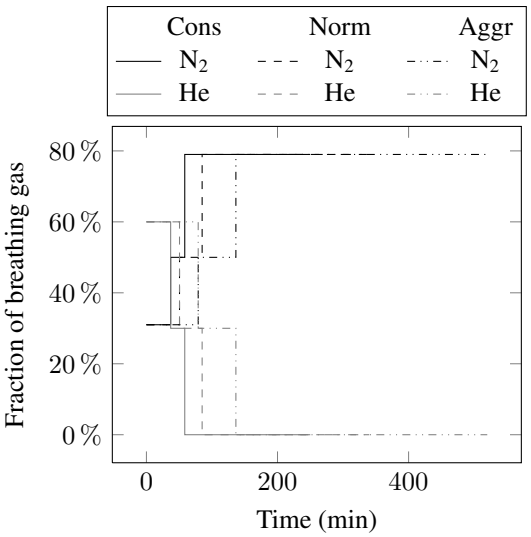

(d) Gas mixture profile: CC

Figure A.3: Dive and gas mixture profiles for trimix dives to 120 metres. Sub-figures (a) and (b) are dives planned for an open-circuit (OC) breathing device and sub-figures (c) and (d) are profiles for a closed-circuit (CC) breathing device.

Dive (80 m) Bottom time	Characteristic	Max bubble radius (μm) **any time** / after surfacing / 30 min SI	
		5 bubbles in tissue	10 bubbles in tissue
15 min	Conservative	**15.5** / 14.6 / 13.3	**14.6** / 13.8 / 12.7
20 min	Normal	**16.2** / 14.9 / 13.7	**14.9** / 13.9 / 12.8
50 min	Aggressive	**17.8** / 12.2 / 10.6	**16.1** / 11.4 / 10.2

Table A.2: Maximum bubble sizes during decompression simulation of trimix dives to 80 metres for various dive profiles. The size is recorded at: any time during the simulation; immediately after surfacing; after a surface interval (SI) of 30 minutes.

Dive (120 m) Bottom time	Characteristic	Max bubble radius (μm) **any time** / after surfacing / 30 min SI	
		3 bubbles in tissue	8 bubbles in tissue
15 min	Conservative OC	**18.4** / 7.2 / 4.5	**18.1** / 11.1 / 9.6
20 min	Normal OC	**19.5** / 2.2 / 2.0	**19.0** / 10.1 / 8.5
30 min	Aggressive OC	**22.0** / 2.2 / 2.0	**19.2** / 3.7 / 2.4
15 min	Conservative CC	**18.4** / 13.1 / 11.6	**18.3** / 14.3 / 12.8
25 min	Normal CC	**21.5** / 11.3 / 9.6	**20.4** / 13.0 / 12.1
40 min	Aggressive CC	**23.9** / 2.3 / 2.2	**22.9** / 9.0 / 8.0

Table A.3: Maximum bubble sizes during decompression simulation of trimix dives to 120 metres for various dive profiles, including open-circuit (OC) and closed-circuit (CC) diving apparatus. The size is recorded at: any time during the simulation; immediately after surfacing; after a surface interval (SI) of 30 minutes.

APPENDIX B

BUBBLE DYNAMICS

B.1 Rayleigh-Plesset equation

The most common form of equation for describing bubble oscillations was first derived by Rayleigh (1917) and subsequently extended by Plesset and Prosperetti (1977) to include surface tension and liquid viscosity. The assumptions for the derivation are that: the bubble oscillations are symmetric; the bubble is in an infinite medium; the bubble radius is much smaller than the wavelength of the driving pressure field (as would be the case for contrast agents *in vivo*); external body forces are ignored; bulk viscous forces can be neglected; the density of the fluid is much larger than the density of the gas; the distribution of the gas remains constant throughout the bubble as does the amount of gas contained in the bubble.

Leighton (2007) showed that it is possible to derive the Rayleigh-Plesset equation by integrating the Navier-Stokes equation or by considering the bubble radius dynamics. The latter, most commonly used, derivation is demonstrated in this chapter.

The fluid velocity around a spherical bubble of radius R in an incompressible medium oscillating as a result of an insonifying field can be written as,

$$\boldsymbol{u}(r,t) = \frac{R^2(t)}{r^2(t)}\dot{R}(t) \tag{B.1.1}$$

As it oscillates, work is done on the bubble by the pressure at that point. Since the wavelength-to-radius ratio is large for biomedical purposes, it is assumed that the pressure can be approximated by the pressure in the far field $p_\infty = p_0 + p(t)$, where p_0 is the ambient (static) pressure and $p(t)$ is the driving pressure. The kinetic energy in the liquid of density ρ is thus equal to the difference between the work done at infinity and the work done by the pressure at the bubble wall p_L,

$$\begin{aligned}\phi_{\mathrm{KE}} &= \frac{\rho}{2}\int_R^\infty 4\pi r^2 u^2 \mathrm{d}r \\ &= 2\pi\rho R^3\dot{R}^2 \end{aligned} \tag{B.1.2}$$

This is rewritten as,

$$\int_{R_0}^{R}(p_L - p_\infty)4\pi R^2 \mathrm{d}r = 2\pi\rho R^3\dot{R}^2 \tag{B.1.3}$$

By differentiating with respect to R,

$$p_L(t) - p_\infty = \rho\left(R\ddot{R} + \frac{3\dot{R}^2}{2}\right) + \mathcal{O}\left(\frac{\dot{R}}{\mathcal{C}}\right) \tag{B.1.4}$$

Therefore the difference between work done at the bubble wall and far from the bubble is equal to the amount of kinetic energy that is given to the liquid. Since the far-field pressure is assumed to comprise of a static and driving component, the Rayleigh-Plesset equation for the motion of the bubble wall is,

$$R\ddot{R} + \frac{3\dot{R}^2}{2} = \frac{1}{\rho}(p_L(t) - p_0 - p(t)) \tag{B.1.5}$$

B.2 The liquid pressure: including the loss mechanisms

In order to further understand the motion of the bubble wall, it is necessary to find an appropriate expression for p_L. To include all loss mechanisms in a fully nonlinear manner would be extremely difficult, so to make progress with the problem, assumptions about losses that can be ignored in the radius frame are made.

B.2.1 Neglecting dissipation

If all forms of dissipation in the system are neglected, then p_L is simply the difference between the pressure inside the bubble p_i and the Laplace pressure p_σ that is introduced due to the effects of surface tension. The internal pressure can then be written as the sum of the gas and vapour pressures p_g and p_v respectively,

$$p_L = p_i - p_\sigma = p_g + p_v - p_\sigma \tag{B.2.1}$$

where, for the surface tension σ,

$$p_\sigma = \frac{2\sigma}{R} \tag{B.2.2}$$

At this point, it is necessary to derive an expression for p_g and the easiest way of doing this is to use a polytropic law. Essentially, the pressure inside the gas in the bubble for a given radius is compared with the case of the bubble at rest, with initial radius R_0. First, the equilibrium values denoted by superscript e's are found,

$$p_i^e = p_g^e + p_v = p_0 + \frac{2\sigma}{R_0} \tag{B.2.3}$$

Hence, using a polytropic relationship with polytropic index γ and equation (B.2.3) for the value of the equilibrium gas pressure,

$$\begin{aligned} p_g &= p_g^e \left(\frac{R_0}{R}\right)^{3\gamma} \\ &= \left(p_0 + \frac{2\sigma}{R_0} - p_v\right)\left(\frac{R_0}{R}\right)^{3\gamma} \end{aligned} \tag{B.2.4}$$

Physically, the polytropic index is used to adjust the rate of thermal flux across the wall of the bubble, in effect a relationship between bubble volume and pressure. This relationship neglects *net* thermal losses within the system as well as radiation forces, which is a result of the assumption that the fluid is incompressible. Combining equations (B.2.1) and (B.2.4) leads to,

$$\begin{aligned} p_L &= p_g + p_v - p_\sigma \\ &= \left(p_0 + \frac{2\sigma}{R_0} - p_v\right)\left(\frac{R_0}{R}\right)^{3\gamma} + p_v - p_\sigma \end{aligned} \tag{B.2.5}$$

B.2.2 Viscous losses

The simplest approach is to include only viscous forces by matching normal stresses across the bubble wall for a fluid with shear viscosity μ_l,

$$p_L = p_i - \frac{2\sigma}{R} - \frac{4\mu_l \dot{R}}{R} \tag{B.2.6}$$

The difference between the pressure at the bubble wall and the pressure at some boundary in the fluid p' is proportional to the normal shear stress at the bubble wall $\epsilon_r' = \partial \boldsymbol{u}/\partial r$,

$$p_L - p' = -2\mu_l \epsilon_r' = -2\mu_l \frac{\partial \boldsymbol{u}}{\partial r} \tag{B.2.7}$$

Substituting the equation for $\boldsymbol{u}(r,t)$ (B.1.1) into (B.2.7) leads to,

$$\begin{aligned} p_L &= p' - 2\mu_l \frac{\partial}{\partial r}\left(\frac{R^2(t)}{r^2(t)}\dot{R}(t)\right) \\ &= p' - 2\mu_l \frac{-2R^2\dot{R}}{r^3} \\ &= p' + \frac{4\mu_l R^2 \dot{R}}{r^3} \end{aligned} \tag{B.2.8}$$

Using Bernoulli's equation for unsteady potential flow to relate the pressure at a boundary in the fluid p' to the radius of the bubble,

$$\frac{p' - p_\infty}{\rho} = -\frac{\partial \psi}{\partial t} - \frac{\boldsymbol{u}^2}{2} \tag{B.2.9}$$

An expression for the velocity potential ψ is now required. If it is assumed that the flow is irrotational, then the fluid velocity can be written in terms of a velocity potential,

$$\boldsymbol{u} = \nabla \psi$$

In addition, if the linear wave equation for the velocity potential is written in spherical coordinates,

$$\frac{1}{\mathcal{C}^2}\frac{\partial^2 \psi}{\partial t^2} - \nabla^2 \psi = 0 \tag{B.2.10}$$

then a solution in the long wavelength limit is found in terms of the amplitude function $A(t)$,

$$\psi = -\frac{A(t)}{r}$$

By applying the boundary condition $\boldsymbol{u}_{r=R} = |\partial\psi/\partial r|_{r=R} = \dot{R}$,

$$\begin{aligned} A(t) &= R^2\dot{R} \\ \implies \psi(r,t) &= \frac{-R^2\dot{R}}{r} \end{aligned} \tag{B.2.11}$$

Subsequently, inserting the expressions for the velocity potential (B.2.11) and the velocity (B.1.1) in equation (B.2.9) and evaluating at the bubble wall results in,

$$\frac{p' - p_\infty}{\rho} = R\ddot{R} + \frac{3\dot{R}^2}{2} \tag{B.2.12}$$

Eliminating p' by making use of equation (B.2.8) evaluated at the bubble wall leads to,

$$R\ddot{R} + \frac{3\dot{R}^2}{2} = \frac{1}{\rho}\left(p_L - \frac{4\mu_l \dot{R}}{R} - p_\infty\right) \tag{B.2.13}$$

Using equation (B.2.5) in (B.2.13) and the assumption that the pressure at infinity is the sum of the static and driving pressures, the Rayleigh-Plesset equation is finally derived, incorporating both surface tension and viscous damping effects,

$$R\ddot{R} + \frac{3\dot{R}^2}{2} = \frac{1}{\rho}\left(\left(p_0 + \frac{2\sigma}{R_0} - p_v\right)\left(\frac{R_0}{R}\right)^{3\gamma} + p_v - \frac{2\sigma}{R} - \frac{4\mu_l\dot{R}}{R} - p_0 - p(t)\right) \quad \text{(B.2.14)}$$

B.3 Linearising the Rayleigh-Plesset equation

The behaviour of the Rayleigh-Plesset equation (B.2.14) is investigated if bubble oscillations are assumed to be small compared to the equilibrium bubble radius R_0. To linearise, $R = R_0\big(1 + x(t)\big)$ is substituted into (B.2.14) assuming a small oscillation amplitude $x(t) \ll 1$, noting that $R^{-1} \approx R_0^{-1}\big(1 - x(t)\big)$ and terms of $\mathcal{O}\left(x^2\right)$ are neglected,

$$R_0^2\big(1+x\big)\ddot{x} + \frac{3}{2}R_0^2\dot{x}^2 = \frac{1}{\rho}\left(\left(p_0 - p_v + \frac{2\sigma}{R_0}\right)\big(1-3x\gamma\big) + p_v - \frac{2\sigma}{R_0}\big(1-x\big) - 4\mu_l\dot{x}\big(1-x\big) - p_0 - p(t)\right)$$

and after rearranging,

$$\rho R_0^2\ddot{x} + 4\mu_l\dot{x} + \left(3\gamma\left(p_0 - p_v + \frac{2\sigma}{R_0}\right) - \frac{2\sigma}{R_0}\right)x = \left(p_0 - p_v + \frac{2\sigma}{R_0} + p_v - \frac{2\sigma}{R_0} - p_0 - p(t)\right)$$

Consequently, the linearised Rayleigh-Plesset equation is,

$$\ddot{x} + \delta\dot{x} + \omega_{\mathrm{N}}^2 x = -\frac{p(t)}{\rho R_0^2} \quad \text{(B.3.1)}$$

where,

$$\delta = \frac{4\mu_l}{\rho R_0^2}$$

$$\omega_{\mathrm{N}}^2 = \frac{1}{\rho R_0^2}\left(3\gamma\left(p_0 - p_v + \frac{2\sigma}{R_0}\right) - \frac{2\sigma}{R_0}\right)$$

Now assuming that,

$$x(t) = \varphi e^{i\omega t}$$

$$p(t) = \bar{p}e^{i\omega t}$$

where φ and $\bar{p}$ account for the phase differences and it is implicit that the real part is taken, these expressions are inserted into (B.3.1),

$$\omega^2 - i\delta\omega - \omega_{\mathrm{N}}^2 = \frac{\bar{p}}{\rho R_0^2\varphi} \quad \text{(B.3.2)}$$

For a given value of $\bar{p}$, the peak amplitude response occurs at a frequency ω_{R} (also known as the "resonance frequency") and is given by the minimum of the spectral radius of the left-hand side,

$$\omega_{\mathrm{R}} = \sqrt{\omega_{\mathrm{N}}^2 - \frac{\delta^2}{2}} \tag{B.3.3}$$

If viscosity and surface tension are neglected, the natural frequency ω_{N} for a single bubble in an infinite liquid is recovered, also known as the Minnaert frequency,

$$\omega_{\mathrm{N}}^2 = \frac{3\gamma(p_0 - p_v)}{\rho R_0^2} \tag{B.3.4}$$

The neglected parameter δ represents the dissipation coefficient due to the liquid viscosity and acts to dampen the pressure field over time.

Additionally, equation (B.3.2) can be solved for φ, yielding,

$$\varphi = \frac{\bar{p}}{\rho R_0^2 \left(\omega^2 - i\delta\omega - \omega_{\mathrm{N}}^2\right)} \tag{B.3.5}$$

The bubble response φ is a complex number such that the real part is the amplitude of the bubble oscillations and the phase of φ gives the phase difference between $p(t)$ and R.

B.4 Acoustic attenuation and scatter

The increased attenuation caused by adding bubbles to a liquid is given by the extinction cross-section Ω, defined in terms of the power absorbed by the oscillating bubble $P_A(R_0, \omega)$ and the intensity of the incoming wave $I^{\mathrm{inc}}(\omega)$,

$$\begin{aligned} \Omega(R_0, \omega) &= \frac{P_A(R_0, \omega)}{I^{\mathrm{inc}}(\omega)} \\ &= \frac{P_A(R_0, \omega)}{|\bar{p}|^2 (2\rho\mathcal{C})^{-1}} \end{aligned} \tag{B.4.1}$$

From equation (B.3.1), the instantaneous power loss is $\rho R_0^3 \delta \dot{x}^2$ and using the linearised definition of $x = \varphi\cos(\omega t)$, the time-averaged power loss over one period is,

$$P_A(R_0, \omega) = \frac{\delta}{2}\rho R_0^3 \omega^2 \varphi^2$$

By inserting this expression into equation (B.4.1) and using (B.3.5), the extinction cross-section is given by,

$$\begin{aligned}\Omega(R_0,\omega) &= 4\pi R_0^2 \frac{\delta\omega^2\mathcal{C}}{R_0\big((\omega^2-\omega_{\mathrm{N}}^2)^2+\delta^2\omega^2\big)} \\ &= \frac{4\pi R_0\delta\omega^2\mathcal{C}}{(\omega^2-\omega_{\mathrm{N}}^2)^2+\delta^2\omega^2}\end{aligned} \tag{B.4.2}$$

The acoustic attenuation $a(\omega)$ is defined as,

$$a(\omega) = 10\log_{10}(e)\Omega(R_0,\omega)$$

In a collection of bubbles at low concentrations, the scattered waves from the bubbles do not interact and the power absorbed by the suspension is the sum of the power absorbed by the individual bubbles. Hence, the acoustic attenuation of the bubble cloud with a concentration density of bubbles with size R given by $n(R)$ is,

$$a(\omega) = 10\log_{10}(e)\int_0^\infty \Omega(R,\omega)n(R)\mathrm{d}R \tag{B.4.3}$$

APPENDIX C

NUMERICAL SIMULATION PARAMETER VALUES

C.1 Bubble diffusion modelling

The values used in the numerical simulations of Chapter 2 are presented in table C.1.

Parameter	Unit	Symbol	Value
Ambient surface pressure	kPa	p_0	101.3
Tissue length: x-direction	m	T_x	5×10^{-4}
Tissue length: y-direction	m	T_y	5×10^{-4}
Tissue space-step	m	$\delta x = \delta y$	2×10^{-6}
Tissue time-step	min	δt	1×10^{-3}
Diffusivity: gas in water	$m^2 \cdot s^{-1}$	D	0.353×10^{-9}
Henry's constant: N_2 in water	$kg \cdot m^{-3} \cdot atm^{-1}$	$k_H^{N_2}$	1.708×10^{-2}
Henry's constant: He in water	$kg \cdot m^{-3} \cdot atm^{-1}$	k_H^{He}	1.48×10^{-3}
Henry's constant: O_2 in water	$kg \cdot m^{-3} \cdot atm^{-1}$	$k_H^{O_2}$	4.16×10^{-2}
Alpha: N_2	$m^3 \cdot atm \cdot kg^{-1}$	α^{N_2}	0.9084
Alpha: He	$m^3 \cdot atm \cdot kg^{-1}$	α^{He}	6.355
Alpha: O_2	$m^3 \cdot atm \cdot kg^{-1}$	α^{O_2}	0.7944
Microbubble nucleus	m	R_0	2×10^{-6}
Surface tension	$N \cdot m^{-1}$	σ	0.07
Viscosity	$N \cdot s \cdot m^{-2}$	μ	0.001
Bulk modulus of tissue	$N \cdot m^{-2}$	B	2.5×10^7
Volume of tissue affected by bubble	m^3	V_T	5.236×10^{-13}
Oxygen metabolism			50%

Table C.1: Parameter values employed in the numerical simulation of bubble growth in tissue during decompression dives.

C.2 Lipid-coated microbubble modelling

The values used in the numerical simulation of Chapters 3 to 5 are presented in table C.2.

Parameter	Unit	Symbol	Value
Ambient pressure	kPa	p_0	101.3
Vapour pressure	kPa	p_v	2.3
Wavespeed in water	$\mathrm{m \cdot s^{-1}}$	$\mathcal{C}$	1500
Density: water	$\mathrm{kg \cdot m^{-3}}$	ρ	1000
Surface tension: air/water	$\mathrm{N \cdot m}$	σ_0	0.07
Surface tension: minimum	$\mathrm{N \cdot m}$	σ_{min}	0.001
Surface tension sigmoid curve parameters		Q	0.9799
		U	138.8
		W	0.9814
		Y	2.926
Viscosity: water	$\mathrm{N \cdot s \cdot m^{-2}}$	μ_l	0.001
Shell viscosity	$\mathrm{kg \cdot s^{-1}}$	μ_{s}	4×10^{-9}
Surfactant concentration in bulk liquid	$\mathrm{kg \cdot m^{-3}}$	C_∞	1.0
Surface concentration: max. as $C_\infty \to C_{\mathrm{sat}}$	$\mathrm{kg \cdot m^{-2}}$	Γ^*	3×10^{-8}
Diffusivity: air/water	$\mathrm{m^2 \cdot s^{-1}}$	D_0^{air}	2×10^{-9}
Diffusivity: air/water minimum	$\mathrm{m^2 \cdot s^{-1}}$	$D_{\mathrm{min}}^{\mathrm{air}}$	1×10^{-14}
Diffusivity: PFC/water	$\mathrm{m^2 \cdot s^{-1}}$	D_0^{PFC}	1×10^{-10}
Diffusivity: PFC/water minimum	$\mathrm{m^2 \cdot s^{-1}}$	$D_{\mathrm{min}}^{\mathrm{PFC}}$	1×10^{-14}
Diffusivity: surfactant/water	$\mathrm{m^2 \cdot s^{-1}}$	D_{s}	1×10^{-12}
Diffusivity: surfactant/water minimum	$\mathrm{m^2 \cdot s^{-1}}$	D_{smin}	1×10^{-14}
Alpha: air	$\mathrm{m^2 \cdot s^{-2}}$	α^{air}	8.5×10^4
Alpha: PFC	$\mathrm{m^2 \cdot s^{-2}}$	α^{PFC}	1.3×10^4
Henry's constant: air in water	$\mathrm{s^2 \cdot m^{-2}}$	k_H^{air}	3.8×10^{-7}
Henry's constant: PFC in water	$\mathrm{s^2 \cdot m^{-2}}$	k_H^{PFC}	9.5×10^{-9}
Adsorption coefficient	$\mathrm{m^3 \cdot kg^{-1} \cdot s^{-1}}$	a_1	1.0
Desorption coefficient	$\mathrm{s^{-1}}$	a_2	0.01

Table C.2: Parameter values employed in the numerical simulation of a surfactant-coated microbubble insonated by ultrasound.

APPENDIX D

EXPERIMENTAL SET-UPS

A brief description of the set-ups of the experiments conducted by Viti et al. (2011), David Thomas (U. Edinburgh, unpublished data) and Sheetal Sanak (U. Oxford, unpublished data) is presented in this chapter.

D.1 Single bubble imaging experiments

Both Viti et al. (2011) and David Thomas carried out experiments on single Definity® contrast agent microbubbles by insonating them with multiple ultrasound pulses and capturing their oscillations using the high-speed Brandaris camera. The experiment was controlled via a Bubble Behaviour Testing (BBT) system which used a computer to coordinate the activation of the acoustical and optical equipment. Two transducers were used: one to generate the ultrasound pulses; the other to receive the echo. The set-up is shown in figure D.1.

A continuous light source was used to illuminate an individual microbubble. In Viti et al.'s experiments, the bubbles were inside a cellulose capillary with an inner diameter of $160\,\mu m$ which was acoustically and optically nearly transparent. David Thomas on the other hand, floated the bubble against a glass plate. In both set-ups, care was taken to ensure that other bubbles were sufficiently far from the focal region of the transducers and microscope that their acoustic scatter had a negligible effect on the target bubble. Furthermore, the experiments were carried out in a tank of water at approximately $22\,^{\circ}C$.

D.2 SonoVue® propagation experiments

A brief description of the experimental set-up used, kindly provided by Sheetal Sanak, is given here and shown in figure D.2.

The apparatus consisted of a single element 2.25 MHz focused transducer, an acoustically transparent chamber and a 75 μm needle hydrophone in a tank of degassed and deionised water with the temperature maintained at approximately 22 °C. A waveform generator was used to produce the desired electrical signal and amplified using a RF amplifier before being sent to the transducer. All signals from the hydrophone were recorded on an oscilloscope.

The chamber had minimal scattering or absorption properties, and was used to contain the microbubble suspension. It was made of a cube of Perspex® with circular windows on all four sides (roughly 12 mm in diameter). The distance between any two opposite windows was 2 cm, i.e. the propagation length. These windows were covered with polyvinylidene chloride film, and the top surface of the chamber was left open and above the tank water level to allow mild agitation of the microbubble suspension in between experiments. The chamber was filled with 4 ml of the sample solution being insonated each time. Loss of signal due to the presence of the chamber (reflection from the windows) was approximately 15% but all measurements were made using the same set-up, and relative to the signal obtained with the chamber full of the microbubble suspending liquid only.

The SonoVue® suspension was prepared according to the manufacturer's instructions and diluted in unfiltered 0.9% w/v phosphate buffered saline to create solutions with the desired concentrations. To prevent bubble flotation and to ensure a uniform distribution, the chamber containing the microbubble suspension was manually agitated at regular intervals between signal acquisitions.

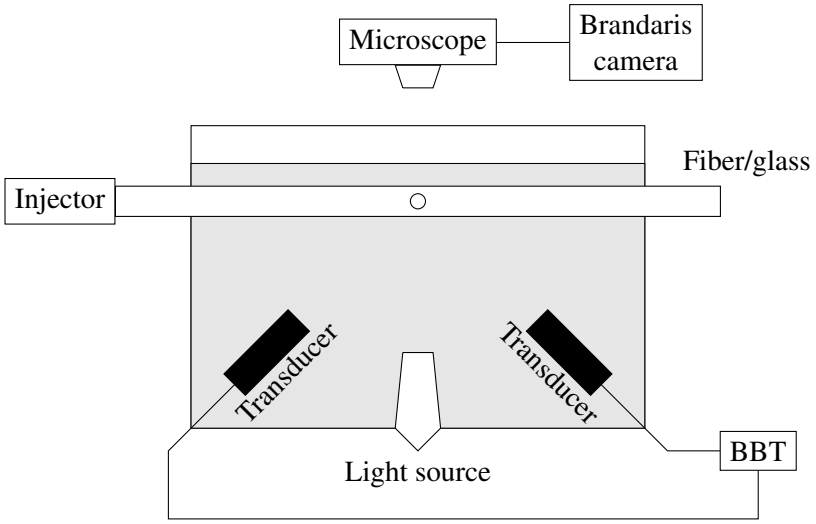

Figure D.1: Single bubble insonation experiment set-up. Two transducers are focused on the bubble: one to transmit the pulse; the other to record the echo. A continuous light source illuminated the microbubble so that the Brandaris high-speed camera could capture images of the oscillations. The coordination between acoustical and optical equipment was controlled via computer using a Bubble Behaviour Testing (BBT) system.

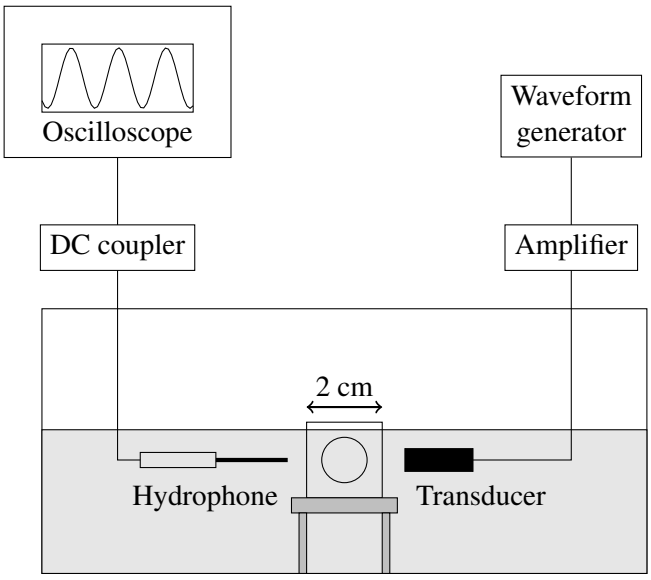

Figure D.2: SonoVue® propagation experiment set-up. A single element focused transducer transmitted the acoustic pulse through an acoustically transparent chamber containing the microbubble suspension and a needle hydrophone recorded the attenuated signal.

REFERENCES

Abramowitz, M. and Stegun, I.A., 1965. *Handbook of Mathematical Functions With Formulas, Graphs and Mathematical Table*. Courier Dover Publications.

Ahuja, A.S., 1972. Formulation of wave equation for calculating velocity of sound in suspensions. *Journal of the Acoustical Society of America*, 51(3B), pp. 916–919.

Ahuja, A.S., 1973. Wave equation and propagation parameters for sound propagation in suspensions. *Journal of Applied Physics*, 44(11), pp. 4863–4868.

Ahuja, A.S. and Hendee, W.R., 1978. Effects of particle shape and orientation on propagation of sound in suspensions. *Journal of the Acoustical Society of America*, 63, pp. 1074–1080.

Allegra, J.R. and Hawley, S.A., 1972. Attenuation of sound in suspensions and emulsions: theory and experiments. *Journal of the Acoustical Society of America*, 51, pp. 1545–1564.

Angel, Y.C. and Aristégui, C., 2005. Analysis of sound propagation in a fluid through a screen of scatterers. *Journal of the Acoustical Society of America*, 118, pp. 72–82.

Atchley, A.A., 1989. The Blake threshold of a cavitation nucleus having a radius-dependent surface tension. *Journal of the Acoustical Society of America*, 85, pp. 152–157.

Atchley, A.A. and Prosperetti, A., 1989. The crevice model of bubble nucleation. *Journal of the Acoustical Society of America*, 86, pp. 1065–1084.

Avetisyan, I.A., 1977. Effect of polymer additives on the acoustic properties of a liquid containing gas bubbles. *Soviet Physics Acoustics*, 23, pp. 285–288.

Behnke, A.R., 1951. Decompression sickness following exposure to high pressures. In: *Decompression Sickness*. Saunders Book Company, pp. 53–89.

Bert, P., 1878. *La Pression Barométrique*. G. Masson ed. Typographie Lahere.

Biancucci, B.A., Deutsch, S., Geselowitz, D.B. and Tarbell, J.M., 1999. In vitro studies of gas bubble formation by mechanical heart valves. *Journal of Heart Valve Disease*, 8(2), pp. 186–196.

Biot, M.A., 1956a. Theory of propagation of elastic waves in a fluid-saturated porous solid. I. Low-frequency range. *Journal of the Acoustical Society of America*, 28, pp. 168–178.

Biot, M.A., 1956b. Theory of propagation of elastic waves in a fluid-saturated porous solid. II. Higher frequency range. *Journal of the Acoustical Society of America*, 28(2), pp. 179–191.

Biot, M.A., 1962a. Generalized theory of acoustic propagation in porous dissipative media. *Journal of the Acoustical Society of America*, 34, pp. 1254–1264.

Biot, M.A., 1962b. Mechanics of deformation and acoustic propagation in porous media. *Journal of Applied Physics*, 33, pp. 1482–1498.

Blake, F.G., 1949. *Onset of Cavitation in Liquids.* PhD. Harvard University.

Blatteau, J.E., Gempp, E., Galland, F.M., Pontier, J.M., Sainty, J.M. and Robinet, C., 2005. Aerobic exercise 2 hours before a dive to 30 msw decreases bubble formation after decompression. *Aviation, Space and Environmental Medicine*, 76(7), pp. 666–669.

Blatteau, J.E., Souraud, J.B., Gempp, E. and Boussuges, A., 2006. Gas nuclei, their origin and their role in bubble formation. *Aviation, Space and Environmental Medicine*, 77(10), pp. 1068–1076.

Borden, M.A., Kruse, D.E., Caskey, C.F., Zhao, S., Dayton, P.A. and Ferrara, K.W., 2005. Influence of lipid shell physicochemical properties on ultrasound-induced microbubble destruction. *IEEE Transactions on Ultrasonics, Ferroelectrics and Frequency Control*, 52(11), pp. 1992–2002.

Bove, A.A., 1998. Risk of decompression sickness with patent foramen ovale. *Undersea and Hyperbaric Medicine*, 25(3), pp. 175–178.

Bove, A.A. and Davis, J.C., 2003. *Bove and Davis' Diving Medicine*. WB Saunders Co.

Boycott, A.E., Damant, G.C.C. and Haldane, J.S., 1908. The prevention of compressed-air illness. *Journal of Hygiene*, 8, pp. 342–443.

Brubakk, A.O., Grip, A., Holand, B., Ornaheim, J. and Tonjum, S., 1981. Pulsed Doppler ultrasound for studying haemodynamic changes and bubbles during simulated diving. In: *Proceedings of the VIth Annual Congress of the EUBS. Cambridge, UK*.

Bühlmann, A.A., 1983. *Decompression – Decompression Sickness*. G. Michel ed. Springer-Verlag.

Butler, B.D. and Hills, B.A., 1979. The lung as a filter for microbubbles. *Journal of Applied Physiology*, 47(3), pp. 537–543.

Caflisch, R.E., Miksis, M.J., Papanicolaou, G.C. and Ting, L., 1985. Effective equations for wave propagation in bubbly liquids. *Journal of Fluid Mechanics*, 153, pp. 259–273.

Chappell, M.A. and Payne, S.J., 2006. A physiological model of the release of gas bubbles from crevices under decompression. *Respiratory Physiology & Neurobiology*, 153(2), pp. 166–180.

Church, C.C., 1995. The effects of an elastic solid surface layer on the radial pulsations of gas bubbles. *Journal of the Acoustical Society of America*, 97, pp. 1510–1521.

Commander, K.W. and Prosperetti, A., 1989. Linear pressure waves in bubbly liquids: comparison between theory and experiments. *Journal of the Acoustical Society of America*, 85, pp. 732–746.

Cross, S.J., Evans, S.A., Thomson, L.F., Lee, H.S., Jennings, K.P. and Shields, T.G., 1992. Safety of subaqua diving with a patent foramen ovale. *BMJ: British Medical Journal*, 304(6825), pp. 481–482.

Crum, L.A., 1980. Measurements of the growth of air bubbles by rectified diffusion. *Journal of the acoustical society of america*, 68(1), pp. 203–211.

Crum, L.A. and Hansen, G.M., 1982. Generalized equations for rectified diffusion. *Journal of the Acoustical Society of America*, 72(5), pp. 1586–1592.

De Jong, N., Cornet, R. and Lancee, C.T., 1994. Higher harmonics of vibrating gas-filled microspheres. Part one: simulations. *Ultrasonics*, 32(6), pp. 447–453.

Devin, C., 1959. Survey of thermal, radiation, and viscous damping of pulsating air bubbles in water. *Journal of the Acoustical Society of America*, 31, pp. 1654–1667.

Dhainaut, M. and Johansen, S.T., 2002. Literature study on observations and experiments on coalescence and breakup of bubbles and drops. *SINTEF Report*, 24, pp. 1–64.

Doinikov, A.A. and Bouakaz, A., 2011. Review of shell models for contrast agent microbubbles. *IEEE Transactions on Ultrasonics, Ferroelectrics and Frequency Control*, 58(5), pp. 981–993.

Doinikov, A.A., Haac, J.F. and Dayton, P.A., 2009. Modeling of nonlinear viscous stress in encapsulating shells of lipid-coated contrast agent microbubbles. *Ultrasonics*, 49(2), pp. 269–275.

Dujić, Ž., Duplančic, D., Marinovic-Terzić, I., Baković, D., Ivančev, V., Valic, Z., Eterović, D., Petri, N.M., Wisløff, U. and Brubakk, A.O., 2004. Aerobic exercise before diving reduces venous gas bubble formation in humans. *Journal of Physiology*, 555(3), pp. 637–642.

Dunning, W.J., 1969. General and theoretical introduction. In: A. Zettlemoyer ed. *Nucleation*. Marcel Dekker Inc., New York City. Ch. 1, pp. 1–67.

Edmonds, C. and Thomas, R.L., 1972. Medical aspects of diving–4. *Medical Journal of Australia*, 2(24), pp. 1367–1370.

Eller, A. and Flynn, H.G., 1965. Rectified diffusion during nonlinear pulsations of cavitation bubbles. *Journal of the Acoustical Society of America*, 37, pp. 493–503.

Epstein, P.S., 1941. On the absorption of sound waves in suspensions and emulsions. In: *Theodore von Karman Anniversary Volume*. California Institute of Technology, pp. 162–188.

Epstein, P.S. and Carhart, R.R., 1953. The absorption of sound in suspensions and emulsions. I. Water fog in air. *Journal of the Acoustical Society of America*, 25, pp. 553–565.

Epstein, P.S. and Plesset, M.S., 1950. On the stability of gas bubbles in liquid-gas solutions. *Journal of Chemical Physics*, 18, pp. 1505–1509.

Evans, J.M. and Attenborough, K., 1997. Coupled phase theory for sound propagation in emulsions. *Journal of the Acoustical Society of America*, 102, pp. 278–282.

Fahlman, A. and Dromsky, D.M., 2006. Dehydration effects on the risk of severe decompression sickness in a swine model. *Aviation, Space and Environmental Medicine*, 77(2), pp. 102–106.

Ferrara, K., Pollard, R. and Borden, M.A., 2007. Ultrasound microbubble contrast agents: fundamentals and application to gene and drug delivery. *Annual Review of Biomedical Engineering*, 9, pp. 415–447.

Feuillade, C., 1996. The attenuation and dispersion of sound in water containing multiply interacting air bubbles. *Journal of the Acoustical Society of America*, 99, pp. 3412–3430.

Feuillade, C., 2002. Comment on "Corrections to Foldy's effective medium theory for propagation in bubble clouds and other collections of very small scatterers". *Journal of the Acoustical Society of America*, 111, pp. 1552–1555.

Fick, R., 1911. Zum Streit um den Gelenkdruck. *Anatomy and Embryology*, 43(2), pp. 397–414.

Fisher, J.C., 1948. The fracture of liquids. *Journal of Applied Physics*, 19(11), pp. 1062–1067.

Foldy, L.L., 1945. The multiple scattering of waves. I. General theory of isotropic scattering by randomly distributed scatterers. *Physical Review*, 67(3-4), pp. 107–119.

Fox, F.E. and Herzfeld, K.F., 1954. Gas bubbles with organic skin as cavitation nuclei. *Journal of the Acoustical Society of America*, 26(6), pp. 984–989.

Fyrillas, M.M. and Szeri, A.J., 1994. Dissolution or growth of soluble spherical oscillating bubbles. *Journal of Fluid Mechanics*, 277, pp. 381–407.

Fyrillas, M.M. and Szeri, A.J., 1995. Dissolution or growth of soluble spherical oscillating bubbles: the effects of surfactants. *Journal of Fluid Mechanics*, 289, pp. 295–314.

Fyrillas, M.M. and Szeri, A.J., 1996. Surfactant dynamics and rectified diffusion of microbubbles. *Journal of Fluid Mechanics*, 311(-1), pp. 361–378.

Gaunaurd, G.C. and Huang, H., 1995. Acoustic scattering by an air-bubble near the sea surface. *IEEE Journal of Oceanic Engineering*, 20(4), pp. 285–292.

Gaunaurd, G.C., Huang, H. and Strifors, H.C., 1995. Acoustic scattering by a pair of spheres. *Journal of the Acoustical Society of America*, 98, pp. 495–507.

Gelderblom, E., Kooiman, K., Böhmer, M., de Jong, N., Lohse, D. and Versluis, M., 2010. Ultra high-speed fluorescence imaging of ultrasound contrast agents for imaging and therapy. In: *Proceedings of 20th International Congress on Acoustics*.

Gilmore, F.R., 1952. *The growth or collapse of a spherical bubble in a viscous compressible liquid*. Research report. Hydrodynamics Laboratory, California Institute of Technology, Pasadena, California, USA.

Giribabu, K. and Ghosh, P., 2008. Binary coalescence of air bubbles in viscous liquids in presence of non-ionic surfactant. *Canadian Journal of Chemical Engineering*, 86(4), pp. 643–650.

Girod, G., Jaussi, A., Rosset, C., De Werra, P., Hirt, F. and Kappenberger, L., 2002. Cavitation versus degassing: in vitro study of the microbubble phenomenon observed during

echocardiography in patients with mechanical prosthetic cardiac valves. *Echocardiography*, 19(7), pp. 531–536.

Glazman, R.E., 1983. Effects of adsorbed films on gas bubble radial oscillations. *Journal of the Acoustical Society of America*, 74, pp. 980–986.

Gorce, J.M., Arditi, M. and Schneider, M., 2000. Influence of bubble size distribution on the echogenicity of ultrasound contrast agents. *Investigative Radiology*, 35, pp. 661–671.

Hamilton, M.F. and Blackstock, D.T., 1998. *Nonlinear Acoustics*. Academic Pr.

Harker, A.H. and Temple, J.A.G., 1988. Velocity and attenuation of ultrasound in suspensions of particles in fluids. *Journal of Physics D: Applied Physics*, 21, pp. 1576–1588.

Harvey, E.N., Barnes, D.K., McElroy, W.D., Whiteley, A.H., Pease, D.C. and Cooper, K.W., 1944. Bubble formation in animals. I. Physical factors. *Journal of Cellular and Comparative Physiology*, 24(1), pp. 1–22.

Henyey, F.S., 1999. Corrections to Foldy's effective medium theory for propagation in bubble clouds and other collections of very small scatterers. *Journal of the Acoustical Society of America*, 105, pp. 2149–2154.

Henyey, F.S., 2002. Reply to: Comment on: Corrections to Foldy's effective medium theory for propagation in bubble clouds and other collections of very small scatterers. *Journal of the Acoustical Society of America*, 111(4), pp. 1556–1559.

Herring, C., 1941. *Theory of the pulsations of the gas bubble produced by an underwater explosion*. Research report. Columbia University, Division of National Defense Research.

Herzfeld, K.F., 1930. Propagation of sound in suspensions. *Philosophical Magazine Series*, 9, pp. 741–751.

Hibbs, K., Mari, J.M., Stride, E., Eckersley, R.J., Noble, A. and Tang, M.X., 2007. Nonlinear propagation of ultrasound through microbubble clouds: a novel numerical implementation. In: *IEEE Ultrasonics Symposium*, pp. 1997–2000.

Hoff, L., Sontum, P.C. and Hovem, J.M., 2000. Oscillations of polymeric microbubbles: effect of the encapsulating shell. *Journal of the Acoustical Society of America*, 107, pp. 2272–2280.

Holt, R.G. and Gaitan, D.F., 1996. Observation of stability boundaries in the parameter space of single bubble sonoluminescence. *Physical Review Letters*, 77(18), pp. 3791–3794.

Hsieh, D.Y. and Plesset, M.S., 1961. Theory of rectified diffusion of mass into gas bubbles. *Journal of the Acoustical Society of America*, 33(2), pp. 206–215.

Hsu, A.A., Wong, T.M., How, J., Tan, J. and Tan, K.T., 1992. Retinal artery occlusion in a diver. *Singapore Medical Journal*, 33(3), pp. 299–301.

Huang, K.L., Wu, C.P., Chen, Y.L., Kang, B.H. and Lin, Y.C., 2003. Heat stress attenuates air bubble-induced acute lung injury: a novel mechanism of diving acclimatization. *Journal of Applied Physiology*, 94(4), pp. 1485–1490.

Imbert, J.P., Paris, D., Hugon, J. and Divetech, F., 2004. The arterial bubble model for decompression table calculations. In: *Proceedings of the 30th Annual Meeting of the European Underwater Baromedical Society, Ajaccio, France*, pp. 15–17.

Jones, S.F., Evans, G.M. and Galvin, K.P., 1999. Bubble nucleation from gas cavities: a review. *Advances in Colloid and Interface Science*, 80(1), pp. 27–50.

Kamath, V. and Prosperetti, A., 1990. Mass transfer during bubble oscillations. In: *Frontiers of Nonlinear Acoustics: Proceedings of the 12th Intl. Symp. on Nonlinear Acoustics, edited by MF Hamilton and DT Blackstock (Elsevier, New York, 1990)*, pp. 503–508.

Kargl, S.G., 2002. Effective medium approach to linear acoustics in bubbly liquids. *Journal of the Acoustical Society of America*, 111, pp. 168–173.

Kaul, S., 2008. Myocardial contrast echocardiography: a 25-year retrospective. *Circulation*, 118(3), pp. 291–308.

Keller, J.B. and Miksis, M., 1980. Bubble oscillations of large amplitude. *Journal of the Acoustical Society of America*, 68(2), pp. 628–633.

Kwan, J.J. and Borden, M.A., 2010. Microbubble dissolution in a multigas environment. *Langmuir*, 26(9), pp. 6542–6548.

Lax, M., 1952. Multiple scattering of waves II. The effective field in dense systems. *Physical Review*, 85(4), pp. 621–629.

Lee, Y.C., Wu, Y.C., Gerth, W.A. and Vann, R.D., 1993. Absence of intravascular bubble nucleation in dead rats. *Undersea and Hyperbaric Medicine*, 20, pp. 289–289.

Leighton, T.G., 1989. Transient excitation of insonated bubbles. *Ultrasonics*, 27(1), pp. 50–53.

Leighton, T.G., Jan. 2007. *Derivation of the Rayleigh-Plesset Equation in Terms of Volume*. Technical report. ISVR University of Southampton.

Leighton, T.G., Meers, S.D. and White, P.R., 2004. Propagation through nonlinear time-dependent bubble clouds and the estimation of bubble populations from measured acoustic characteristics. *Proceedings of the Royal Society A: Mathematical, Physical and Engineering Sciences*, 460(2049), pp. 2521–2550.

Linton, C.M. and Martin, P.A., 2005. Multiple scattering by random configurations of circular cylinders: Second-order corrections for the effective wavenumber. *Journal of the Acoustical Society of America*, 117, pp. 3413–3423.

Lloyd, P. and Berry, M.V., 1967. Wave propagation through an assembly of spheres: IV. Relations between different multiple scattering theories. *Proceedings of the Physical Society*, 91(3), pp. 678–688.

Löfstedt, R., Barber, B.P. and Putterman, S.J., 1993. Toward a hydrodynamic theory of sonoluminescence. *Physics of Fluids A*, 5, pp. 2911–2928.

Marmottant, P., van der Meer, S., Emmer, M., Versluis, M., de Jong, N., Hilgenfeldt, S. and Lohse, D., 2005. A model for large amplitude oscillations of coated bubbles accounting for buckling and rupture. *Journal of the Acoustical Society of America*, 118, pp. 3499–3505.

Martin, P.A., 2006. *Multiple Scattering: Interaction of Time-Harmonic Waves With N Obstacles*. Cambridge University Press.

Mazurel, G., Hee, J., Giacomini, L. and Guillerm, R., 1985. Ultrasonic detection of circulating bubbles in ewes exposed to simulated dives deeper than 800m under isobaric conditions and with unchanged gas mixtures. In: *Proceedings of the XIth Annual meeting of the EUBS. Goteborg, Sweden*.

McDonough, P.M. and Hemmingsen, E.A., 1984a. Bubble formation in crabs induced by limb motions after decompression. *Journal of Applied Physiology*, 57(1), pp. 117–122.

McDonough, P.M. and Hemmingsen, E.A., 1984b. Bubble formation in crustaceans following decompression from hyperbaric gas exposures. *Journal of Applied Physiology*, 56(2), pp. 513–519.

McDonough, P.M. and Hemmingsen, E.A., 1985a. A direct test for the survival of gaseous nuclei in vivo. *Aviation, Space and Environmental Medicine*, 56(1), pp. 54–56.

McDonough, P.M. and Hemmingsen, E.A., 1985b. Swimming movements initiate bubble formation in fish decompressed from elevated gas pressures. *Comparative Biochemistry and Physiology Part A: Molecular & Integrative Physiology*, 81(1), pp. 209–212.

Medwin, H., 1977. Counting bubbles acoustically: a review. *Ultrasonics*, 15(1), pp. 7–13.

Minnaert, M., 1933. XVI. On musical air-bubbles and the sounds of running water. *Philosophical Magazine Series*, 16(104), pp. 235–248.

Miura, M. and Vinogradov, O., 2008. The effect of probability of coalescence on the evolution of bubble sizes in a turbulent pipeline flow: a numerical study. *Computers and Chemical Engineering*, 32(6), pp. 1257–1264.

Morris, J., Ingenito, E.P., Mark, L., Kamm, R.D. and Johnson, M., 2001. Dynamic behavior of lung surfactant. *Journal of Biomechanical Engineering*, 123, pp. 106–113.

Mroz, K., 2012. *Decompression Modelling & Sensitivity Analysis of a Dual-Phase Model*. UCL CoMPLEX report. MSc. University College London.

Mulvana, H., Stride, E., Hajnal, J.V. and Eckersley, R.J., 2010. Temperature dependent behavior of ultrasound contrast agents. *Ultrasound in Medicine & Biology*, 36, pp. 925–934.

Mulvana, H., Stride, E., Tang, M.X., Hajnal, J.V. and Eckersley, R.J., 2012. The influence of gas saturation on microbubble stability. *Ultrasound in Medicine & Biology*, 38(6), pp. 1097–1100.

Nishimura, N., 2002. Fast multipole accelerated boundary integral equation methods. *Applied Mechanics Reviews*, 55, pp. 299–325.

O'Brien, JP., 2010. *The unified or complete decompression model for divers*. Technical report. VR Technology, 23/25 Bridge Street, Baille Gate Industrial Estate, Sturminster Marshall, Dorset, BH21 4DB, UK.

O'Brien, JP., 2011. Decompression model for divers. In: 53rd British Applied Mathematics Colloquium (11th–13th Apr. 2011). Birmingham, UK.

O'Brien, JP., Ovenden, N., Mulvana, H., Eckersley, R., Tang, M. and Stride, E., 2010. Nonlinear propagation models for ultrasound propagation through a polydisperse bubble population. In: 16th European Symposium on Ultrasound Contrast Imaging (19th–21st Jan. 2010). Rotterdam, The Netherlands.

O'Brien, JP., Ovenden, N. and Stride, E., 2011a. Accounting for the stability of microbubbles to multi-pulse excitation using a lipid-shedding model. *Journal of the Acoustical Society of America*, 130(4), EL180–EL185.

O'Brien, JP., Ovenden, N. and Stride, E., 2011b. On the dissolution of microbubble contrast agents in an ultrasound field. In: *Proceedings of Meetings on Acoustics*. Vol. 12.

O'Brien, JP., Stride, E. and Ovenden, N., (in press). Surfactant shedding and gas diffusion during pulsed ultrasound through a microbubble contrast agent suspension. *Journal of the Acoustical Society of America*. (Accepted for publication in April 2013).

Parlitz, U., Englisch, V., Scheffczyk, C. and Lauterborn, W., 1990. Bifurcation structure of bubble oscillators. *Journal of the Acoustical Society of America*, 88, pp. 1061–1077.

Paul, S., Katiyar, A., Sarkar, K., Chatterjee, D., Shi, W.T. and Forsberg, F., 2010. Material characterization of the encapsulation of an ultrasound contrast microbubble and its subharmonic response: strain-softening interfacial elasticity model. *Journal of the Acoustical Society of America*, 127(6), pp. 3846–3857.

Plesset, M.S., 1949. The dynamics of cavitation bubbles. *Journal of Applied Mechanics*, 16(3), pp. 227–282.

Plesset, M.S. and Prosperetti, A., 1977. Bubble dynamics and cavitation. *Annual Review of Fluid Mechanics*, 9(1), pp. 145–185.

Postema, M., Van Wamel, A., Lancée, C.T. and de Jong, N., 2004. Ultrasound-induced encapsulated microbubble phenomena. *Ultrasound in Medicine & Biology*, 30(6), pp. 827–840.

Powell, M.R., Waligora, J.M. and Norfleet, W., 1992. Decompression in simulated microgravity; bedrest and its influence on stress-assisted nucleation. In: *Annual Scientific Meeting*. Undersea and Hyperbaric Medical Society, Inc.

Prince, M.J. and Blanch, H.W., 1990. Bubble coalescence and break-up in air-sparged bubble columns. *AIChE Journal*, 36(10), pp. 1485–1499.

Prosperetti, A., 1984. Bubble phenomena in sound fields I. *Ultrasonics*, 22(3), pp. 115–124.

Prosperetti, A., Crum, L.A. and Commander, K.W., 1988. Nonlinear bubble dynamics. *Journal of the Acoustical Society of America*, 83, pp. 502–514.

Prosperetti, A. and Lezzi, A., 1986. Bubble dynamics in a compressible liquid. part 1. First-order theory. *Journal of Fluid Mechanics*, 168, pp. 457–478.

Rayleigh, L., 1896. *The Theory of Sound*. Macmillan.

Rayleigh, L., 1917. On the pressure developed in a liquid during the collapse of a spherical cavity. *Philosophical Magazine Series*, 34(200), pp. 94–98.

Sarkar, K., Katiyar, A. and Jain, P., 2009. Growth and dissolution of an encapsulated contrast microbubble: effects of encapsulation permeability. *Ultrasound in Medicine & Biology*, 35(8), pp. 1385–1396.

Sarkar, K., Shi, W.T., Chatterjee, D. and Forsberg, F., 2005. Characterization of ultrasound contrast microbubbles using in vitro experiments and viscous and viscoelastic interface models for encapsulation. *Journal of the Acoustical Society of America*, 118, pp. 539–550.

Sette, D. and Wanderlingh, F., 1962. Nucleation by cosmic rays in ultrasonic cavitation. *Physical Review*, 125(2), pp. 409–417.

Sewell, C.J.T., 1911. The extinction of sound in a viscous atmosphere by small obstacles of cylindrical and spherical form. *Philosophical Transactions of the Royal Society of London, Series A*, 210, pp. 239–270.

Skaropoulos, N.C., Yagridou, H.D. and Chrissoulidis, D.P., 2003. Interactive resonant scattering by a cluster of air bubbles in water. *Journal of the Acoustical Society of America*, 113, pp. 3001–3011.

Stride, E., 2008. The influence of surface adsorption on microbubble dynamics. *Philosophical Transactions of the Royal Society of London, Series A*, 366(1873), pp. 2103–2115.

Stride, E., Ovenden, N. and O'Brien, JP., 2011. Numerical methods in nonlinear acoustics in bubbly liquids. In: C. Vanhille and C. Campos-Pozuelo eds. *Computational Methods in Nonlinear Acoustics: Current Trends*. Research Signpost, pp. 47–68.

Stride, E. and Saffari, N., 2003. Microbubble ultrasound contrast agents: a review. *Proceedings of the Institution of Mechanical Engineers, Part H: Journal of Engineering in Medicine*, 217(6), pp. 429–447.

Stride, E. and Saffari, N., 2005. Investigating the significance of multiple scattering in ultrasound contrast agent particle populations. *IEEE Transactions on Ultrasonics, Ferroelectrics and Frequency Control*, 52(12), pp. 2332–2345.

Strutt, J.W., 1871. XV. On the light from the sky, its polarization and colour. *Philosophical Magazine Series*, 41(271), pp. 107–120.

Tikuisis, P. and Gerth, W.A., 2003. Decompression theory. In: A. Brubakk and T. Neuman eds. *Bennett and Elliott's Physiology and Medicine of Diving*. Saunders Book Company. Ch. 10, p. 419.

Todnem, K., Nyland, H., Skeidsvoll, H., Svihus, R., Rinck, P., Kambestad, B.K., Riise, T. and Aarli, J.A., 1991. Neurological long term consequences of deep diving. *British Journal of Industrial Medicine*, 48(4), pp. 258–266.

Trilling, L., 1952. The collapse and rebound of a gas bubble. *Journal of Applied Physics*, 23(1), pp. 14–17.

Tsiglifis, K. and Pelekasis, N.A., 2008. Nonlinear radial oscillations of encapsulated microbubbles subject to ultrasound: the effect of membrane constitutive law. *Journal of the Acoustical Society of America*, 123, pp. 4059–4070.

Twersky, V., 1962a. On scattering of waves by random distributions. I. Free-space scatterer formalism. *Journal of Mathematical Physics*, 3, pp. 700–715.

Twersky, V., 1962b. On scattering of waves by random distributions. II. Two-space scatterer formalism. *Journal of Mathematical Physics*, 3, pp. 724–734.

Urick, R.J., 1947. A sound velocity method for determining the compressibility of finely divided substances. *Journal of Applied Physics*, 18, pp. 983–987.

Urick, R.J. and Ament, W.S., 1949. The propagation of sound in composite media. *Journal of the Acoustical Society of America*, 21, pp. 115–119.

Van Liew, H.D. and Burkard, M.E., 1993. Density of decompression bubbles and competition for gas among bubbles, tissue and blood. *Journal of Applied Physiology*, 75(5), pp. 2293–2301.

Van Wijngaarden, L., 1968. On the equations of motion for mixtures of liquid and gas bubbles. *Journal of Fluid Mechanics*, 33(03), pp. 465–474.

Vanhille, C. and Campos-Pozuelo, C., 2009. Nonlinear ultrasonic waves in bubbly liquids with nonhomogeneous bubble distribution: numerical experiments. *Ultrasonics Sonochemistry*, 16, pp. 669–685.

Vann, R.D., 2004. Mechanisms and risks of decompression. In: A. Bove and J. Davis eds. *Diving medicine. 4th ed. Philadelphia*. Saunders Book Company. Ch. 7, pp. 127–164.

Vann, R.D., Butler, F.K., Mitchell, S.J. and Moon, R.E., 2011. Decompression illness. *Lancet*, 377(9760), pp. 153–164.

Viti, J., Mori, R., Guidi, F., Tortoli, P. and de Jong, N., 2011. Nonuniform oscillations of deflating bubbles - a pilot study. In: *The 16th European Symposium on Ultrasound Contrast Imaging*, pp. 7–9.

Walder, D.N. and Evans, A., 1974. In vivo nuclear fission in the aetiology of decompression sickness. *Nature*, 252, pp. 696–697.

Ward, C.A., Johnson, W.R., Venter, R.D., Ho, S., Forest, T.W. and Fraser, W.D., 1983. Heterogeneous bubble nucleation and conditions for growth in a liquid–gas system of constant mass and volume. *Journal of Applied Physics*, 54(4), pp. 1833–1843.

Waterman, P.C. and Truell, R., 1961. Multiple scattering of waves. *Journal of Mathematical Physics*, 2, pp. 512–537.

Wienke, B.R., 1990. Reduced gradient bubble model. *International Journal of Biomedical Computing*, 26, pp. 237–256.

Wienke, B.R., 2008. *Basic decompression: theory and application*. Best Pub Co.

Wisløff, U., Richardson, R.S. and Brubakk, A.O., 2003. NOS inhibition increases bubble formation and reduces survival in sedentary but not exercised rats. *Journal of Physiology*, 546(2), pp. 577–582.

Wisløff, U., Richardson, R.S. and Brubakk, A.O., 2004. Exercise and nitric oxide prevent bubble formation: a novel approach to the prevention of decompression sickness? *Journal of Physiology*, 555(3), pp. 825–829.

Workman, R.D., 1957. *Calculation of air saturation decompression tables*. Technical report. U.S. Navy Experimental Diving Unit.

Ye, Z. and Ding, L., 1995. Acoustic dispersion and attenuation relations in bubbly mixture. *Journal of the Acoustical Society of America*, 98, pp. 1629–1636.

Ye, Z. and Hsu, H., 2001. Phase transition and acoustic localization in arrays of air bubbles in water. *Applied Physics Letters*, 79, pp. 1724–1726.

Yount, D.E., 1979. Skins of varying permeability: a stabilization mechanism for gas cavitation nuclei. *Journal of the Acoustical Society of America*, 65(6), pp. 1429–1439.

Yount, D.E., 1982. On the evolution, generation and regeneration of gas cavitation nuclei. *Journal of the Acoustical Society of America*, 71, pp. 1473–1481.

Yount, D.E. and Hoffman, D.C., 1986. On the use of a bubble formation model to calculate diving tables. *Aviation, Space and Environmental Medicine*, 57(2), pp. 149–156.